Galectin-1:
A Synthetic and Biological Study of a Tumor Target

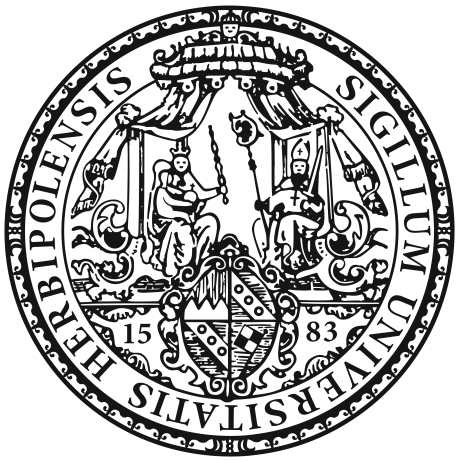

Dissertation

zur Erlangung des naturwissenschaftlichen Doktorgrades
der Julius-Maximilians-Universität Würzburg

vorgelegt von
Diplom-Chemikerin

Nadja Luisa Bertleff-Zieschang

aus Viernheim

Würzburg 2014

Eingereicht bei der Fakultät für Chemie und Pharmazie am: 17.06.2014

Gutachter der Dissertation:

1. Gutachter: Prof. Dr. Jürgen Seibel

2. Gutachter: Prof. Dr. Utz Fischer

Prüfer des öffentlichen Promotionskolloquiums:

1. Prüfer: Prof. Dr. Jürgen Seibel

2. Prüfer: Prof. Dr. Utz Fischer

3. Prüfer: Prof. Dr. Tobias Hertel

4. Prüfer: Prof. Dr. Christoph Lambert

5. Prüfer: Prof. Dr. Markus Sauer

Datum des öffentlichen Promotionskolloquiums: 28.07.2014

Doktorurkunde ausgehändigt am:

Experimental studies of the presented work were performed from March 2010 until April 2014 at the Institute of Organic Chemistry, Julius-Maximilians-Universität Würzburg under supervision of Prof. Dr. Jürgen Seibel.

List of Publications

Peer-reviewed Publication

J. Seibel, S. König, A. Göhler, S. Doose, E. Memmel, N. Bertleff, M. Sauer, *Expert Rev. Proteomics* **2013**, *10*, 25-31.

"Investigating infection processes with a workflow from organic chemistry to biophysics: the combination of metabolic glycoengineering, super-resolution fluorescence imaging and proteomics"

Non Peer-reviewed Publication

N. Bertleff, J. Seibel *Chem. unserer Zeit* **2013**, *47*, 144.

"Galectin: Sweet Future for Cancer"

Profile

N. Bertleff *Scientific American* **2013**.
http://www.scientificamerican.com/article/2013-lindau-nadja-bertleff/

"30 under 30: Designing New Ways to Stop Tumors"

Conference Lectures

N. Bertleff *17th European Carbohydrate Symposium*, Tel Aviv, Israel, 11. July **2013**.

"Galectin-1: A sweet way to fight cancer"

N. Bertleff *63rd Lindau Nobel Laureate Meeting* Lindau, Germany, 04. July **2013**.

"Galectin-1: Sweet prospects for cancer research"

N. Bertleff *5th European Conference for Chemistry of Life Sciences* Barcelona, Spain, 10. June **2013**.

"Galectin-1 - Sweet weapons in the fight of cancer"

N. Bertleff *Vernetzungs- und Informationssymposium SPP1623* Berlin, Germany, 20. Oct. **2011**.

"Synthetic metabolic glycoengineering for cell surface modification"

Poster Presentations

N. Bertleff, C. Grimm, J. Seibel *Chem-SyStM 2012* Würzburg, Germany, 07. Dec. **2012**.

"Galectin-1: A sweet approach to fight cancer"

N. Bertleff, M. Timm, A. Göhler, S. Doose, M. Sauer, C. Grimm, J. Seibel *243rd National Meeting & Exposition* San Diego, USA, 25.-29. March **2012**.

"Self-generating synthesis for the design of galectin-1 inhibitors"

To my parents

Contents

Chapter 1

Motivation

"The same kind of concentrated effort that split the atom and took man to the moon should be turned toward conquering this dread disease." (Richard Nixon, 1971)
The signing of the US National Cancer Act of 1971 by the then President Richard Nixon is commonly seen as the beginning of the so-called "War on Cancer". Despite indisputable progress since then cancer still is one of the predominant health threats of our generation. The World Health Organization (WHO) states on its homepage[i] that cancer accounted for 8.2 million deaths in 2012 and prognoses indicate that the numbers will continuously rise within the next years even though cancer mortality can be significantly reduced if the disease is diagnosed at an early stage.
Historically, cancer treatment has progressed from nitrogen mustard medication in the 1940s, over surgery and radiotherapy to current targeted chemotherapies.[1] However, cancer is a highly complex disease and shows a large degree of versatility and resilience. Several cancer types have developed multidrug resistance - one of the major challenges in the present combat against cancer - and do not respond to chemotherapeutics anymore.[1] Further the administration of effective chemotherapeutics often affects healthy tissue as well and leads to severe side effects.
Tremendous effort has been made during the last years to gain a better understanding of cancer biology and to translate these findings into diagnostic tools and therapeutic approaches. In a seminal paper Hanahan and Weinberg proposed hallmark cancer traits that comprise general physiological aberrancies and provide a basic framework for characterization of neoplastic tissue (Fig. 1.1).[2] During transformation from healthy to tumorigenic tissue cells progressively acquire these capabilities and finally become malignant. Malignant cells follow an aberrant reproduction program and control proliferation independently of extracellular growth signals. They are capable of developing mechanisms of resistance to evade the immune response and even more insidious, cancer cells can migrate from the tumor lesion to distal sites of the body in a

[i] "Cancer". *who.int*. World Health Organization. Web. 14 May 2014. <http://www.who.int/cancer/en/>

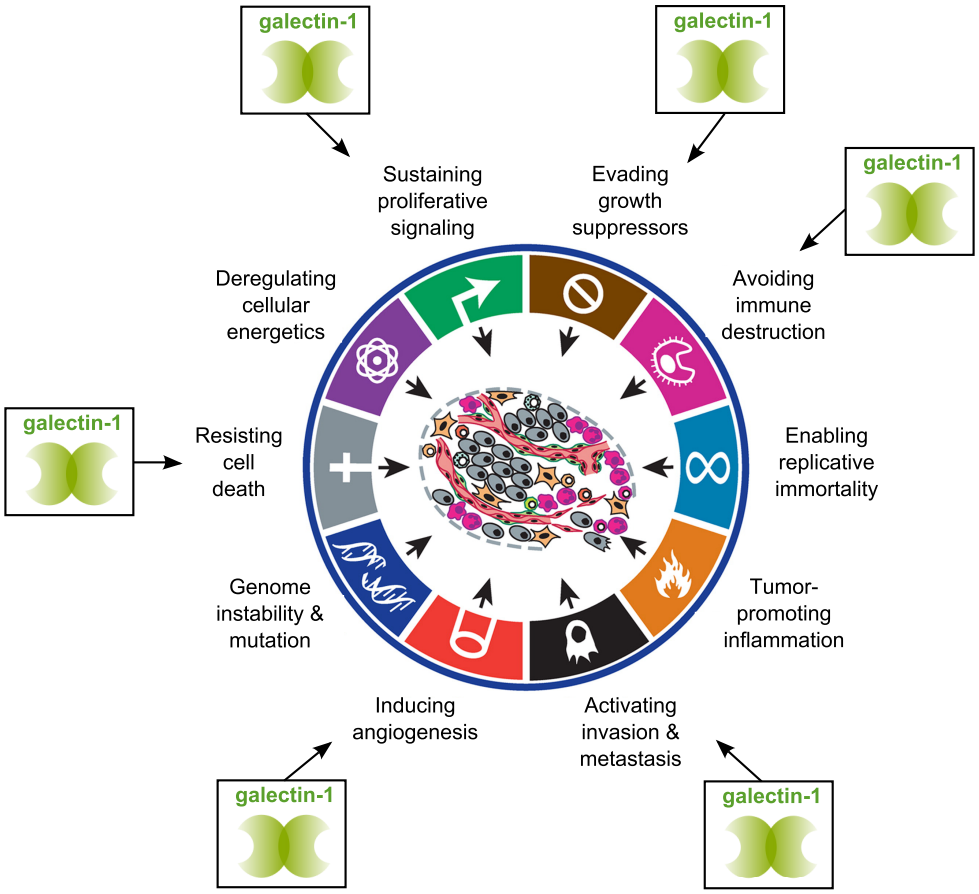

Fig. 1.1 Hallmarks of cancer as proposed by Hanahan and Weinberg.[2] Galectin-1 modulates various of these pathological processes.[3] Adapted and modified with permission from ref. 2. Copyright © 2011, Elsevier.

process called metastasis that drastically reduces the chance of a lasting cancer cure.[4] Further, ostensibly normal cells are efficiently recruited from maligant cells to form a specific and highly complex tumor microenvironment.[2] The tumor-associated stroma is actively involved in angiogenesis, the formation of novel blood vessels from preexisting ones, for proliferation and migration of neoplastic tissue. Indeed, the complexity of tumors has increasingly been considered to reach or even surpass that of healthy organs.[2] Hanahan and Weinberg envisioned that interfering with key players of one or even more hallmark traits may lead to a collapse of the sophisticated interplay in tumor physiology and inspire novel therapeutic targets.[2]

Galectin-1, a β-galactoside binding protein, has evolved to a protagonist in current cancer research in this context and experimental evidences indicate that galectin-1 modulates various of the illustrated hallmark processes (Fig. 1.1).[3] The homodimeric protein is highly overexpressed by tumor cells and induces proliferative, angiogenetic and migratory signals through interacting with carbohydrate-based binding epitopes

of glycan structures on cell surfaces.[3] Galectin-1 further has a striking impact on the negative regulation of T cell survival and confers immune privilege to malignant tissue.[5] Due to its participation in multiple tumor-associated processes galectin-1 has been proposed as promising target for therapeutic and diagnostic application. However, first galectin-1-directed cancer drugs are yet to reach the market and most of the cellular signaling pathways remain concealed.[3]

This situation strongly motivated the work of this thesis at the interface of chemistry, biophysics and medicine to develop and evaluate potent galectin-1 ligands for future-oriented drug candidates and diagnostic tools. The introductory chapter will give an overview of current drug discovery strategies and provide a comprehensive insight into the protein family of galectins, the involvement of galectin-1 in cancer progression and efforts to target this protein *in vitro* and *in vivo*. Chapter 3 expresses the objectives and envisioned goals of this work followed by an outline of the relevant methods and theoretic backgrounds for performing and assessing the experimental work (chapter 4). Chapter 5 comprises the results of the presented thesis structured along three galectin-1 projects (1) the design and evaluation of tailor-made galectin-1 ligands, (2) their implementation in diagnostic approaches and (3) the investigation of galectin-1 communication pathways on Neuroblastoma cell surfaces by high resolution microscopy. The work concludes with a summary and the experimental section of biochemical and synthetic studies.

Chapter 2

Introduction

2.1 Drug Development: State of the Art

Drug discovery has evolved dramatically since the first isolation of morphine from opium extract by F. W. Sertürner in the early 19th century[6] to target-directed structure design in modern times. At the turn of the 20th century Paul Ehrlich constituted the idea that parasites, bacteria and tumor cells display specific chemoreceptors different to those of healthy human cells.[7] This pioneering concept introduced a novel therapeutic era and he successfully implemented the first chemotherapy by combating spirochaetes bacteria in patients, a pathogen causing Syphilis, with the arsenic compound Arsphenamine (manufactured as Salvarsan by Hoechst AG).[8] The following decades were coined by Alexander Fleming's discovery of penicillin[9] and the availability of antibiotics opened the door for curative treatment of a wide range of bacterial infections.
Since then, medicinal chemistry, pharmacology and the advent of molecular biology pushed major efforts in new drug developments and determined medicinal progress in an unrivaled manner.[10] Genomic science and the access to recombinant protein technologies as well as the production of monoclonal antibodies contributed to novel therapeutic strategies and permitted a deeper understanding of cellular processes on a molecular level. Improvements in biotechnical engineering has made available a large number of medically relevant targets and molecular modeling has enabled the prediction of potential drug candidates with the preferable pharmacokinetic profile.[11,12] Advances in structural biology and in analytic tools such as NMR spectroscopy and X-ray crystallography have contributed to the elucidation of molecular interactions and facilitated the assessment of structure activity relation (SAR).[13] The associated accelerating process of identifying novel targets and increasing compound libraries have demanded for faster screening methods as well as automatization and miniaturization techniques and have influenced industrial drug research and development lastingly.[14] While natural products represented a main source for investigation in pharmaceutical

companies in the period of 1970-1980 and 49% of all approved drugs in the subsequent 20 years were either natural products, semi-synthetic analogues or naturally inspired synthetic compounds numbers have been steadily decreasing during the last decade.[15] This finding can be attributed to several reasons but is essentially based on high-throughput screening (HTS) assays, the predominant identification method of novel lead structures. Libraries of so-called "screen-friendly" pure and small molecules cover a wide range of chemical diversity, are examined in rather short time and are attractive for combinatorial approaches.[14,15] Further, leading pharmaceutical organizations tend to negotiate infectious diseases, a field that was dominated by natural molecules in the past,[16] and natural products themselves inherently feature unfavorable characteristics[14,15] such as seasonal and environmental fluctuations, potential loss of source and collection uncertainties arising from the Rio Convention of Biodiversity.[17] Isolation of a promising compound may provide only insufficient amounts for screening assays or structure determination and a predominant concern in industrial companies is the risk of duplication or in other words the isolation of a known, non-patentable structure.[14]

HTS is the prevailing methodology in pharmaceutical drug investigation[18] and the screen of large libraries of up to 10^6 compounds is a versatile approach to rapidly evaluate various medically relevant receptors.[19] However, this strategy suffers from several drawbacks arising from the generalization aspect of individual targets. Compounds in HTS assays are rather large molecules with a molecular weight M of 250-600 g/mol and hit structures usually involve only few atoms or functional groups in the interaction, thus molecules are generally highly inefficient binders (Fig. 2.1).[19] False positives result from *in vitro* bioassays due to poor thermodynamic solubility and aggregation

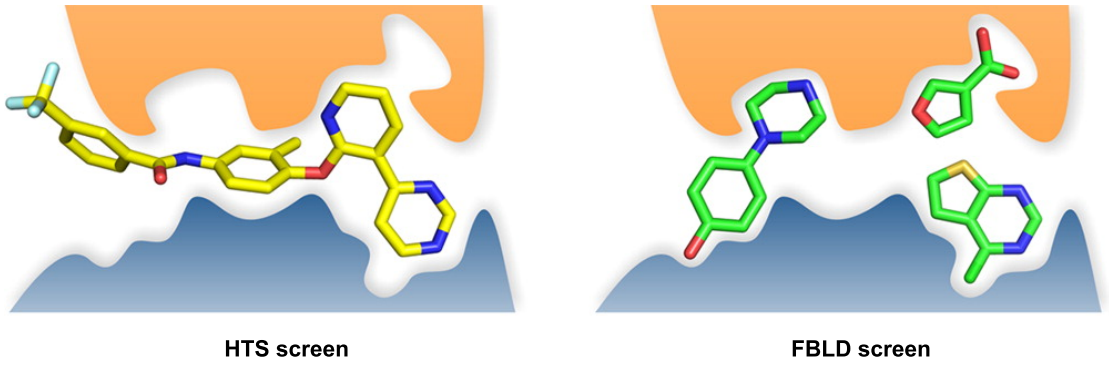

Fig. 2.1 Illustrated HTS and FBLD screening by comparison. Hits resulting from HTS are low efficient binders and epitopes interact suboptimal with the target while the fragment approach provides highly specific though low affine ligands. Reprinted with permission from ref. 13. Copyright © 2012, American Chemical Society.

effects. Additionally, even genuine hits may not represent attractive lead structures and the lack of structural details about the binding event may essentially hamper the subsequent optimization process. Finally, high structural diversity of a screening library from a chemist's perspective does not necessarily reflect diversity as "perceived" by a physiological target.[10] In this regard, Dixon and Villar demonstrated that a protein recognizes a wide variety of diverse compounds with a similar affinity while minor changes in the structure of strong ligands significantly decrease affinities.[20]

Fragment-based lead discovery (FBLD) has evolved during the past 20 years as a complementary approach in drug research[19,21] to overcome the limitations of HTS and became established in pharmaceutical industry through major contributions of Abott[22] and Astex Pharmaceuticals[23,24]. The conceptual origin of FBLD can be traced to a landmark paper of Jencks[25] who envisioned that a strong binder can be dissected into small, low affine but high efficient[i] fragments each contributing to build a potent drug compound (Fig. 2.1). As the number of potential ligands for a specific target decreases exponentially with the number of heavy atoms the fragment approach requires significantly less compounds to be experimentally or virtually screened to comprehensively address chemical variety.[27] Another advantageous aspect of FBLD is the control of physicochemical properties during lead progression. Lipinski *et al.* pointed out that promising drug-like molecules for oral administration conform the "rule of five" including constraints regarding the molecular mass (< 500 Da), lipophilicity ($\log P < 5$) and sum auf hydrogen bonds (≤ 5).[28] The high attrition rate in pharmaceutical industry from initial hit to drug approval is largely owed to poor absorption, distribution and metabolism attributes. In this context, FBLD offers the chance to directly influence the pharmacological profile during fragment linking and growing rather than during lead optimization of drug-like molecules identified by HTS. Despite the optimistic outline FBLD is confronted with two major challenges, first, the synthetic linkage or expansion of fragments in an enthalpic and entropic favorable manner and second, the implementation of sensitive biophysical detection methods and structure-based analysis to identify low affine low-molecular-weight ligands with simultaneous or subsequent elucidation of the binding mode. The following techniques have succeeded in addressing this demand and find widespread application in academia and pharmaceutical industry (Fig. 2.2).

Fluorescence-based thermal shift (TS) permits rapid and label-free identification of fragments that bind and thereby stabilize the three-dimensional arrangement of the targeted protein.[29] The screening technique exploits fluorescence activity of a variety of dyes in a hydrophobic environment such as non-polar sites of denaturated proteins while radiated emission is quenched in aqueous solution. Hence, the assay tracks the

[i] ligand efficiency is defined as "the ratio of free energy of binding to the number of heavy atoms"[26], cf. section 5.1.4

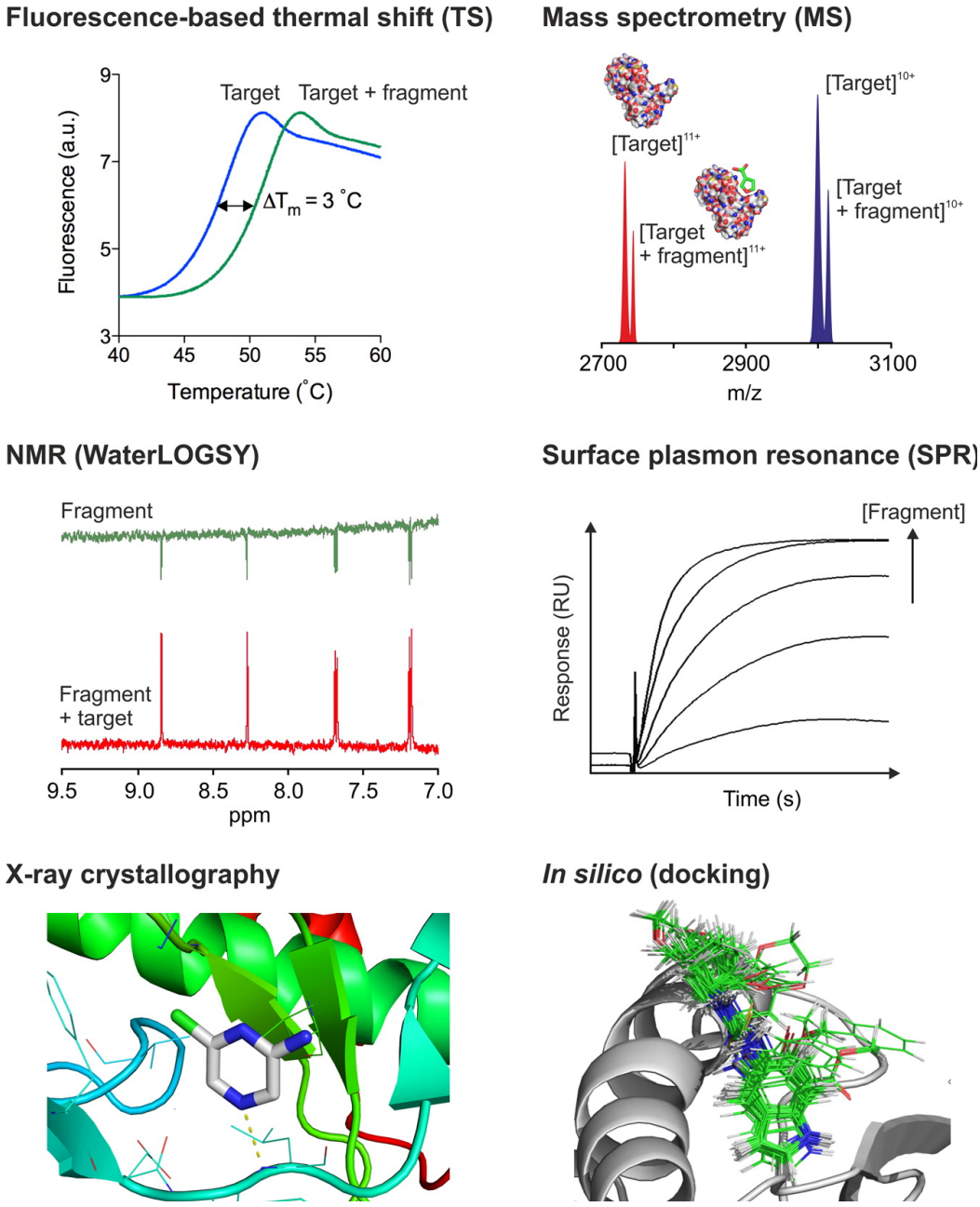

Fig. 2.2 Outline of techniques for probing fragment-target interactions. TS monitors the increase of thermal stability caused by fragment binding. MS detects formation of noncovalent fragment-target complex in the gas phase. NMR (e.g. WaterLOGSY) techniques are used to display magnetization transfer from the target to the bound fragment. SPR measures fragment affinity in relation to the response given at individual fragment concentrations. X-ray crystallography unambigouosly elucidates the binding geometry of even weak binders. *In silico* screens provide valuable and complementary information to experimental methods. Reprinted with permission from ref. 13. Copyright © 2012, American Chemical Society.

thermal unfolding process of the protein in presence of a fluorescent dye and monitors the thermal shift upon ligand binding compared to free protein. SYPRO orange is an attractive dye for TS screens due to its excitation wavelength $\lambda_{exc} = 492$ nm and the 500% increase in fluorescence intensity when surrounded by unfolded protein versus aqueous solution.[29,30] **Electronspray ionization mass spectrometry (ESI-MS)** represents a further label-free method for detection of noncovalent protein-ligand interactions.[31,32] For a long time, MS played a minor role in the drug development process and served primarily as analytical tool for evaluating molecule purity or the analysis of the compound-specific pharmacokinetic properties from drug absorption over metabolism to excretion.[33] In seminal work Ganem *et al.* gave experimental evidence that noncovalent molecule complexes can be transferred from solution into the gas phase by soft ESI and analyzed according to their mass spectrometric profile.[31] ESI-MS as tool for detection of novel interactions facilitates screening of entire ligand cocktails, where each binding event is characterized by the fragment's specific fingerprint defining the *x*-axis of the mass spectrum.[33,34] Relative signal intensities on the *y*-axis contribute valuable insights into affinity and specificity of the interaction and have been exploited for characterization of distinct biomolecular complexes as well as the assessment of dissociation constants of different size (nM-mM).[35–37] Automatization of mass spectrometric analyses and the high sensitivity of this technique requiring nominal quantities of protein and ligands are additional benefits.

Isothermal titration calorimetry (ITC) unravels enthalpic and entropic contributions of a receptor-ligand interaction and provides valuable information about affinity and stoichiometry of the binding event.[38,39] ITC monitors the change in binding enthalpy by measuring the heat released or absorbed upon ligand addition to the protein sample.[40] The method is label-free and necessitates no immobilization of the protein of study, however, its application as screening technique is limited to individual measures rather than to investigate fragment mixtures. Further the study of low-affinity systems requires essential amounts of both, receptor and ligand which might be a confining factor.

In contrast, **surface plasmon resonance (SPR)** assays demand minimal quantities of the receptor that is covalently attached to an activated dextran functionalized gold chip connected to a microfluidic flow channel for fragment interaction.[41] The technique is essentially based on the generation of surface plasmons by electromagnetic radiation in the gold layer that is coated on the interface of two media with different refractive indices (glass-water). The energy and momentum required for excitation of these plasmons (plasmon resonance wavelength) is highly dependent on the chemical nature of the gold environment and hence, differs when interaction between the immobilized receptor and the injected ligand increases surface mass.[13] SPR biosensors are capable of assessing affinity (dissociation constant), kinetic parameters (association and dissociation rates) and the inhibitory potential (IC_{50}) of a distinct binding event. Moreover, reliable screening of

whole fragment libraries and evaluation of small fragments with low molecular masses ($\geq$ 100 Da) have become feasible due to recent developments in SPR technology.[42,43] All techniques and approaches described so far give experimental evidence of a binding event between a potential ligand and the targeted receptor, however, they provide no information about SAR and the binding geometry, a crucial aspect not only in FBLD. In this context, NMR spectroscopy and X-ray crystallography are prevailing methods to gain detailed insights into structural aspects of molecular interactions.[13] **NMR spectroscopy** is performed in highly concentrated aqueous solution rather than in solid phase crystals and allows observation and identification of dynamic processes. Common NMR methods for binding evaluation are based on the transfer of saturated magnetization and include water-ligand observation with gradient spectroscopy (WaterLOGSY)[45,46] and saturation transfer difference (STD) NMR spectroscopy[47]. The former comprises the saturation of bulk water resonances and the concomitant saturation transfer to ligands via interfacial water networks on the protein surface. The method is highly sensitive and signals of binding molecules appear with opposite sign in the resulting spectrum, however, without characterizing the ligand binding geometry and active site. In an STD NMR experiment the protein itself is saturated by irradiation at frequencies of exclusive protein resonances (-1 ppm) and magnetization transferred from the receptor to the ligand. Substraction of a spectrum without pre-irradiation generates a difference spectrum in which only resonances of binding fragments remain with signal intensities reflecting binding participation as interacting epitopes gain a higher degree of saturation.[47] The STD NMR experiment allows rapid screening of fragment mixtures with isolated resonances of each compound as sole prerequisite and requires only few amounts of protein (5-10 μg per NMR sample).[44] Abbott were the first to successfully implement SAR by NMR for the development of potent inhibitors of the FK506 binding protein (FKBP), an inhibitor of the serine-threonine phosphatase and T cell activator calcineurin.[22] FKBP was ^{15}N labeled and screened against a library of fragment compounds. ^{15}N-heteronuclear single-quantum correlation (^{15}N-HSQC) detected fragment binding by changes of the backbone ^{15}N- or ^{1}H-amide chemical shifts and allowed the assignment of several low affine fragments addressing distinct but proximal sites within the binding domain. Structural

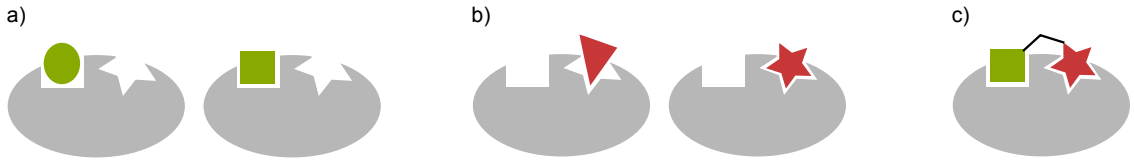

Fig. 2.3 Schematic illustration of SAR. Binding fragments are identified either by NMR or X-ray crystallography and optimized with regard to their targeting ability (a, b). Efficient binders are linked to a potent and highly target-specific ligand (c). Adpated from ref. 44.

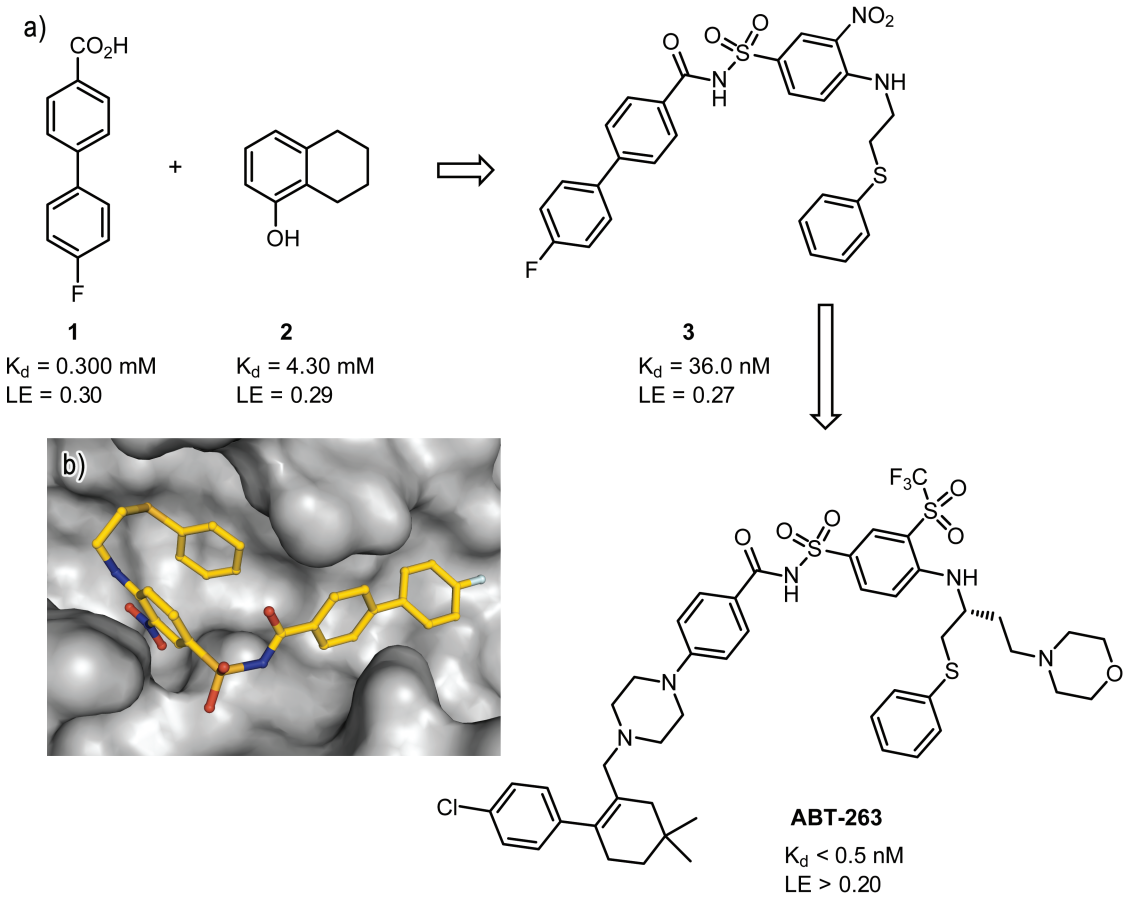

Fig. 2.4 Design of Bcl-X_L inhibitor ABT-263. a) 2D NMR spectroscopy identified initial binding fragments **1** and **2** that address proximal sites within the binding domain.[48] Synthetic elaboration provided the lead structure **3** which guided the development of ABT-263 with optimized properties regarding the pharmacokinetic profile and oral bioavailability. ABT-263 is currently in clinical trials against lung cancer and hematological malignancies.[49] b) Binding mode of **3** as determined by NMR experiments (pdb code 1YSI).[49]

optimization of individual binders and the design of an appropriate linker unit to connect fragments without introducing steric clashes or imposing an altered binding geometry on the fragments finally provided an inhibitor molecule with nanomolar affinities (Fig. 2.3). Similarly, Elmore *et al.* constructed the inhibitor ABT-263 of Bcl-2 family proteins to interfere with the helical peptide structure of the interaction partner (Fig. 2.4).[27,49] Bcl-2 and Bcl-X_L are members of the Bcl-2 family and play a key role in the regulation of programmed cell death.[48] Overexpression of both representatives by tumor cells is asscociated with inhibition of apoptosis and the chemo-resistance to therapy. 2D NMR spectroscopy identified initial binding fragments and attributed interactions at proximal sites within the binding domain.[48] Optimization of lead structure **3** with regard to the pharmacokinetic profile and oral bioavailability led to ABT-263[49] currently in clinical

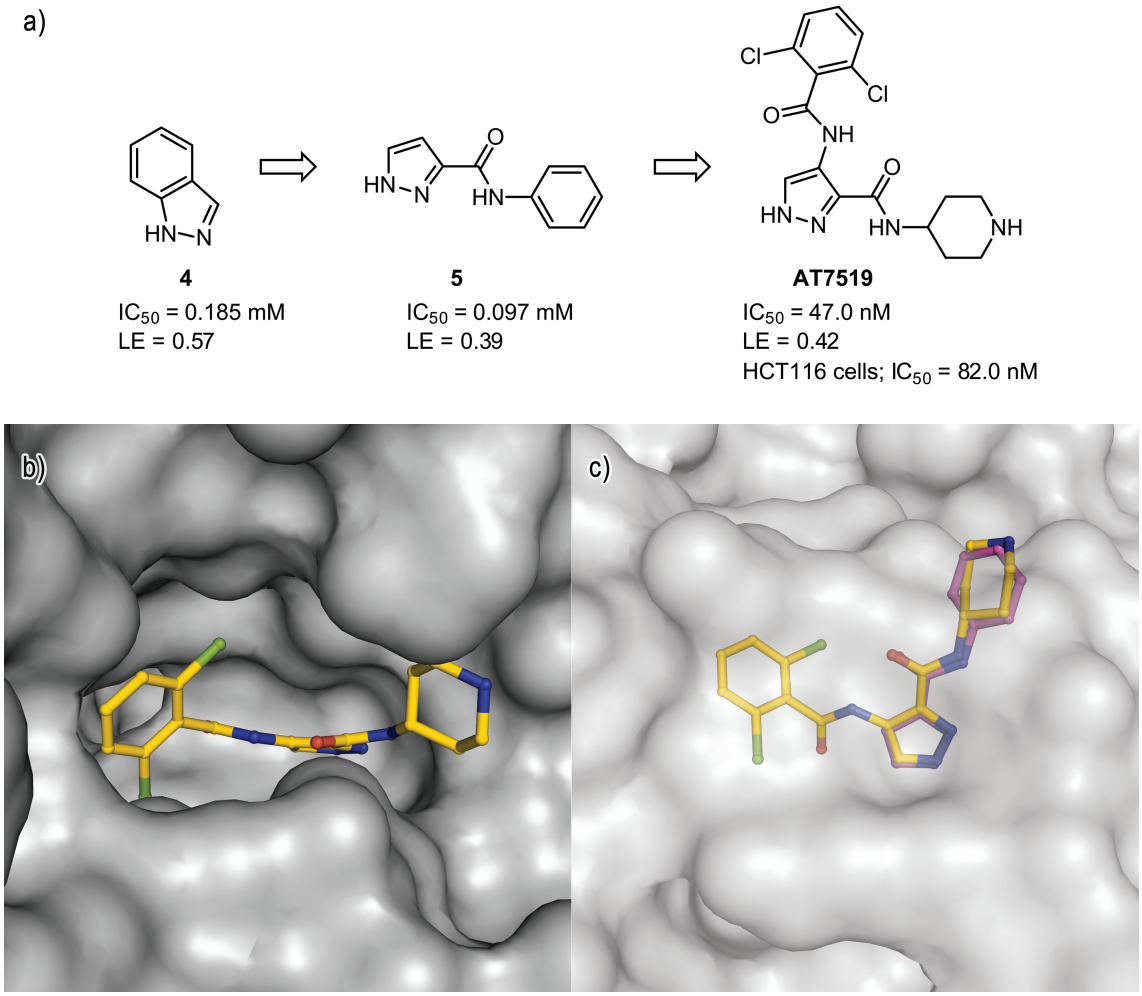

Fig. 2.5 Design of CDK 1 and 2 inhibitor **AT7519**. a) Indazole **4** binds to the ATP kinase binding pocket as experimentally determined by X-ray crystallography.[50] Structural expansion of the ligand scaffold led to **AT7519** with excellent cell activity and *in vivo* efficacy and now in phase I/II clinical trials against tumor growth.[13] b) Binding mode of **AT7519** within the deep and narrow binding pocket of CDK2 (pdb code 2VU3).[50] c) Superposition of **AT7519** and **5** shows a highly conserved binding mode of the growing inhibitor (pdb code 2VU3, 2VTL).[50]

trials against lung cancer and hematological malignancies.[27,49,51] Protein isotope labeling for twodimensional NMR experiments is a powerful tool to identify ligands and to define the binding domain, however, it requires substantial amounts of protein and is limited to polypeptides with a molecular mass of less than 30 kDa.[52]

The second technique to investigate receptor ligand interactions on an atomic level, **X-ray crystallography** of macromolecules, permits characterization of the ligand-binding site with high structural precision. A variety of soluble biomolecules proved to be crystallizable[52] and advances in automation and miniaturization of single crystallization

steps, in-house access to X-ray radiation (rotating anode, synchrotron) and progress in software development for data evaluation have promoted X-ray crystallography to a versatile tool for guiding structure-based drug design.[23,52] Ligand binding is validated either by soaking crystals of the biomolecule of interest with high-concentration single molecules or fragment cocktails where individual components essentially differ in shape to unambiguously assign electron densities to binding fragments. Cocrystallization represents an alternative approach for generating receptor-ligand complexes if soaking fails or induces large conformational shifts that damage the crystal. Diffraction to better than 2.0-2.5 Å is generally prerequisite to obtain high-resolution data for the following optimization and expansion procedure.[13] Astex Pharmaceuticals is leading in fragment screening with high throughput X-ray crystallography and succeeded in designing a potent cyclin-dependent kinase 2 (CDK2) inhibitor by this approach.[50] CDKs belong to the family of serine-threonine kinases and play a key role in the regulation of cell cycle progression.[53,54] Malfunction of this control element is asccociated with tumor growth and aberrant cell proliferation, hence CDK inhibition presents a promising strategy in cancer chemotherapy. By screening a library of 500 fragments against CDK2 Wyatt and coworkers identified more than 30 low-affinity hits, all addressing the kinase ATP binding domain within the cocrystals.[50] Target-directed optimization of indazole, an efficient low-molecular weight binder, and consideration of pharmacokinetic properties as well as the cellular activity against HCT116 tumor cells guided the development of **AT7519**, currently in phase I/II clinical trials against tumor growth (Fig. 2.5).[13,27,50]

Advances in molecular biology and biophysical analysis during the last decades have constituted a new generation of lead discovery based on the increasing understanding of complex physiological correlations and aberrations. Target-directed development of tailor-made drugs in combination with analytical tools to profoundly study binding properties and cellular activity has already entered the pharmaceutical market and it remains to be seen how drug development will be shaped in the future.

2.2 Galectins

"God must love galectins; He made so many of them"[55] These words formed the title of an early mini review by Cooper and Barondes in 1999 and highlighted the growing interest in the protein family at the end of that decade. Since then, the number of research articles has steadily increased[56] with more than 1000 publications in 2012 and 2013 found in Scifinder with the search subject "galectin" (Fig. 2.6). Nowadays the heading, however, is questionable as experimental evidence clearly implicate the involvement of many galectins in tumor and inflammation related pathological processes like proliferation, angiogenesis as well as metastasis[3,57–63] and the expression rate of galectin-1, one of the most prominent members, strongly correlates with the aggressiveness and progression of the cancer disease.[64–66]

Galectins belong to the protein class of non-enzymatic, carbohydrate-binding lectins[67,68] and the first isolation of an animal galectin is dated from the mid-1970s by works of Teichberg *et al*. who extracted a β-D-galactoside binding protein from the electric organ tissue of *Electrophorus electricus* and thus called it electrolectin.[69] Discoveries and classifications of further members coined the term S-type lectin[70] where the S label indicated the dependence on thiols or other reducing agents to maintain binding activity of the lectin. However, it became apparent that this finding only applies for very few S-type lectins and communication about these proteins was hampered for a long time due to the absence of a generally accepted nomenclature.[71] Then, in 1994 leading scientists on this research field introduced the term galectin as follows:[71] "Membership in the galectin family requires fulfillment of two criteria: affinity for β-galactosides and significant sequence similarity in the carbohydrate-binding site, the relevant amino acid residues of which have been identified by X-ray crystallography[72]".

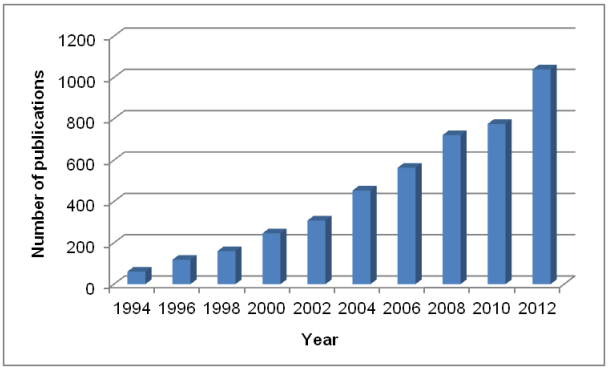

Fig. 2.6 Number of publications containing the subject "galectin" from 1994 to 2012 (SciFinder).

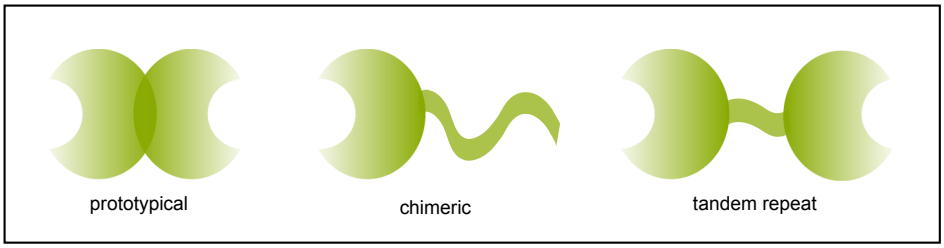

Fig. 2.7 Galectins are subdivided into three major groups: prototypical galectins with a single CRD that associate to a homodimeric structure, chimeric galectins with a single CRD and a collagen-like *N*-terminus for assembling into oligomeric structures and tandem repeat galectins with at least two CRDs within the polypeptide sequence that are connected via a short polypeptide linker.[73]

2.2.1 Structural Features

To date, fifteen different galectins have been identified in mammals but only twelve occur in humans.[63] They all feature fundamental similarities in the canonical carbohydrate recognition domain (CRD) comprising approximately 130 amino acids of 14.5 kDa with eight invariant residues that form contacts with the carbohydrate ligand.[73] Based on the conserved galectin CRD and further structural characteristics the proteins have been subdivided into three main groups (Fig. 2.7):[68,73]

- prototypical galectins that contain a single CRD within the polypeptide sequence but can associate to a homodimeric structure. Prototypes include galectin-1, -2, -7, -10, -13, -14.
- chimeric galectins with a single CRD and a large *N*-terminal collagen-like domain that is rich in proline, glycine and tyrosine residues and facilitates self-aggregation into oligomers. Galectin-3 is the only known lectin of this subtype in vertebrates.
- tandem-repeat galectins that enclose at least two CRDs within a single polypeptide sequence. The recognition motifs are linked by a short peptide domain of five to more than 50 amino acids in length. This subtype includes galectin-4, -8, -9, -12.

So far, human galectin-1,[74,77,78]-2,[72] -3,[75,79]-7[76,80], -8,[81] and -9[82](hGal-1, -2, -3, -7, -8, -9) were crystallized in presence and absence of a bound ligand and structure determination contributed valuable information about the three-dimensional arrangement of the proteins. All members share a highly conserved CRD, depicted in Fig. 2.8, and feature the "jelly-roll" topology as typical folding pattern of galectins.[74,83] In more detail, this folding comprises a β-sandwich of two antiparallel β-sheets consisting of five and six individual strands, respectively, and is deficient of α-helices.[74] In

dimeric galectins, like hGal-1, -2, and -7, monomeric subunits are related by a non-crystallographic two-fold rotational axis perpendicular to the β-sheets.[73] The carboxyl and amino termini of each subunit are located at the dimer's interfaces and binding domains are positioned at the far ends of the monomers. While the CRDs in hGal-1 are positioned on the same side of the protein surface within a distance of 44 Å (Fig. 2.8a) the orientation of the subunits in hGal-7 is different, so that the CRDs of the dimer face in opposite directions and the spacing between the binding domain is 50 Å (Fig. 2.8c).[74] Cho and Cummings found that galectin-1 from Chinese hamster ovary cells dissociates into the monomeric subunits at low concentration and they determined a dissociation constant (K_d) of 7 μM for the active monomer-dimer equilibrium and a relatively slow equilibration time of $t_{1/2}$ = 10 h.[84] Monomeric galectin-1 still shows carbohydrate binding activity and is able to regain the dimer structure at higher protein concentrations. A further striking characteristic of some galectins is the susceptibility to oxidation in absence of a reducing agent. In this context, vertebrate galectin-1 is the most labile protein as the formation of intramolecular disulfide bonds between Cys2-Cys130, Cys16-Cys88 and Cys42-Cys60 induces major conformational changes and restricts dimerization as well as ligand recognition.[85,86] The presence of galectin-1 ligands reduces oxidation sensitivity of hGal-1 by shifting the monomer-dimer equilibrium[84,87,88] and covalent modification of the thiol groups or C2S mutagenesis[84] completely prevents the oxidation process. Experimental evidences indicate that physiologically occurring oxidized hGal-1

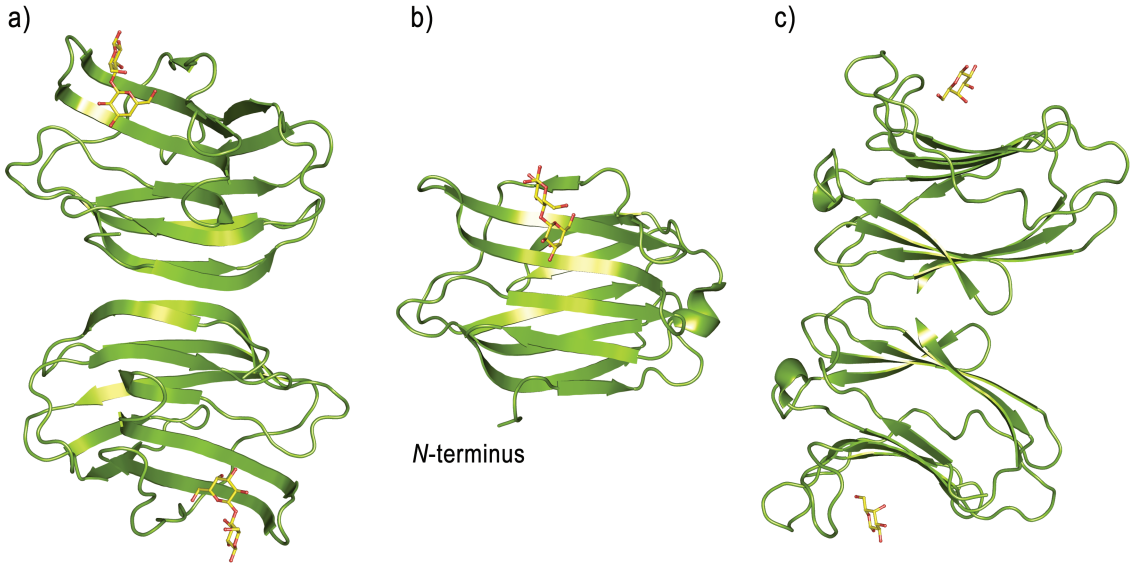

Fig. 2.8 X-ray structures of galectin-carbohydrate complexes. a) prototypic human galectin-1 in complex with lactose (pdb code: 1GZW)[74], b) truncated CRD of human galectin-3 in complex with lactose (pdb code: 3ZSJ)[75] and c) prototypic human galectin-7 in complex with galactose (pdb code: 2GAL)[76].

features a monomeric structure[85] and no longer possesses carbohydrate binding activity. Instead, the protein has a positive impact on axonal regeneration in peripheral nerves[85] and the functional recovery after peripheral nerve injury.[89] Galectins, probably a unique characteristic among animal lectins, are found both inside and outside cells despite the deficiency of an *N*-terminal signal sequence for efficient and quantitative secretion via the classical endoplasmic reticulum/Golgi pathway.[90–92] Extracellular galectins mediate interactions via their CRD and functioning is essentially based on the carbohydrate binding activity whereas intracellular galectins act by protein-protein interactions. Physiological implications of both types will be described in detail below. hGal-1 features typical properties of cytoplasmic proteins with an acetylated amino terminus and has been reported to occur in the cell nucleus, cytosol and at the intracellular side of cell membranes.[93] Experimental evidences implicate that hGal-1 is secreted to the extracellular matrix (ECM) by an unconventional transport mechanism[90,94] and the absence of a signal peptide indicates a tightly controlled balance between intra- and extracellular protein species.[91,92,95] Later studies complemented that hGal-1 secretion is presumably initiated by direct translocation from the cytoplasm to the outside of the cell via the plasma membrane[95–97] and identified the β-galactoside binding activity as an essential prerequisite for hGal-1 export to the ECM.[95] Experiments with hGal-1 mutants lacking this activity or cell lines deficient in producing glycoproteins and -lipids as counterreceptors for hGal-1 resulted in an impaired secretion process. This finding can be considered as a control element to guarantee the export of only properly folded and active hGal-1 for interactions with binding partners on the cell surface.[93] It was further demonstrated that hGal-1 isolated from extracellular space exhibits a slightly higher molecular mass (15 kDa) than the 14 kDa protein of cell lysates, proposing post-translational modifications involved in the secretion mechanism of hGal-1.[98]

2.2.2 Galectin-1 and Cancer

Numerous intra- and extracellular functions have been documented for the galectin family ranging from modulation of signal pathways, involvement in mRNA splicing, regulation of apoptotic signaling to the mediation of cell-cell interactions[99] and promoted these proteins to key players in various pathological processes such as inflammation[60,62], diabetes[100], infection[101,102] and cancer[3,58,63,103,104]. Experimental evidences suggest that galectins, in particular galectin-1, participate in multiple aspects of cancer biology and have a strong impact on tumor progression by effecting immune surveillance, proliferation, angiogenesis, tumor cell migration and adhesion.[3] Moreover, studies with different cancer cell lines have corroborated a correlation between galectin expression and tumor stage and aggressiveness leading to a poor prognosis of the disease.[105–111]
In this context, upregulated galectin-1 expression has been observed in a large number of

cancer types such as colon[108], ovarian[112], prostate[109], head and neck[113], breast[107], pancreatic[114], gastric[110], and lung[115] carcinomas as well as in Kaposi's sarcoma[105], gliomas[116], myeloproliferative neoplasia[117] and Hodgkin lymphoma[118]. Further, tumor surrounding stroma cells and cancer-associated endothelial cells are affected by increased galectin-1 concentrations[65,98] highlighting the potential of this protein to act as tumor marker and therapeutic target in clinical cancer treatment.

In contrast to healthy cells, where galectin-1 mainly occurs in the cytoplasm and nucleus,[119] the protein is secreted at high levels to the extracellular compartment in cancer and tumor-associated cells.[105,120,121] Here, the binding to membrane-anchored β-galactoside containing glycoproteins and -lipids accounts for both homo- and heterotypic tumor cell aggregation and interactions with receptors of the ECM, such as laminin, and fibronectin,[122] are important factors for cell-cell and cell-ECM adhesion and tumor invasion.[123,124] Altered adhesion behavior of tumor cells is part of cancer metastasis and facilitates both detachment from the primary spot and attachment to endothelial cells at distal sites.[3,125] In studies with colon cancer cells Ito and Ralph found galectin-1 binding to surface molecules CD44 and CD326, colon cancer stem markers, that participate in extravasation of metastatic cells by supporting cancer cell adhesion to the endothelium.[126]

Converse findings have been reported about galectin-1 involvement in tumor growth and cell cycle regulation. Detjen *et al.* observed an antiproliferative effect of extracellular galectin-1 upon binding the $\alpha 5\beta 1$ integrin in hepatocarcinoma, breast, colon, melanoma and ovarian carcinoma.[127] Functional interaction between the lectin and integrin resulted in a considerable inhibition of the Ras-MEK-ERK pathway coming along with transcriptional induction of CDK inhibitor p27 and tumor growth restriction. An opposite effect was described by Le *et al.* and mice transfected with Lewis lung carcinoma showed galectin-1 correlated tumor growth.[128] This finding was corroborated in further studies and galectin-1 inhibition with antisense mRNA[129] or siRNA[130] as well as downregulation of protein expression led to an efficient tumor growth restriction in ovarian[123], cervical[131] and breast carcinoma[107].

Experimental evidence indicate that galectin-1 is also involved in tumor-induced angiogenesis[132,133] that comprises the aberrant growth of vascular structures and the formation of new capillaries from preexisting blood vessels to address the increased need of oxygen in proliferating cells.[134] This pathological process is induced by secreted, extracellular factors, like the vascular endothelial growth factor (VEGF) and galectin-1 is described to promote the proangiogenic effect by activating the VEGF signaling pathway.[106,109,135,136] Along with it Rabinovich *et al.* recently showed that hypoxic conditions induce elevated galectin-1 expression in Kaposi's sarcoma and interactions between the secreted protein and specific surfacial *N*-glycans on endothelial cells activate pathological angiogenesis.[105] While the mechanism proposed by the authors

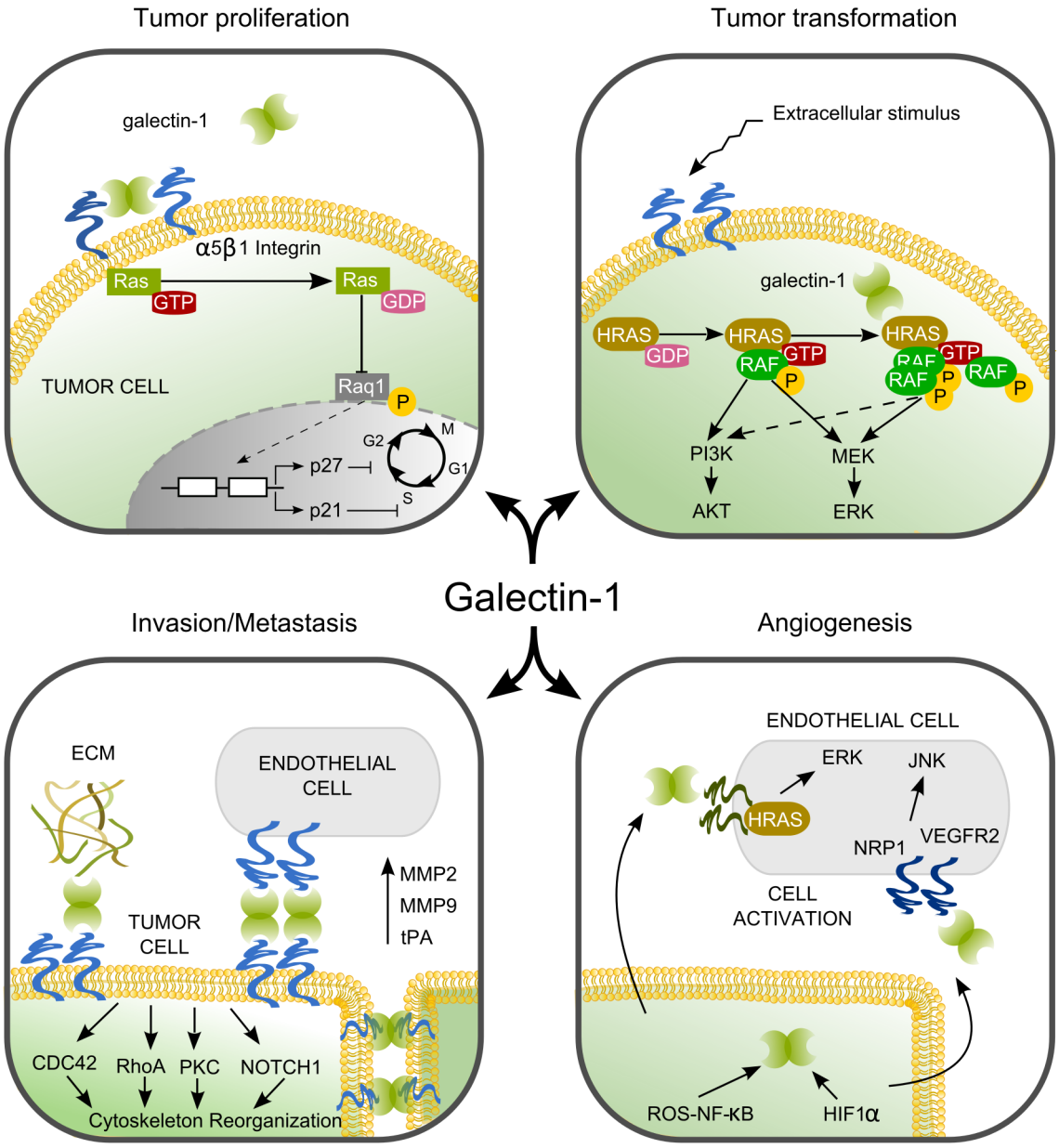

Fig. 2.9 Galectin-1 participates intra- and extracellularly in protein-protein and protein-carbohydrate interactions to modulate various stages in tumor progression from cell transformation, tumor proliferation, angionesis to metastasis. Adapted from ref. 3.

is independent of hypoxia-inducible factor (HIF) 1α and HIF-2α and relies on reactive oxygen species that activate nuclear factor κB Zhao *et al.* demonstrated that HIF-1α enhances both galectin-1 mRNA and lectin expression in colon cancer cells.[137]
Galectin-1 further plays a crucial role in tumor progression through immune surveillance and conferring immune privilege to cancer cells.[5] Upon binding of surface epitopes CD45, CD4+ and CD8+ on activated T helper cells in breast, melanoma and Lewis

lung tumors galectin-1 induces apoptosis thereby promoting the tumor to evade from the T cell dependent immune response.[138] Rabinovich *et al.* demonstrated that blocking of galectin-1 T cell interactions in tumor tissue decreases tumor size and increases tumor rejection along with the development of a strong tumor-specific T1-type immune response.[5] Physiological implications of galectin-1 in tumor progression such as cell adhesion, metastasis, cell proliferation, angionesis and immune surveillance involve the protein's capability of recognizing and cross-linking β-galactoside-containing glycoconjugates in the extracellular compartment.[3] Intracellular galectin-1 participates in distinct signaling pathways and protein-protein interactions independent of its CRD, even though the lectin preserves carbohydrate binding activity. Wang *et al.* demonstrated that nuclear extracts deficient of galectin-1 and galectin-3 lack splicing activity of pre-mRNA which can be restored by exogenous proteins, either galectin-1 or galectin-3.[139] This finding as well as the identification of Gemin4, a component of the Survival of Motor Neurons (SMN) complex and key player in ribonucleoprotein assembly,[140] as binding partner for galectin-1,-3 strongly suggest a fundamental role of the lectins in the splicing machinery. In the context of tumor genesis and development the intracellular interaction between galectin-1 and the *N*-terminal farnesyl modification of H-Ras-guanosine triphosphate (H-Ras-GTP, activated form of H-Ras) is attributed to cell proliferation and cell transformation.[141] Membrane-associated H-Ras-GTP mobilizes cytosolic galectin-1 to the cell membrane and binding between H-Ras-GTP and the hydrophobic pocket of the lectin essentially stabilizes membrane-anchorage[142] and nanocluster formation[143] of H-Ras-GTP, a prerequisite for the MEK-ERK signaling pathway.[144] A single point mutation in the binding pocket of galectin-1 inhibits the biological activity of H-Ras-GTP and in studies with galectin-1 antisense RNA cell transformation was prevented.[145]

2.2.3 Targeting Galectin-1: Current State of Research

Findings about the physiologic implications of galectin-1 in cancer biology during the last years have promoted this lectin to an attractive target for novel tumor therapies. So far, a number of approaches have been developed for inhibition of galectin-1. β-Galactoside containing carbohydrates, the natural binding motif, have inspired various groups and motivated the synthesis of structures with promising properties for a therapeutic application. Rabinovich *et al.* reported about the preparation of mono- and divalent lactulose amines and their potential to specifically inhibit galectin-1 and galectin-3 carbohydrate binding.[147] Blocking the interactions between the lectins and the highly glycosylated protein 90K resulted in a decrease of homotypic tumor-cell aggregation of melanoma cells and an inhibition of endothelial cell morphogenesis, a typical process during angiogenesis. Further, incubation of the synthetic β-galactosides with human

small cell lung carcinoma cells, a cell line that expresses substantial amounts of both galectins, induced tumor-cell apoptosis that may arise from the anti-adhesive effect of the lactulose amines. Control experiments with resting T lymphocytes and a nontumorigenic cell line that do not produce galectin-1 and galectin-3 were not affected by the same concentrations of synthetic carbohydrates, demonstrating selective effectiveness on different physiological targets. Obviously, homotypic cell aggregation, endothelial cell morphogenesis and tumor-cell apoptosis are mediated by galectin interactions and all these critical events in tumor progression can be influenced by targeting the lectin with β-galactoside ligands.[147]

Multivalent carbohydrate structures have been intensively investigated with regard to their targeting ability and inhibitory potential.[146,148,149] One approach comprises the synthesis of wedgelike dendrimers presenting either two, four or eight terminal lactose molecules with 3,5-di-(2-aminoethoxy)benzoic acid as branching unit (Fig. 2.10).[146] A solid phase inhibition assay with immobilized glycoproteins for cell surface mimicking was applied to determine the relative inhibitory activity of the dendrimers. Glycoproteins human pentraxin serum amyloid P (SAP), lactosylated bovine serum albumin (LacBSA) and asialofetuin (ASF) contain either di- or triantennary glycans or display a complex heterogenous *N*-glycan profile to compete with lactosyl dendrimers for galectin-1 binding. Interestingly, the relative binding potency towards the lectin strongly depends on the mode of carbohydrate presentation and a 1667-fold increase per lactose unit was

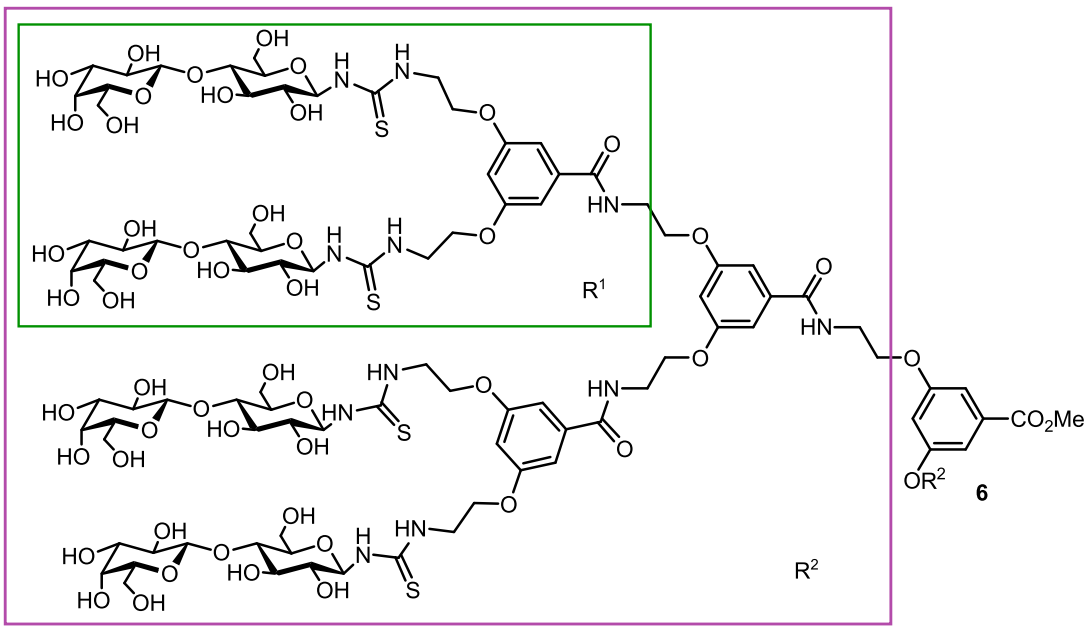

Fig. 2.10 Glycodendrimers bearing either two (R^1, green box), four (R^2, magenta box) or eight (**6**) terminal lactose units. The tetravalent structure exhibits the highest relative binding affinity per lactose indicating a strong dependence on both, number and presentation of galectin-1 ligands.[146]

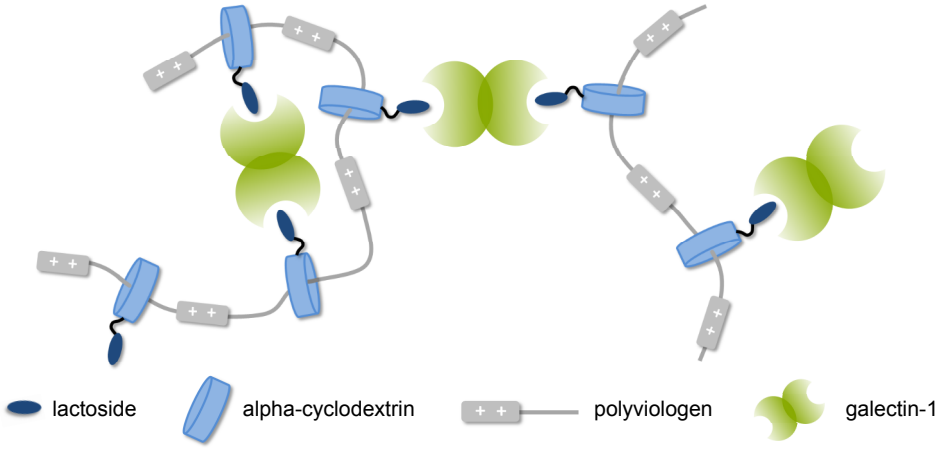

Fig. 2.11 Self-assembled pseudorotaxanes comprise lactoside-functionalized α-cyclodextrins beaded onto a linear polyviologen polymer. Cationic dipyridinium spacers impart translational and rotational flexibility for optimal multivalent networking with galectin-1.[150]

observed for the binding experiment with biantennary glycan SAP as matrix and the tetravalent lactosyl dendrimer compared to free lactose. In contrast, the increase was only 76-fold in studies with the maxiclusters of LacBSA or 662-fold with the octavalent dendrimer on SAP. Evidently, efficient inhibition of galectin-1 relies on an optimal ligand display rather than simply enhancing multivalency.[146] To address this issue Baum *et al.* developed a supramolecular architecture of self-assembled pseudopolyrotaxanes including lactoside-presenting α-cyclodextrins beaded onto a "linear polyviologen string".[150] The structural arrangement offers a high degree of geometric flexibility and allows translational and rotational movements of the lactoside-bearing cyclodextrins (Fig. 2.11). The inherent dynamic adaptability of carbohydrate presentation promises improved targeting capacities. Indeed, investigations of the pseudopolyrotaxanes about their potential to inhibit galectin-1-mediated T-cell agglutination resulted in a 10-fold increase over free lactose and was significantly greater than the effects of trivalent lactosyl glycoclusters underscoring the benefit from flexible multivalent architectures.[150,151]

GM-CT-01 (formerly Davanat®) is a multivalent α-galactomannan and passed Phase II clinical trials[ii] against metastatic colorectal cancer by Galectin Therapeutics© (www.galectintherapeutics.com). The active compound is isolated from the seeds of guar gum (*Cyamopsis tetragonoloba*) and the polymer backbone consists of (1→4)-linked β-D-mannopyranosyl units.[152] Single α-D-galactopyranosyl moieties are connected in periodic sequences via a (1→6)-linkage leading to a repeating unit of approximately 17 β-D-Man and 10 α-D-Gal residues while an average polymer molecule comprises about

[ii] "GM-CT-01 Plus 5-Fluorouracil as Third- or Fourth-Line Therapy for Metastatic Colorectal Cancer". *clinicaltrials.gov*. U.S. National Institutes of Health. Web. 1 June 2014. <http://clinicaltrials.gov/ct2/show/NCT00110721>

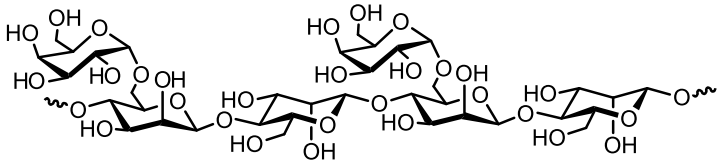

Fig. 2.12 The polymer backbone of **GM-CT-01** consists of (1→4)-linked β-D-mannopyranosyl units. Single α-D-galactopyranosyl moieties are connected in periodic sequences via a (1→6)-linkage leading to a repeating unit of approximately 17 β-D-Man and 10 α-D-Gal residues.[152,153] 2D NMR spectroscopy unraveled an extended binding domain at hGal-1, alternative to the CRD, for **GM-CT-01** interactions.[152,154]

12 of these units (Fig. 2.12).[152,153] ^{1}H-^{15}N HSQC NMR spectroscopy of ^{15}N-enriched galectin-1 interacting with α-galactomannan demonstrated that the relatively large ligand binds predominantly at alternative sites situated on the opposite of the canonical CRD and at the dimer interface with an apparent K_d of 10 μM.[152,154] This finding was corroborated by simultaneous NMR binding experiments of **GM-CT-01** and lactose to galectin-1.[152] Resulting spectra indicate that lactose still binds the complex of galectin-1/ **GM-CT-01** with the same affinity while lactose interactions apparently induce minor conformational changes in galectin-1 thereby modulating the affinity between the protein and the α-galactomannan. In preclinical studies, a reduction of colon tumor growth was observed with **GM-CT-01** treated mice and disease stabilization without significant side effects documented for patients with metastatic colorectal cancer in Phase I and II clinical trials.[154] Further, van der Bruggen *et al.* reported that **GM-CT-01** treatment of isolated tumor-infiltrating lymphocytes (TIL) from cancer patients reactivates the immune response by promoting cytotoxicity of CD8+ TIL and the release of IFN-γ.[155]
Monovalent thiodigalactoside (**TDG**), a synthetic and non-metabolizable disaccharide, complements the class of carbohydrate-based ligands to address galectin-1 associated tumor progression (Fig. 2.13). Ralph *et al.* observed significant suppression of tumor growth in breast cancer upon treatment of **TDG**.[156] They attributed this finding to the inhibitory effect of the thio derivative by blocking the CRD of galectin-1. **TDG** blockade of the galectin-1 CRD further affected the proangiogenic function of the lectin and reduced endothelial cell proliferation as well as binding to glycoproteins of the extracellular matrix such as laminin. Apparently, **TDG** binding enhances oxidative stress on the tumor cell and by blocking the protective interactions with galectin-1 endothelial cells are subjected to hypoxia-induced apoptosis.[156] Simultaneously, the number of tumor-infiltrating CD8+ and CD4+ lymphocytes are substantially increased and galectin-1-associated immune privilege disabled. Taken together, experimental evidences implicate that **TDG** has a strong inhibitory effect on galectin-1 related immune

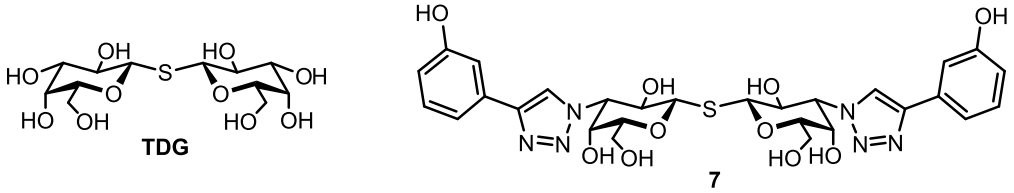

Fig. 2.13 Thiodigalactoside **TDG** and structural optimized TDG **7** for targeting of hGal-1. K_d values of hGal-1 and hGal-3 for **7** are 13 nM and 22 nM, respectively.[158]

dysregulation, angiogenesis and protection against oxidative stress which makes the disaccharide an attractive drug candidate.[156] In this context, synthetic optimization and functionalization of *O*-3 of **TDG** were realized to further enhance the binding affinity towards tumor target galectin-1.[157,158] Resulting structures exhibit dissociation constants in the nanomolar range but with no preferred binding selectivity and similar affinities for various galectins.[157]

A different strategy focuses on galectin-1-specific monoclonal antibodies (mAB) to neutralize tumor-promoting binding events. Rabinovich *et al.* recently demonstrated that therapeutic administration of the specific mAB (F8.G7) prevents galectin-1-*N*-glycan interactions and induces tumor regression in established Kaposi's sarcoma.[105] F8.G7 proved to be highly specific for targeting of galectin-1 to impede endothelial cell proliferation, invasion and migration while binding events of other galectin members, like galectin-3 and -8, remained unaffected. Experimental evidences indicate that treatment with anti-hGal-1 mAB decreases tumor vascularization and further promotes activation or recruitment of infiltrating natural killer (NK) cells. Obviously, disrupting the binding between galectin-1 and *N*-glycans of distinct cell surfaces, such as endothelial cells or immune cells, reduces tumor growth as a result of impaired cell proliferation and enhanced NK cell-mediated immune response.[105]

Anginex (βpep-25), a synthetic peptide with a three-dimensional β-sheet structure similar to β-chemokines, is a potent candidate among a series of artificial peptides with strong antiangiogenic activity.[134,159,160] Griffioen *et al.* identified galectin-1 as target of anginex by yeast two-hybrid (Y2H) analysis and evaluated the binding event with NMR and plasmon resonance spectroscopy.[132] Experimental data suggest that dimerized anginex interacts with galectin-1 and dissociates as monomers with K_d values of 6.4 μM and 90 nM for dissociation of the first and second anginex molecule, respectively. To probe the influence of galectin-1 in tumor progression wild-type and galectin-1-null (galectin-1-deficient) mice were transfected with teratocarcinoma cells and tumor growth observed in all mice after three days, indicating that tumor outcome and initial growth is independent of galectin-1 expression. However, further tumor progression was substantially impaired in galectin-1-null mice compared with wild-type mice. Further, βpep-25 treatment of the both subtypes resulted in a significant

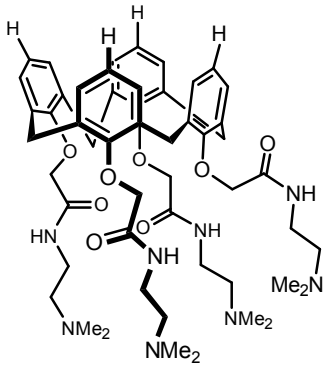

0118

Fig. 2.14 Calixarene **0118** is a nonpeptidic mimetic of anti-angiogenetic anginex. The molecule interacts with hGal-1 at an alternative site to the CRD as determined by ^{15}N-^{1}H HSQC NMR spectroscopy.[168]

decrease of tumor growth in galectin expressing mice while no effect was observed for the mutant animals demonstrating the proangiogenic activity of galectin-1. To enhance the antitumor effect anginex administration has been combined with diverse other cancer therapies like radiotherapy or chemotherapy.[161–166] In this context, βpep-25 treatment of tumor-bearing mice followed by radiotherapy increased the antiproliferative activity of the peptide, presumably by sensitizing endothelial cells to radiation.[161] Mayo *et al.* investigated cancer treatment of a human ovarian carcinoma mouse model by combining anginex or angiostatin administration with chemotherapy and reported synergistic effects in tumor growth suppression.[163,167]

Inspired by promising results from previously conducted anginex studies various peptidic and nonpeptidic molecules mimicking structural features and the crucial β-sheet conformation[164] of βpep-25 have been introduced.[3] Structures were designed to minimize therapeutic dosage and to reduce the peptidic character while preserving the amphiphatic and cationic structure. Calixarene **0118** is a topomimetic of galectin-1-binding anginex (Fig. 2.14) and interacts with the lectin at an alternative site to the CRD as determined by ^{15}N-^{1}H HSQC NMR spectroscopy.[168] HSQC-based lactose titrations further revealed that galectin-1 still binds to the disaccharide, however, with a decreased affinity, suggesting **0118** to be a non-competetive, allosteric inhibitor.[168] Calixarene **0118** inhibits cell proliferation of distinct human cancer cell lines in a dose-dependent manner and exhibits attractive features for a therapeutic drug candidate due to its smaller molecular size compared to anginex and the aryl-crown, nonhydrolyzable structure appears less likely to metabolic degradation.[168] Currently, **0118** is in a Phase I clinical trial with tumor patients.[168]

The design of novel and potent galectin-1 inhibitors and subsequent *in vivo* assays for therapeutic cancer agents during the last decade have contributed to a better understanding

of galectin-1-associated cancer biology and gives an idea of how target-selective tumor treatment may look like in the future. In this regard it is indispensable to consider eventual side effects arising from an effective interference with the physiological interactions of the protein. So far, preclinical and clinical studies with galectin-1 inhibitors are in early stages and information about related cross reactions are preliminary.[3] However, studies with galectin-1-null mice have shown an increased threshold for nociceptive thermal stimuli and altered primary afferent neuronal anatomy[169] and attributed endogenous galectin-1 a role in axonal repair and functional recovery.[170] In contrast, Tribulatti *et al*. reported about redundant and antagonistic functions between galectin members and a joined participation in the initial phase of the immune response.[171] These findings suggest that galectin functions may converge to permit a survival of galectin-1-null mice or that galectin-1 only affects post-developmental processes.

Concerning galectin-1 targeted tumor drug design the absence of strong phenotypic effects in galectin-1-null mice[172] prompts optimism that inhibition of the protein will not produce severe side effects[3] but findings about galectin-1's implication in neuronal recovery also encourage to develop compounds that regulate rather than eliminate the pathological binding events in galectin-1-related angiogenesis, metastasis and cell-mediated immunity.

Chapter 3

Objectives and Project Planning

Previous studies have attributed galectin-1 a key role in tumor progression of numerous cancer types and revealed that the expression rate of this protein directly correlates with the tumor malignancy and the poor outcome for patients. Interference of the physiological interplay either on the DNA level (siRNA, knockdown) or by inhibition with galectin-1 ligands have demonstrated a positive impact on tumor regression and envisioned the great potential of galectin-1 as tumor target. Based on these findings the development of potent and selective galectin-1 ligands and the characterization of their targeting modes are of extreme importance to gain a more precise understanding of the physiological

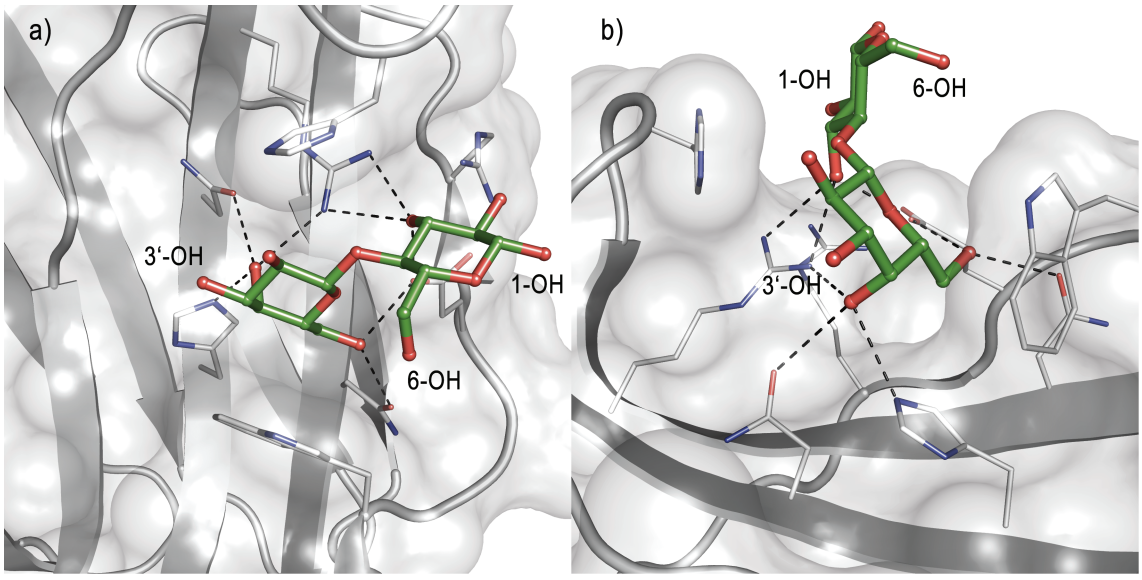

Fig. 3.1 Crystallographic data of human galectin-1 in complex with lactose (pdb code 1GZW).[74] Interactions between the protein and hydroxyl groups of the disaccharide are presented as dashed lines. Hydroxyl groups not interacting with hGal-1 are labeled and motivate the introduction of synthetic modifications.

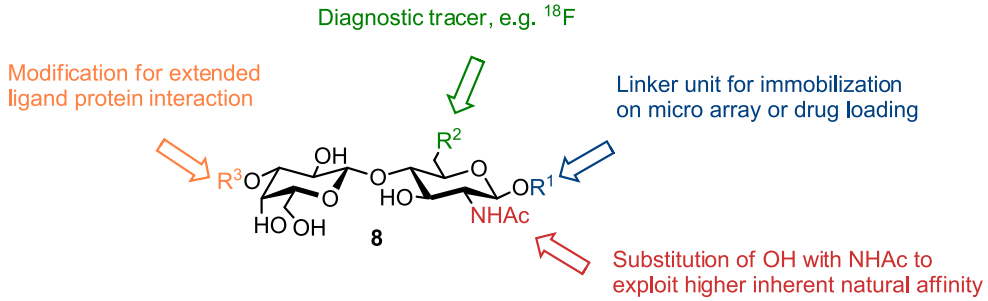

Fig. 3.2 Proposed LacNAc derivative **8** that comprises i) a synthetic modification (R^3) for extended interactions with hGal-1, ii) a tracer isotope (R^2) for diagnostic detection, iii) a linker unit (R^1) for immobilization on a microarray or for loading a chemotherapeutic and iv) an *N*-acetyl substituent at *C*-2 to exploit the inherently higher natural affinity.

interactions. Beyond that resulting molecules promise to find an application in both future cancer treatment and early tumor detection of elevated protein concentrations.

The crystallographic data of human galectin-1 in complex with lactose[74] motivates a strategy for designing tailor-made galectin-1 binding partner that has not been adopted by other groups so far. Fig. 3.1 highlights hydroxyl groups within the lactose molecule that are not involved in interactions with the protein. Evidently, the disaccharide represents an excellent ligand template and the binding mode further suggests that synthetic modifications of selected positions would not significantly influence the binding capacity of the carbohydrate scaffold but render a multifunctional galectin-1 ligand. The 3'-OH group faces towards a potential binding domain adjacent to the CRD proposing this position for synthetic extensions to generate specific and additional interactions with galectin-1. In contrast, the reducing end (1-OH) of lactose is situated at the open end of the protein implicating a certain spatial flexibility and the tolerance of a linker unit for immobilizing the optimized carbohydrate on a diagnostic microarray or to load chemotherapeutics. The 6-OH group protrudes from the protein cleft and seems to accept minor structural changes such as tracer isotopes (e.g. ^{18}F) for positron emission tomography (PET). In addition, substituting the hydroxyl group at *C*-2 with an *N*-acetyl group will increase the inherent natural affinity considering that *N*-acetyllactosamine binds galectin-1 by a factor five stronger than lactose. All these structural reflections lead to the envisioned LacNAc derivative **8** in Fig. 3.2 and guide the experimental performance of the three following galectin-1 projects from prediction to tailor-made drug candidates and diagnostic tools.

Project I: Rational ligand design for hGal-1 drug candidates and diagnostic tools

The synthesis and functionalization of even small saccharide structures like di- or trisaccharides can be highly challenging due to the chemical and structural character of carbohydrates. Carbohydrates exhibit several hxdroxyl groups with very similar reactivity which makes them difficult to distinguish in the synthesis or modification of saccharide structures. While nature solves this problem with a toolbox of different glycosyltransferases - enzymes with highly conserved catalytic centers that ensure the stereo- and regiospecific linkage of monomers - synthetic chemists are commonly

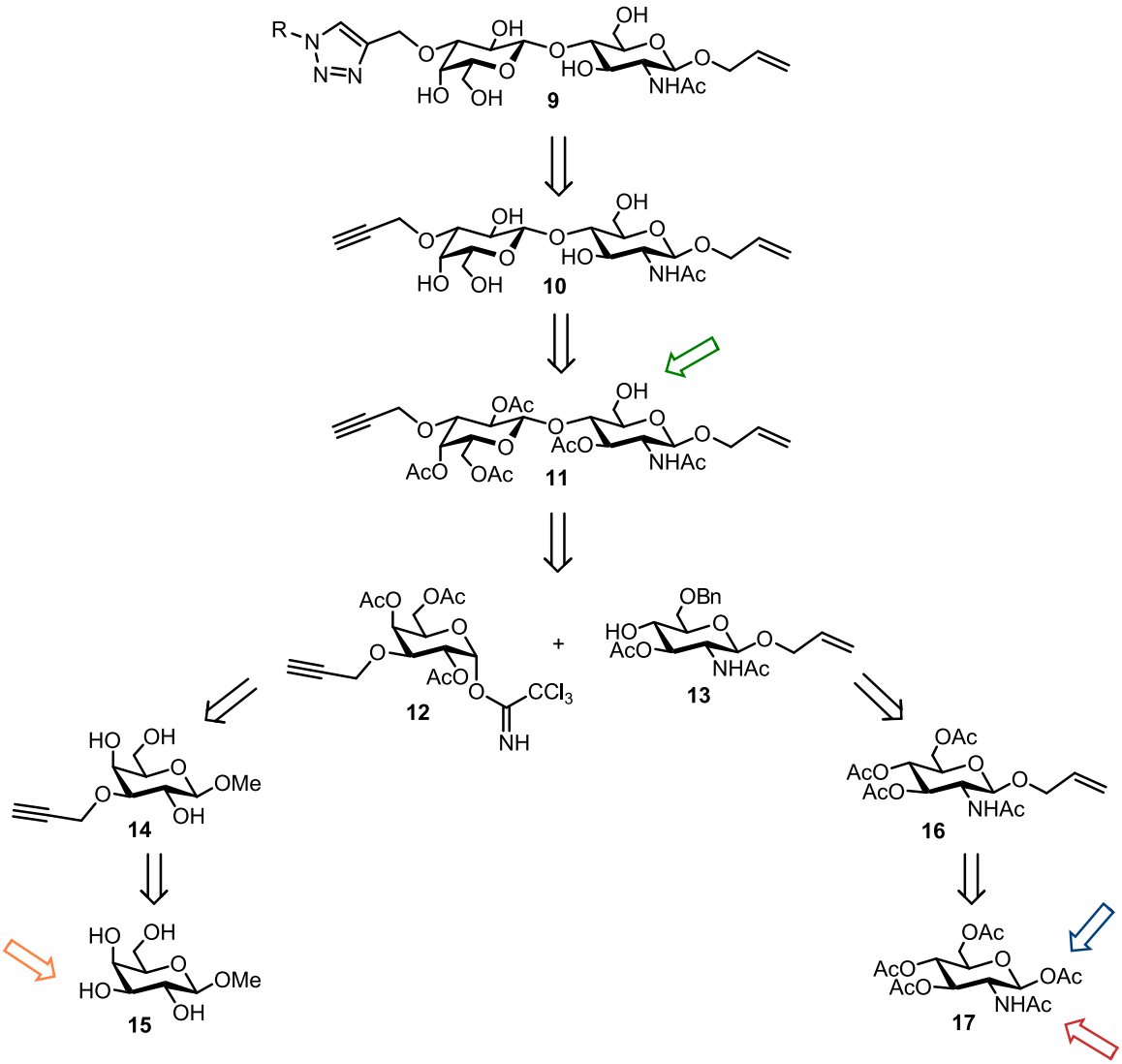

Scheme 3.1 Retrosynthetic approach considering the choice of functional group and the time of introduction at *C*-3' (orange arrow), *C*-1 (blue arrow) and *C*-6 (green arrow). The *N*-acetyl substituent at *C*-2 (red arrow) derives from the *N*-acetylglucosamine derivative **17**.

confronted with multi-step reactions including protecting-group manipulations. Thus, it is of predominant interest to devise a synthetic strategy that addresses the proposed structural modifications of **8** in a straightforward approach considering both, the choice of the chemical modification and the respective time of introduction. It is well known that the anomeric position of carbohydrates can be easily converted with nucleophiles starting either from the peracetylated or unprotected saccharide. Similarly, it has been described that 1-*O*-protected galactosides are regioselectively alkylated at 3-OH without involving further protecting group manipulations. These early stage modifications of *C*-3' and *C*-1 imply the installation of complementary functional groups that permit individual conversion later on to address the respective function. The Cu(I)-catalyzed 1,3-dipolar cycloadditon between an alkyne and an azide is an attractive reaction in this context due to its tolerance of a wide range of functional groups, the mild reaction conditions and the successful performance in polar and protic solvents. The early introduction of an alkyne group at *C*-3' and following conversion with organic azides at a late stage of the synthesis permits to cover a high structural diversity for novel interactions with galectin-1. The alkene group fulfills likewise the listed merits and was chosen for *C*-1 to confer reactivity towards thiols, tetrazines and alkenes for immobilization on a microarray or drug loading. The *N*-acetyl substituent at *C*-2 derives from the starting *N*-acetyl glucosamine derivative **17**.
Beside *C*-3' and *C*-1 position *C*-6 is important to consider in the retrosynthetic approach. The selective access to this position can be achieved by an appropriate protecting group system releasing exclusively the 6-OH group upon specific deprotection conditions. The hydroxyl group can react as a nucleophile afterwards.

Synthetic suggestions are summarized in Scheme 3.1.

The strategy towards novel galectin-1 ligands places a special emphasis on evaluating single steps of the growing LacNAc derivative and intends to elucidate the binding mode and targeting abilities by X-ray crystallography. The crystallographic data of galectin-1/ ligand complexes would provide the basis for rationally predictable triazoles in an unrivaled manner and are expected to make the following contributions:

- Crystallization of galectin-1 in complex with LacNAc proves the transferability of structural inspirations from lactose to LacNAc.

- Crystallization of galectin-1 in complex with **10** probes the influence of synthetic modifications at *C*-3' and *C*-1 on the binding mode and provides the basis for a comprehensive computational screen to select promising azides as reaction partners.

- Crystallization of galectin-1 in complex with resulting click products gains a profound understanding of novel interactions and the geometric orientation of the carbohydrate scaffold with the extended ligand.

Further, the characterization of galectin-1/ligand complexes will be complemented by surface plasmon resonance (SPR) and isothermal titration calorimetry (ITC) to monitor changes in binding affinities and thermodynamic properties. Resulting structures will be tested and evaluated for their diagnostic potential within the scope of Project II.

Project II: Development of diagnostic tools for hGal-1

Tumor diagnosis at an early stage of the disease greatly enhances the chance for a successful and lasting cancer cure. Consequently it is of great scientific and social importance to develop specific and highly sensitive detection screens to identify and treat malignant tissue early on.
Carbohydrate microarrays bear the potential to trace and visualize tumor-associated elevated galectin-1 concentration. The project involves the immobilization of potent click products from Project I on the thiol-presenting array surface via the 1-*O*-allyl modification (Fig. 3.3). Synthesis of "attachable" analogues of the natural binding motifs lactose and *N*-acetyllactosamine will allow the performance of comparative studies and the evaluation

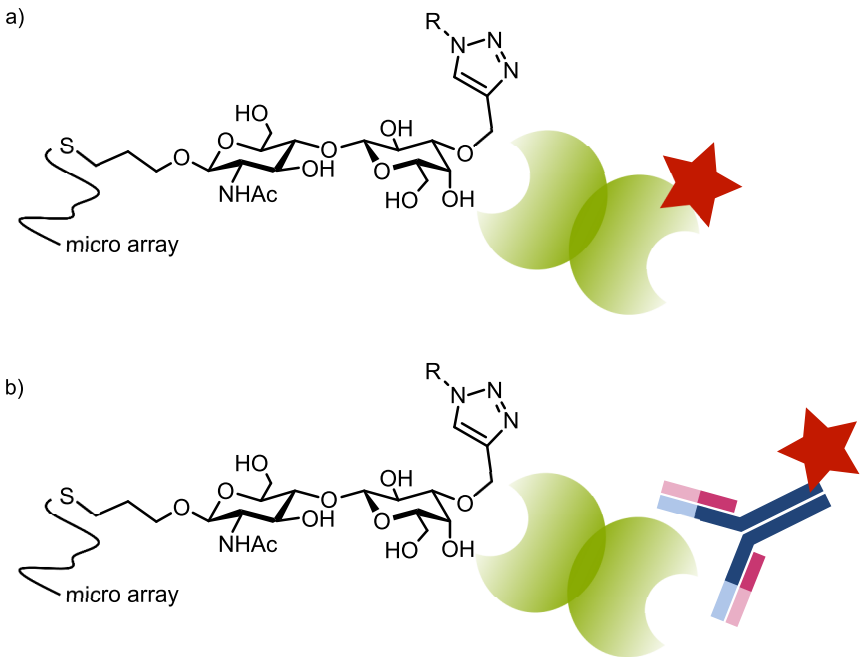

Fig. 3.3 Potent triazole-based hGal-1 ligands developed in Project I will be covalently attached to a microarray surface. hGal-1 binding can either be detected by a) fluorophore-labeled hGal-1 or b) a fluorophore-labeled anti-hGal-1 antibody.

of individual click products regarding their diagnostic potential. The binding event itself can either be visualized by fluorophore-labeled hGal-1 or by sandwich formation with a fluorophore-labeled anti-hGal-1 antibody.
The development of diagnostic tools for hGal-1 will further comprise the synthetic elaboration of a PET tracer. PET is a non-invasive, diagnostic imaging method to monitor aberrant expression pattern or metabolic anomalies. It is to be expected that affine and selective hGal-1 ligands accumulate within tumor tissue of upregulated lectin expression. The installation of a tracer isotope such as ^{18}F in the ligand structure would then permit the detection and localization of neoplastic cells. The project includes the implementation of a PET precursor **18** with a good leaving group (LG) at *C*-6 and the ^{19}F-reference compound **19** (Fig. 3.4). In cooperation, Dr. Reik Löser, Helmholtz-Zentrum Dresden-Rossendorf, will introduce the radioactive isotope locally and perform the *in vivo* studies regarding physiological stability, distribution and accumulation.

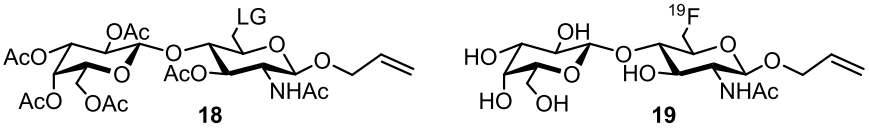

Fig. 3.4 LacNAc-based PET precursor **18** and ^{19}F-reference **19**.

Project III: Investigation of hGal-1 communication pathways on human cell surfaces

Proliferating cells show increased secretion rates of hGal-1 from the inside of the cell to the extracellular matrix where the lectin triggers various cell signaling processes that are beneficial for tumor growth, spread and survival. To better understand these highly complex communication pathways and to exploit the information for future therapeutic

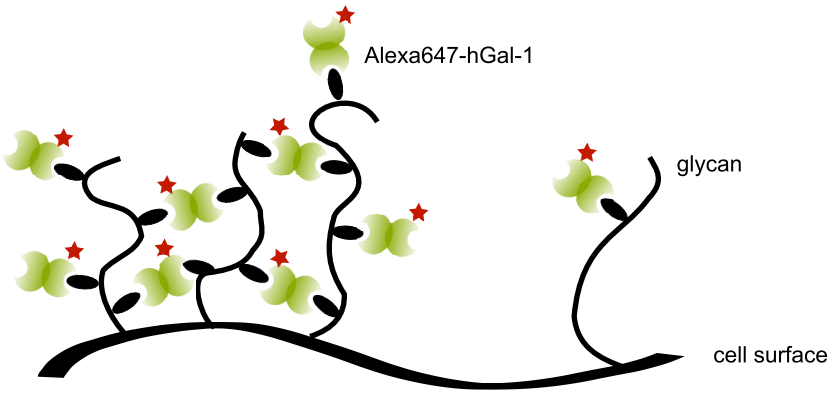

Fig. 3.5 hGal-1 clustering on human cell surfaces.

treatment it is of special interest to analyze the local and temporal distribution of hGal-1 in its physiological environment, the tumor cell surface. High resolution fluorescence microscopy is a powerful tool in this context and achieves resolution far beyond the diffraction limit. In cooperation with Prof. Dr. Markus Sauer, University of Würzburg, clustering effects of Alexa647 labeled hGal-1 on Neuroblastoma cells are studied. Analysis of high resolution data are expected to significantly improve the comprehension of hGal-1 networking on a molecular level (Fig. 3.5).
Further, high resolution imaging experiments will include the investigation of hGal-1 interactions on metabolically glycoengineered Neuroblastoma cells. Metabolic glycoengineering has emerged as an impressive route to introduce bioorthogonal tags within the surface glycan domain for doing chemistry on living cells even in entire organisms. Studies intend to incorporate an azido-functionalized glucosamine derivative into glycoconjugates of the cell surface and to "click" an alkyne lactose derivative (Fig. 3.6). Following incubation with labeled hGal-1 and high resolution imaging will probe the impact of a modulated glycan coat with elevated β-galactoside presentation. Findings might contribute to a better understanding of cell signaling processes induced upon hGal-1 binding to epitopes on the cell surface of T helper or endothelial cells.

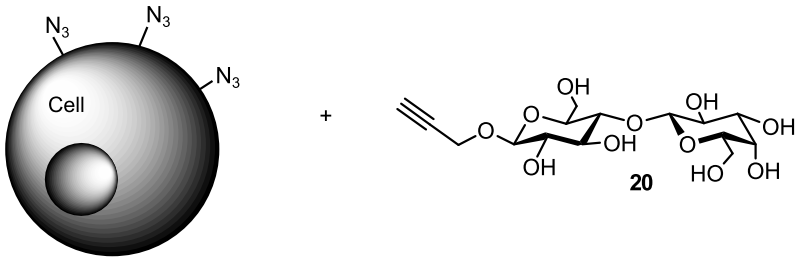

Fig. 3.6 Functionalization of metabolically glycoengineered cell surfaces with hGal-1 binding motif lactose **20**.

Chapter 4

Methods and Theoretic Background

The following chapter outlines the basic concepts that are essential for performing and evaluating experimental studies conducted in this thesis and is subdivided into three parts. The first section explains biochemical techniques associated with the design of novel hGal-1 ligands, such as recombinant protein production, protein crystallization and assays for probing protein-ligand affinity. The second part gives a brief introduction into diagnostic technologies addressed by this work, positron emission tomography (PET) and carbohydrate microarrays. The chapter concludes with a theoretical description of high resolution imaging and its strategy to overcome the diffraction limit. Metabolic glycoengineering is presented as one approach to label human cell surfaces for investigation by high resolution imaging.

4.1 Target-based Ligand Design

A rational target-based ligand design demands an interdisciplinary strategy involving recombinant production of the protein target, synthesis of novel binding partners and subsequent biophysical interpretation of the binding event. X-ray crystallography of protein-ligand complexes provides structural details about the binding geometry while SPR and ITC assays allow evaluating the binding affinity and thermodynamic properties.

4.1.1 Molecular Cloning: From Gene to Protein

DNA technology and molecular cloning have experienced a rapid development from first discoveries in the 1960s to recombinant protein expression (e.g. insulin production) in an industrial scale of nowadays. The early advent of modern recombinant technologies was established by Werner Arber, Daniel Nathans and Hamilton O. Smith who were awarded the Noble Prize in Physiology or Medicine in 1978 "for the discovery of

restriction enzymes and their application to problems of molecular genetics".[i] The introduction of the polymerase chain reaction (PCR) in 1983 by Kary Mullies (Nobel Prize for Chemistry in 1993) was a milestone in the development of molecular cloning and allowed for the first time the almost unlimited enzymatic amplification of DNA molecules. Today, recombinant DNA technologies are standard methods for investigation of transcriptional and translational processes, for site-directed mutagenesis or recombinant protein expression. The theoretical background of recombinant DNA technology has been described in textbooks[173,174], thus this part focuses on main aspects of DNA amplification and cloning, transformation of recombinant DNA and subsequent protein expression and purification.

Amplification of DNA by PCR

A breakthrough of enzyme-catalyzed *in vitro* DNA multiplication by PCR was the discovery of the heat-stable Taq DNA polymerase of *Thermus aquaticus*, a thermophilic

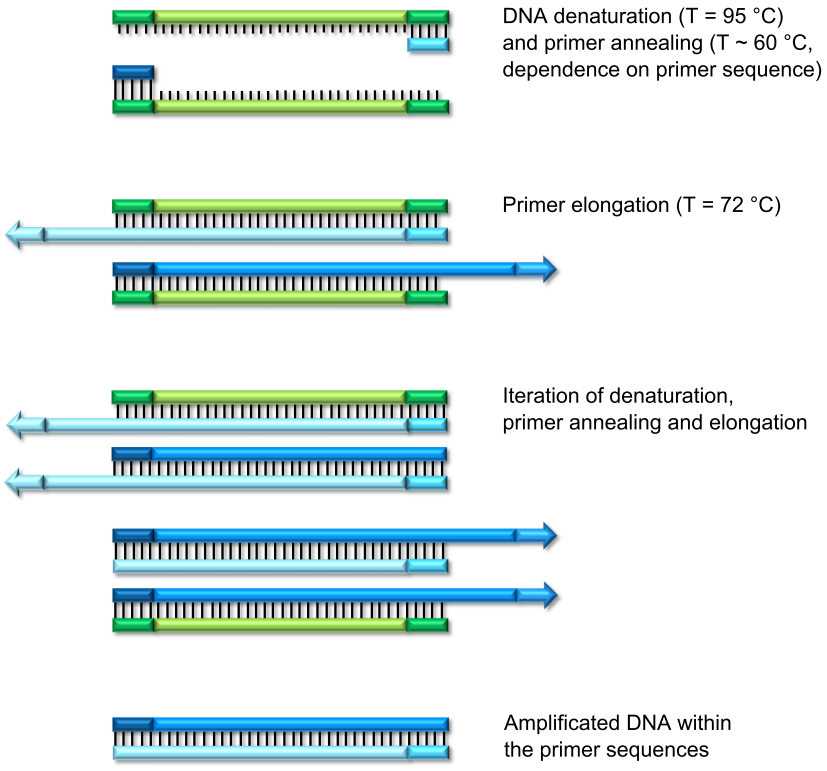

Fig. 4.1 DNA amplification by PCR involves three steps, denaturation of double-stranded DNA, primer annealing and elongation. Iteration of multiple cycles leads to billion-fold multiplication of DNA within the primer sequences.

[i] "The Nobel Prize in Physiology or Medicine 1978". *Nobelprize.org*. Nobel Media AB 2013. Web. 13 May 2014. <http://www.nobelprize.org/nobel_prizes/medicine/laureates/1978/>

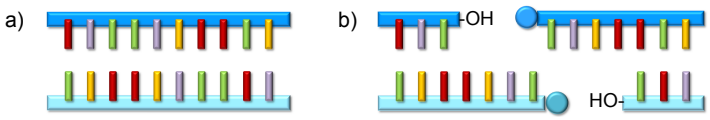

Fig. 4.2 a) Double-stranded DNA sequence. b) DNA restricted in a staggered manner by type II endonuclease to generate cohesive ends (circles indicate 5'-phosphate groups).

bacterium living in hot springs of the Yellowstone National Park, USA.[174] The Taq polymerase withstands more than 90 °C and allowed for the first time the performance of repeated DNA production cycles with temperatures between approximately 60 °C and 95 °C. This procedure leads to a billion-fold multiplication of a targeted DNA sequence and basically involves three steps (Fig. 4.1):[173] Initially, double-stranded DNA is thermally denaturated into single strands, followed by annealing of site-specific, complementary oligonucleotides, so-called primers, of 20-30 DNA bases at an individual annealing temperature. Then, the primer sequence is elongated by a DNA polymerase which requires Mg^{2+} cations for complementary nucleotide linkage via the free 3'-OH group as defined by the single-stranded DNA template. Iteration of 28 to 35 cycles exponentially generates copies of the region within the primers.

DNA cleavage by restriction enzymes

Type II endonucleases cleave site-specifically short (4-8 bp) and palindromic DNA sequences in presence of Mg^{2+}. The enzymes are characterized by a homodimeric structure and each subunit binds loosely and unspecifically at the double-strand while moving along the DNA sugar-phosphate backbone.[173] Upon reaching the recognition site the endonuclease cuts the covalent phosphodiester bond of the DNA duplex and releases 5'-phosphate and 3'-OH ends. The mode of action depends on the individual enzyme and generates either cohesive ("sticky") ends when cutting in a staggered manner (Fig. 4.2) or blunt ends when cleaving both strands at the same spot.

Ligation of restricted DNA

DNA ligases catalyze the covalent bond formation between linear DNA fragments. T4 DNA ligase is a popular enzyme for DNA linkage and derived from the bacteriophage T4.[173,174] The ligation process itself is initiated by annealing of complementary cohesive DNA ends through hydrogen bonds. DNA ligase then connects the 5'-phosphate of one nucleotide with the 3'-hydroxyl group of another to form a covalent phosphodiester bond. Even though the enzyme is capable of also linking blunt end DNA the ligation is less efficient and elevated enzyme concentrations are necessary.

Choice of vector system

Cloning vectors act as carrier system for DNA fragments and permit subsequent recombinant protein expression in a host system. Vectors typically replicate autonomously within the host genome with a high copy rate per host cell (pUC vectors > 200 copies per cell, pET vectors 20-50 copies per cell)[ii], contain multiple unique

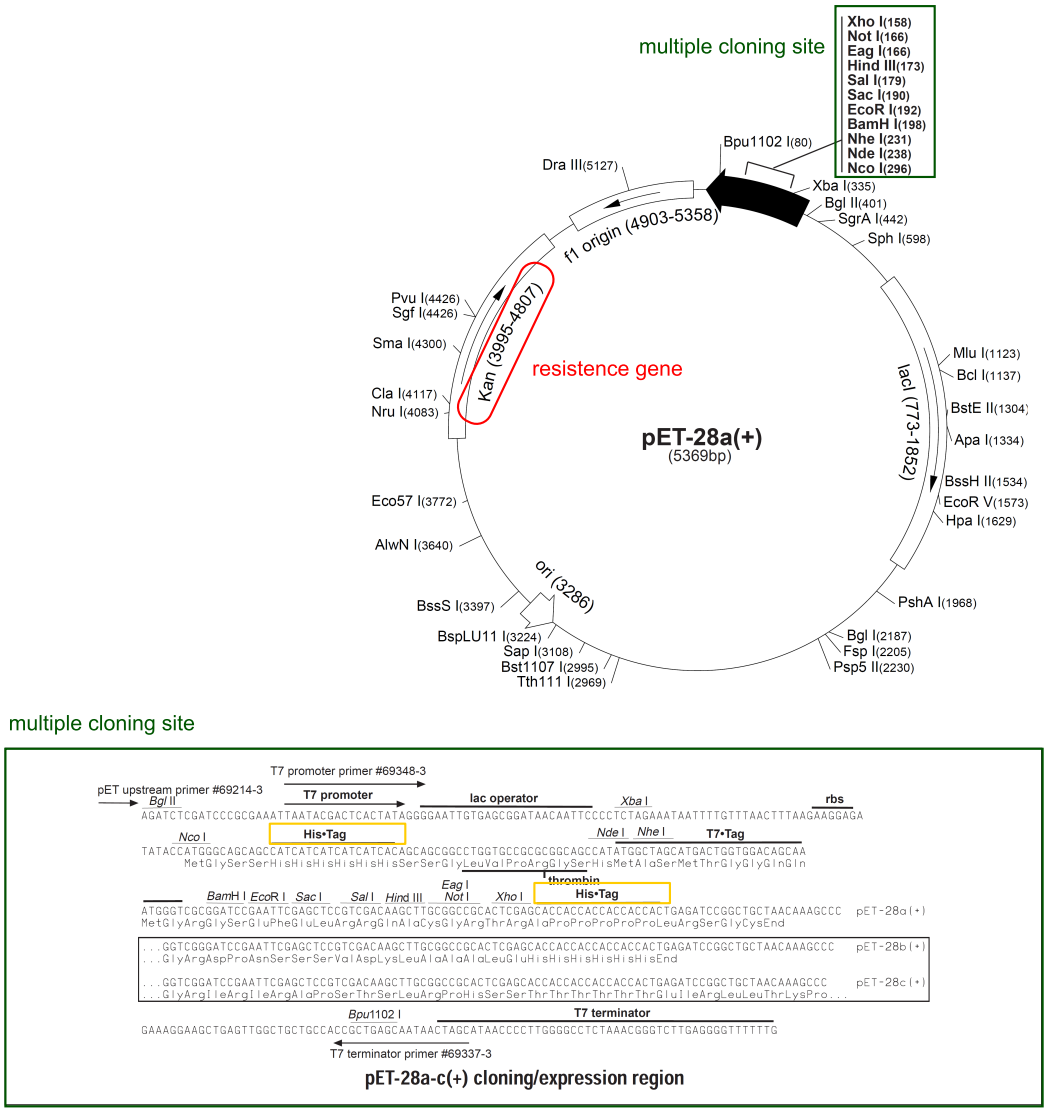

Fig. 4.3 Vector pET28 by *Novagen*. The multiple cloning site is marked in green and depicted enlarged at the bottom. The vector carries a resistence gene for kanamycin (red) and encodes for a His-tag (yellow) at both the 5'- and 3'-terminus of the multiple cloning site.

[ii] "pET System Manual". *novagen.com*. Novagen. Web. 23 May 2014. <http://richsingiser.com/4402/Novagen% 20pET% 20system% 20manual.pdf>

endonuclease restriction sites that occur only once within the DNA and are equipped with an antibiotic resistance gene to discriminate host cells with incorporated vector from those devoid of recombinant DNA.
Cloning vectors can accommodate DNA of different size and reach from plasmids, phages, cosmids to artificial chromosomes like bacterial artificial chromosome (BAC), yeast artificial chromosome (YAC) and mammalian artificial chromosome (MAC).[173] The latter were basically introduced to map whole gene sequences with more than 100 kb. In contrast, plasmids are circular, double-stranded DNA and most commonly employed for recombinant protein production in the bacterial host system *Escherichia coli* (*E. coli*). The amplified DNA fragment is inserted into the multiple cloning site of the plasmid and prior preparation with endonucleases that produce different cohesive ends guarantees the right orientation of the insert within the vector and avoids plasmid self-ligation. Fig. 4.3 depicts vector pET28 that was employed for recombinant hGal-1,-3 expression of the presented work.

Transformation of bacterial host with recombinant plasmid DNA

Plasmids with DNA inserts are transferred into host cells via the cell membranes during a process called transformation.[173,174] Stress conditions such as elevated temperature, high calcium ion concentrations or electroporation dilate the membrane pores and facilitate uptake of the extrachromosomal DNA. "Competent" cells bear and survive those conditions and mutant bacteria strains tolerate foreign DNA that lack the correct methylation pattern without degradation. Transformed bacteria grow on agar plates supplemented with an antibiotic according to the resistance gene of the plasmid. An elegant way to distuingish nonrecombinant from recombinant transformants represents the blue-white selection screen by use of vector pUC18. Growth medium additionally contains the colorless chromogenic molecule 5-bromo-4-chloro-3-indolyl-β-D-galactoside (X-gal) that is cleaved by a β-galactosidase to release a blue chromophore. The *N*-terminal portion of this enzyme is encoded in the *lacZ'* region. If a DNA insert is introduced in the multiple cloning site of pUC18 the *lacZ'* coding region is disrupted. Consequently, no active enzyme is produced and recombinant transformants result in white colonies easily to distinguish from nonrecombinant blue ones. Alternative to a blue-white selection plasmids can be recovered from a single bacterial colony and subjected to an endonuclease restriction with the same enzyme used earlier in the cloning procedure. DNA separation by gel electrophoresis elucidates existence and size of a DNA insert.

Gene transcription and translation into protein

For protein expression bacterial cells of a single colony carrying the recombinant plasmid vector are transferred sterilely to liquid growth medium.[173,174] During the growth period

protein expression is suppressed to focus bacterial energy on amplification. Transcription of genes within the multiple cloning site is regulated by the *lac* operon. Physiologically, the *lac* operon controls transcription of lactose permease and β-galactosidase to guarantee an energy supply from lactose if the disaccharide is the most efficient energy source. The *lac* repressor is modulated in an allosteric manner by allolactose, an early metabolite. In recombinant protein expression the *lac* repressor is typically addressed with isopropyl-β-D-1-thiogalactoside (IPTG) due to its stability against β-galactosidases. Upon binding of IPTG a conformational change of the enzyme is induced leading to a release of the tetrameric repressor from the *lac* operon and initiating gene transcription of the gene in the multiple cloning site. Translation into the polypeptide sequence and proper folding to the three-dimensional structure occurs subsequently. Proteins produced by *E. coli* lack posttranslational modifications of eukaryotic cells such as glycosylation, ubiquitinylation and phosphorylation.

Protein isolation and purification

The use of recombinant DNA technologies facilitates the expression of a broad range of proteins, even if structure, location or function has not been fully determined.

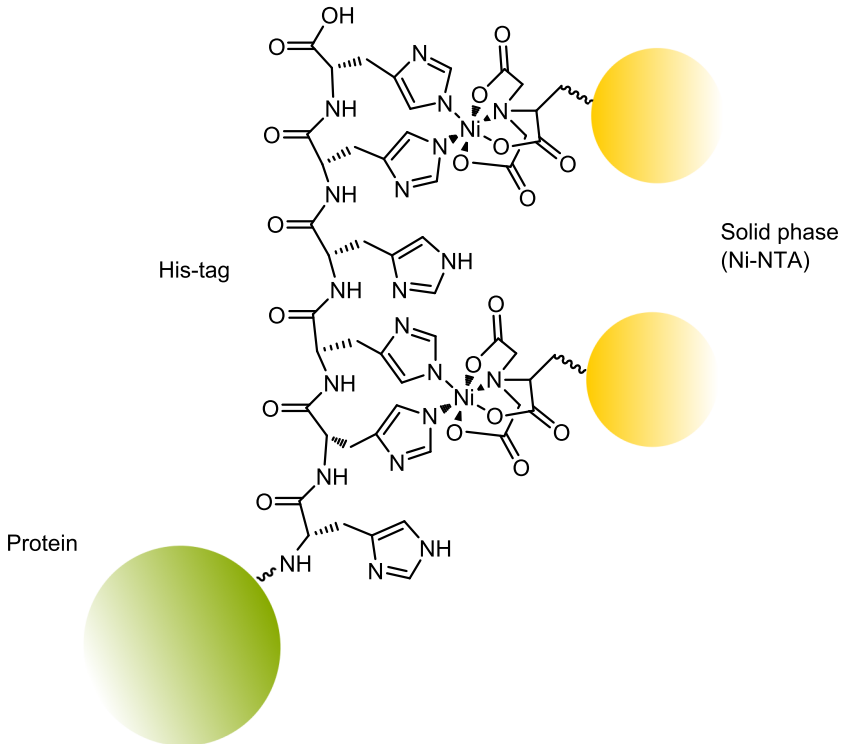

Fig. 4.4 Schematic illustration of protein purification on Ni-NTA solid phase via a terminal polyhistidine sequence.

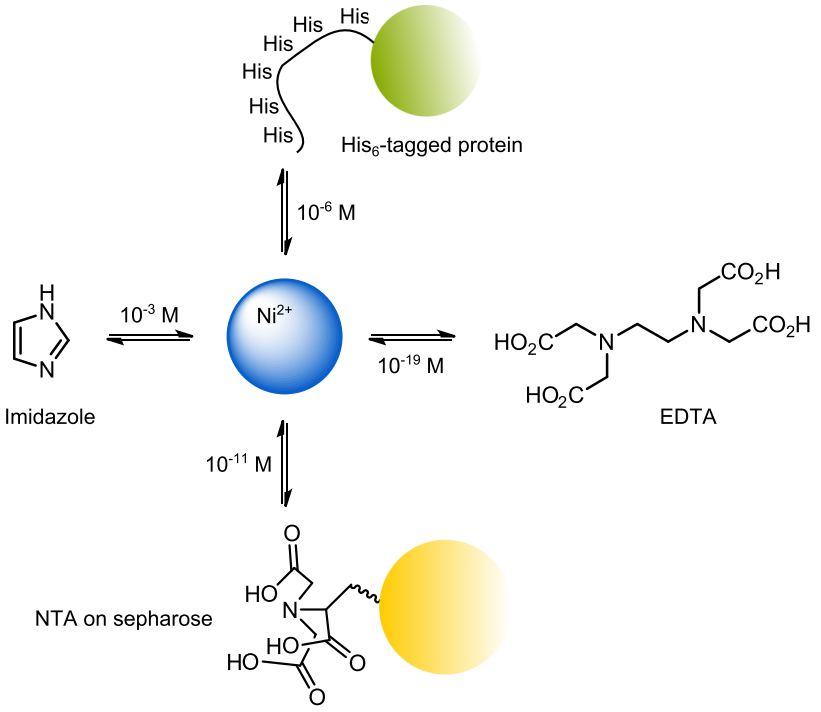

Fig. 4.5 Schematic presentation of interactions with Ni^{2+} and corresponding binding constants during protein purification by IMAC on Ni-NTA. His_6-tagged proteins are eluted with moderate concentrations of imidazole under mild conditions while Ni^{2+} cations remain bound to the solid phase. Regeneration of the column material and removal of Ni^{2+} is achieved with EDTA. Adapted from ref. 175.

Challenges during the isolation and purification process is stability and solubility of the overexpressed protein as well as the choice of an appropriate purification system. Popular purification techniques work with peptidic affinity tags[176,177] that are introduced on DNA level and are characterized by strong and selective interaction with their binding motifs. Immobilized metal affinity chromatography (IMAC) is a widespread purification strategy and the polyhistidine sequence (His-tag) an attractive affinity tag due to its low immunogenicity and small size.[176] Additionally, many proteins and enzymes tolerate the *N*- or *C*-terminal extension and protein functioning does not necessarily require tag removal after purification. Hochuli *et al.* developed a Ni(II)-nitrilotriacetic acid (Ni-NTA) matrix as an inexpensive and regenerative material to purify recombinant His-tagged proteins (Fig. 4.4).[178] Unspecific binding can be controlled by the incubation time and supplementary imidazole while pure protein is eluted upon changing the pH or addition of imidazole in high concentration. Fig. 4.5 illustrates interactions with Ni^{2+} and corresponding binding constants that allow mild elution condition of His_6-tag bound proteins by moderate concentrations of imidazole.[175]

However, this strategy is not applicable to metalloproteins as the metal itself could bind to

the column material and the Strep-tag®, an eight amino acid oligopeptide (WRHPQFGG) binding to the streptavidine core, is an attractive alternative for metalloproteins or proteins to be purified under anaerobic conditions.[179,180] Strep-Tactin®, a variant of streptavidin, exhibits enhanced flexibility and affinity to Strep-tag® II (WSHPQFEK) and has been engineered for more efficient purification.[181,182] The Strep-tag® II addresses the same binding pocket as biotin and thus, can be eluted after incubation and washing steps with biotin derivatives.
An affinity tag is redundant if the protein to be purified has an intrinsic binding motif which can be immobilized on sepharose and exploited for affinity chromatography. It is noteworthy to mention that the binding motif is recognized selectively by the recombinant and not by a host protein.
In some cases the affinity tag might affect the protein folding or biological function and has to be removed after purification. A protease cleavage site can be encoded on DNA level between the protein sequence and the affinity tag. Common proteases are enterokinase[183], SUMO protease[184], tobacco etch virus (TEV)[185] and thrombin[186]. TEV protease recognizes the seven amino acid sequence ENLYFC↓S/G and cleaves between glutamine and serine or glycine. TEV is an attractive protease for tag removal because it is highly specific, active on various substrates and cleaves efficiently at low temperatures. It might occur that cleavage is not optimal when the recognition site is not well accessible. However, the insertion of a peptidic linker usually improves structural flexibility and cleaving efficiency.[177]

4.1.2 Protein X-ray Crystallography

"The great complexicity of proteins makes it unlikely that a complete structure determination for a protein will ever be made by X-ray methods alone."[187] With these words Linus Pauling speculated in 1939 about the impact of protein X-ray crystallography for the future - five years after Bernal and Crowfoot recorded the first protein diffraction pattern.[188] In 1934 the scientists could already deduce precious structural coherences of the three-dimensional arrangement in pepsin, however, technological progress was still far away from elucidating structures of complex macromolecules and seemed to explain Pauling's scepticism. Unequivocally, protein X-ray crystallography entails various challenging steps, not only with regard to structure determination, and thus it was not until 1960 that myoglobin[189] and hemoglobin[190] were the first protein structures solved by X-ray diffraction and subsequent Fourier transformation alone. Nowadays, rotating anode tubes generate 1.542 Å CuK_α radiation and synchrotrons with wavelengths between 0.7 and 1.8 Å are prevailing X-ray sources to reach resolution on an atomic scale[191,192] and in April 2014 the RCSB protein database (www.pdb.org) comprised 99472 structures, 89% of those determined by X-ray crystallography. Despite of advances during the

last decades in molecular biology, computational power as well as the development of automated software programs protein crystallography remains a highly demanding discipline, not least due to its predominant empirical character and poor predictability of successful crystallization conditions.[191,192] The subsequent sections delineate the crystallization procedure from growing of initial crystals to refinement of the Fourier transformed protein model.

Crystallization

Proteins are large and highly flexible macromolecules with many diverse inter- and intramolecular interactions and so far no method can reliably predict conditions for the self-assembly into a periodic, well-diffracting crystal lattice.[191,192] Thus, experimental trial screens with the pure protein sample are inevitable to probe various conditions that reduce protein solubility and initiate the formation of monocrystals. The vapor diffusion method is the prevailing technique in this context (Fig. 4.6 a) where the protein (c $\geq$ 10 mg/ml) is supplemented with a precipitant and equilibrated in a closed atmosphere comprising a reservoir of higher concentrated precipitant (Fig. 4.6 a).[191,192] The resulting concentration gradient evokes that the reservoir solution slowly absorbs water from the protein/precipitant sample, thereby generating a supersaturated, thermodynamically metastable state and introducing spontaneous formation of crystal

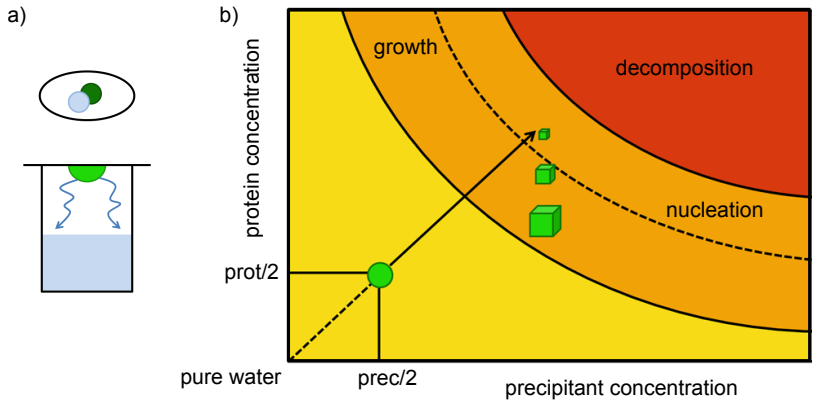

Fig. 4.6 a) Schematic illustration of the hanging drop vapor diffusion method. Protein sample (green) and precipitant (light blue) are mixed in equal amounts and transferred to a closed atmosphere of higher precipitant concentration. Through a concentration gradient water diffuses from the protein drop to the reservoir solution, thereby increasing protein and precipitant concentration. b) The phase diagram depicts the transition from the soluble state to the supersaturated state (orange region, above dashed line) during vapor diffusion. Nuclei form spontaneously and lowered protein concentration lead to subsequent crystal growth (orange region, below dashed line). Adapted from ref. 191.

nuclei. In an optimal crystallization process the protein concentration is decreased upon appearance of initial nuclei (Fig. 4.6 b, orange part above dashed line) to vertically reach the region diagram below the dashed line in the phase where crystals grow to full size. Instead, if nucleation conditions persist countless minuscule nuclei form and impede the expansion into larger crystals required for data collection. Too high precipitant concentrations cause a different scenario and transfer the protein into an unstable decomposing state (red region) while insufficient concentrations keep the sample in the unsaturated state (yellow region) and provide no crystals at all. Parameters in the precipitation mix that can be adjusted and fine-tuned are the choice and concentration of the precipitant itself, polyethylene glycol (PEG) or $(NH_4)_2SO_4$ as prominent representatives, buffer pH, temperature level and additives.[191,192]
Once grown to optimal size crystals are transferred to buffers with cryoprotectants, such as glycerol, PEG or glucose, to prevent the formation of ice crystals when flash-cooled in liquid nitrogen. During data collection protein crystals are exposed to intense ionizing X-rays that cause damage through generation of free radicals. As early as 1966 Low *et al.* reported that the kinetic degradation process of proteins can be limited by diffracting a crystal at low temperatures (-150 °C)[193] and since the 1990s it is common to center the protein crystal in a stream of dry nitrogen gas (-173 °C) to reduce radiation damage by cryogenic cooling.[194]

Diffraction of X-rays by crystals

A monocrystal is a periodic well-ordered three-dimensional array of molecules arranged by noncovalent inter- and intramolecular interactions. Such a crystal can be reduced to an individual unit cell, the smallest representative volume element, which in turn is translated into all three space directions by integral multiples of the unit cell vectors.[191,192] X-ray

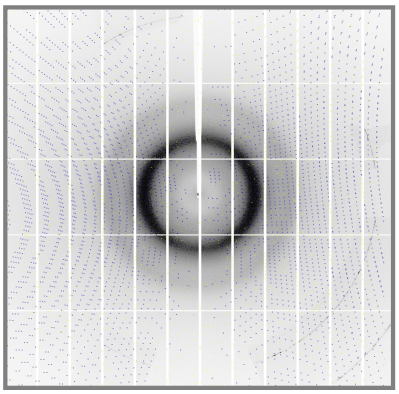

Fig. 4.7 Diffraction pattern of a well-diffracting crystal. Outer reflections contribute to high resolution data.

scattering from single molecules is extremely weak and hardly detectable in the noise caused by scattering from surrounding air and thus constitutes the urgent need of a regular arrangement of multiple molecules for structure determination.[191,192]
X-ray wavelengths are in the magnitude of chemical bonds and employed to excite electrons of the protein crystal. The electrons can normally be regarded as free electrons (in case of anomalous dispersion this approximation is invalid) and act as oscillating dipoles that emit secundary radiation of the same frequency. The constructive or destructive interference of coherently emitted radiation of all electrons leads to the unique diffraction pattern (Fig. 4.7) described by Bragg's law (Eq. 4.1):

$$\frac{2d_{hkl}sin\Theta}{\lambda} = n \tag{4.1}$$

with *hkl* as the Miller indices of the lattice planes of the unit cell (this paragraph refrains from giving a complete mathematical description considering the three-dimensional character of the crystal in the scattering process and contents can be found in corresponding reference books[191,192]). The spacing in the protein crystal and the angle of diffraction are correlated by an inverse relationship, coining the term "reciprocal space" for the diffraction space, and thus outer reflections in the diffraction pattern represent short distances in the object and contribute to a high resolution.

Fourier Transformation and Reconstruction of Electron Density

The transition from the diffraction pattern in reciprocal space to electron density ρ(x,y,z) in real space is realized by Fourier transformation that in itself exhibits no difficulties but requires two terms, that are the structure factor amplitudes F_{hkl} and the relative phase angles α_{hkl} for each detected reflection.[191,192] The structure factor amplitudes are directly accessible and proportional to the square root of the measured intensities of the reflections (Eq. 4.2):

$$\rho(x,y,z) = \frac{1}{V}\sum_{-h}^{h}\sum_{-k}^{k}\sum_{-l}^{l} F_{hkl} \cdot e^{-2\pi i(hx+ky+lz-\alpha_{hkl})} \tag{4.2}$$

where V indicates the unit cell volume and *hkl* the Miller indices of the unit cell.
The relative phase angles α_{hkl} are not directly provided by the experimental data though their knowledge is crucial as they determine the interference pattern and contain the information about electron localization. This dilemma constitutes the phase problem in protein X-ray crystallography (Fig. 4.8) and to date, several approaches are available to overcome this obstacle.[191,192] The **Patterson function** is a variation of the Fourier sum and depends exclusively on the amplitudes of the structure factors. While the contour map of the Fourier transformation represents the electron density $\rho(x,y,z)$ of

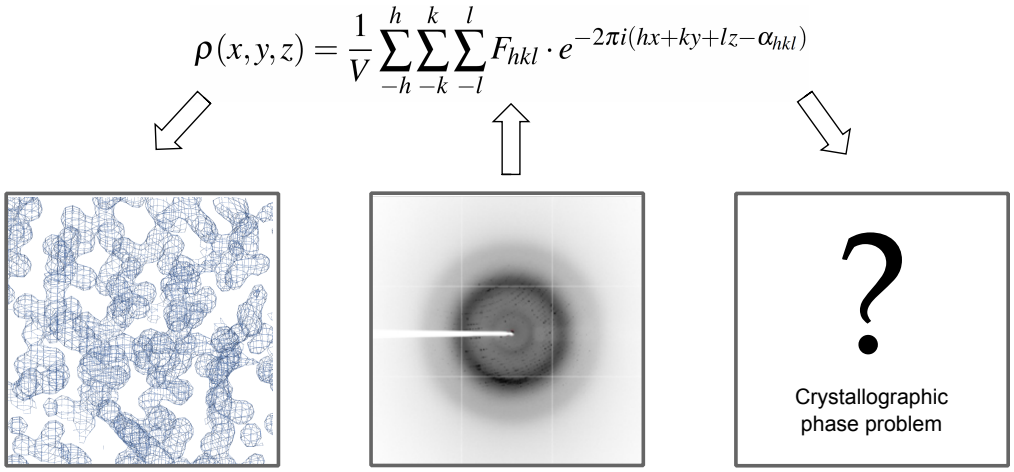

Fig. 4.8 Schematic illustration of the crystallographic phase problem. Fourier transformation from the diffraction pattern in reciprocal space to electron density ρ(x,y,z) in real space requires the structure factor amplitudes F_{hkl}, proportional to the square root of the measured intensities of the reflections, and the relative phase angles α_{hkl} that are not provided by the experiment. Adapted from ref. 191.

the macromolecule and peaks of high intensity locate individual atoms, maxima of the Patterson map rather display vectors of interatomic distances. It is easy to imagine that a Patterson map quickly becomes sophisticated as there are far more interatomic vectors than there are atoms and consequently, the Patterson function is restricted to small molecules. Nevertheless, this strategy is of great importance to also solve the structure of complex proteins when combined with **isomorphous replacement**. It includes the preparation of heavy-atom derivatives of the protein under investigation and requires isomorphous crystal packing of derivated and native crystal. That means, soaking with ions of Hg, Pt or Ag may not disturb crystal conformation or unit cell dimensions but introduces strong diffractors of X-rays which contribute with additional, characteristic reflections to the diffraction pattern when located at identical sites in all unit cells of the protein crystal. Hg^{2+} ions react readily with thiols of surfacial cysteines and side chains of cysteine, histidine or methionine form stable complexes with Pt^{2+} by replacing a chloride anion of $PtCl_4$. In the first approximation it can be assumed that differences of structure factor amplitudes ($\Delta|\vec{F}|$) between the native and derivated crystals are based exclusively on the heavy metal atoms. The significantly simplified difference Patterson map then allows determination of initial phase angles for the structure factors of the whole protein. Isomorphous replacement usually demands diffraction of several independent isomorphous heavy metal derivatives (multiple isomorphous replacement, MIR), however, in some cases a single derivative might be sufficient to determine protein phases for subsequent refinement (single isomorphous replacement,

SIR). **Multiple anomalous dispersion (MAD)** is a further approach to solve the phase problem and exploits the phenomenon of anomalous scattering (or dispersion) near the absorption edge of an element. Quantized energy of electrons in light atoms of a protein such as carbon, nitrogen, oxygen or hydrogen are not in the range of X-ray wavelengths used for X-ray crystallography, but absorption edges of heavy atoms are at lower energy and accessible by synchrotron radiation. Diffraction patterns of a single crystal comprising one or more heavy atoms at multiple wavelengths can provide adequate phase information for solving the macromolecular structure. MAD is a powerful tool to solve the phase problem in X-ray crystallography and finds widespread application since synchrotrons offer X-rays of different wavelengths.
Alternatively, if the crystal structure of the protein, of a homologous structure or of a congruent subunit has been solved before the phase angles can be applied as initial estimates in a process called **molecular replacement (MR)** with the known structure as phasing model. This approach does not necessitate further phasing experiments and allows a rapid determination of initial phases but entails the risk of a model bias. Reconstruction of the electron density is dictated by phase information during Fourier transformation, such that the search model strongly influences the protein structure to be solved. Thus, methods to remove phase bias are essential to build the correct electron density map.

Model Refinement and Structure Determination

Fourier transformation of the measured reflection intensities and a suited phase model lead to a contour map of the protein's electron density. Interpretation of this map includes building a model of the protein structure that is in good conformity with the electron density. Initial models certainly exhibit errors concerning bond lengths and angles, show modest backbone geometry and unlikely torsion angles, all together demand for subsequent structure refinement.[191,192] The refinement process adjusts atomic parameters with the objective to minimize differences between observed and calculated diffraction data and is evaluated by the crystallographic ***R*-value** (Eq. 4.3):

$$R = \frac{\sum_h |F_{obs} - F_{calc}|}{\sum_h F_{obs}} \tag{4.3}$$

were h indicates a single reflection.
The R-value is optimized during the iterative refinement program and consequently the structure model becomes more and more accurate. At a certain point the R-value will still improve mainly due to an overparametrization but the model will not.[191] For this reason the R-value is cross-validated after each successive round by an $\boldsymbol{R}_{free}$**-value**. The idea of cross-validation is to exclude a small fraction of the experimental data (ca. 5% of reflections) from the refinement process. Appropriate introduction of refining parameters

will also improve R_{free} as the whole model becomes more complete. Converging R- and R_{free}-factors indicate that the model is optimal.

The ***B*-factor**, the atomic displacement or temperature factor, gives further valuable information for the evaluation of the obtained structure and is indispensable in the refinement process as it is part of the model.[191] While the R-value is a universal measure that can only judge the model as a whole the B-factor rates individual parts like side chains of amino acids or ligands. B-factors are introduced in the refinement process as it is expected that surfacial amino acids exhibit more translational and rotational freedom than amino acids buried in the hydrophobic protein interior. Diffraction is affected by a higher degree of movements and considering motions in the refinement process makes the model more realistic and hence more precisely. In addition, the B-factors calculated and optimized during refinement provide valuable information about the dynamics of the large and static model.

4.1.3 Surface Plasmon Resonance (SPR)

The phenomenon of surface plasmon resonance was first described by Turbadar in 1959[196] and basically relies on the occurrence of total intern reflection (TIR) and the concomitant induction of an evanescence electric field and surface plasmon waves.[41,197,198] Total intern reflection takes place at the interface of non-absorbing media of different refractive indices (water-glass, air-glass) when a propagating light beam impinges the second medium above a critical angle Θ.[195] Even though the reflected light carries the same netto energy as the incident beam an electric field (evanescence wave) is induced in the second medium that declines exponentially with the increasing distance. When the interface of both media is coated with a thin layer ($d \leq \lambda$) of

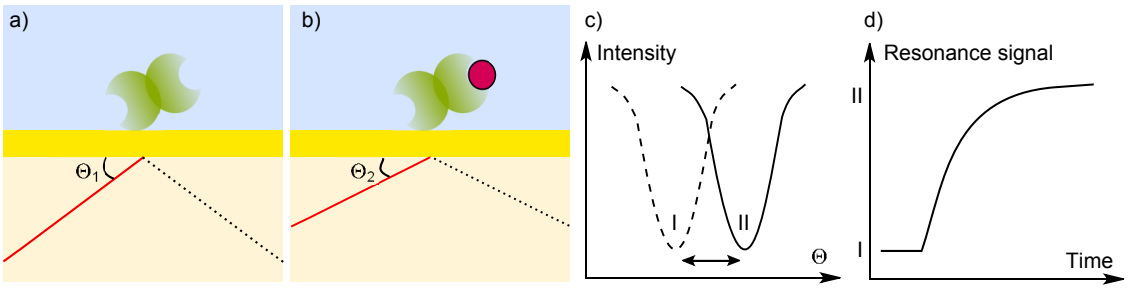

Fig. 4.9 Surface plasmons are generated upon excitation with electromagnetic radiation in the gold layer at the glass-water interface and the required resonance wavelength at a specific angle Θ_1 (dashed line) is absent in the total reflected light (a). Excitation of surface plasmons strongly depends on the chemical environment (b) and minor changes in the mass result in an altered resonance angle (c). Differences in the resonance angle arising from minor mass changes upon ligand binding are translated into a response signal (d). Adapted from ref. 195 and 40.

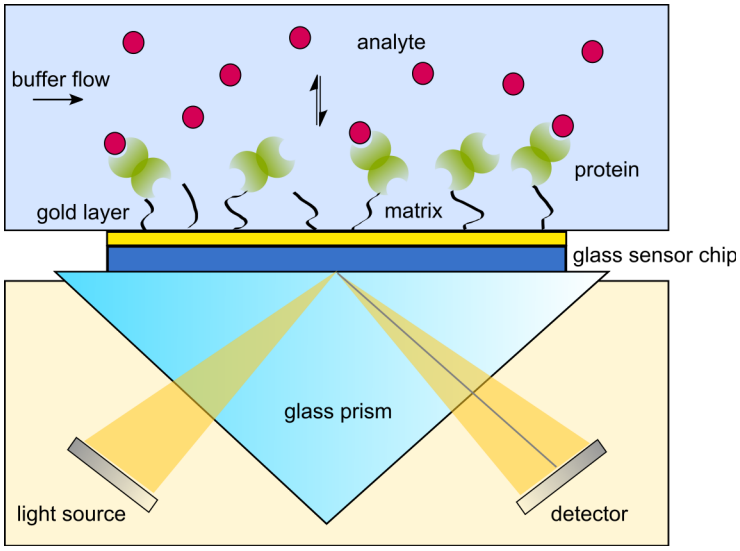

Fig. 4.10 Experimental setup of an SPR biosensor. The protein is immobilized on the functionalized dextran matrix of the sensor chip. The interaction between receptor and injected analyte is followed via the mass difference upon ligand binding and the consequent change in resonance angle of absorbed light. Adapted from ref. 195.

a conducting metal surface plasmons are generated during this process.[199] Surface plasmons are fluctuating electron density in the material and correspond to photons in the case of light.[195] The excitation of plasmons decisively depends on energy and momentum of the incident light beam and strongly responds to minor changes in the chemical environment (Fig. 4.9 a and b).[199]

Common biosensors exploit this phenomenon to analyze ligand-receptor binding via emerging mass differences during the affinity study.[iii] The core element of biosensors is a gold coated glass sensor chip. The chip surface is further functionalized with a hydrophilic carboxymethyl dextran matrix to allow covalent immobilization of a non-denaturated biomolecule, such as proteins, nucleic acids, liposoms or carbohydrates and represents a threedimensional quasi-liquid environment. The sensor chip is connected to a continuous flow system (sample side) for injection of the interaction partner and to a glass prism at the detector side.[200] Biomolecular interactions on the chip surface influence the surface resonance wavelength and result in a changed absorption which is manifested in a shift of the intensity dip (Fig. 4.9 c). This change in angle directly correlates with the mass alteration, coining the term "mass detectors" for SPR biosensors, and can be converted into a response signal (Fig. 4.9 d) that was experimentally determined for protein interactions to (Eq. 4.4):[201]

$$1RU \equiv 1pg/mm^2 \tag{4.4}$$

[iii] *Surface plasmon resonance (Technology Note 1)*, Biacore AB, 2011.

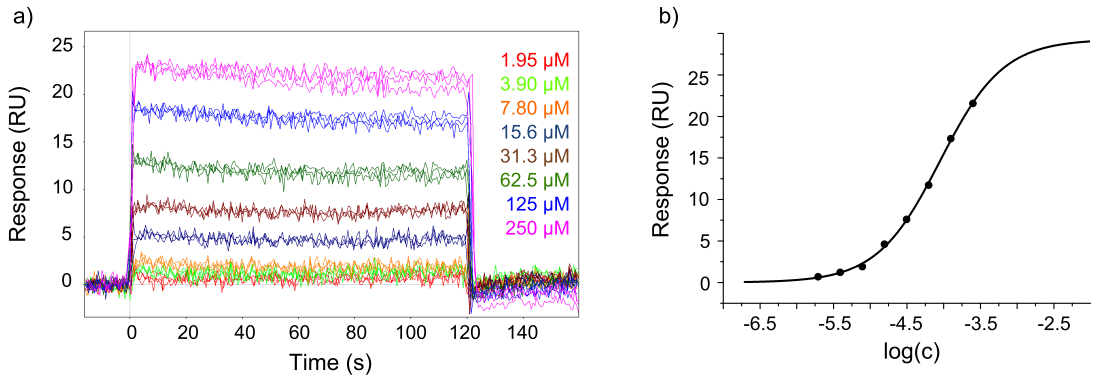

Fig. 4.11 a) Typical SPR sensogram. Response units increase with ligand concentrations b) Sigmoidal curve fitting of experimental data and logarithmic plotting indicates the K_d value as inflection point.

A typical SPR experiment comprises the immobilization of the receptor molecule (either macromolecule or ligand) and investigates interaction affinity and kinetics upon addition of the analyte in various concentrations.[40] The aqueous analyte sample is injected via a flow cell to avoid diffusion and convection processes that might occur during mass transport to the sensor surface in a stationary system (Fig. 4.10). The signal response as shift in resonance angle can be tracked in real-time and a plot versus time gives insights into association (k_{on}) and dissociation (k_{off}) rates that define the dissociation constant K_d as described by Eq. 4.5:

$$K_d = \frac{k_{off}}{k_{on}} \tag{4.5}$$

Fig. 4.11 a depicts a characteristic SPR sensogram. Before injection of the binding partner the sensor chip is flushed with running buffer to define a stable baseline. Operation of a second measuring cell in series permits to correct the gross signal from unspecific binding. Upon ligand addition the signal response rapidly increases to reach a steady state. The signal response depends on the ligand concentration and a sigmoidal fit over the experimental data directly provides the dissociation constant as inflection point of the curve (Fig. 4.11 b).

In previous SPR experiments with galectins either the protein or the carbohydrate ligand were immobilized on the chip surface.[202–205] The covalent attachment of the protein and injection of the mobile carbohydrate allows investigation of the monovalent binding event between multivalent galectins and monomeric disaccharides. In contrast, signal response of measures with immobilized carbohydrate and mobile protein are affected by multivalent effects and present a different binding scenario (cf. section 5.2.1).

In SPR experiments of this work it was of predominant interest to study the monovalent binding event as the resulting K_d values facilitated the evaluation and comparison of

single steps of the rational ligand design without being distorted by multivalent effects.

4.1.4 Isothermal Titration Calorimetry (ITC)

Molecular interactions are dictated by comprehensive binding forces and formation of receptor-ligand complexes usually demands desolvation processes and loss of conformational freedom of both, macromolecule and ligand.[206,207] Binding thermodynamics describe these processes and elucidate enthalpic as well as entropic factors to ΔG (Eq. 4.6), the Gibbs free binding energy, that ideally contribute constructively to a high affinity binding.[40,208,209]

$$\Delta G = -RTln(K_a) = \Delta H - T\Delta S \tag{4.6}$$

ITC is an analytic method for the experimental determination of the thermodynamic nature of protein-ligand interactions and provides entropic (ΔS) and enthalpic (ΔH) contributions as well as the affinity (association constant K_a) and stoichiometry (n) of the binding event in a single experiment.[39,210] The calorimeter instrument comprises two identical cells, the measure cell and the reference cell, placed within an adiabatic jacket (Fig. 4.12).[iv] The measure cell contains a buffered solution of the protein of interest while the reference cell holds the same volume of pure buffer. During the experiment the ligand is titrated to the measure cell and both cells maintained at isothermic conditions (ΔT = 0). If the interaction between protein and ligand is exothermic heat is released

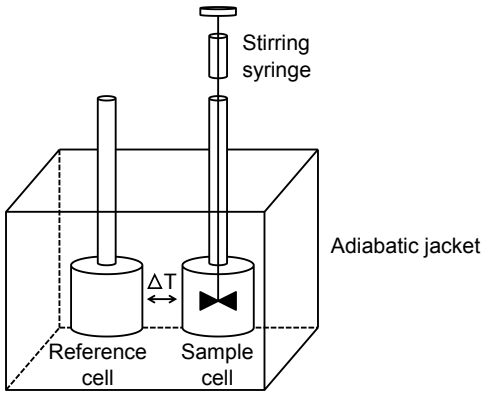

Fig. 4.12 Adiabatic calorimeter for evaluation of thermodynamic properties of receptor-ligand interactions. Sample and reference cells are maintained at isothermic conditions and heat changes are monitored that arise from addition of the buffered ligand. Adapted from ref. 40

[iv] "Divided we fall? Studying low-affinity fragments of ligands by ITC". *gelifesciences.com*. GE Healthcare Life Sciences. Web. 27 May 2014. <http://www.gelifesciences.com/gehcls_images/GELS/Related%20Content/Files/1314823637792/litdoc28987044_20140311181217.pdf>

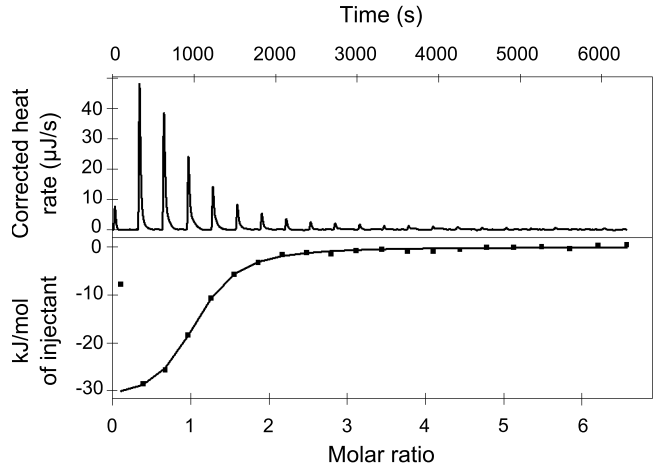

Fig. 4.13 Typical ITC diagram. The upper part depicts the corrected heat amount necessary to maintain both cells at isothermal conditions during titration of the ligand. The lower part shows the integrated heat change per ligand injection and the sigmoidal fit curve from the fitting process. The inflection point indicates the stoichiometry n of the interaction.

and more energy has to be supplied to the reference cell than to the sample cell. In case of an endothermic reaction the required energy supply for isothermal conditions is *vice versa*. A plot of the corrected heat rate (μJ/s) related to each successive addition of ligand against time (s) results in a series of peaks - the characteristic ITC profile - with ΔH determining the y-intercept as well as the integral of the peaks (upper part of Fig. 4.13). Fig. 4.13 shows that at the beginning of the titration experiment large amounts of energy are supplied to the reference cell indicating an exothermic interaction and a significant increase of receptor-ligand complex formation. Heat changes are declining with continuing titrations reflecting that most binding sites are occupied and that ligand dilution accounts for the small differences. This observation implies a fundamental prerequisite for the experimental realization, that is the solvation of receptor and ligand in a physically identic buffer to avoid heat changes that arise by dilution effects.
The interpretation of an ITC experiment essentially relies on a correct extraction of the thermodynamic data with a nonlinear least square curve-fitting and the use of a model that represents the studied interaction appropriately. The lower part of Fig. 4.13 shows a typical sigmoidal ITC titration curve resulting from the fitting process. The inflection point indicates the stoichiometry n of the proposed binding model and the overall shape of a titration curve depends on the concentration of receptor binding sites $n[M]$ and the binding constant K_a. The Wiseman parameter c links the affinity with the experimental realization and is the product of both (Eq. 4.7):[210]

$$c = n[M] \cdot K_a \tag{4.7}$$

Wiseman *et al*. demonstrated that for c values > 10 the titration curve is clearly sigmoidal and ΔH, K_a and n can be determined accurately when c is between 10 and 500.[210] Whereas the investigation of high affinity systems is not restricted by this demand the study of low binding affinities such as carbohydrate lectin interactions can be quite challenging due to solubility problems and the large amounts of receptor and ligand necessary for an experiment.

4.2 Diagnostic Tools

Reliable and rapid detection screens are key elements in the diagnosis of pathologic alterations and have a striking impact on the course of the disease and the prospect of treatment success. Positron emission tomography is an established *in vivo* technique for tracking elevated metabolites or aberrant expression patterns associated with distinct disorders. Microarrays represent an efficient *in vitro* tool to identify a variety of pathological reporters by binding to immobilized specific ligands or antibodies on the chip surface.

4.2.1 Positron Emission Tomography (PET)

Positron emission tomography (PET) technology is based on findings of C.A. Anderson in 1932 who discovered a novel particle "carrying a positive charge but having a mass of the same order of magnitude as that normally possessed by a free negative electron"[211] while studying cosmic rays in a cloud chamber. He entitled his positively-charged electron a positron and gave first experimental evidence for the existence of antimatter suggested by Paul Dirac a few years earlier in 1928.[212] The translation into a medical application more than 50 years ago now relies on the annihilations of positrons and electrons and the detection of resulting γ-rays.[213]
Beside cosmic rays and high energy collision processes PET isotopes ${}^{I}_{1}p$ are principal sources for positrons and characterized by a spontaneous β^+-decay into a neutron ${}^{I}_{0}n$, an electric neutral neutrino ν_e and a positron e^+ (Eq. 4.8):[213]

$$ {}^{1}_{1}p \rightarrow {}^{1}_{0}n + e^+ + \nu_e \tag{4.8} $$

If such a decay occurs in the body of a patient the freed positron covers a distance of few millimeters of elastic collisions before it finally collides with an electron of the appropriate energy. The annihilation of this positron and its antiparticle releases energy in form of two high energy photons radiated in an angle of 180 °.[213] Detectors that are circularly arranged around the human body record time and loction of arriving γ-rays and reconstruct a three-dimensional image of the origins of annihilation. Consequently,

Table 4.1 Half-life periods of common PET isotopes.[213]

	^{64}**Cu**	^{18}**F**	^{68}**Ga**	^{11}**C**	^{13}**N**	^{15}**O**
Half-life period [min]	762	110	68.1	20	10	2

the linkage of a PET isotope to a biological active compound and following intravenous administration allows the detection of accumulated PET tracers at the addressed physiological spot(s). Further, PET permits the implementation of individual, tailor-made tracer molecules to track biochemical processes based on pathological alterations. In combination with imaging methods like computer tomography (CT) or magnetic resonance tomography (MRT) high resolution images of the tissue morphology and corresponding biochemical functions are accessible.[213]

To date, several PET isotopes have found entrance to chemical and biomedical research for various medical purposes (Table 4.1). ^{64}Cu and ^{68}Ga are attractive isotopes as their half-life periods of 12.7 h and 68.1 min, respectively, allow certain synthetic manipulations before the resulting radiotracers are injected to the body. PET isotopes of carbon, nitrogen and oxygen suffer from rather short half-life periods but provide tracer molecules consisting of exclusively endogenic atoms which may have a positive impact on physicochemical and pharmacophoric properties. However, the most prevalent PET isotope in clinical applications is ^{18}F ($t_{1/2}$ = 110 min) due to disposability aspects, the ease of synthetic integration and its low influence on solubility, lipophilicity and binding activity of the biomedically relevant molecule.[213] The introduction of ^{18}F, in principle by conventional fluorination methods, needs to tolerate common functional groups of biological active compounds and occur at a late stage of the synthesis to evade unproductive decay. In general, the time for synthesis, purification and formulation of the PET tracer for administration should not exceed two half-lives of the radionuclide.[214] Thus, the ideal method, either with $^{18}F_2$ in an electrophilic or with $^{18}F^-$ in a nucleophilic approach, proceeds fast and functional group tolerant affording one single fluorination product that is isolated in a straightforward purification process.[214,215]

PET tracers in tumor diagnosis

PET is a powerful tool in medicinal clinic and applied for diagnosis of Alzheimer and neuronal diseases, cardiac imaging and monitoring of brain activity.[213] So far, cancer diagnosis and oncologic imaging are prevailing applications of PET and the following paragraph resumes clinically approved radiotracers featuring the ability to track elevated metabolic rates.

The most prominent radiotracer [^{18}F]fluoro-2-deoxy-D-glucose **[^{18}F]FDG**, developed in

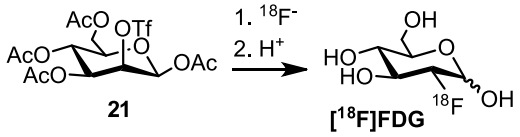

Scheme 4.1 Synthesis of radiotracer **[^{18}F]FDG** from mannose triflate derivative **21** with nucleophilic $^{18}F^{-}$, developed by Hamacher *et al.*[216]

the late 1970s (Scheme 4.1), mimics D-glucose by its almost identic structure which is essential for the energy supply of human cells.[217] Both molecules, **[^{18}F]FDG** and D-glucose, are assimilated by organs and tissues with a high energy demand including brain, kidney and tumor cells via the specific GLU-1 transporter.[213,218] While D-glucose enters the metabolic pathway of glycolysis after phosphorylation and is degraded to pyruvate **[^{18}F]FDG** accumulates within the cells as the phosphorylated glucose analogue is neither a substrate for the isomerase nor for the backtransport to exit the cell.[219] Thus **[^{18}F]FDG** is metabolically trapped in proliferating cancer cells which is exploited in PET for detection and localization of the tumor (Fig. 4.14). A drawback of this method is the incapability of **[^{18}F]FDG** to detect slowly prospering tumors like the prostate adenocarcinoma.[213] Additionally, **[^{18}F]FDG** accumulates in inflammatory tissue or tissue of tuberculosis that are likewise characterized by an elevated glucose metabolism.
The employment of radiotracer [^{18}F]choline[221] and [^{11}C]choline[222] (Fig. 4.15) also takes advantage of the altered biochemistry of tumor cells by addressing the biosynthesis of cell walls. Cholin is an important precursor of phospholipids and derivatives of this compound even permit imaging of slowly proliferating tumors. Choline is phosphorylated within the cells to phosphorylcholine by the enzyme cholinkinase that is upregulated in malignant tissues.
A different approach addresses the high cell division rates of proliferating tumors that imply an increased demand of nucleosides for replication of DNA. This pathological

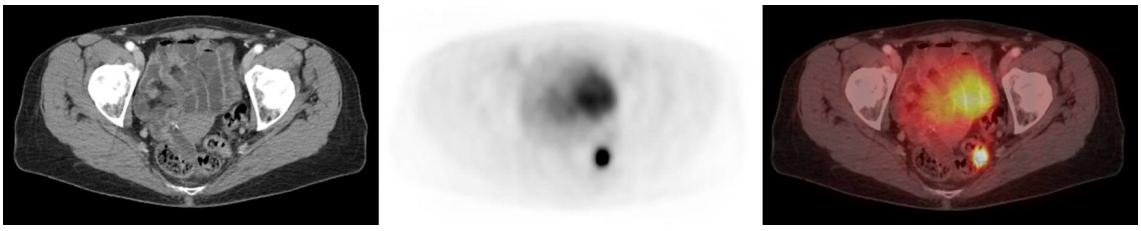

Fig. 4.14 Detection of metastatic breast cancer by a combined **[^{18}F]FDG**-PETCT scan. The left image displays a contrast-enhanced CT, the middle shows the corresponding PET cut-out and a fusion of both is depicted on the right (CT ≙ computer tomography). Reprinted with permission from ref. 220. Copyright © 2009, Elsevier.

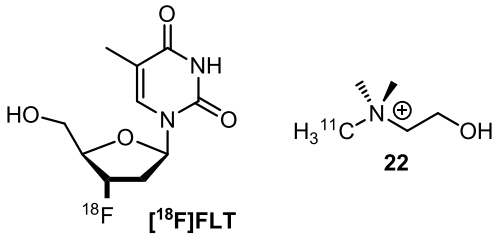

Fig. 4.15 ^{18}F thymidine[224] **[^{18}F]FLT** and ^{11}C choline[222] **22** radiotracers.

finding motivates the implementation of radiolabeled thymidine as this nucleobase is exclusively incorporated in DNA and not in RNA. Thymidine derivatives with ^{14}C, ^{11}C, ^{3}H and also ^{18}F PET isotopes have been successfully tested so far (Fig. 4.15).[223]
Mäcke *et al.* reported about a radiotracer for diagnosis of prostate cancer by tracking gastrin-releasing peptide receptors on the tumor cell surface.[225] To this end, they developed a conjugate of a specific peptide ligand and the chelator 1,4,7,10-tetraazacyclododecane-1,4,7,10-tetraacetic acid (DOTA) for coordination of cationic ^{68}Ga. The radiolabeled conjugate was specifically uptaken by prostate tumor and pancreas and accumulated within the tumor while a fast elimination was monitored from pancreas and other abdominal organs.[225]

4.2.2 Microarrays

In the last decade, various approaches have been developed for construction of glycan arrays to investigate interactions between carbohydrates and proteins, whole cells, RNA or viruses.[226–229] These methods include the preparation of self-assembled monolayers on gold chips via alkane-thiol functionalized carbohydrates,[230] the fixation of saturated

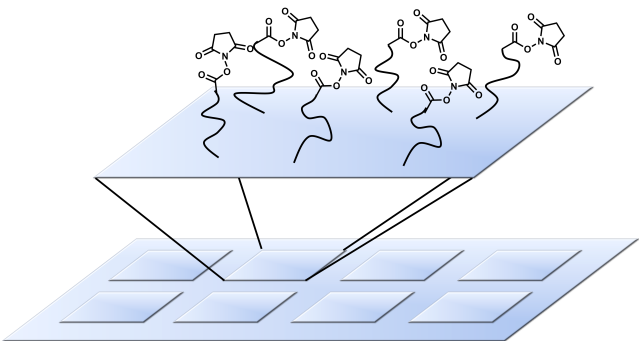

Fig. 4.16 Microarray coated with a functional polymer and terminal reactive NHS ester groups for covalent linkage of amines. Compartments allow for simultaneous screening of different conditions.

hydrocarbons to polystyrene microtiter plates[231] and the affinity-based attachment of biotinylated carbohydrates on a streptavidin surface[232]. However, the covalent linkage of modified carbohydrates to glass slides coated with an activated polymer dominates the many different microarray formats.[233–235] Typically, a reactive group is presented by the polymer layer and the carbohydrate equipped with a compatible functional group is attached to the chip surface. Compatible functional groups comprise amines and *N*-hydroxysuccinimides (NHS) (Fig. 4.16),[233,234] thiols and maleimides,[236] azides and alkynes[231] or photoreactive groups[237]. Initially, glycan microarrays were applied to probe the ligand specificity for carbohydrate binding of lectins.[233,238] Today, glyco chips find widespread application in inhibitor screens and the determination of IC_{50} values,[239] to calculate kinetic constants by assessing binding intensities at different dilutions[240] or to investigate adhesion and interaction of an entire organism like whole cells[241] or viruses[233]. Another promising field for glycan microarrays is their use as a diagnostic tool to detect pathogens[241,242] or disease-specific antibodies in blood sera.[228]

4.3 High Resolution Imaging of Cell Surfaces

Fluorescence microscopy is a powerful tool for investigation of dynamic cellular processes in living organisms with temporal resolution not accessible by static imaging methods like electron microscopy.[243] However, the spatial resolution was dictated for a long time by the diffraction barrier, first described by Ernst Abbe in 1873,[244] which prevented the imaging of subcellular organization events smaller than half the wavelength of the light and to a maximal resolution of 200 nm with visible light. To bypass this restriction several concepts have been elaborated in recent times and contributed to obtain valuable insights into structural features and biological organization processes at near-molecular level.[243,245] All of these microscopic approaches that have overcome the resolution limit are based on either deterministic (e.g. stimulated emission depletion (STED))[246] or stochastic (e.g. stochastic optical reconstruction microscopy (STORM,[247] *d*STORM)[248]) imaging methods. Deterministic approaches generate specific light patterns while stochastic techniques reduce the number of simultaneously emitting fluorophores.[243] Thus to detect the full information the latter require recording several thousand to ten thousand of images in a short period so that molecular dynamics do not influence the resolution.

4.3.1 *d*STORM

In a *d*STORM experiment biomolecules are labeled with photoswitchable fluorophores such as Alexa647 and experimental realization guarantees that only a small subset of fluorophores populates the fluorescing on state while the majority is reversibly transferred

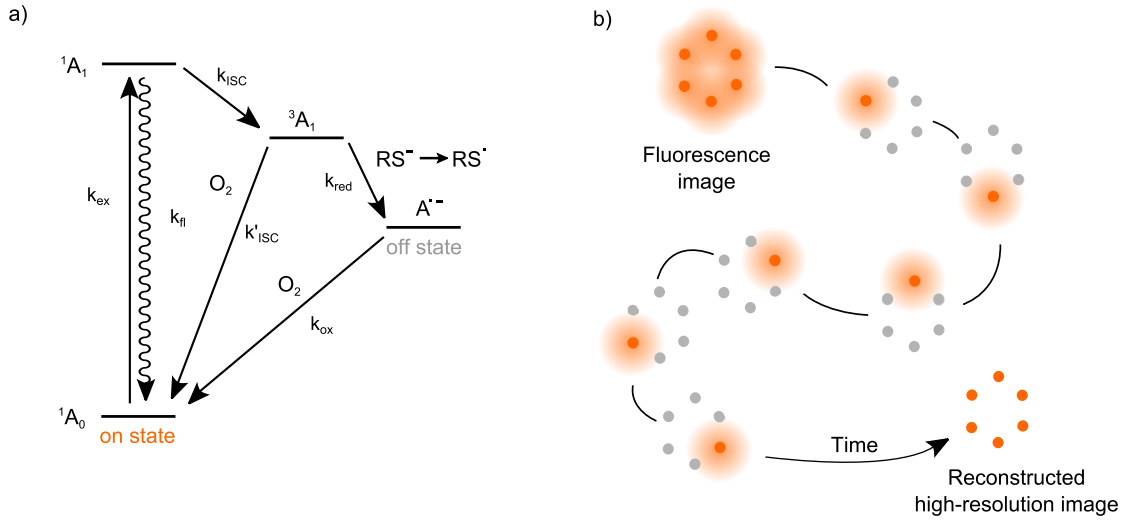

Fig. 4.17 Schematic illustration of *d*STORM. a) Upon irradiation fluorophores are excited to the $^1A_1$ state and either return to the ground state $^1A_0$ by emission of fluorescence or occupy the triplet state $^3A_1$. The triplet can be reduced by thiols to the stable radical nonfluorescent radical anion $A^{\bullet -}$. Repopulation of $^1A_0$ ocurrs either by oxidation of molecular oxygen or stimulated by irradiation. Experimental realization guarantees that only a small subset of fluorophores are in the fluorescent on state (orange) while the majority is captured in the nonfluorescent off state (grey). b) Recordance of several thousands to ten thousands images and reconstruction of stochastically determined fluorophores permit resolution up to 20 nm.

to a stable nonfluorescent (dark) off state at a given time (Fig. 4.17 a).[248,249] To this end, the sample is irradiated at 647 nm and the Alexa647 fluorophores transferred to the first electronic excited state $^1A_1$ (Fig. 4.17 a). Fluorophores can either return to the ground state $^1A_0$ under emission of fluorescence or transition into the triplet state $^3A_1$ by intersystem crossing (ISC) and react with reducing thiols like DTT, β-ME or glutathion, to form a stable nonfluorescent radical anion $A^{\bullet -}$. The radical anion of Alexa647 exhibits an absorption band at around 500 nm which is exploited for controlled irradiation and repopulation of the on state $^1A_0$. The transfer of fluorophores from $^3A_1$ and $A^{\bullet -}$ to the ground state is favored by molecular oxygen and is prevented by use of an oxidation scavenger system.

A fine-tuned adjustment of thiol concentration, pH value, intensity and rates of laser pulses for activation and deactivation permits the temporal separation of fluorescing molecules and a Gaussian fit of each fluorescence image (usually around 5000-40000 images, frame rate 5-40 Hz) reconstructs the fluorescing sites in dependence of emitted photons with a resolution up to 20 nm (Fig. 4.17 b).[248]

4.3.2 The Glycocalyx and Metabolic Glycoengineering

Surfaces of eukaryotic cells are coated with highly complex and type-specific carbohydrate structures by membrane-anchored glycoproteins or- lipids (Fig. 4.18).[250] The most prominent representatives of proteoglycans are characterized by an *N*- or *O*-linkage between the glycoside and the polypeptide backbone. *N*-glycans are commonly linked to an asparagine residue within the Asn-X-Ser/Thr consensus sequence of the polypeptide while *O*-glycans are attached to the hydroxyl groups of serine or threonine, typically via an *N*-acetylgalactosamine building block.[250,251] The distinct glycans are synthesized in the cytoplasm from nucleotide-activated monosaccharides and migrate subsequently to the inside of the Golgi apparatus and the endoplasmatic reticulum (ER) for posttranslational modification of the respective polypeptide. Alternatively, activated monosaccharides are attached successively to the proteins in the ER.[250] It is noteworthy to mention that the glycan sequence is not encoded by a direct template (such as genes or proteins) and the chemical nature of carbohydrates permits myriads of different structures that vary in size, composition and linkage. In this context, the field of glycomics has emerged to study the many diverse roles of the posttranslational modification and to elucidate the specific glycosylation patterns with regard to the cell type and developmental state, physiological conditions and pathological anomalies.[252] Evidently, the covalent attachment of glycans to peptide structures multiplies the genomic information and provides glycoforms with different biological roles even though resulting from a single gene. Thus it is not surprising that glycan-mediated processes span a wide scope of physiological roles ranging from modulatory and structural functions, cell-cell signaling, recognition events to pathological processes such as virus infection, tumor development or inflammation.[250,253]

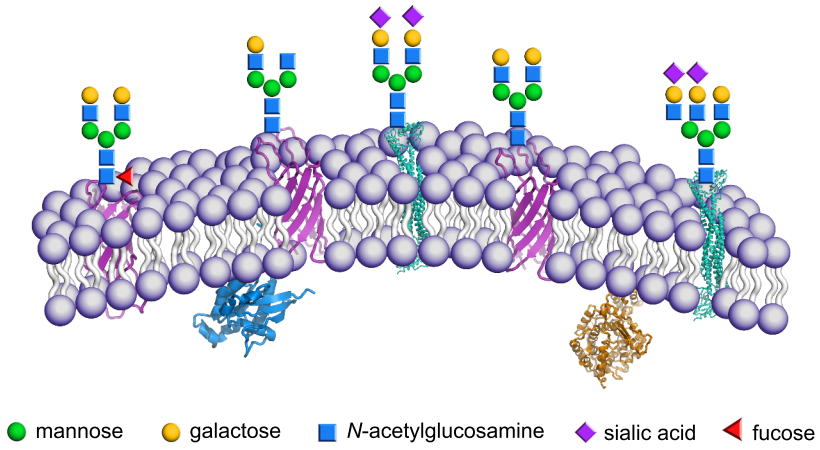

Fig. 4.18 Schematic representation of an eukaryotic cell surface (pdb codes for depicted proteins are 4H8S, 1DOA, 1KZO, 1QG9).

To date, different strategies have been chosen to investigate the role and underlying biological mechanisms of glycoconjugates on cell surfaces and to interfere with pathological processes.[254,255] One approach encompasses the down- or upregulation of distinct glycosyltransferases responsible for the construction of glycan structures and facilitates the study of their biosynthesis, secretion pathways and physiological functioning.[254] Alternatively, receptors can be inhibited by exogenous carbohydrate ligands or aglycons as binding partners to suppress or promote a specific immune response.[256] Metabolic glycoengineering directly targets the resulting glycan motif and exploits the finding that synthetic monosaccharides bearing a small chemical modification are tolerated in the biosynthesis of complex carbohydrates.[257] In pioneering work Reutter *et al.* demonstrated that *N*-propanoyl-D-glucosamine and *N*-propanoyl-D-mannosamine are converted to *N*-propanoyl-D-neuraminic acid in rat models[257] by passing the biosynthetic pathway of sialic acids[258] and are integrated in both membrane and serum glycoconjugates. Natural *N*-acetyl-D-neuraminic acid belongs to the family of sialic acids and is a typical terminal unit of glycoproteins on cell surfaces. In a later study Reutter *et al.* investigated virus binding and infection of cells treated with synthetic D-mannosamine derivatives bearing either a propanoyl (ManNProp), butanoyl (ManNBut)

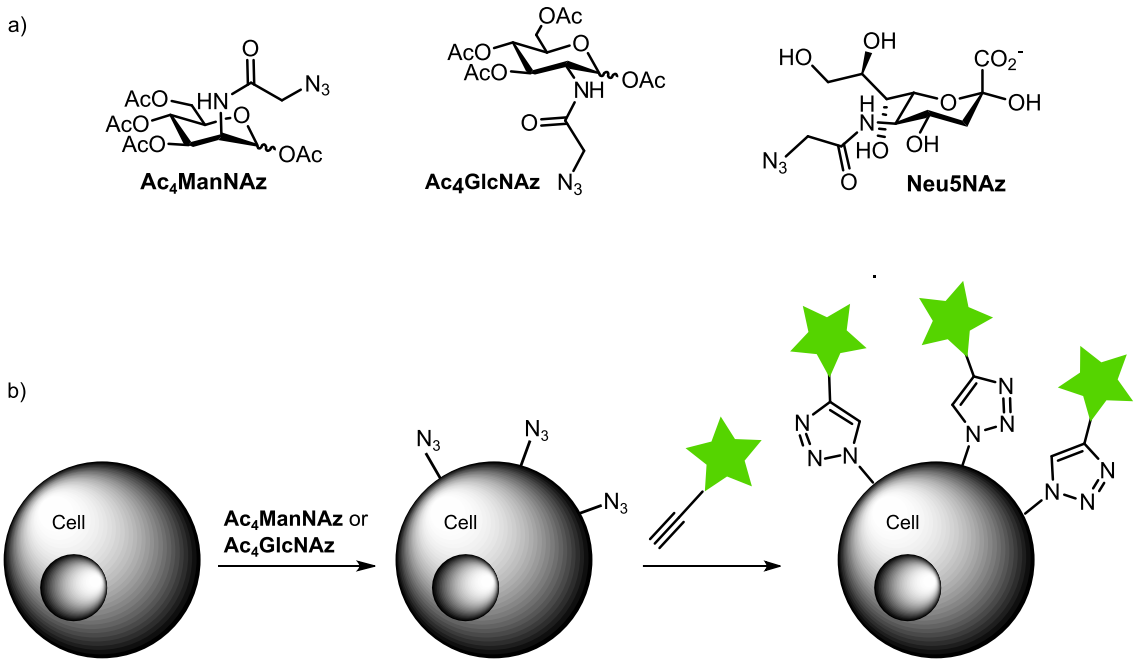

Fig. 4.19 a) Monosaccharide analogues of the sialic acid biosynthetic pathway. b) Synthetic carbohydrates bearing an azide tag are incorporated in the complex glycan structure of the cell surface and presented as terminal sialic acid. Conversion with functional alkynes (e.g. fluorophores, depicted as green star) permits a spatiotemporal investigation of glycoconjugates or a structural modification of the natural glycocalyx.

or pentanoyl (ManNPent) *N*-substituent.[259] They observed that Vero cells pretreated with ManNProp and ManNBut are more susceptible for infection by human polyoma virus BK (BKV) (up to seven-fold) while ManNPent conferred a high degree of resistance to BKV infection.

These initial studies inspired scientists to introduce chemical tags into the outer sphere of the glycocalyx by monosaccharide analogues and to perform chemistry with living cells, or even whole organisms.[260–268] So far, D-mannosamine and D-glucosamine have been modified with a variety of functional groups and the most prominent representatives are ketones, alkenes, alkynes, and azides. Feeding of cells with these synthetic sugars renders the cell surface reactive for conversion with the respective counterparts (Fig. 4.19) to either label the artificial glycoconjugate with a fluorophore or to attach bioactive molecules. In seminal work Bertozzi *et al.* synthesized the ketone *N*-levulinoylmannosamine (ManLev) and condensed the synthetic monosaccharide with biotin hydrazide once presented on the surface of human cancer cell lines.[260] Streptavidin, a biotin receptor, was loaded with highly toxic ricin via a disulfide bridge and directed the toxin to the glycoengineered cells where the drug was released. Taking into consideration that sialic acids are typical binding epitopes on cancer cells this strategy was a first approach towards selective cancer treatment by metabolic glycoengineering. In a following study Bertozzi *et al.* converted the surface ketone of the sialic acid analogue with lactose hydrazide and analyzed the remodeled carbohydrate presentation of Jurkat and HeLa cells with lactose-binding and FITC-labeled ricin by flow cytometry.[261]

The reaction between azide alkyne counterparts,[269–271] commonly known as click reaction[272], has been extensively applied to metabolic glycoengineering due to its bioorthogonal character[264,268,273] and extended to cyclic octynes to perform the ring-strain promoted reaction *in vivo* without cytotoxic Cu(I).[266,274–276] Bertozzi and coworkers gained impressive insights into spatiotemporally differences of glycan populations of zebrafish with progressing developmental state.[276] Zebrafish embryos were grown with supplemental Ac_4GalNAz that passes the GalNAc salvage pathway and is incorporated into mucin-type *O*-linked glycoconjugates. Carbohydrate analogues on the cell surface were subsequently labeled with fluorophore-cyclooctynes (DIFO-647, DIFO-555 or DIFO-488). Three-colour staining at different times of the zebrafish development permitted the investigation of the *de novo* glycan biosynthesis.[276]

Chapter 5

Results & Discussion

Results of this work are discussed in three sections starting with the rational design of novel hGal-1 ligands (section 5.1), that directly guided the development of diagnostic tools for detection of human galectin-1 (hGal-1) associated tumors (section 5.2). The chapter concludes with the presentation of results obtained from high resolution microscopy of hGal-1 networking on Neuroblastoma cell surfaces (section 5.3).

5.1 Ligand Design for hGal-1 Drug Candidates and Diagnostic Tools

To date, several synthetic carbohydrate-based ligands for hGal-1 have been introduced and investigated with regard to their binding affinity and potential to reduce tumor growth (cf. section 2.2.3). The here presented ligand design distinguishes from previously conducted studies as it systematically expanded the natural binding carbohydrate scaffold *N*-acetyllactosamine (LacNAc) and monitored the growing ligand by X-ray crystallography. This approach permitted to address a selected and well-defined potential binding domain adjacent to the carbohydrate recognition domain (CRD) and included computational predictions rather than synthesizing a large library that only statistically covers a certain functional diversity. The feedback provided by X-ray data of hGal-1 ligand complexes directly guided the subsequent procedures and facilitated to shape tailor-made ligands that optimally fit to the protein's geometry, essential for increasing both affinity and selectivity of the binding partners. Beyond that, the chosen strategy allowed integrating structural features for diagnostic purposes as X-ray crystallography unambiguously displayed and proved the impact of those modifications, especially in molecules combining distinct functional groups.

The first section discusses the recombinant expression and crystallization procedure of hGal-1 and the solved structure of hGal-1 in complex with LacNAc demonstrates

the transferability of structural inspirations drawn from the hGal-1/lactose complex. These initial results were followed by the synthesis and spectroscopic analysis of LacNAc-based precursor **10**. Further, a second precursor molecule that is devoid of the alkyne group at *C*-3' and only bears the allyl modification at *C*-1 was prepared (section 5.1.2). The characterization of complexes between hGal-1 and the precursor molecules by X-ray crystallography and SPR probed and compared the influence of the synthetic modifications and enabled a comprehensive computational screen to identify promising ligands which derived from a virtual reaction between the alkyne **10** and a library of organic azides (section 5.1.3). The subsequent section includes the organic synthesis leading to the predicted click products and section 5.1.5 highlights the structural characterization of those hGal-1-ligand complexes by X-ray crystallography and examined it by comparison of the envisioned geometry.

5.1.1 Preliminary Studies: Expression & Crystallization of hGal-1

Recombinant expression of hGal-1 and purification on lactosyl sepharose via the protein's inherent binding affinity has been described earlier[77,277,278] and was adopted in this work except of the purification strategy. Crystallization conditions were screened according to those previously published[74,78,279–281] and hGal-1 structures so far deposited with the pdb database provided valuable phasing models during structure determination.

Expression of hGal-1

The DNA sequence of hGal-1 was known from literature[278] and purchased as synthetic DNA optimized for expression in *E.coli*. The 5'- primer was designed to introduce an *N*-terminal TEV protease cleavage site for removal of the His-tag provided by the cloning vector pET28a (Fig. 5.1). The 5'-primer further encoded for the restriction site *Eco*RI,

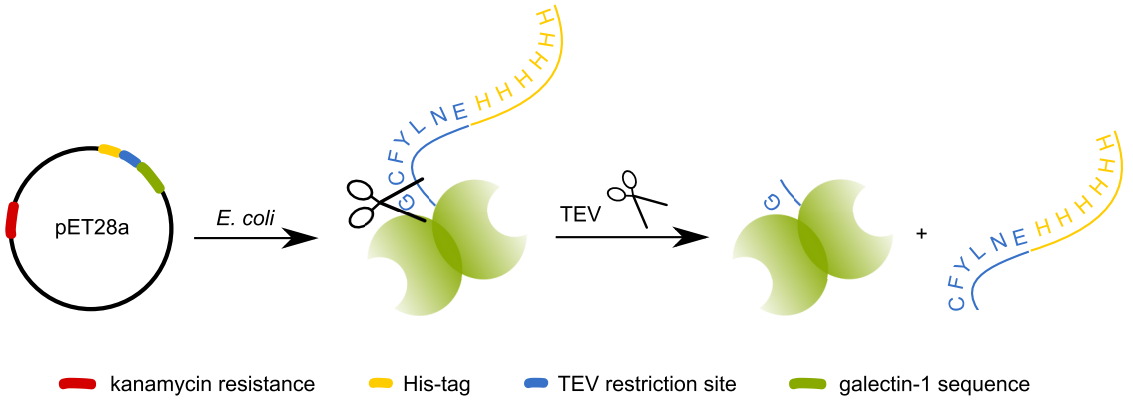

Fig. 5.1 Schematic illustration of recombinant hGal-1 production and TEV cleavage after His-tag purification. Isolated hGal-1 distinguishes from the wildtype in a single *N*-terminal glycine.

while the 3'-primer adjoined a Stopp codon and the *Xho*I restriction site to the hGal-1 sequence. PCR of the synthetic hGal-1 DNA with the forward and reverse primers yielded a construct that was confirmed by DNA sequencing before transformation into and expression by *E. coli* BL21 Star^{TM} cells. Purification via Ni-NTA affinity column chromatography and subsequent cleavage with the TEV protease led to a protein that distinguishes from the wildtyp hGal-1 in a single *N*-terminal glycine and arises from the cleavage sequence. As described in section 2.2.1 hGal-1 is sensitive to oxidation of surfacial cysteines and the formation of intramolecular disulfide bonds between Cys2-Cys130, Cys16-Cys88 and Cys42-Cys60 induces significant conformational changes that restricts dimerization as well as ligand recognition.[85,86] To protect hGal-1 all steps after cell lysis were conducted with buffers containing a reducing agent like β-mercaptoethanol (β-ME) or tris(2-carboxyethyl)phosphine (TCEP). For high resolution imaging experiments (section 5.3) cysteines of hGal-1 were covalently modified by reaction with iodoacetamide (IAA).[282]

Crystallization experiments with hGal-1

Initial hGal-1 crystallization experiments figured out successful crystallization conditions and focused then on the generation of hGal-1/ligand complexes. To date, several groups succeeded in solving structures of Gal-1/ligand complexes for both, natural and synthetic binding partners.[74,78,279–281] Amongst these studies are complexes of hGal-1 with lactose[74], a C2S mutant of hGal-1 with LacNAc[74] and bovine Gal-1 with LacNAc[280] which provided valuable information for the experimental realization of crystal growth and subsequent structure determination.
In agreement with these studies ligand-free hGal-1 (20 mg/ml) readily crystallized under various conditions containing either $(NH_4)_2SO_4$ (Table 5.1) or PEG 4000 (Table 5.2) as precipitant. In general, protein crystals appeared within a few days and were harvested or

Table 5.1 Conditions for hGal-1 crystal growth with variable parameters regarding $(NH_4)_2SO_4$ concentration and pH. Precipitation buffer contained additionally 1% β-ME. Brackets indicate crystal growth in the absence of 1% β-ME.

	c[$(NH_4)_2SO_4$]					
pH	**2.6 M**	**2.4 M**	**2.2 M**	**2.0 M**	**1.8 M**	**1.6 M**
6.0		X				
5.5	X		X			
5.0	X		X	X (X)	X	(X)
4.5			X (X)	X	X (X)	X (X)

Table 5.2 Conditions for hGal-1 crystal growth with variable parameters regarding PEG4000 concentration and pH. Precipitation buffer contained additionally 0.2 M $(NH_4)_2SO_4$ and 1% β-ME. Brackets indicate crystal growth in the absence of 1% β-ME.

	pH					
c[PEG4000]	**4.6**	**5.5**	**6.5**	**7.5**	**8.5**	**8.8**
24%	X (X)	X	X			
27%	X (X)	X	X		X	
30%	X (X)	X (X)	X	X	X	
33%	X (X)	X	X		X	

subjected to soaking and seeding experiments after a growth period of one week and up to several months.

Crystallization of hGal-1/ligand complexes

Two different approaches proved to be successful for producing hGal-1/ligand complexes. First, ligand-free protein crystals grown in 2.0 M $(NH_4)_2SO_4$, 100 μM Bis-Tris pH 5.0, 1% β-ME were seeded in a cocrystallization screen containing the same precipitating buffer supplemented with hGal-1 (20 mg/ml) and differing concentrations of LacNAc (50 mM, 25 mM, 12.5 mM and 6.75 mM). Crystals dissolved within a few hours under all conditions, but reappeared after few days in wells with 50 mM, 25 mM and 12.5 mM LacNAc with a different shape. Proteins recrystallized in 12.5 mM LacNAc (Fig. 5.2 d) were used for structure determination of the hGal-1/LacNAc complex. Second, soaking experiments proved to be successful for introducing synthetic ligands. To this end, crystals grown in 2.0 M $(NH_4)_2SO_4$ at pH 5 were soaked with the disaccharides dissolved in soaking buffer, respectively. The soaking period depended on the individual ligand as few disaccharides provoked a visible damage on the crystal quality (Fig. 5.2 i).
In cocrystallization experiments crystal growth was observed for hGal-1 and 1 mM alkyne precursor **10** in 24%, 27%, 30% and 33% PEG 4000 with pH 5. However, structure determination of cocrystals (BESY, Berlin) revealed electron density for the ligand-free protein only due to inacceptable close contacts between two homodimers at the CRD which will be discussed in detail in the following section. Thus, soaking and seeding experiments were focused on $(NH_4)_2SO_4$ conditions.

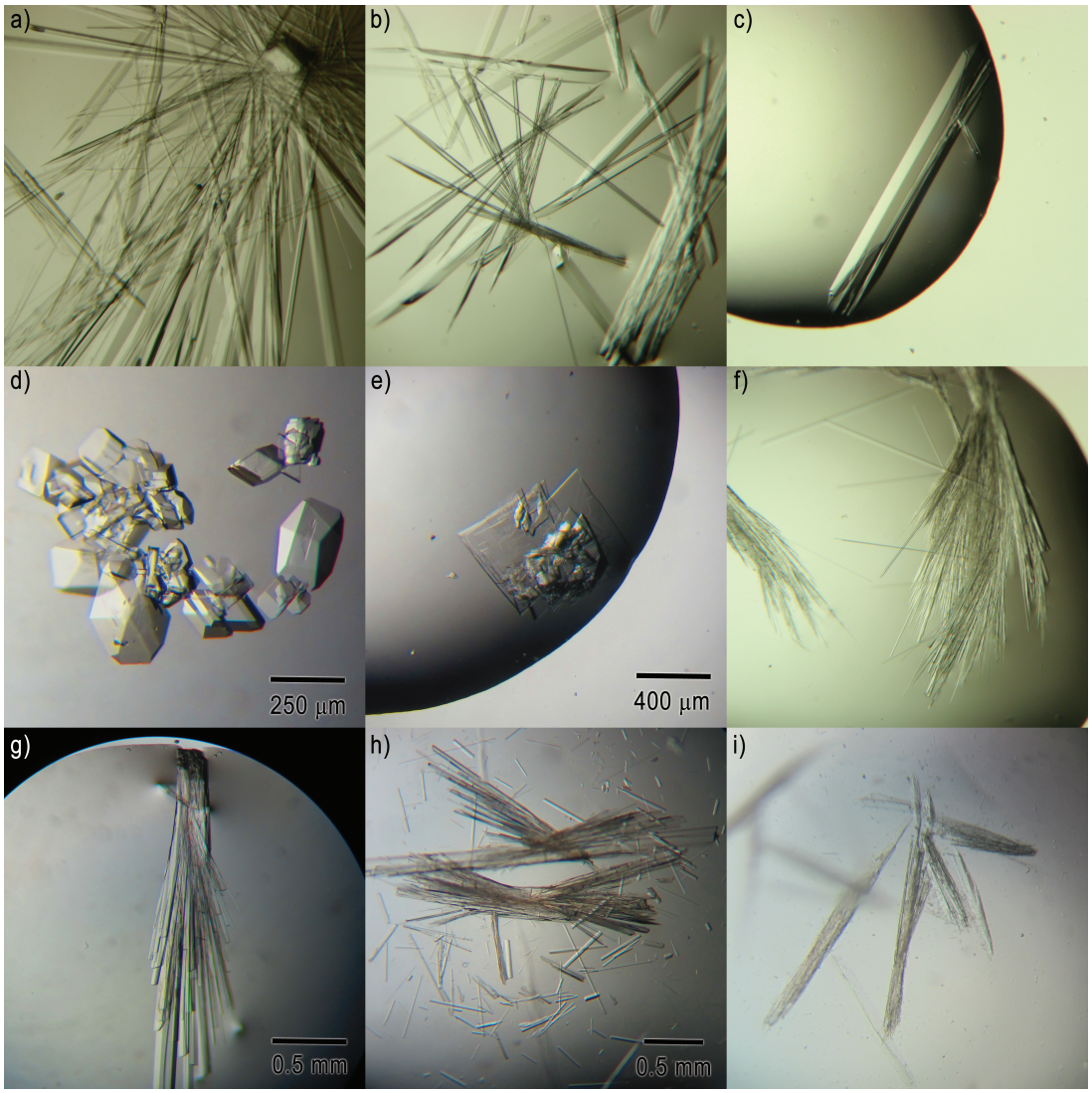

Fig. 5.2 hGal-1 crystals appeared in different size and shape depending on the individual growth conditions at 16 °C. For all examples, the protein concentration was 20 mg/ml, the buffer 100 μM Bis-Tris pH 5.0 and the precipitant supplemented with 1% β-ME. The growth period is indicated in brackets. a) 27% PEG4000, 0.2 mM $(NH_4)_2SO_4$, 100 mM **14** (10 d). b) 27% PEG4000, 0.2 mM $(NH_4)_2SO_4$ (13 d). c) 24% PEG4000, 0.2 mM $(NH_4)_2SO_4$, 1 mM **10** (7 d). d) Recrystallized protein of seeded crystals in 2.0 M $(NH_4)_2SO_4$, 12.5 mM LacNAc (2.5 months). e) 2.0 M $(NH_4)_2SO_4$, 12.5 mM LacNAc (15 d). f+g) 2.0 M $(NH_4)_2SO_4$, h) 2.0 M $(NH_4)_2SO_4$, soaked with 20 mM **10** for 24 h. i) 2.0 M $(NH_4)_2SO_4$, soaked with 20 mM **9h** for 3 h.

Structures of hGal-1/LacNAc and ligand-free hGal-1

Diffraction data of the complex hGal-1/LacNAc were recorded on beamline ID14-4, ESRF, Grenoble, and diffraction data of ligand-free hGal-1 on beamline BL 14.2, BESY, Berlin. Crystal structures were solved by molecular replacement with the coordinates of PDB entry 3T2T[78] in cooperation with Dr. Clemens Grimm and an omit map calculated

for the ligand to eliminate model bias. Different crystal forms were observed for hGal-1 recrystallized in the presence of LacNAc and for the ligand-free protein grown in 27% PEG4000. For the PEG crystal a single homodimer was located in the asymmetric unit while the recrystallized complex comprised two homodimers. The crystals feature cell parameters that differ substantially from hGal-1 structures known to literature so far.

Complex of hGal-1 & LacNAc

The complex of hGal-1 and LacNAc was solved at 1.40 Å with a clearly defined electron density for the disaccharide. The structure features high similarity to that of a previously solved complex of hGal-1 and lactose (pdb code: 1GZW, RMSD 0.28 Å)[74] and to a complex of bovine Gal-1 and LacNAc (pdb code: 1SLT, RMSD 0.55 Å)[280]. The disaccharide ligand displays the common binding mode within the two CRDs of the hGal-1 homodimer in all three structures which was discussed in detail by Herzberg *et al.*[280] Briefly, the interplay between hGal-1 and LacNAc is mainly mediated by the galactose unit that anchors the ligand within a cleft on the protein surface (Fig. 5.3). Its axial 4'-OH group, a key determinant in galectin specificity, is coordinated by His44, Arg48 and Asn46. The aromatic indole in the side chain of Trp68 favors *van der Waals* interactions with the galactopyranoside ring and tolerates no equatorial substituent at *C*-4' due to undesirable close contacts. Functionalizations at *C*-6' are also disadvantageous because the 6'-OH group is orientated towards the protein cleft and interacting with Glu71 and Asn61. However, position *C*-2' and *C*-3' are exposed and only involved in water-mediated hydrogen bonding. The 3'-OH group has been proposed earlier for introducing a modification to adress the pocket adjacent to the CRD.[158,280,283,284] The contribution of the GlcNAc moiety is less pronounced and mainly mediated by interactions between the 3-OH group and Arg48, Arg73 and Glu71. Side chains of Arg48 and Glu71 interact with hydroxyl groups of both monosaccharides and stabilize their orientation. Similar to the finding of Herzberg *et al.* the carbohydrate crystallizes exclusively as α-anomer of the GlcNAc unit.[280] In contrast, Romero *et al.* identified the β-anomer of Glc in their hGal-1/lactose complex.[74] The 1-OH group is not involved in protein interactions but completely solvated, thus giving no hint for the observed anomeric preferences. A change from lactose to LacNAc effects a four-fold increase in affinity[74] which can be explained by the crystallographic data. Arg73 and Glu71 are located within a distance of 3.3-3.8 Å to the *N*-acetyl group, thus providing additional weak, electrostatic binding.
Thiol groups of Cys16, Cys60 and Cys130 are covalently linked to β-mercaptoethanol via a disulfide bond which might increase the structural stability and explain the observed successful crystallization conditions in presence and absence of the reducing agent as listed in Table 5.1.
Structure determination of the complex hGal-1/LacNAc successfully proved the

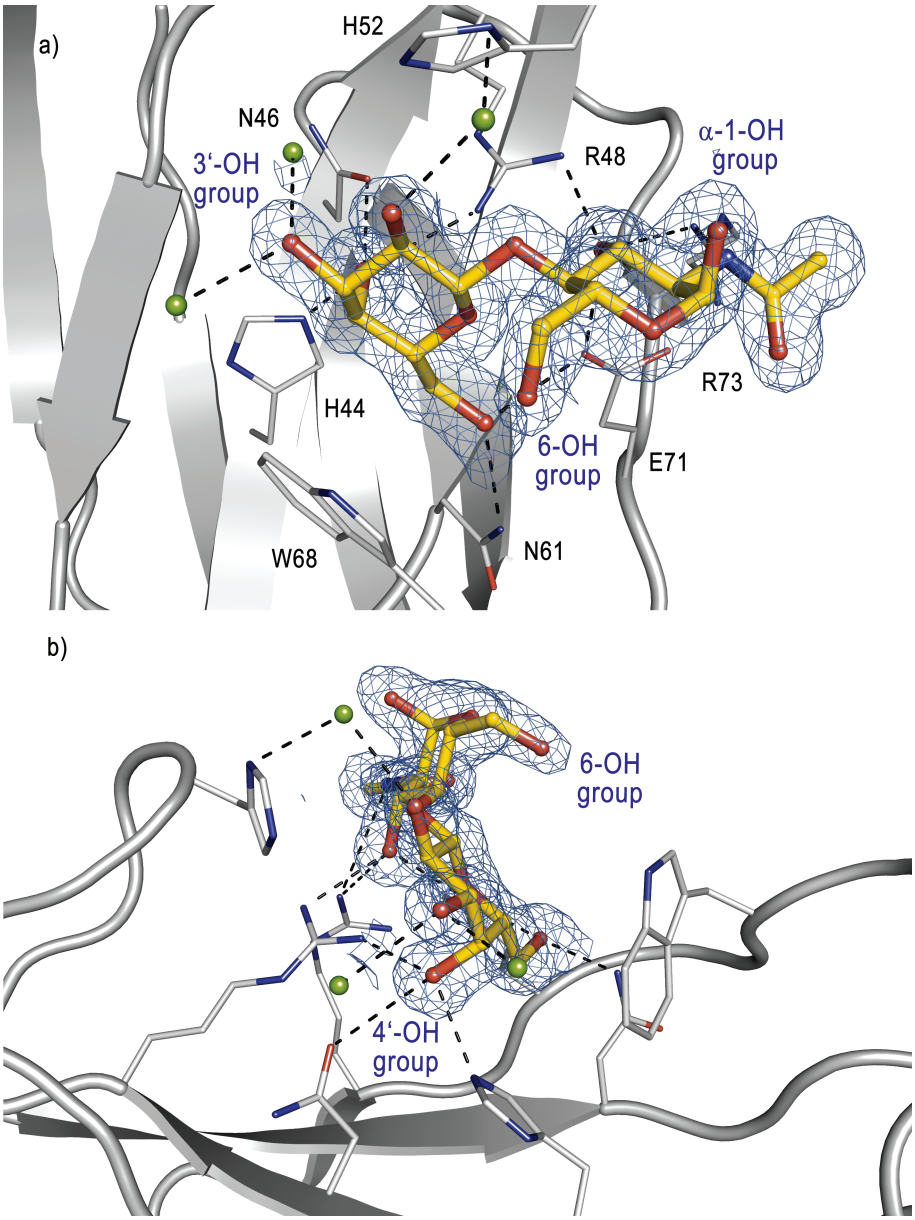

Fig. 5.3 Complex of hGal-1 and LacNAc. Electron density is presented as $2F_{obs}$-F_{calc} map and contoured to a σ-level of 1.0. a) The galactosyl moiety is involved in various interactions and is essential for the recognition process while the contribution of the *N*-acetylglucosamine unit is less pronounced. 3'-OH, 6-OH and 1-OH groups are not interacting with the protein and suited for modifications. b) Different perspective to highlight the binding cleft of hGal-1 that is filled by the galactosyl moiety.

transferability of structural inspirations from lactose to LacNAc and underpinned the idea of functionalizing distinct hydroxyl groups. Modifications at *C*'-3, *C*-6 and *C*-1 (as β-anomer) are expected to preserve natural interactions and thus providing a reactive precursor molecule.

Ligand-free hGal-1

Diffraction of hGal-1 crystals grown in 27% PEG4000 at pH 5.0 and following structure determination revealed an electron density exclusively for the protein. This finding can be explained by the crystal package of hGal-1 where two homodimers are located in close proximity of the CRD. Fig. 5.4 shows an alignment of the PEG structure (slight grey) and the complex of hGal-1 and **10** derived from $(NH_4)_2SO_4$ conditions (dark grey).[i] The carbonyl oxygen of the *N*-acetyl group and the hydroxyl group in the side chain of Thr70 would be located at a distance of 1.7 Å. Even strong hydrogen bonds that are almost linearly arranged with an angle of 175-180° for donor, acceptor and hydrogen atom include distances of more than 2.2 Å between donor and acceptor atom. Evidently, the distance between the *N*-acetyl group of LacNAc and Thr70 of hGal-1 in the PEG crystal structure would be too short to accomodate a LacNAc-derived ligand. Considering the *van der Waals* radius of oxygen R_{vdW} = 1.4 Å both atoms would be exposed to

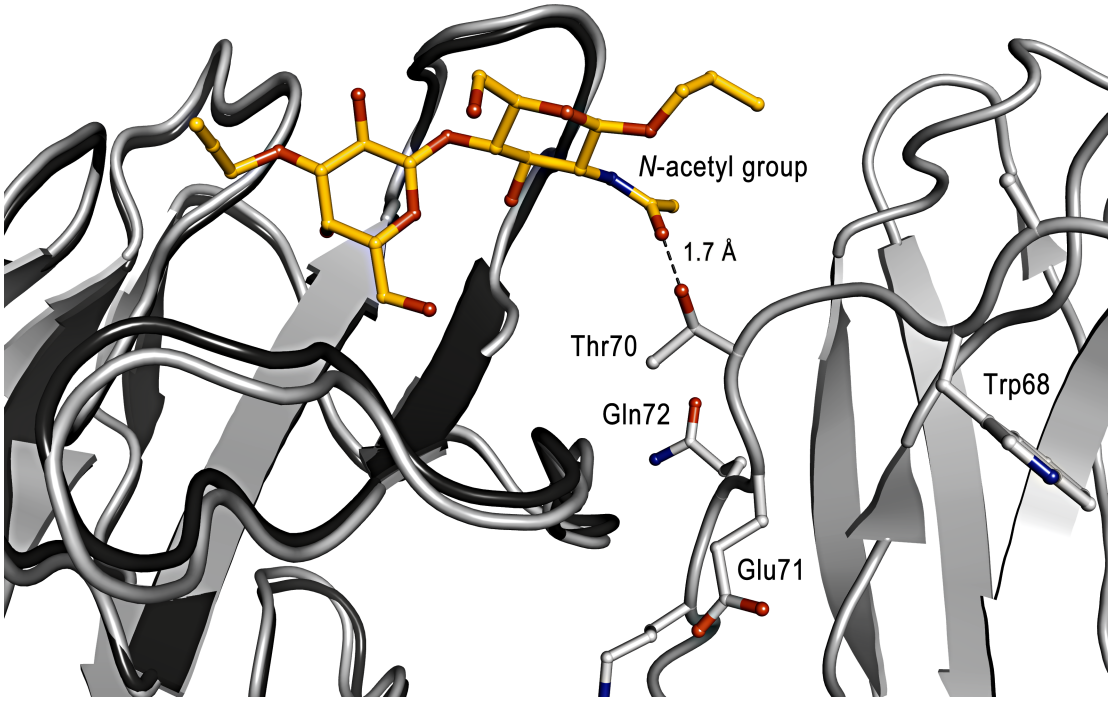

Fig. 5.4 Structure of hGal-1 crystallized under PEG conditions is presented in slight grey. Superposition of the complex between hGal-1 and **10** (dark grey, grown under $(NH_4)_2SO_4$ conditions) highlights unfavorable close contacts between the side chain of Thr70 and the carbonyl oxygen of the *N*-acetyl group.

[i] An alignment of the complex of ligand-free hGal-1 with hGal-1/LacNAc is not possible due to different crystal structures.

strong repulsive forces due the free electron pairs in the outer sphere of oxygen. (Note: Structures that were solved for further hGal-1 ligand complexes from soaking experiments exhibit the same space group and unit cell parameters. However, the distances between the *N*-acetyl group and Thr were more than 2.9 Å. Whether this shift is derived from the different crystallization conditions or induced by the ligand itself remains unclear.)

5.1.2 Synthesis of *N*-Acetyllactosamine-based Ligand Precursors

Motivated by the crystallographic data of section 5.1.1 precursor molecules **10**[ii] and **23** (Fig. 5.5) were synthesized according to the retrosynthetic considerations outlined in chapter 3.

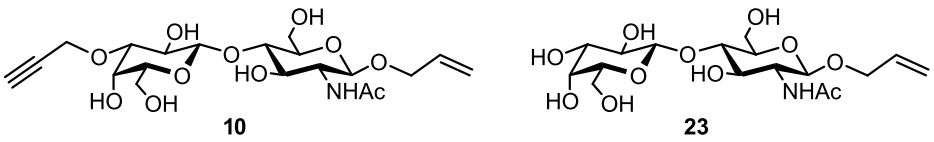

Fig. 5.5 Precursor molecules **10** and **23**.

The synthesis of both molecules involved various protecting group manipulations and started with the monosaccharides *N*-acetyl-D-glucosamine and D-galactose. The identity of carbohydrate derivatives were confirmed by 1D (^{1}H, ^{13}C, DEPT), 2D ^{1}H-^{1}H- and ^{1}H-^{13}C-correlation (COSY, HSQC, HMBC) NMR spectroscopy, mass spectrometry (MALDI, HRMS ESI) and polarimetry.

1,3,6-*O*-protected *N*-acetyl-β-D-glucosamine building block 13

The synthetic route to **13** with the 4-OH as single unprotected group for coupling with an activated galactosyl donor started with peracetylated *N*-acetyl-β-D-glucosamine (**17**) (Scheme 5.1). The *C*-1 of **17** was functionalized with allyl alcohol similar to the procedure described by Martín-Lomas *et al.*[286] It is anticipated that Lewis acidic TMSOTf promoted the deacetylation of the anomeric acetyl group to form the oxocarbenium ion species **24** which was attacked by the neighboured *N*-acetyl group to build oxazolin **24a** presumably with α-configuration as described by Lemieux *et al.*[287,288] *In situ* conversion of **24a** with allyl alcohol yielded selectively the β-anomer of monosaccharide **16** in 62% yield. Subsequent deprotection of the acetates with NaOMe according to standard Zemplén conditions yielded **25** in quantitative yield.[289] Selective protection of the 4- and 6-OH group was achieved by treatment with dimethyl

[ii]Optimized synthesis of **10** was adapted by Anne Neumann who performed her bachelor thesis[285] under my supervision.

benzaldehyde and catalytic amounts of the organic Brønsted acid camphor-10-sulfonic acid (CSA).[290] Cyclic acetale formation to the six-membered ring involving *C*-4 and *C*-6 is favored over the five-membered ring with *C*-3 and *C*-4, thus providing glucosamine derivative **59** in quantitative yields. The protection group for 3-OH was chosen according to those of the hydroxyl groups in the galactoside building blocks to minimize final deprotection steps and to allow a discrimination of position *C*-6. Acetate esters are attractive protecting groups because they are introduced under mild conditions with acetic anhydride in pyridine and readily hydrolyzed in basic NaOMe. Acetylation of **59** in pyridine led to fully protected **26** in excellent yields (Scheme 5.1).

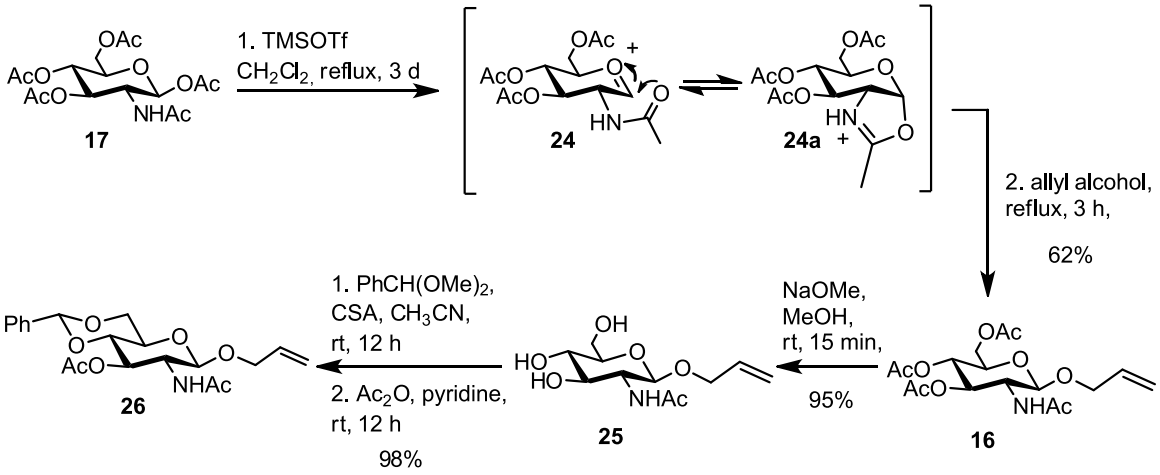

Scheme 5.1 Synthesis of fully protected *N*-acetyl-D-glucosamine derivative **26**.

Following regioselective reductive acetale opening of **26** with TFA, TFAA and $HSiEt_3$ as hydride reagent gave access to the *N*-acetyl glucosamine acceptor **13** (Scheme 5.2).[291]

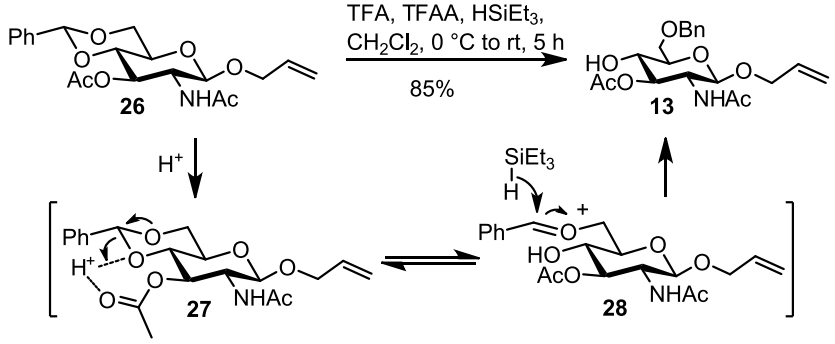

Scheme 5.2 Synthesis of **13** by regioselective reductive benzylidene opening.

Recently, Kartha *et al.* discussed common 4,6-*O*-benzylidene reductions and attributed

the regioselective formation of 4- or 6-*O*-benzyl ether to the size of the acidic reagent while the steric demand of both the hydride donor and the *C*-3 substituent is less significant.[292] Protic acids (TFA, HCl) and lewis acids such as $BF_3{\cdot}Et_2O$ coordinate the electron richer secundary *O*-4 (**27**). Subsequent cleavage of the 4,6-*O*-benzylidene carbon is favored by the resonance stabilized intermediate **28** and reduction with the silyl hydride leads to the 6-*O*-benzyl ether after aqueous workup. In contrast, bulky lewis acids like $AlCl_3$, Bu_2BOTf, TMSOTf or $CoCl_2$ preferably complex with the sterically less hindered *O*-6 and introduce the formation of the 4-*O*-ether. Typically, the reductive ring opening with TFA and $HSiEt_3$ provided **13** as single product in yields between 70% and 85%. In few reactions tlc monitored the formation of a side product that was characterized by NMR correlation spectra to 2-acetamido-4-*O*-acetyl-1-*O*-allyl-6-*O*-benzyl-2-deoxy-β-D-glucopyranoside **29**. Acyl migration is a common phenomenon in partially acetylated carbohydrates[293,294] and was described earlier by Ogawa *et al.* to occur during reductive opening of benzylidene acetals (Scheme 5.3).[295]

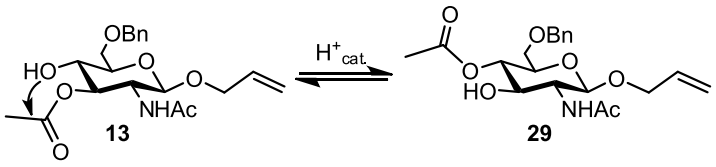

Scheme 5.3 Acyl migration from *O*-3 to *O*-4 during reductive ring opening.

Discussion of the spectroscopic data

A common feature of all structures in the ^{1}H NMR spectra is the appearance of a multiplet between δ = 5.95 and 5.80 ppm, characteristic for the intern vinylic proton *H*-2'. This signal comprises vicinal couplings of *H*-2' with the terminal vinylic protons *H*-3'$_{cis}$ and *H*-3'$_{trans}$ and with the allylic protons *H*-1'a and *H*-1'b. The latter are diastereotopic due to the proximal chiral carbon *C*-1. Protons *H*-3' resonate as a doublet of doublet of doublet of doublet at $\delta \cong 5.2$ ppm, respectively, while the vicinal coupling of the proton in trans-position to *H*-2' is large ($^3J \cong 17$ Hz) and smaller for the cis-positioned *H*-3' ($^3J \cong 10$ Hz). The geminal ^{1}H-^{1}H coupling depends on the *s*-character of the hybrid orbital and ^2J is positive with a value of around 2 Hz for protons in sp^2-hybrid orbitals. Thus, the geminal coupling of *H*-3'$_{trans}$ and *H*-3'$_{cis}$ ($^2J \cong 1.7$ Hz) is similar to the long range coupling of these protons with *H*-1'a and *H*-1'b ($^4J \cong 1.6$ Hz). This fact is reflected in the shape of the doublet of doublet of doublet of doublet that rather appears as a doublet of quartet. In contrast, the geminal coupling of the methylene protons *H*-1'a and *H*-1'b is negative but with a large absolute value of around 13 Hz.

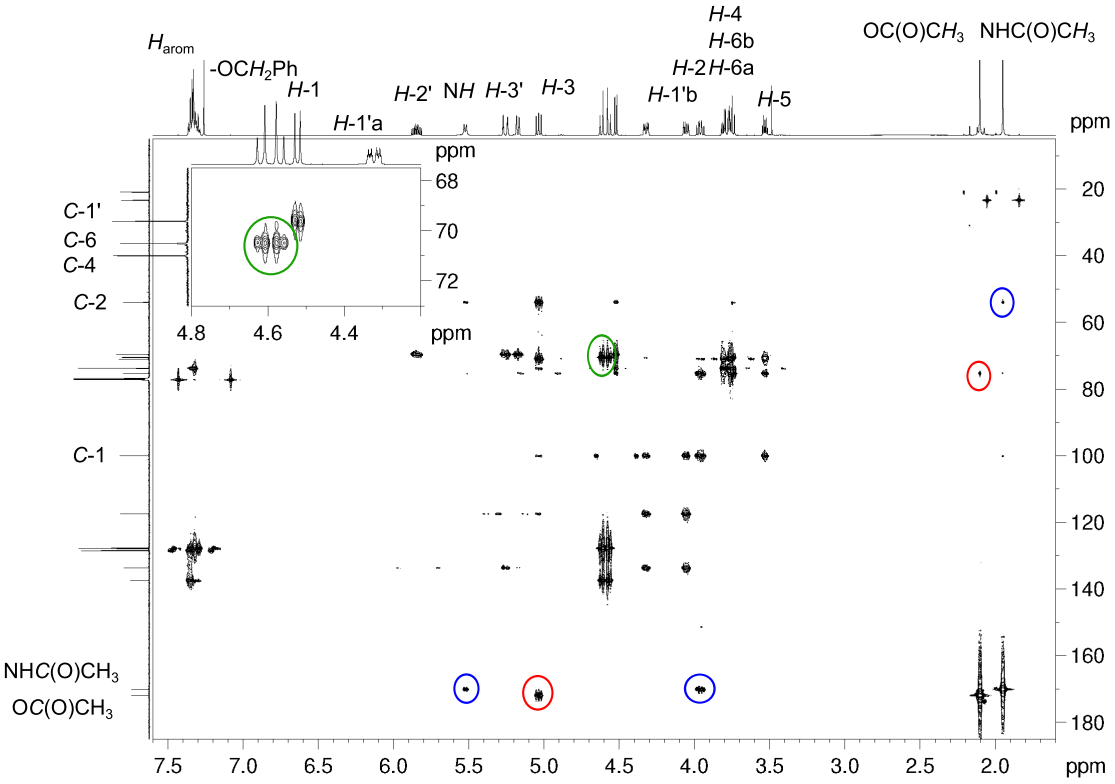

Fig. 5.6 HMBC correlation spectrum of reduction product **13**. Long range couplings between position 3 of the carbohydrate scaffold and the *O*-acetyl group are marked in red, couplings between the position 2 and the *N*-acetyl group in blue. The inlet depicts a magnification of resonances of -OCH_2Ph and *C*-6 to illustrate the correlation of both positions (green label). Annotations of ^{13}C are reduced to relevant carbons for reasons of clarity.

A further striking signal in the ^{1}H NMR spectra is the doublet at 4.71 ppm which can be assigned to *H*-1 as all other carbohydrate protons show more sophisticated splitting patterns. The size of the vicinal coupling between *H*-1 and the axial-positioned *H*-2 in the *N*-acetylglucosamine derivatives elucidates the stereo information at the anomeric position. A value of 8.3 Hz is typical for an *axial-axial*-coupling and indicates a β-configuration of the monosaccharides. Remaining protons of the carbohydrate scaffold resonate between δ = 5.10 and 3.20 ppm and signals split with large ^3J coupling constants due to the all-axial-configuration of protons in glucopyranoside derivatives. The assignment of single protons was faciliated with the help of 2D ^{1}H-^{1}H and ^{1}H-^{13}C correlation spectra (COSY, HSQC). The amidic N*H* proton only splits into a doublet in aprotic solvents like $CDCl_3$ and is absent in MeOD as a result of the fast H/D exchange while the -CH_3 moiety of the *N*-acetyl group appears in all spectra as a singlet at $\delta \cong$ 2 ppm. Protons of the *O*-acetyl groups in **16**, **26** and **13** resonate at

a same field. Signals of aromatic protons of **59** and **26** appear as two multiplets at $\delta \cong 7.50$ and 7.35 ppm and the singlet at $\delta \cong 5.5$ ppm can be assigned to the acetalic proton *H*-1" having no geminal or vicinal coupling partners. The appearance of a single spectral dataset indicates a preferred configuration of the six membered benzylidene ring, presumably the all-equatorial position as depicted for **59** and **26**. Reductive regioselective ring opening to **13** affects the chemical shift of the aromatic protons that give rise to a single multiplet between δ = 7.37 and 7.28 ppm, typical for a phenyl group. The benzylic protons formed by reductive cleavage with $HSiEt_3$ resonate as two douplets at δ = 4.57 and 4.62 ppm with a large geminal coupling of ^2J = 11.9 Hz.
^{13}C-NMR and DEPT spectra allowed a facile assignment of the anomeric carbon resonating at low field ($\delta \cong 100$ pm) and secundary *C*-6 and *C*-1' appearing with opposite sign in the DEPT spectra. Further carbons of the carbohydrate scaffold resonate between δ = 83 and 54 ppm. Carbonyl carbons of the acetyl groups can be assigned to signals at $\delta \cong 170$ and 22 ppm, respectively. Signals for sp^2-hybridized carbons of the allyl group appear at $\delta \cong 135$ and 117 ppm with the latter assigned to the terminal carbon by DEPT spectra. Carbons of the aromatic moieties resonate between $\delta \cong 138$ and 126 ppm.
The position of the acetyl substituent in **13** and in the acyl migration product **29** were allocated by ^{1}H-^{13}C correlation spectra (HMBC) via the long range couplings of *H*-3 and *H*-4 with the carbonyl carbon of the acetate, respectively, and the benzylic protons with *C*-6 (Fig. 5.6).

1-*O*-activated-α-D-galactose building blocks 12 and 37

Glycosylation reactions require activated donor molecules that in nature are UDP-glycosides for stereospecific linkage with glycosyl acceptors by glycosyltransferases. Enzymes that form the glycosidic bond from nucleotide-activated sugars are called after their discoverer Luis Leloir.[296,297] However, UDP-glycosides are expensive and difficult of access and thus, not suited for synthetic manipulation in gram scale. Standard non-enzymatic glycosylation reactions[298–300] are dated from works by Königs and Knorr[301], Fischer[302] and Schmidt[303,304]. Both the Königs-Knorr method with galactosyl bromides and the method of Schmidt with glycosyl trichloroacetimidates were applied for establishing a glycosidic bond between donor and acceptor molecules in the synthesis of LacNAc derivatives.
The synthesis of both galactosyl donor molecules, one of those bearing an alkyne modification at *O*-3, started with commercially available 1,2,3,4,6-penta-*O*-acetyl-β-D-galactopyranoside **32**. The preparation of activated alkyne-modified galactopyranoside **12** required additional reaction steps with the regioselective alkylation of the 3-OH group as crucial step. David and Hanessian reported about a regioselective functionalization of distinct hydroxyl groups in monosaccharides via organotin derivatives.[305] The

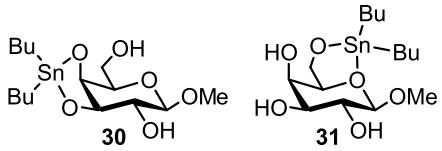

Fig. 5.7 Organotin-mediated regioselective functionalization of monosaccharides via intermediate complexation of cis-diols.[305]

conversion of 1-*O*-protected galactopyranosides with dibutyltin oxide strongly enhances the nucleophilicity of *O*-3 by an intermediate tin complex through coordination of the 3- and 4-OH group (Fig. 5.7). Five-membered rings of cis-diols are favored over trans-diols or six-membered rings, thus explaining the coordination pattern of galactosides. An alternative complex intermediate is presented by the coordination of the 6-OH group and the intracyclic oxygen to the tin organyl leading to an increased reactivity of *O*-6. Recently, Ramström *et al*. compared the organotin-mediated regioselective protection with the observed tendency of acyl migration in partially protected glycosides.[306] They found out that the organotin-mediated acetylation of cis-diols primarily results in products with an equatorial ester group, while the situation in acyl migration is vice versa and mainly provides products with a protected axial hydroxyl group (Scheme 5.4). For less-favored trans-diols regioselectivity is observed when the diol is enclosed by one axial and one equatorial substituent. In this case, organotin-mediated reactions mainly give products where the functionalized hydroxyl group is adjacent to the axial position, while acyl migration provides the complementary product. Both, the five-membered cis-diol and the less-favored trans-diol during organotin-mediated acylation promote the *O*-3 functionalization of galactosides.[306]

Obviously, the organotin-mediated regioselective functionalization and the acyl migration show the same selectivity pattern. Ramström *et al*. complemented the experimental

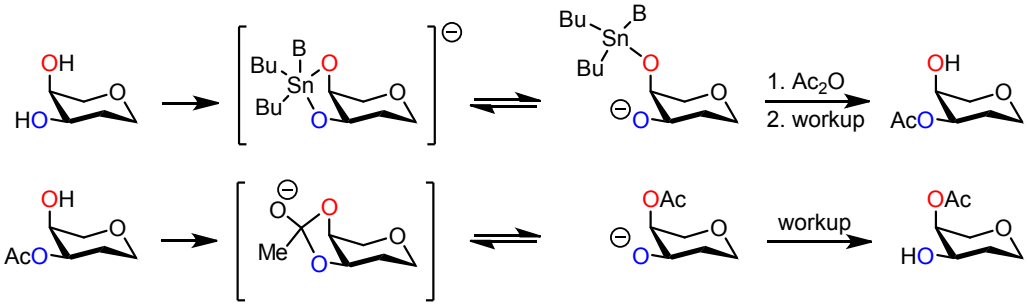

Scheme 5.4 Comparison of the regioselective opening of a dioxastannolane and a dioxolane ring in organotin-mediated functionalization (upper part) and in acyl migration (lower part). B represents a Lewis base.[306]

observations with computational studies that revealed that the acyl migration from *O*-3 to *O*-4 is thermodynamically favored.[306] This outcome is rather surprising as the axial position commonly prefers sterically less demanding substituents than the equatorial position and presumably has to be attributed to electronic effects. Although the involvement of complex stannylene structures has been proposed for the regioselective alkylation of galactosides[305,307] this study indicates that the regioselectivities arise from the inherent carbohydrate structures rather than from complex, multimeric stannylene structures.[306]

The functionalization of galactosides with dibutyltin oxide is straightforward and provides access to the envisioned alkyne-modified galactoside building block in few steps. To this end, 1-*O*-methyl-β-D-galactopyranoside (**15**) was synthesized from peracetylated 1,2,3,4,6-penta-*O*-acetyl-β-D-galactopyranoside (**32**). Treatment of **32** with 33% HBr in acetic acid provided **33** in quantitative yield after aqueous workup[iii] as pure alpha anomer due to a strong negative hyperconjugation (anomeric effect) of a free electron pair from the oxygen with a σ^*-orbital of the C-Br bond. Glycosylation of the activated galactosyl donor with MeOH as acceptor molecule was promoted by Ag_2CO_3 and inverted the configuration of the anomeric center to provide 2,3,4,6-tetra-*O*-acetyl-1-*O*-methyl-β-D-galactopyranoside (**60**) in 68% yield. Following deprotection of the acetate esters with NaOMe yielded **15** (Scheme 5.5).[iv]

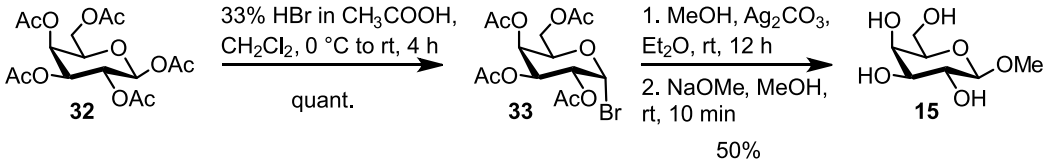

Scheme 5.5 Synthesis of the 1-*O*-protected galactopyranoside **15**.

Next, **15** was refluxed in anhydrous MeOH with dibutyltin oxide until the reaction

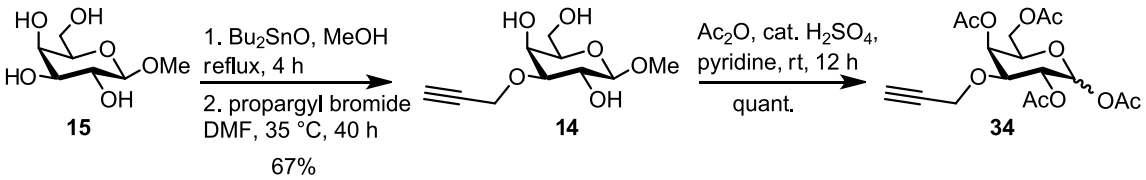

Scheme 5.6 Synthetic steps to alkyne functionalized peracetylated galactoside **34**.

[iii] Column chromatography was performed for conversion of **33** with NaN_3 and reduced the yield to 62% presumably due to hydrolysis on slightly acidic silica gel.

[iv] Galactoside **15** is commercially available and was purchased from Carbosynth Ltd. for ongoing syntheses.

formed a clear yellowish solution, usually after four to five hours. The solvent was removed in vacuum and the intermediate tin complex converted *in situ* in anhydrous DMF and propargyl bromide at 35 °C to **14**. Tlc monitored the formation of a single reaction product after few hours with considering amounts of remaining starting material. Even prolonged reaction times did not achieve a complete conversion of the educt explaining for the rather low yields of 50-67%. Column chromatography yielded the desired regioselective monoalkylation product **14** (Scheme 5.6). Treatment of **14** with acetic anhydride and catalytic amounts of sulfuric acid cleaved the acetal structure at the anomeric position and converted the monosaccharide into an anomeric mixture of peracetylated **34** with an α/β ratio of 3.3:1 (Scheme 5.6). With molecule **34** and **32** in hands, both peracetylated galactosides were activated for the glycosylation reaction in two steps, including regioselective deprotection of *O*-1 with basic hydrazine acetate to **36** and **35**, followed by conversion into the trichloroacetimidates **12** and **37** with $CNCCl_3$ and the amine base 1,8-diazabicyclo[5.4.0]undec-7-ene (DBU) (Scheme 5.7). The activation procedure yielded exclusively the α-anomer for both donors as the C-O bond to the electronegative trichloroacetimidate group exhibits a low σ^* orbital for a pronounced negative hyperconjugation with a lone pair at the intracyclic oxygen (anomeric effect).

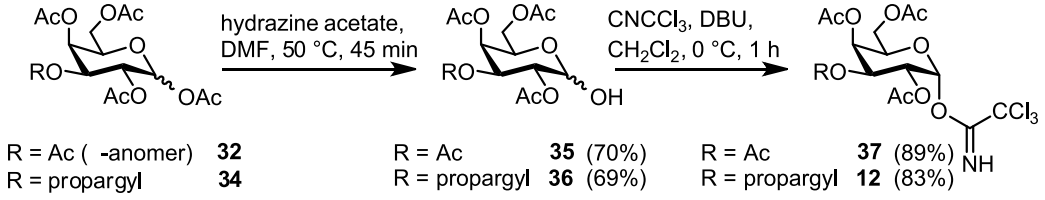

Scheme 5.7 Activation of galactosyl building blocks with $CNCCl_3$.

Discussion of the spectroscopic data

Synthetic manipulations at *C*-1 and *C*-3 were confirmed with ^{1}H and ^{13}C NMR spectroscopy and mass spectrometry. As described above the vicinal coupling of *H*-1 to the axial-positioned *H*-2 provides valuable information about the configuration of the glycosidic bond. *H*-1 in **33** resonates at δ = 6.69 ppm and splits into a doublet with ^3J = 4.0 Hz. This value is typical for *axial-equatorial*-couplings and suggests an α-configuration while the considerable low field shift can be deduced to the electronegative bromine substituent. Protons *H*-2, *H*-3 and *H*-4 resonate in the ^{1}H-NMR spectra between δ = 5.51 and 5.05 ppm and split into a doublet of doublet with a large and small vicinal coupling as all protons are neighboured by an *axial*- and *equatorial* coupling partner. The signal for proton *H*-5 appears as a multiplet between δ = 4.50 and 4.46 ppm and diastereotopic protons *H*-6 resonate in a doublet of doublet, respectively, with a large

geminal coupling of ^{2}J = 11.4 Hz and a minor vicinal coupling with *H*-5 of ^{3}J = 6.5 and 6.8 Hz, respectively. Singlets between δ = 2.15 and 2.01 ppm can be assigned to the acetate groups. MALDI experiments with **33** reflected the incorporation of the bromine with an m/z peak at 433.01 for $[M+Na]^{+}$ with the main isotop ^{79}Br and a second peak at 435.01 for $[M+Na]^{+}$ with the minor isotop ^{81}Br.

Compared to **33** the anomeric proton of the tetraacetylated galactoside **60** resonates high field shifted at δ = 4.40 ppm and splits into a doublet with ^{3}J = 7.9 Hz indicative for an inversion of the configuration and a β-glycosidic bond. The CH_3 group resonates as a singlet at 3.45 ppm and is a further proof for a successful glycosylation. A comparison of the ^{13}C spectra of **33** and **60** reveals striking differences in the shift of the anomeric carbon. Whereas *C*-1 of the bromine substituted galactoside **33** resonates at δ = 88.90 ppm, the signal for *C*-1 in **60** is noticeably low field shifted to δ = 102.09 ppm. The structure of **14** was substantiated with the help of ^{1}H-^{1}H (COSY) and ^{1}H^{13}C

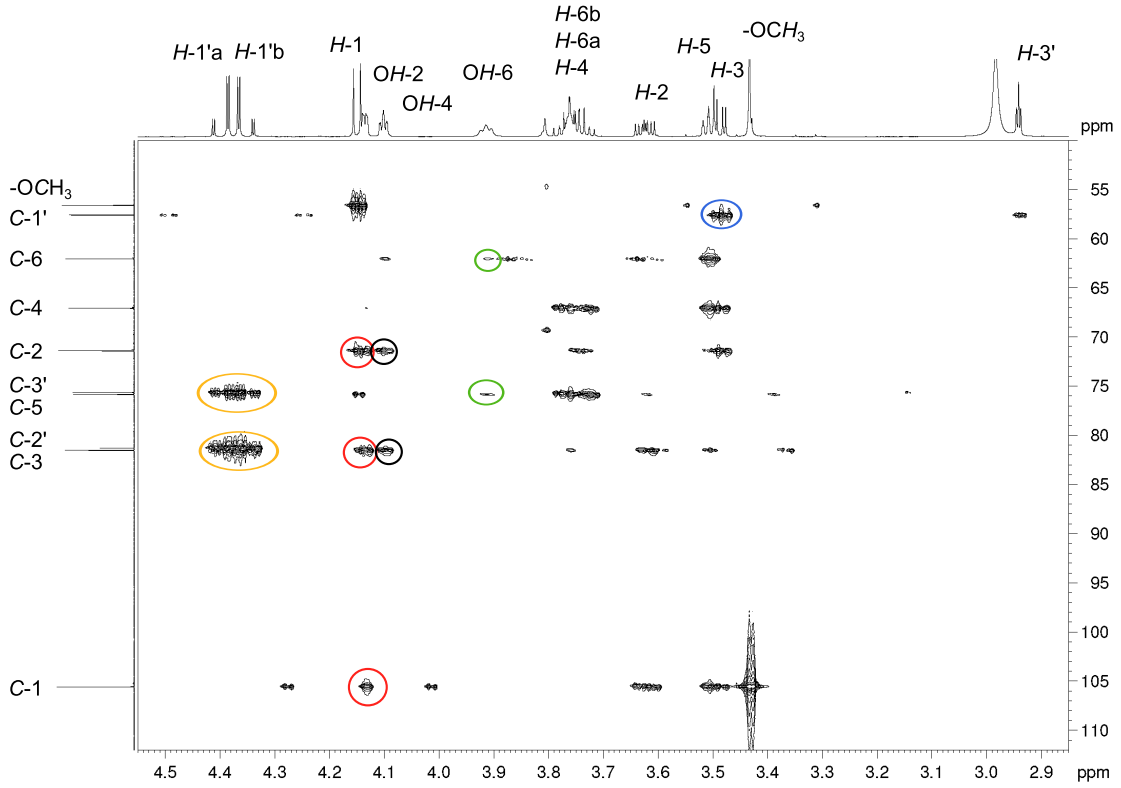

Fig. 5.8 HMBC correlation spectrum of regioselective, monoalkylated galactoside **14**. The long range coupling between *H*-3 and *C*-1' is marked in blue, between *H*-1' and *C*-3, *C*-2', *C*-3' in orange, between O*H*-2 and *C*-1, *C*-3, *C*-2 in red, between O*H*-4 and *C*-3, *C*-2 in black and between O*H*-6 and *C*-5, *C*-6 in green.

Table 5.3 Correlation of $^{1,2}J(^{13}C^{1}H)$ and the *s*-character of the carbon hybrid orbital.[308]

Ligand	hybridization	$^{1}J(^{13}C^{1}H)$ [Hz]	$^{2}J(^{13}C^{1}H)$ [Hz]
Ethan	sp^3	125	-4.5
Ethylene	sp^2	156	-2.4
Acetylene	sp	248	50

(HSQC, HMBC) correlation spectra. The alkyne proton *H*-3' was assigned in the ^{1}H-NMR spectrum to a triplet-like doublet of doublet at 2.94 ppm for coupling with the diastereotopic protons *H*-1' (^{4}J= 2.5, 2.4 Hz) that resonate at lower field (δ = 4.40 and 4.35 ppm) with a large geminal coupling of ^{2}J = 15.8 Hz. A COSY spectrum facilitated the assignment of further galactosyl protons and a HMBC spectrum was recorded to unambiguously allocate the position of the propargyl modification. The spectrum correlates *H*-3 with *C*-1' (blue label, Fig. 5.8) and the use of an aprotic solvent like d_6-acetone further permitted the detection of hydroxylic protons. The heteronuclear couplings of the hydroxylic protons with ^{13}C give correlations for *C*-1, *C*-2 and *C*-3 to the hydroxylic proton O*H*-2 (red labels), for *C*-2 and *C*-3 to O*H*-4 (black labels) and finally for *C*-6 and *C*-5 to O*H*-6 (green labels). The assignment of the terminal and intern alkynyl carbons was complicated as the size of the $^{1}J(^{13}C^{1}H)$ and $^{2}J(^{13}C^{1}H)$ of *sp*-hybridized carbons are different from values of sp^3- and sp^2-hybridized carbons (Table 5.3). Thus the HSQC spectrum provided cross signals for the alkynyl proton with both, the terminal and intern alkynyl carbon. The DEPT NMR experiment optimized for $^{1}J(^{13}C^{1}H)$ = 145 Hz, which is standardly performed to distinguish differently substituted sp^3- and sp^2-hybridized carbons, resulted in weak signals for the carbons at δ = 81.31 and 75.66 ppm with the same sign (Fig. 5.9 a). An additional DEPT experiment optimized for $^{1}J(^{13}C^{1}H)$ = 240 Hz provided the decisive information and led to a strong signal for the carbon resonating at δ = 75.66 ppm which was thus assigned to the terminal carbon (Fig. 5.9 b). ^{1}H- and ^{13}C-NMR spectroscopy of **34**, **36** and **35** provided two datasets, respectively, each for the α- and β-configured monosaccharide. The individual anomeric ratio was inferred from the signal integrals. ^{1}H-NMR spectra of trichloracetimidates **12** and **37** show singlets at δ = 8.65 ppm for =N*H* and a low-field shifted doublet at δ = 6.60 ppm for *H*-1 with a coupling constant of ^{3}J = 3.6 Hz, typical for α-substituted galactosides. Carbons of the trichloroacetimido group resonate at $\delta \cong$ 161 (*C*=NH) and 91 ppm (CCl_3).

^{35}Cl and ^{37}Cl are the two principal stable isotopes of this element with an isotopic abundance of 75.77% and 24.23%. This ratio is reflected in the mass spectra and HRMS ESI spectra of **12** and **37** provided the characteristic isotope pattern for molecules

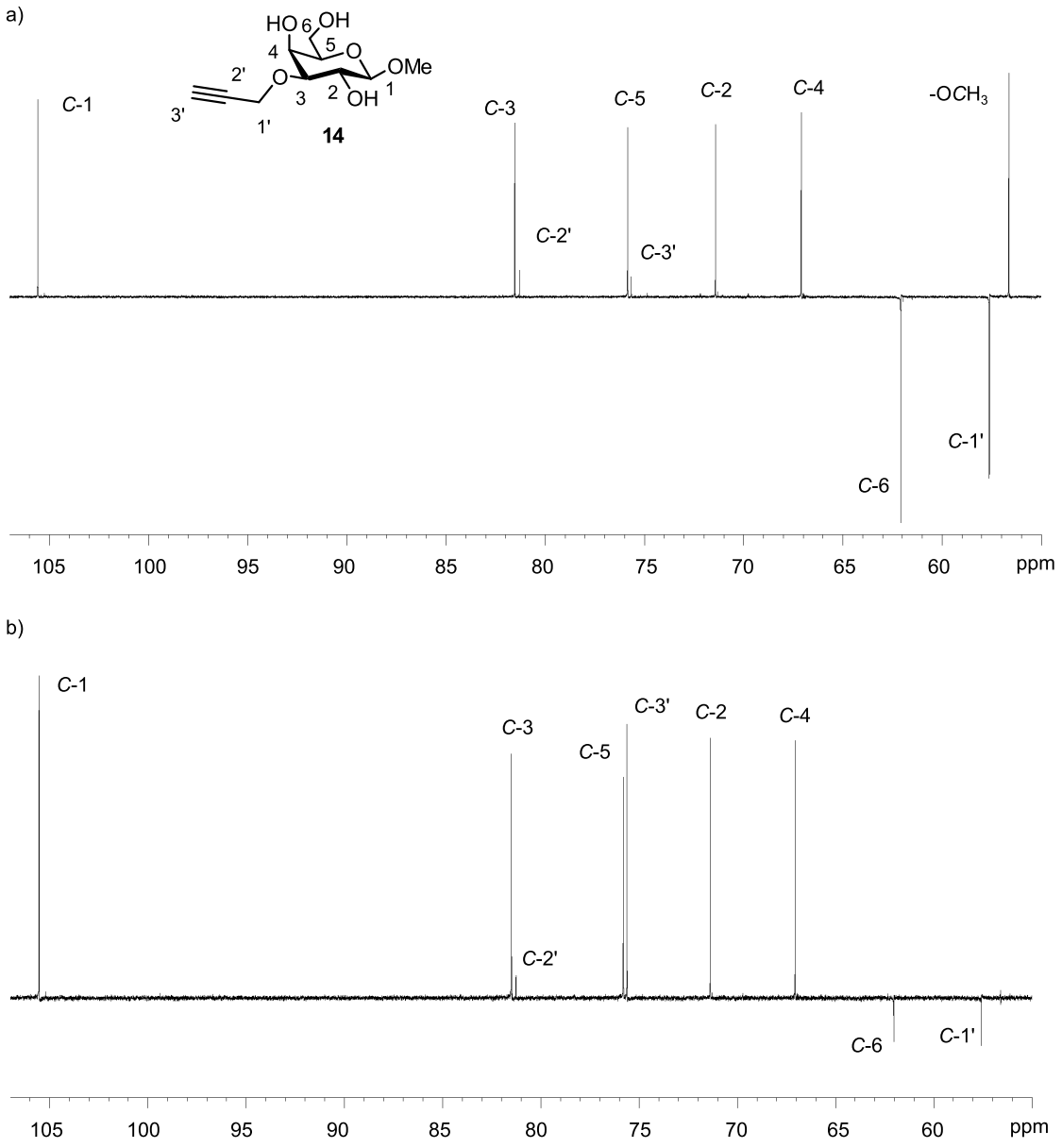

Fig. 5.9 ^{13}C DEPT spectra of alkyne modified galactoside **14** for assignment of *C*-2' and *C*-3'. a) DEPT spectrum optimized for $^{1}J(^{13}C^{1}H)$ = 145 Hz. b) DEPT spectrum optimized for $^{1}J(^{13}C^{1}H)$ = 240 Hz.

containing three chlorine atoms. In the spectrum of **37** three main peaks appear at m/z of 514.00417, 516.00150 and 518.00016. The first was assigned to $[M+Na]^+$ with $-C^{35}Cl_3$, the second to $[M+Na]^+$ with $-C^{35}Cl_2{}^{37}Cl$ and the third to $-C^{35}Cl^{37}Cl_2$. Similarily, the spectrum of **12** gives rise to main peaks for $[M+Na]^+$ with different chlorine isotope abundances at m/z of 510.00926, 512.00649 and 514.00420.

N-acetyl-β-D-lactosamine precursors

Regioselective protected *N*-acetylglucoseamine acceptor **13** and activated galactosyl donors **37** and **12** were converted in glycosylation reactions with lewis acidic $BF_3 \cdot Et_2O$ to provide the β-linked disaccharides **38** and **39** in good yields (Scheme 5.8).

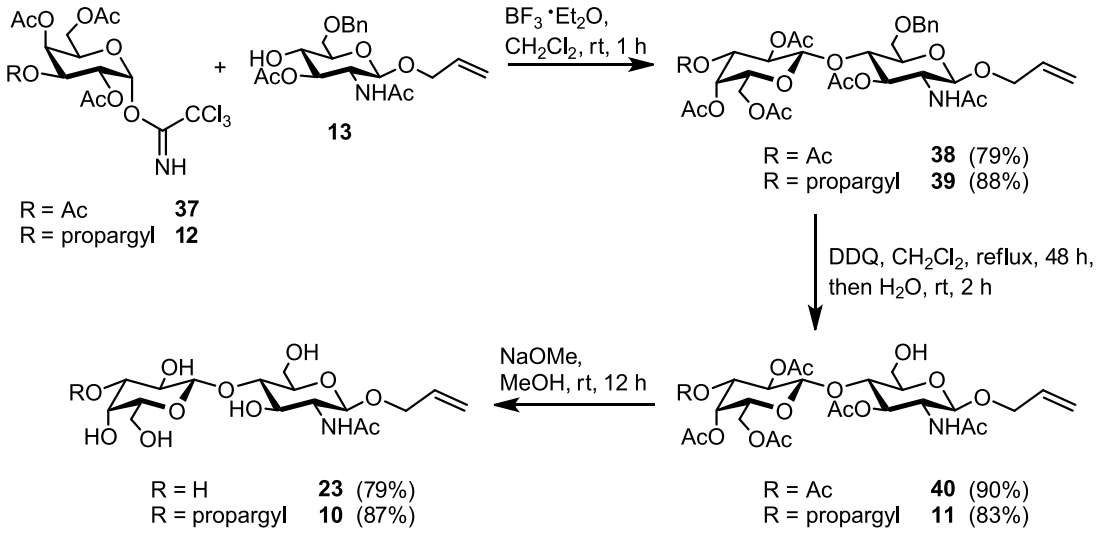

Scheme 5.8 Synthesis of disaccharide precursors **23** and **10**.

Deprotection of the benzyl group at position *O*-6 represented a critical step as classical removal by Pd-catalyzed hydration entails the risk to further remove the allyl function at *C*-1. Thus, a highly selective deprotection strategy was obligatory. Karskela *et al.* reported about a similar disaccharide that also beared an allyl function at *C*-1 and a benzyl protecting group at *O*-6. Selective cleavage of the benzyl group was achieved by oxidative deprotection with DDQ and H_2O and also proved to be the method of choice for debenzylation of **38** and **39**. Resulting disaccharides **40** and **11** are important intermediates in the synthesis of 6-*O*-modified *N*-acetyllactosamine based hGal-1 PET ligands (see section 5.2.2).
In a last step, *O*-acetates were cleaved with basic NaOMe to provide precursor molecules **23** and **10**.

Discussion of spectroscopic data

Spectroscopic data of the *N*-acetyllactosamine derivative **10** are discussed representative for the disaccharides **38**, **39**, **40**, **11** and **23**. All compounds feature similar signals for the carbohydrate scaffold and the *N*-acetyl group. Spectra of disaccharides **40** and **11** comprise additional signals for the *O*-acetyl units and spectra of **38** and **39** are further

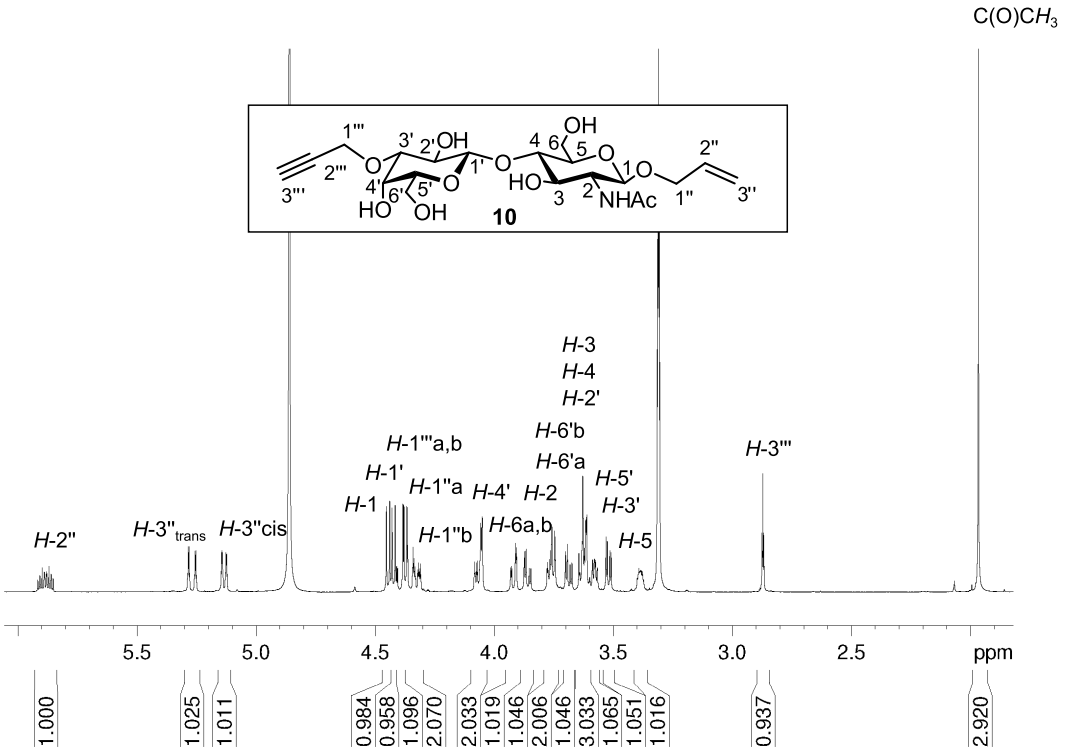

Fig. 5.10 ^{1}H-NMR spectrum of alkyne precursor **10**.

characterized by signals of the benzyl moiety.

Chemical shifts and splitting patterns of the monosaccharide subunits do not differ substantially from *N*-acetylglucosamine **13** and galactoside **14** discussed earlier in the relevant sections. However, the assignment of *H*-1' was of special interest as the vicinal coupling of this proton to the axial-positioned *H*-2 in the galactoside unit reveals the configuration of the novel glycosidic bond (Fig. 5.10). Two doublets at δ = 4.47 and 4.42 ppm can be assigned unambiguously to the anomeric protons as both signals are correlated in the HSQC to carbons resonating at characteristic low field of δ = 100.52 and 100.01 ppm. The corresponding vicinal couplings for the two doublets are in the size of ^{3}J = 8.0 Hz and thus the result of *axial-axial* couplings of two β-configured glycosidic bonds. To further assign signals to individual carbohydrate protons in each monosaccharide subunit *H*-1 was identified via the long range coupling $^{4}J(^{1}\mathrm{H}^{13}\mathrm{C})$ to the allylic carbon *C*-2" in the HMBC spectrum. Further cross signals arise for *H*-3'/*C*-1''' (*C*-3'/*H*-1''') and *H*-4/*C*-1' (*C*-4/*H*-1') and with the help of a COSY spectrum remaining protons of the carbohydrate scaffold with resonances between δ = 5.05 and 3.48 ppm were assigned.

The ^{13}C-NMR spectrum shows signals at δ = 104.96 and 101.90 ppm for both anomeric

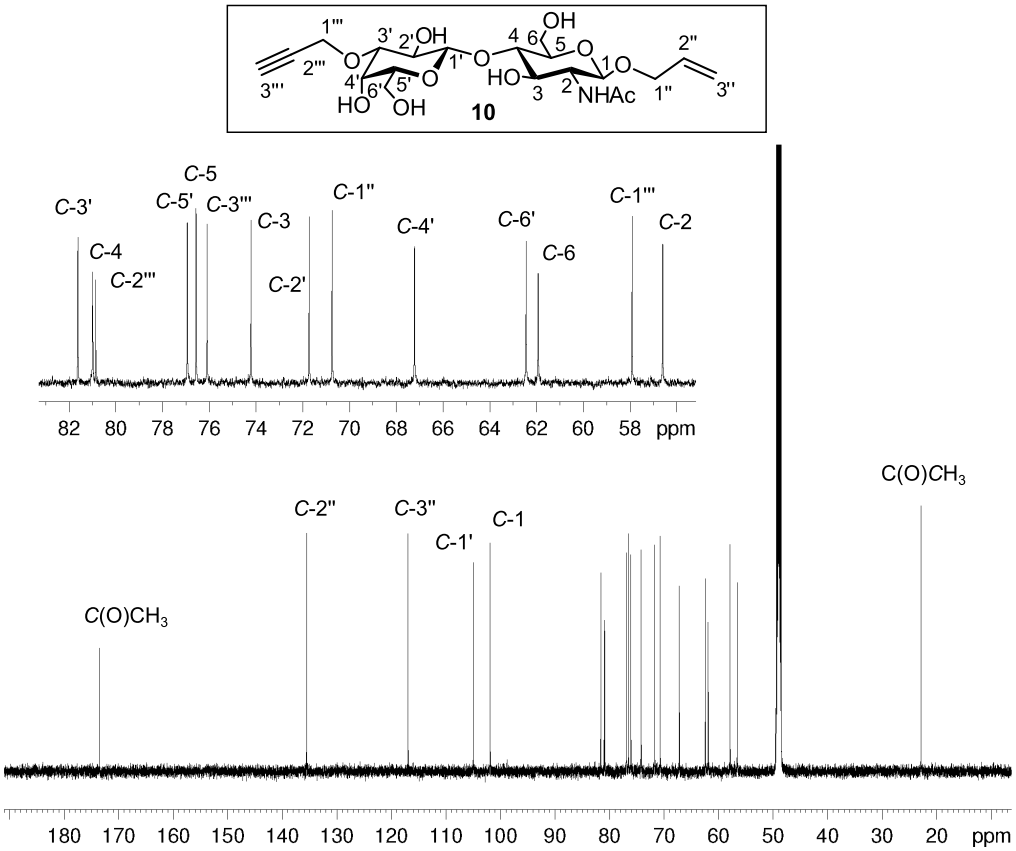

Fig. 5.11 ^{13}C-NMR spectrum of alkyne precursor **10**.

carbons and between δ = 80.99 and 56.60 ppm for carbons of the disaccharide scaffold (Fig. 5.11). The carbonyl carbons of the acetates in **38**, **39**, **40** and **11** resonate at low field at $\delta \cong 170$ ppm while the CH_3 units give rise to signals at high field ($\delta \cong 21$ ppm). Signals of the aromatic carbons of the benzyl groups in **40** and **11** are low-field shifted and can be divided in a signal for the quarternary carbon at $\delta \cong 138$ ppm and the remaining carbons at $\delta \cong 128$ ppm.

5.1.3 hGal-1 Binding Evaluation of Ligand Precursors

To probe the influence of synthetic modifications at *O*-3' and *O*-1 in ligand precursors **10** and **23** regarding their targeting abilities towards hGal-1 both molecules were evaluated by SPR and X-ray crystallography and compared with data obtained for the hGal-1/LacNAc interaction.

Surface Plasmon Resonance

SPR studies with LacNAc and immobilized hGal-1 resulted in a K_d value of 91.4 ± 4.62 μM and is in good agreement with a previously determined binding constant.[74] As anticipated neither the β-1-*O*-allyl group nor the 3-*O*-alkyne extension have a striking influence on the binding affinity and experiments resulted in K_d values of 107 ± 8.80 μM and 135 ± 36.0 μM for **10** and **23**, respectively (Table 5.4). The observed similar binding affinities of LacNAc, **10** and **23** are a first indication of a conserved binding mode of the carbohydrate scaffolds but demand for experimental verfication by crystallization studies with hGal-1 and **10** and **23** to corroborate the assumption.

Table 5.4 Results of SPR experiments with immobilized hGal-1 and disaccharides LacNAc, **10** and **23**. [a]K_d values were determined with runs in eight concentrations from $1.95 \cdot 10^{-6}$ to $2.50 \cdot 10^{-4}$ M and measured in triplicates. [b]K_d value was determined with runs in six concentrations from $5.00 \cdot 10^{-6}$ to $1.00 \cdot 10^{-3}$ M and measured in duplicate.

Ligand	LacNAc	10	23
hGal-1 K_d [μM]	91.4 ± 4.62[a]	107 ± 8.80[a]	135 ± 36.0[b]

Cocrystallization of hGal-1 and *N*-acetyllactosamine precursors

To experimentally probe the binding geometry of ligand precursors **23** and **10** both structures were subjected to soaking experiments with hGal-1 crystals grown in 2.0 M $(NH_4)_2SO_4$. Data collection at beamline ID 14-4 of the ESRF, Grenoble, structure solution and the refinement process was performed as described in section 5.1.1. Both complexes feature the same cell parameters as the PEG crystal structure.

Complex of hGal-1 & alkyne precursor 10

The structure of the complex between hGal-1 and **10** was determined with a resolution of 1.20 Å. The high resolution data allowed to precisely allocate the ligand orientation (Fig. 5.12). As for LacNAc the galactosyl moiety has low B-factors and is located in the protein cleft formed by His44, Asn46, Asn61 and Arg48. The anomeric position of the GlcNAc unit was fixed to the β-anomer by acetal formation with allyl alcohol. The $2F_{obs}$-F_{calc} omit map (contoured to a level of 1 σ, dark blue mesh) lacks electron density for the allyl group indicating that this residue has neither a defined binding mode nor does it disturb natural interactions of the GlcNAc unit. On the opposite site of the ligand the model shows a well-defined electron density for the 3-*O*-alkyne extension of

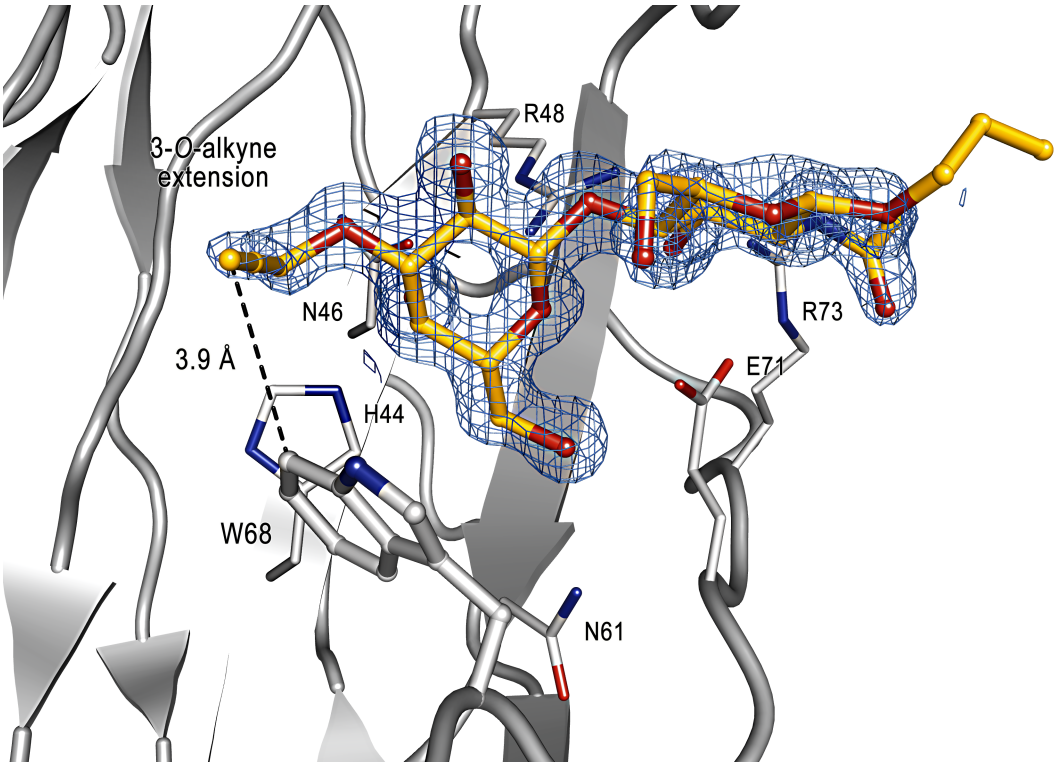

Fig. 5.12 Complex of hGal-1 and **10**. Electron density is presented as $2F_{obs}$-F_{calc} map and contoured to a σ-level of 1.0. The alkyne extension shows a clearly defined orientation due to T-shaped arene interactions with W68.

the galactosyl moiety. The alkyne group is positioned within a distance of 3.9 Å to Trp68 and might interact by weak T-shaped arene interactions with the indole side chain.[309] Fig. 5.13 depicts a superposition of the crystal structures of complexes hGal-1/**10** (yellow)

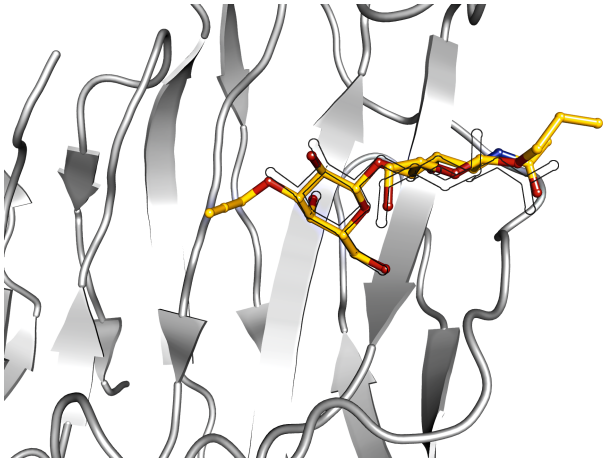

Fig. 5.13 Superposition of **10** (yellow) and LacNAc (black line) in complex with hGal-1 shows a conserved binding mode of the carbohydrate scaffolds.

and hGal-1/LacNAc (black line) to highlight that the carbohydrate scaffolds are arranged in a highly conserved geometric orientation and that all natural interactions of the disaccharide are maintained.
The crystal structure of the complex between hGal-1 and alkyne template **10** impressively confirm the concept of gradually expanding ligand size and functionality without disturbing the fine-tuned network of carbohydrate-ligand interactions. The crystallographic data of this complex was the starting point for an extensive computational screen that aimed at predicted organic azides with residues to address the region located next to the CRD.

Complex of hGal-1 & 23

To probe a potential influence of the alkyne functionality precursor **23** was subjected to soaking experiments as well. **23** is equipped with the 1-*O*-β-allyl group but lacks the alkyne group at *C*-3. The complex hGal1-/**23** shows a clearly defined electron density for the galactosyl moiety, however it is less detailed for the *N*-acetylglucosamine unit (Fig. 5.14, contoured to a level of 1 σ, dark blue mesh). Still, the binding mode of **23** is highly conserved with characteristic interactions of the galactosyl moiety and the 3-OH group of the *N*-acetylglucosamine unit that fix the disaccharide in the protein cleft described in detail for hGal-1/LacNAc in section 5.1.1. Similar to **10** no electron density was observed for the flexible allyl group. This finding is important for following microarray experiments where the carbohydrate ligand is covalently attached via the allyl group to a functionalized polymer surface. Crystallographic data imply that such an immobilization will not hinder hGal-1 binding.

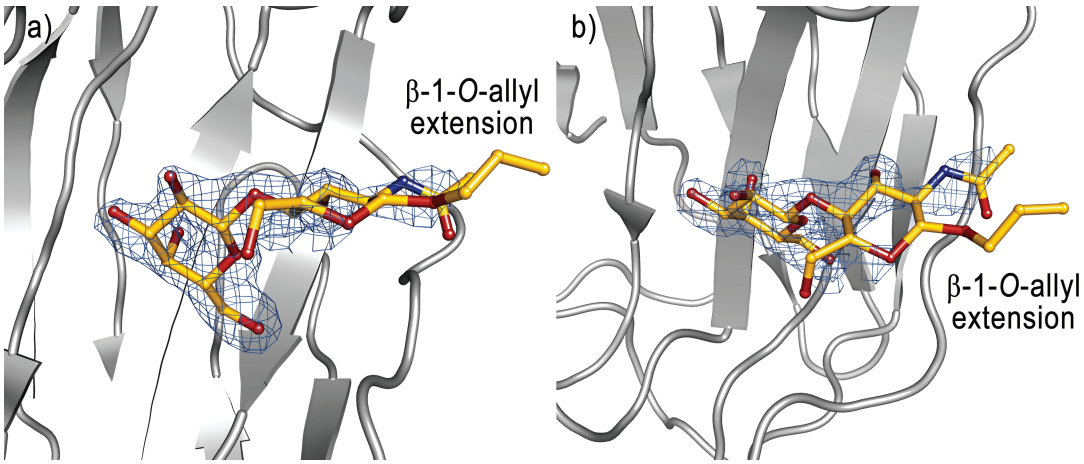

Fig. 5.14 Complex of hGal-1 and **23**. Electron density is presented as $2F_{obs}$-F_{calc} map and contoured to a σ-level of 1.0. The density map is clearly defined for the galactoside unit and reflects a high degree of flexibility for the 1-*O*-allyl extension.

5.1.4 Synthesis of Computationally Predicted Ligands from Precursors

The crystallographic data of **10** in complex with hGal-1 was the starting point for a comprehensive computational screen to predict triazoles that adress the extended CRD. Recently, Paulson *et al.* identified highly affine sialoside analogues for sialic-acid binding proteins by immobilizing azido- (or alkyne-) modified sialic acid derivatives on a microarray.[234] Carbohydrates were subsequently converted with a library of functional alkynes (or azides) in a high-throughput approach. Promising ligands were visualized by incubation with fluorophore-labeled lectins. However, this combinatorial strategy is not capable of generating ligands that address a selected protein area with a specific binding mode which strongly motivated the integration of computational studies in the presented ligand design of this thesis rather than producing a library of triazoles.
The computational work was performed by Dr. Michael Reutlinger, ETHZ, and provided bromides and azides that are accessible with few synthetic steps. Briefly, triazoles were virtually synthesized from an azide database and alkyne **10** by using MOE 2011.10 (The Chemical Computing Group Inc., Montreal, Canada). This procedure provided a total of 397 click products that were docked with the GOLD v.5.0.1 software. An area of 8 Å radius around the precursor **10** was defined as binding domain and disaccharide bound water molecules were retained. Docking results were evaluated by the ChemPLP (PLP ≙ piecewise linear potential) scoring function and further assessed by their ligand

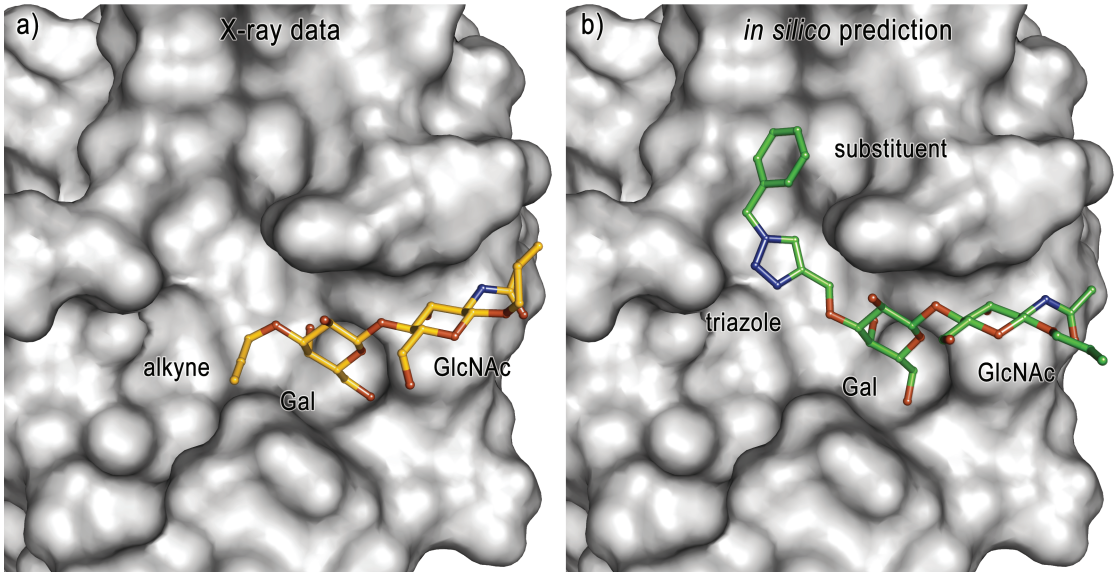

Fig. 5.15 Comparison of a) the experimentally determined complex between hGal-1 and alkyne precursor **10** and b) the computationally predicted complex between hGal-1 and topranked triazole **9a**.

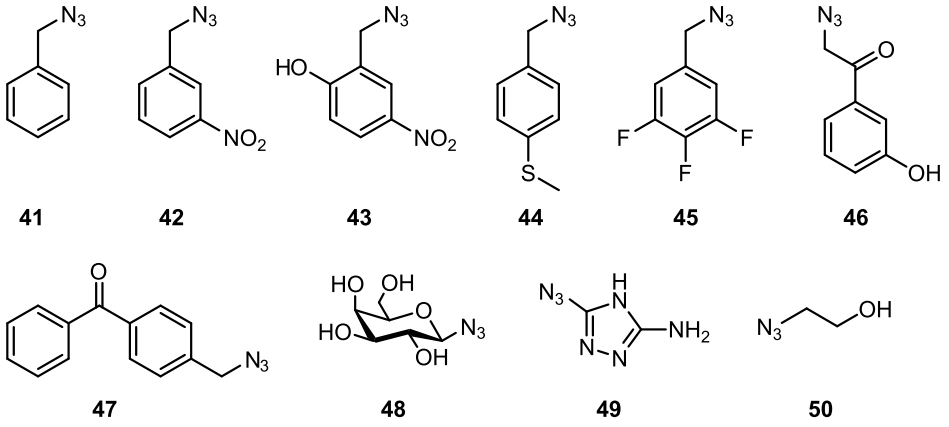

Fig. 5.16 Corresponding organic azides of topranked click products predicted by the computational screen.

efficiency (ChemPLP score divided by number of heavy atoms). Fig. 5.15 contrasts the complex between hGal-1 and alkyne precursor **10** obtained experimentally by X-ray crystallography and a computionally predicted complex between hGal-1 and the topranked triazole **9a**. Corresponding azides of further topranked click products are depicted in Fig. 5.16.

Synthesis of organic azides

Benzyl azides **41**-**45** and **47** were synthesized according to a general protocol with the corresponding bromides as starting material (Scheme 5.9). Stark *et al.* reported a microwave-assisted quantitative conversion of benzyl bromide to benzyl azide in aqueous solution at 120 °C for 30 min.[310] This synthetic route was adopted for the preparation of benzyl azides from Fig. 5.16 with a prolonged reaction time of 1 h. Still, a complete conversion was not achieved for all substances and ^{1}H-NMR spectroscopy indicated remaining starting material. Organic bromides were expected to be tolerated in the Cu(I) catalyzed cycloaddition, thus the amount of starting material was determined and considered in the following click reaction. The carbohydrate azide **48** was prepared

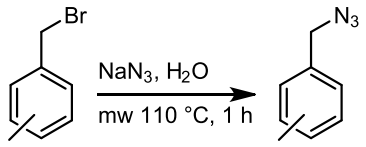

Scheme 5.9 General protocol for the synthesis of benzyl azides.

from the α-galactosyl bromide **33** in a Königs-Knorr-like coupling reaction with NaN_3

(Scheme 5.10). The different solubility of the galactoside bromide **33** and NaN_3 required the use of a two-phase system with CH_2Cl_2 and sat. $NaHCO_3$ solution. Tetrabutylammonium hydrogensulfate (TBAHS) was applied as phase transfer catalyst and tetraacetylated galactosyl azide **61** was obtained in excellent yield. Subsequent deacetylation provided 1-azido-β-D-galactopyranoside (**48**) for conversion with the alkyne precursor. ^{1}H-NMR spectroscopy confirmed the successful conversion to **48** with

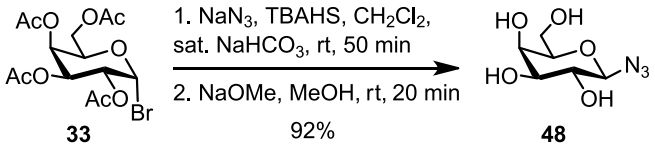

Scheme 5.10 Synthesis of galactosyl azide **48**.

a doublet at δ = 4.59 ppm. Compared to the galactosyl bromide **33** this signal is more than 2 ppm high field shifted and splits with ^3J = 8.7 Hz indicative for a β-configured galactoside. As the presence of the azide group can only be detected indirectly in ^{1}H- and ^{13}C-NMR spectra, mass spectrometry and IR spectroscopy were applied to further prove the structure of **48**. In the ESI spectrum appears as basis peak a complex of the molecule ion with sodium (m/z = 228.05909) and a second peak corresponds to twice the molecule mass with sodium. Striking signals in the IR spectrum at $\tilde{\nu}$ = 2125 cm^{-1} and $\tilde{\nu}$ = 1350 cm^{-1} were assigned to the symmetric and asymmetric stretch mode of the azide.

Synthesis of *N*-acetyllactosamine-based triazoles

N-acetyllactosamine-based triazoles were synthesized from alkyne precursor **10** and organic azides **41**-**50**. In the 1960s Huisgen *et al.* thoroughly investigated the thermal reaction between the counterparts equally leading to 1,5- and 1,4-substituted 1*H*-1,2,3-triazoles.[269,311,312] The reaction experienced a second boom in 2002 when Sharpless *et al.*[271] and Meldal *et al.*[270] independently discovered that catalytic amounts of Cu(I) drive the reaction towards the 1,4-substituted reaction product that was isolated as single isomer. Nowadays the the Cu(I) catalyzed 1,3-dipolar cycloaddition between an organic azide and an alkyne is the most prominent representative of the "click reactions" and commonly referred to as CuAAC (Cu(I)-catalyzed alkyne-azide cycloadditon).[272]
In their pioneering work Sharpless *et al.* proposed a catalytic mechanism for the Cu(I) catalyzed azide alkyne cycloaddition and attributed the intermediate Cu(I) acetylide specie a key role in the reaction course (Scheme 5.11).[271] DFT calculations[314,315] confirmed the stepwise, regiospecific catalytic sequence initiated by a π-coordination of the alkyne to the Cu(I) species and followed by facile deprotonation in aqueous media to form the σ-acetylide Cu(I) complex. Activation of the organic azide occurs

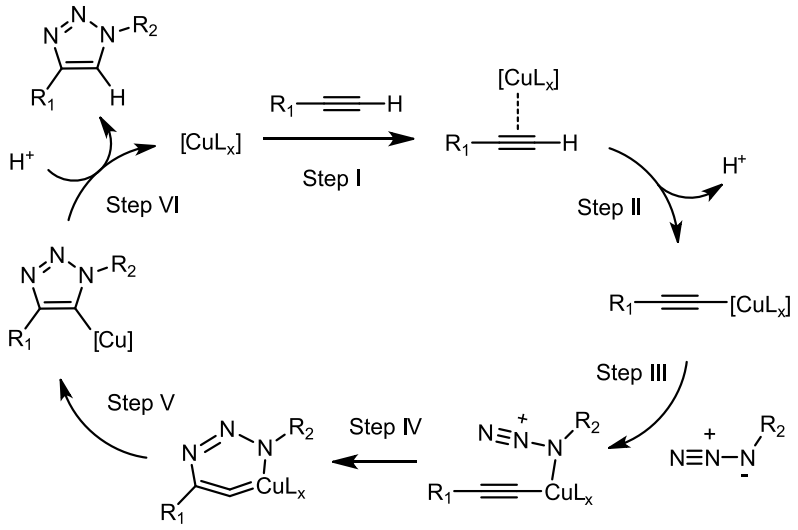

Scheme 5.11 Proposed regioselective, stepwise reaction cycle of Cu(I) catalyzed alkyne azide cycloaddition.[271]

by coordination of the nucleophilic nitrogen proximal to the carbon (Step III), thereby enhancing the electrophilicity of the azide's terminus. In the next step, the distal nitrogen of the azide is attacked from the intern acetylide carbon and the first C-N bond formation leads to a strained six-membered Cu(III) metallacycle. The formation of a Cu(I) triazolide by ring contraction resulted to be energetically favorable in the DFT study.[314] Further, the authors state that alternative pathways like a concerted reaction

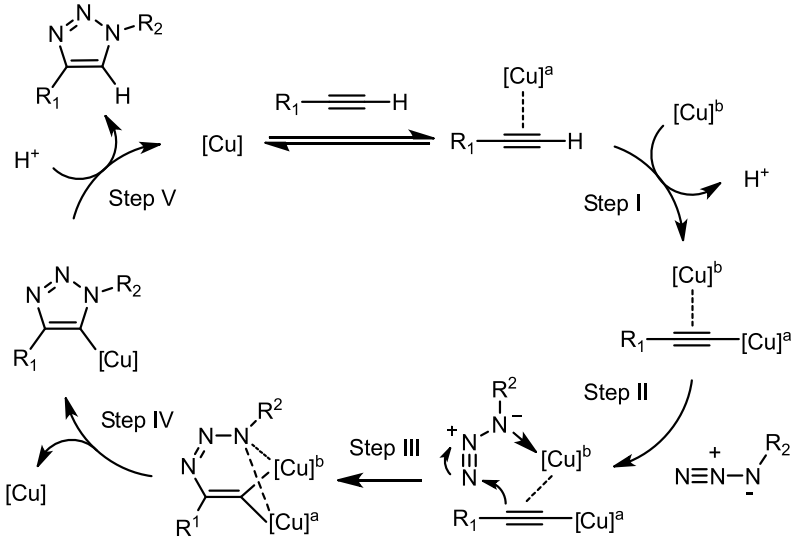

Scheme 5.12 Proposed catalytic cycle involving two copper atoms. Mechanistic details were substantiated by copper isotope labeling experiments.[313]

of the azide and the Cu(I) acetylide or a coordination of the terminal nitrogen to Cu(I) as proposed by Meldal and Tornøe[316] are energetically disfavored and can be excluded.[315] Recently, Fokin *et al*. provided experimental evidence about the involvement of a second copper atom in the reaction mechanism.[313] Isotopic labeling of an exogenous ^{63}[Cu] catalyst ([Cu]^b, Scheme 5.12) and treatment with a copper acetylide ([Cu]^a) of the natural isotope abundance (^{63}Cu:^{65}Cu 69:31) led to an enrichment of ^{63}[Cu] (^{63}Cu:^{65}Cu 85:15) within the resulting copper triazolide as determined by mass spectrometry. In control experiments the authors ruled out that the isotopic enrichment occurred via the acetylide or triazolide intermediate and explained their observation by Step IV of the catalytic cycle (Scheme 5.12) and the statistical release of either the exogenous ^{63}[Cu] or the former acetylide $^{63/65}$[Cu].

The Cu(I)-catalyzed reactions performed in this work were conducted in absence of additional ligands.

Nevertheless it is noteworthy to mention, that amino chelate ligands are often employed to increase the reaction rate and to protect the Cu(I) species from oxidation by oxygen.[316,317] A second aspect in Cu(I) catalysis is the formation of a variety of Cu(I)-ligand clusters within the reaction mixture while the equilibrium between the cluster strongly depends on the individual reaction conditions. The addition of ligands, tris[(1-benzyl-1*H*-1,2,3-triazol-4-yl)methyl]amine (TBTA) is one of the most prominent representatives,[317] probably affects the equilibrium distribution as well as the rate of equilibration, thereby also promoting the formation of the most active clusters.

Triazoles of type **9** were prepared according to a standard protocol[318] for highly polar substrates in aqueous reaction medium (*tert*-BuOH/H_2O 2:1) as depicted in Scheme 5.13.[v] Product formation was monitored with UV light (λ = 254 nm) and facilitated the discrimination between alkyne **10** and the triazoles as they have similar R_f values.

Previously, Liang *et al*. reported about an efficient *in situ* strategy for the preparation

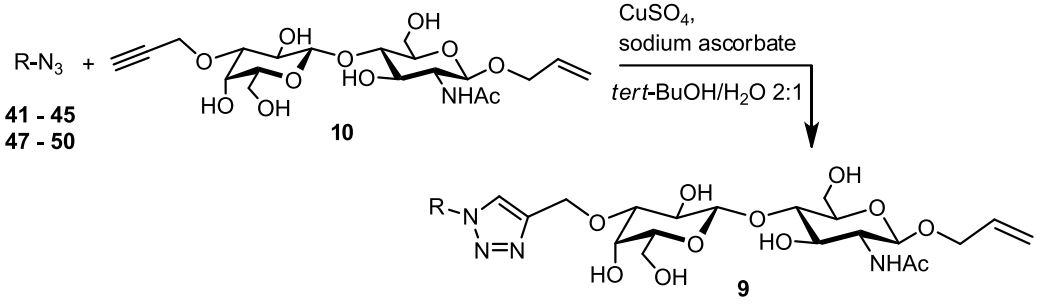

Scheme 5.13 Cu(I)-catalyzed cycloaddition of organic azides **41**-**45**, **47**-**50** and alkyne precursor **10**.

[v]Click products **9f**, **9g** and **9i** were synthesized by Anne Neumann during her bachelor thesis.[285]

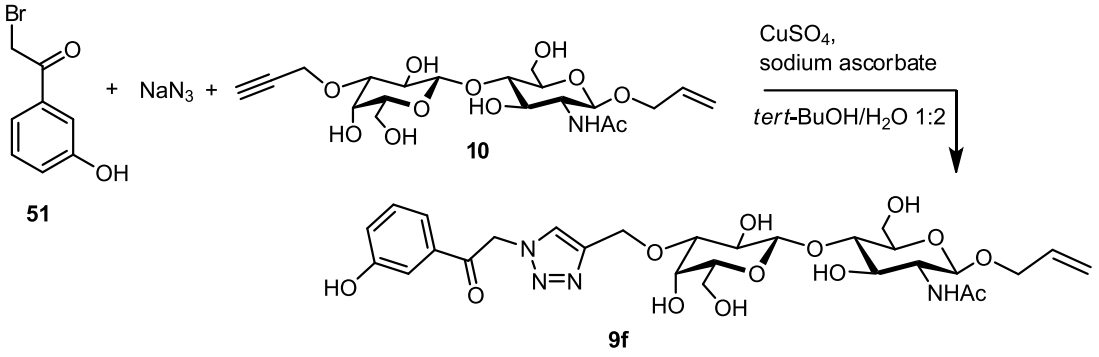

Scheme 5.14 *In situ* click reaction with alkyne precursor **10**, bromide **51** and NaN_3.

of 1-aryl-1*H*-1,2,3-triazoles from aryl halides and terminal alkynes in the presence of NaN_3.[319] In a proof-of-concept experiment this one-pot synthesis was applied to synthesize click product **9f** from alkyne **10**, bromide **51** and NaN_3 (Scheme 5.14). Bromide **51** and NaN_3 were solved in H_2O, mixed at 40 °C for 2 h and supplemented with **10** in *tert*-BuOH for 24 h at 40 °C (Scheme 5.14). Column chromatography yielded the pure product in 76% yield that is comparable to the yields of the two-step syntheses, thus offering an alternative approach to triazole-based hGal-1 ligands. Fig. 5.17 gives an overview of *N*-acetyllactosamine-based triazoles that were synthesized in this work and investigated regarding their binding activity towards hGal-1 in following studies.

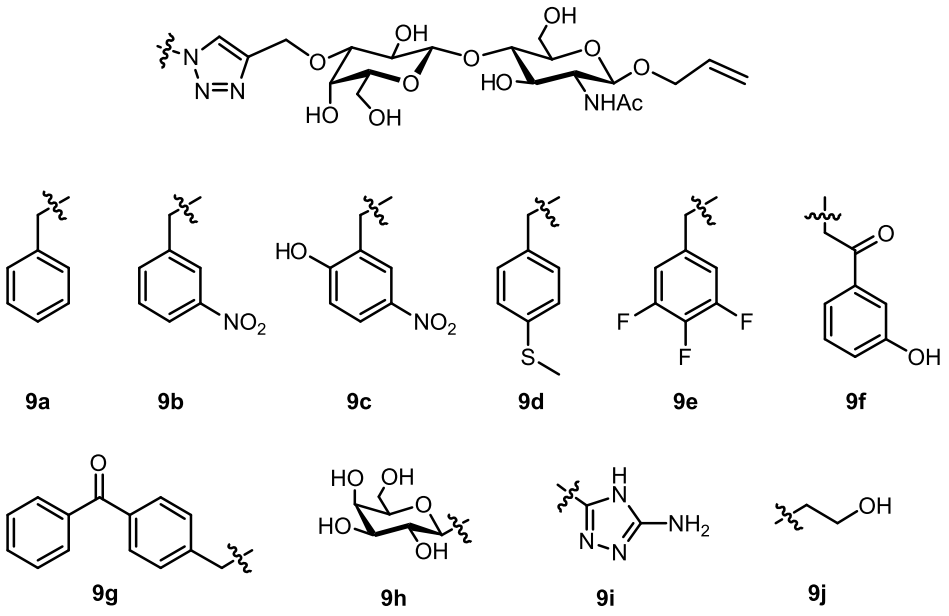

Fig. 5.17 Overview of synthesized *N*-acetyllactosamine-based triazoles with high scores in the computational screen.

Discussion of the spectroscopic data

^{1}H- and ^{13}C-NMR spectra of *N*-acetyllactosamine-based triazoles feature similar signals and splitting patterns and thus, are representatively discussed for click product **9d**. Additionally, the signals of the carbohydrate scaffold differ only slightly from alkyne precursor **10** so that only characteristic differences are highlighted in the following.
A first indication for the identity of triazole **9d** gives the signal at δ = 7.97 ppm that appears as a singlet and can be assigned to *H*-3''' due to the characteristic low field shift of the proton in 1,4-substituted 1*H*-1,2,3-triazoles (Fig. 5.18). Protons *H*-1''' are diastereotopic due to the proximal stereo center of *C*-3' and resonate as doublets at δ = 4.81 and 4.72 ppm, respectively, with a large geminal coupling of ^{2}J = 12.2 Hz. The benzylic protons are distal from a chiral carbon and thus resonate low field shifted at δ = 5.55 ppm as a singlet with an integral of two. Compared to **10** resonances of *H*-1''' are slightly low field shifted and the characteristic doublet of doublet at δ = 2.87 ppm of the terminal alkyne proton does not appear in the spectrum indicating a conversion of the alkyne to the triazole. Aromatic protons resonate as a single signal at δ = 7.27 ppm, even though only a set of meta- and ortho- positioned protons are chemically equivalent.

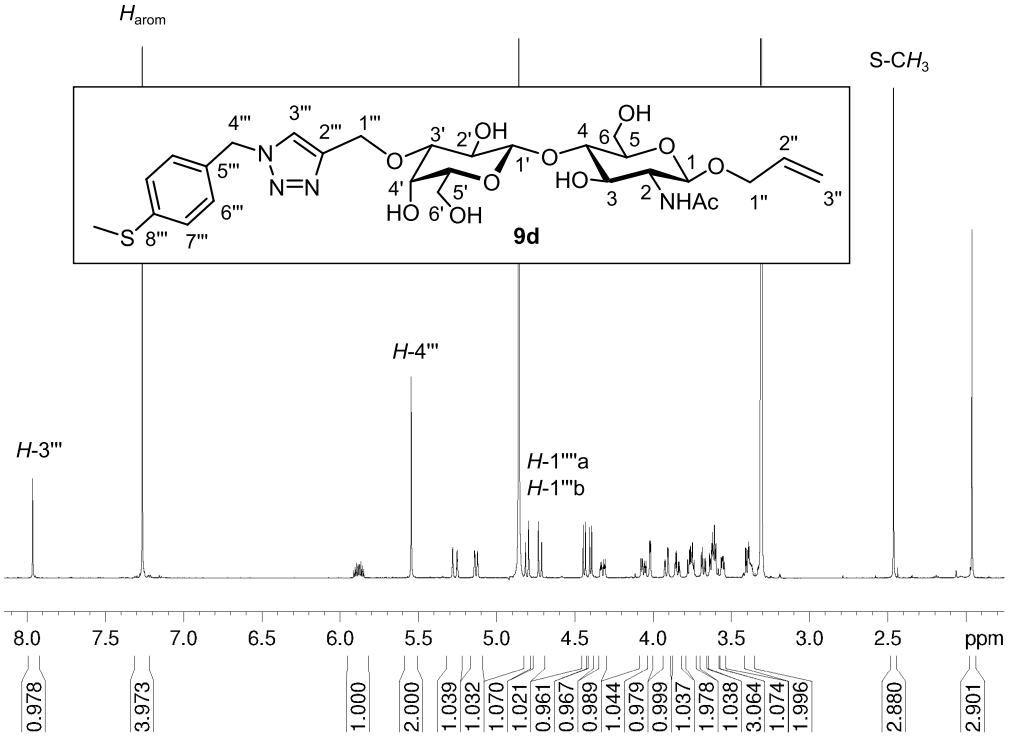

Fig. 5.18 ^{1}H NMR spectrum of click product **9d**. For reasons of clarity only characteristic "click" protons are assigned in the spectrum.

Obviously, shielding and deshielding effects of the chemical environment of all protons are similar and thus they are accidental isochron. The thiomethyl group resonates as a singlet at δ = 2.46 ppm.

The ^{13}C-NMR spectrum features characteristic signals for the triazole group with signals at δ = 146.62 and 124.92 ppm for *C*-2''' and *C*-3''', respectively. In spectra of **9f**, **9j**, **9a**, **9e** either the signal of one or of both *C*-2''' and *C*-3''' are absent, however, further signals and mass spectrometry proved unambiguously the identity of all click products. Surprisingly, the ^{1}H as well as ^{13}C NMR spectrum of **9f** also misses signals for *H*-4''' and *C*-4''' but HRMS ESI provided as basis peak the molecule ion with one sodium (m/z = 661.23300). Aromatic carbons resonate at δ = 141.06, 133.20, 129.77 and 127.69 ppm with the latter two signals assigned to the chemical equivalent carbons *C*-6''' and *C*-7''' (Fig. 5.19). Signals for the methylene carbons were assigned in the DEPT spectrum and appear at δ = 63.59 ppm (*C*-1''') and at δ = 54.54 ppm (*C*-4'''). The thiomethyl carbon resonates isolated and high field shifted at δ = 15.41 ppm.

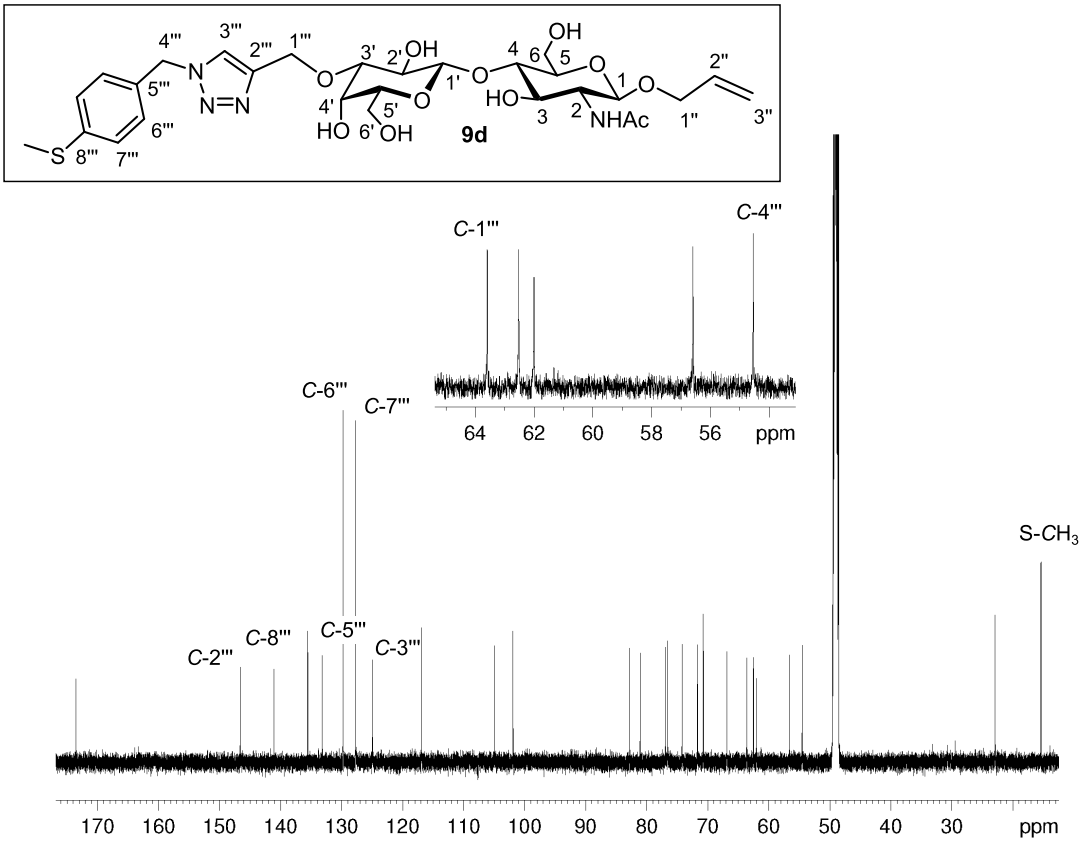

Fig. 5.19 ^{13}C NMR spectrum of click product **9d**. For reasons of clarity only characteristic "click" carbons are assigned in the spectrum.

5.1.5 hGal-1 Binding Evaluation of Computationally Predicted Ligands

The successful preparation of ten click products allowed an investigation of the structure activity relation by SPR and X-ray crystallography to probe the power of combining organic synthesis, X-ray crystallography and computational prediction. Additional ITC experiments intended to gain further insights into the thermodynamic properties of individual binding events.

Cocrystallization of hGal-1 and triazole-based ligands

Click products were introduced to hGal-1 crystals by soaking experiments. Resulting complexes were measured at beamline ID23-1, ESRF, Grenoble, and provided high resolution data for hGal-1 in complex with **9a**, **9f** and **9i**. Soaking of further click products led either to the structure of ligand-free protein or afforded electron density only for hGal-1 and the carbohydrate scaffold but not for the substituted triazole. These findings might be attributed to a hindrance of ligand binding by the clicked part and/or an unspecific and

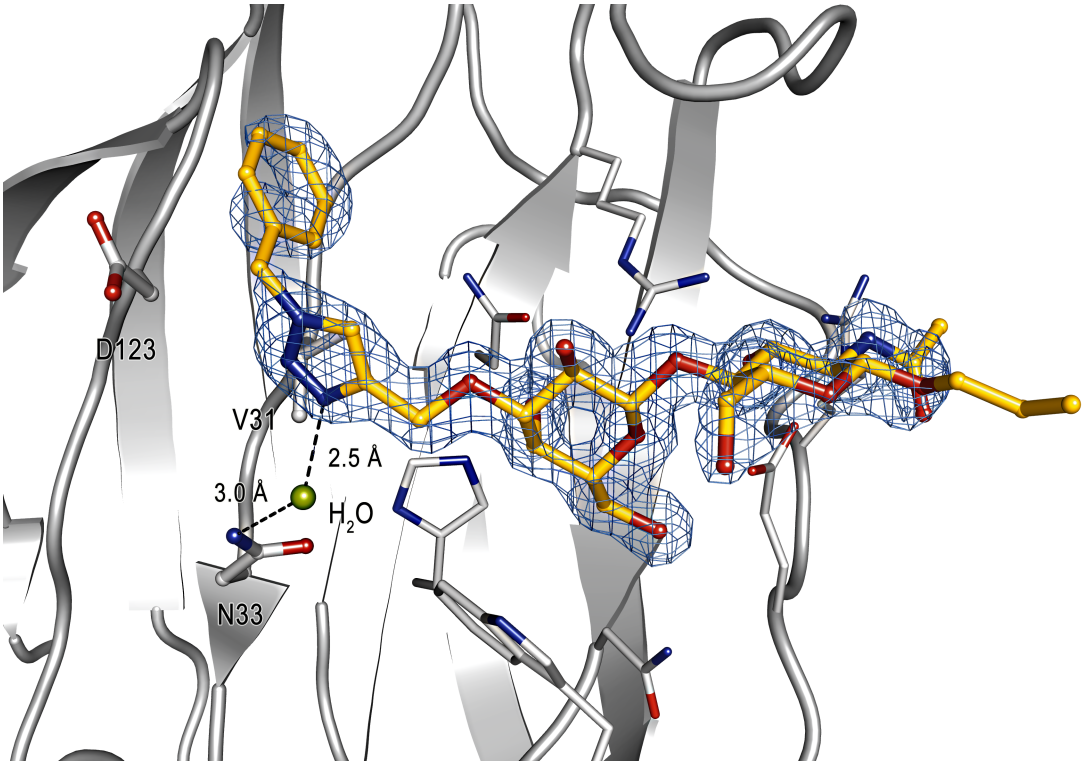

Fig. 5.20 Complex between hGal-1 and ligand **9a**. Electron density at a resolution of 1.42 Å is contoured at a level of 0.9 σ and is clearly defined for the extended disaccharide. The interaction between the triazole nitrogen and Asn33 is water-mediated.

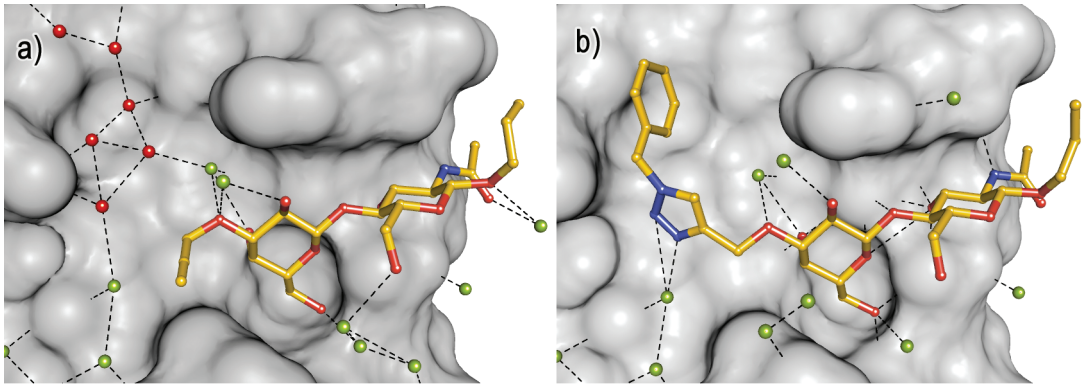

Fig. 5.21 The region adjacent to the CRD is solvated by a distinct water network (depicted in red color) that is displaced upon binding of extended LacNAc **9a**.

less pronounced interaction of the substituted triazole.

Complex of hGal-1 and 9a

Data collection and structural refinement of hGal-1/**9a** provided a complex with a resolution of 1.42 Å. The difference electron density (Fig. 5.20, contoured to a level of 0.9 σ) clearly located the extended *N*-acetyllactosamine derivative within the CRD and further solved the location of the subsituted triazole. Remarkably, the binding mode equals that of LacNAc and **10** and is highly conserved. Even tough the introduced residue possesses no functionality for hydrogen bonding or strong electrostatic interactions the electron density does not indicate a high flexibility for any part of the ligand. The triazole is fixed by a water-mediated interaction with Asn66 and evidently fulfills its role as linker unit to space the carbohydrate scaffold with residues that address the area adjacent to the CRD. The aromatic benzyl group of **9a** covers the hydrophobic region formed by Val33 and its parallel orientation towards the carboxyl group of the side chain of Asp123 might favor π-π interaction. Fig. 5.21 depicts a comparison of the water network on the shallow mainly hydrophilic protein surface in the complex of hGal-1/**10** and hGal-1/**9a**.[vi] While **10** binds exclusively to the CRD with six water molecules arranged on the targeted area **9a** is expanded in this direction and displaces water molecules by the substituted triazole. Water displacement is an important aspect in drug design and high entropic gains are mostly attributed to this phenomenon.[320] How this finding impacts on ligand affinity and thermodynamic properties will be discussed in context of the SPR and ITC results.
Fig. 5.22 depicts a superposition of the experimentally determined binding mode of triazole **9a** (yellow molecule) and a selected docking result for **9a** (green molecule).

[vi] a direct comparison with hGal-1/LacNAc is not possible due to different crystal forms that inherently provoke different solvation stati.

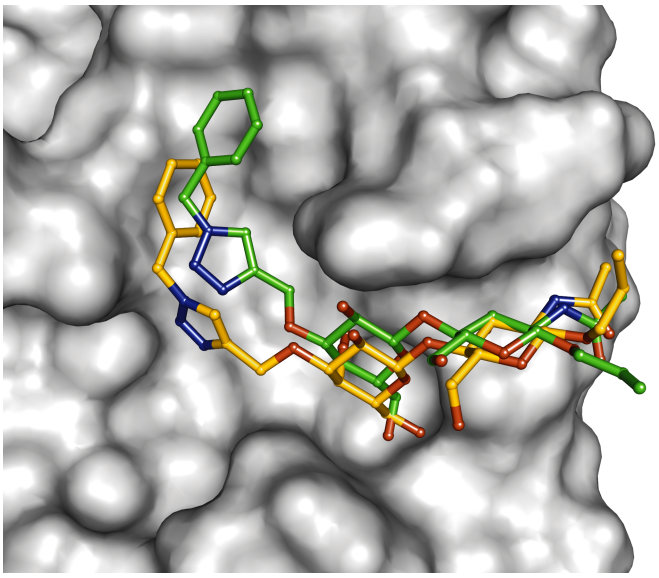

Fig. 5.22 hGal-1 in complex with triazole **9a**. The experimentally determined binding mode is depicted in yellow and compared to the computationally predicted binding geometry in green.

The displayed docking pose yielded the best score in the computational evaluation and additionally, showed the highest agreement with the experimental obtained binding geometry. The *in silico* screen successfully reconstructed the carbohydrate trunk in the CRD with the right direction of the substituted triazole. The binding area adjacent to the CRD in the complex hGal-1/**9a** is widened compared with the complex between hGal-1 and **10** (cf. Fig. 5.15 a) and allows to harbour the triazole with the observed geometry.

Complex of hGal-1 and 9f

The crystal structure of the complex between hGal-1 and **9f** was solved at a resolution of 1.47 Å (Fig. 5.23). Even though and electron density is visible for the whole ligand it is less distinct for the acetophenone moiety. Still the geometric orientation of **9f** is unambiguous and allows no other binding mode that fits the density map. As for **9a** the carbohydrate scaffold shows a highly conserved binding mode that is not disturbed by the extensions at the 3-OH group. The triazole is fixed by a water-mediated interaction with Asn33 and functions as linker unit. The aromatic hydroxyl group interacts via hydrogen bonding with Asp125. Additionally, the aromatic residue of **9f** is orientated to interact by CH-π stacking with the main chain of Gly124 and covers the hydrophobic side chain of Val31.

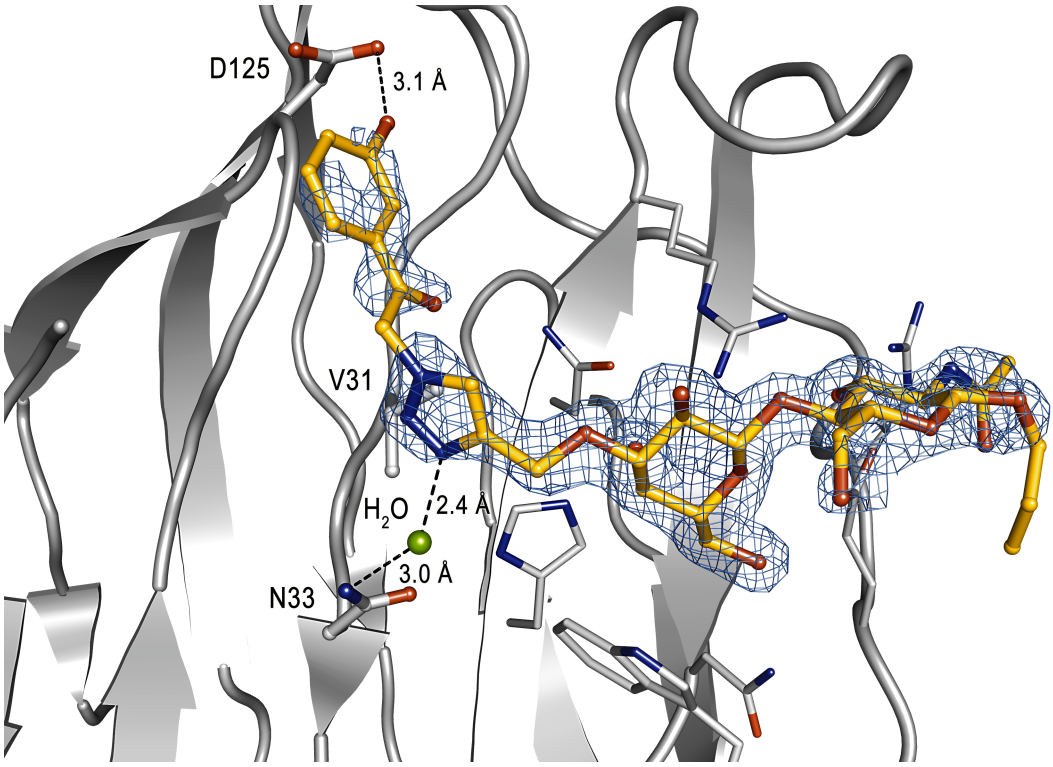

Fig. 5.23 Complex between hGal-1 and ligand **9f**. Electron density at a resolution of 1.47 Å is contoured at a level of 0.8 σ. The triazole interacts water-mediated with Asn33 and the aromatic hydroxyl group forms a hydrogen bond with Asp125.

Complex of hGal-1 and 9i

The electron density of **9i** in complex with hGal-1 (1.36 Å) is less defined for the clicked part and clearly demonstrates a higher degree of freedom for the substituted triazole

(Fig. 5.24). Again, the carbohydrate scaffold is arranged in a highly conserved manner. The crystallographic data show that the amino substituent of the 4*H*-1,2,4-triazole forms a hydrogen bond with the hydroxyl group of the side chain and with the carboxylic oxygen of the main chain of Ser29. A common feature of all three complex structures is the water-mediated interaction between the 1*H*-1,2,3-triazole and Asn33, evidently a key element in triazole elongated ligand binding.

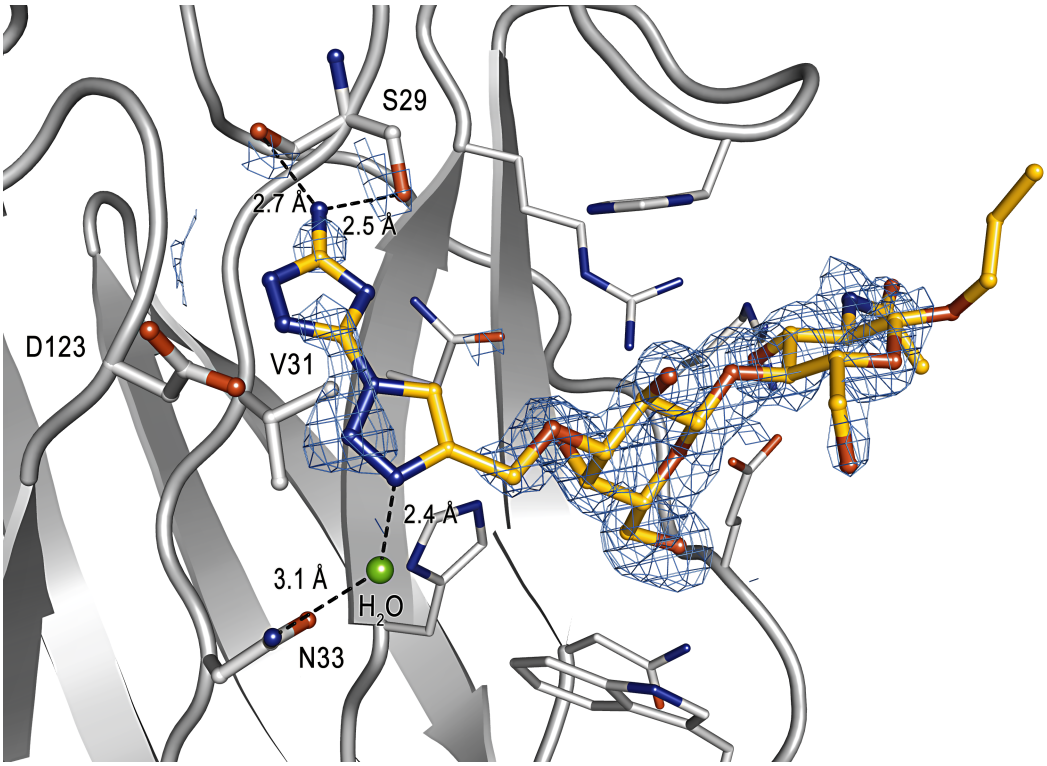

Fig. 5.24 Complex between hGal-1 and ligand **9i**. Electron density at a resolution of 1.36 Å is contoured at a level of 0.8 σ.

Surface Plasmon Resonance

SPR experiments with immobilized hGal-1 and ten click products identified several click products with an increased affinity compared to the precursor alkyne **10**, among those the ligands **9a**, **9f** and **9i** that were successfully crystallized in complex with hGal-1. Fig. 5.25 a illustrates the sensogram of the hGal-1/**9f** experiment with increasing response units at higher **9a** concentrations. Fig. 5.25 b depicts the binding curve and sigmoidal fit for the hGal-1/**9a** interaction resulting from the response units for each concentration. The inflection point of the fit curve indicates the K_d value of 43.6 $\pm$ 1.2 μM. Table 5.5 shows that the triazole-based ligands throughout proved a higher binding affinity, however, an

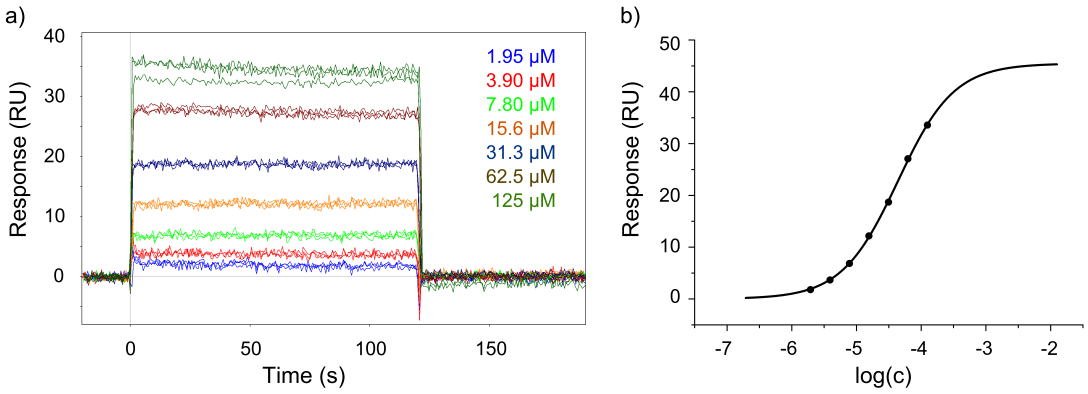

Fig. 5.25 SPR data for the interaction between hGal-1 and **9a**. a) Sensogram for concentrations from 1.95 μM to 125 μM. b) Binding curve and sigmoidal fit.

only three-fold increase is rather surprising considering the well-defined binding modes of **9a** and **9f** with novel established hydrogen bonds, π-π and CH-π stacking as well as hydrophobic interactions. ITC experiments were subsequently performed to evaluate ligand binding of **9a** and **9f** more profoundly on the basis of enthalpic and entropic contributions.

Table 5.5 Results from SPR experiments with immobilized hGal-1 and the click products. K_d values were determined with runs in eight concentrations from $1.95 \cdot 10^{-6}$ to $2.50 \cdot 10^{-4}$ M and measured in [a] triplicates or [b] duplicates. [c] K_d values were estimated in a single-concentration screen (100 μM) and measured in duplicates.

Ligand	hGal-1 K_d [μM]
Alkyne **10**	$108 \pm 9^{[a]}$
9a	$43.6 \pm 1.2^{[a]}$
9b	$94^{[c]}$
9c	$72.6 \pm 7.3^{[b]}$
9d	$31.3 \pm 2.5^{[a]}$
9e	$76^{[c]}$
9f	$37.5 \pm 1.7^{[a]}$
9g	$57.3 \pm 9.6^{[b]}$
9h	$75^{[c]}$
9i	$62.2 \pm 2.7^{[a]}$
9j	$116 \pm 8^{[a]}$

Results of ITC assay

ITC experiments were conducted to study thermodynamic contributions and the nature of the interaction between hGal-1 and selected disaccharides in solution (Table 5.6). ITC experiments were performed for ligands **9a** (Fig. 5.26) and **9f** (Fig. B.1, appendix) that showed well-defined electron densities in crystallization experiments with hGal-1. ITC data were expected to allow a thermodynamic evaluation of the binding event and to evaluate the K_d values obtained by SPR measures. Additionally, LacNAc (Fig. B.3, appendix) and the click product **9j** (Fig. B.2, appendix) with a weak binding affinity according to SPR experiments were investigated by ITC. The monomer concentration of hGal-1 was used in the fitting process and all titration data fitted best to a model with one binding site per protein (n = 1). This finding is in agreement with the results of Romero *et al.*[74] and indicates that both CRDs in the hGal-1 homodimer bind independently and equivalently. Table 5.6 lists binding affinities, enthalpic as well as entropic contributions. ITC showed for all complexes that the interaction between hGal-1 and the disaccharides is enthalpically driven and changes in enthalpy reflect interactions of hGal-1 and the disaccharide with the solvent as well as between hGal-1 and the disaccharide. These interactions include hydrogen bonding, electrostatic, hydrophobic and *van der Waals* interactions and can be assigned in the crystallographic data of the complexes. Further, the trend was observed that entropy decreases with increasing enthalpy (Fig. 5.27). An enthalpy-entropy compensation is common for lectin-carbohydrate interactions[321] and has been published earlier for hGal-1/LacNAc.[74] At first sight this finding is rather surprising because upon disaccharide binding water molecules are displaced and Fig. 5.21 illustrates that with growing size of the ligand the number of displaced water increases. However, an entropic gain is mainly observed when the addressed pocket is of hydrophobic nature and when water displacement occurs by ligand binding to bury unfavorable contacts to the aqueous surrounding. Recently, Klebe *et al.* discussed

Table 5.6 Thermodynamic parameters for the binding of LacNAc, **9a**, **9f** and **9j** to hGal-1. Titration data fitted best to a model with one binding site per protein (monomer concentrations).

Ligand	K_a **[1/mM]**	ΔH **[kJ/mol]**	K_D **[μM]**	ΔS **[J/mol·K]**	ΔG **[kJ/mol]**
LacNAc	12.3 ± 1.9	-32.9 ± 1.1	81	-31.9	-23.4
9a	12.7 ± 2.9	-34.4 ± 1.6	78	-36.8	-23.4
9f	9.6 ± 1.9	-30.8 ± 1.4	104	-27.0	-22.8
9j	6.3 ± 1.4	-27.3 ± 1.8	158	-18.9	-21.7

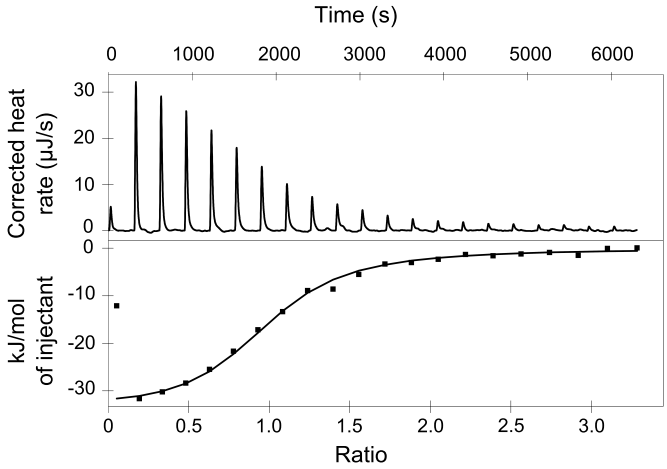

Fig. 5.26 ITC titration diagram of **9a** (10.0 mM) to hGal-1 (1.00 mM) (upper part) and integrated heat change per titration with best fitted curve (lower part).

impressively the role of water displacement, enthalpic and entropic effects in ligand binding to thermolysin.[322] By variation of hydrophic side chains in their peptido ligand they unraveled varying enthalpic and entropic contributions to ΔG upon binding to the hydrophobic pocket. In contrast to thermolysin, the pocket of hGal-1 to be adressed with substituted triazoles is of predominantly hydrophilic nature. Thus, solvation of these polar amino acids in the ligand-free state reduces the enthalpy for the system and may result in an enhanced internal mobility of the protein.[74,321] By coordinating an extended LacNAc derivative the protein becomes more rigid and forfeits spatial flexibility. Further, the ligand itself looses rotational and translational degrees of freedom upon binding well-defined as rigid body. The consequences are a loss in entropy but an enthalpic contribution due to specific and assigned interactions.

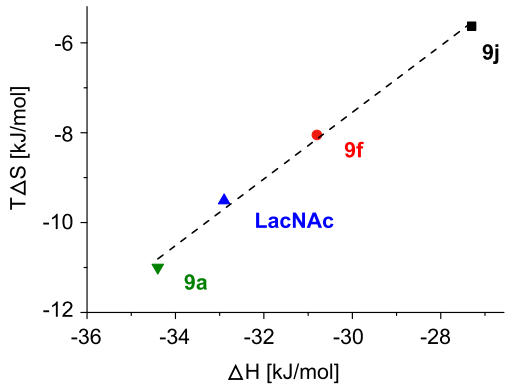

Fig. 5.27 Plot of TΔS vs ΔH for all hGal-1 disaccharide complexes at room temperature. The dashed line is a linear fit of the thermodynamic data and indicates the enthalpy-entropy compensation of hGal-1 binding.

5.1.6 Concluding Remarks and Future Directions

The presented strategy involving X-ray crystallography, organic synthesis, computational prediction and biophysical affinity assays (SPR, ITC) successfully provided first tailor-made hGal-1 ligands and permitted a detailed analysis of the respective protein-ligand interactions. X-ray crystallography of complexes between hGal-1 and the natural binding motif LacNAc and alkyne precursor **10** elucidated the individual binding modes and uniquely allowed to evaluate the influence of the aglyconic modification (Fig. 5.28 a and b). The integration of computational studies and synthesis of virtually predicted triazoles significantly lowered the number of molecules to be synthesized and this rational approach was clearly favored over randomly producing a library of click products. And indeed, all of the ten topranked and subsequently prepared triazoles bound with at least the same affinity as the natural ligand. Crystallographic data for three of those (**9a**, **9f** and **9i**) in complex with hGal-1 further proved that the 3-*O*-extensions address the targeted binding site adjacent to the carbohydrate recognition domain as anticipated (shown for **9a** in Fig. 5.28 c) and impressively demonstrated the power of the chosen strategy. A common feature in complexes with the click products is the water-mediated interaction between the triazole and Asn33, evidently a key determinant, while the respective substituents bind specifically to individual side chains of the targeted area. The affinity of the monovalent interaction between hGal-1 and best binding triazoles **9d**, **9f** and **9a** is still in the μM range and measured K_d values indicate rather low binding affinities similar to biologically occurring interactions. Nature strikingly parades how to cope with low affinities and modulates protein ligand communication by multivalent effects and high avidity bindings which compensates for a low affine monovalent interaction but essentially demands specific recognition. In this regard the introduced ligands bear the potential to dramatically increase the binding capacity by

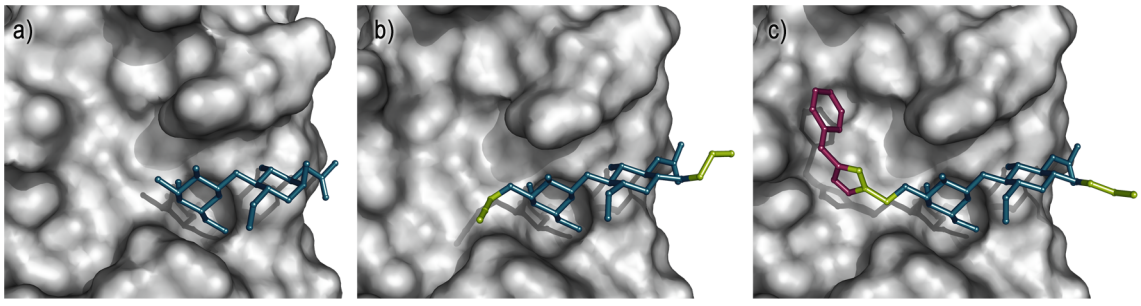

Fig. 5.28 Picture book story of the rational hGal-1 ligand design. a) The natural binding motif *N*-acetyllactosamine (blue) was b) equipped with reactive modifcations at crystallographic-inspired sites (green). c) Synergistic combination of X-ray crystallography, computational predictions and organic synthesis provided ligand **9a** for addressing the region adjacent to the CRD.

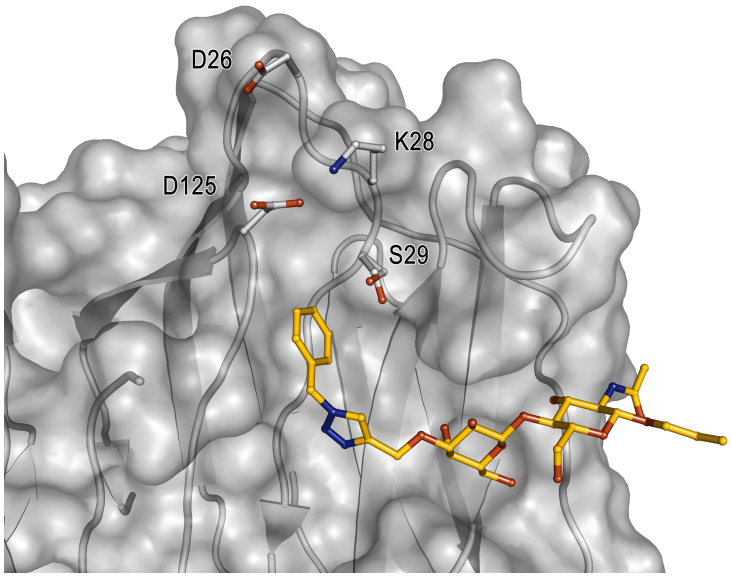

Fig. 5.29 Triazole **9a** bridges the space between the hydrophilic cleft of the CRD and polar to ionic amino acids in the northern part of the targeted protein area that are promising to be adressed in future optimization cycles.

presenting them as multivalent structures either covalently attached to a functionalized surface, dendrimer or nanoparticle via their 1-*O*-allyl group. It can be expected that the sterically demanding 3-*O*-extension significantly enhances specificity and presumably permits targeting discrimination between galectins and other physiologically relevant β-galactoside binding proteins. Within the scope of Project II this aspect is investigated on multivalent surfaces of microarrays and the potential of selected immobilized click products to detect galectin-1 tested in comparison to LacNAc and lactose.

Beside multivalency as approach to increase the targeting ability of click products the X-ray structure provides precious information to further optimize the ligands in a future project. **9a** in complex with hGal-1 shows that the benzyl-substituted triazole bridges the space between polar amino acids of the CRD and hydrophilic to ionic side chains in the northern part of the targeted area such as aspartic acid (D126, D26), serine (S29)and lysine (K28) (Fig. 5.29). Installation of either cationic (ammonium, guanidinium) or anionic (carboxy, sulfonate) phenyl substituents appear promising to establish ionic interactions with the aspartates or lysine, respectively, resulting in a strong enthalpic gain of the binding event. For future ligand design it should be taken into consideration that the binding of click products suffers from a negative entropic contribution as binding is accompanied by a loss of translational and rotational freedom. The incorporation of rigid units with a ionic terminus might account for this aspect and have a positive impact on both enthalpic and entropic properties.

5.2 Development of Diagnostic Tools for Tumor-associated hGal-1

Tumor diagnosis at an early stage of the disease greatly enhances the chances for a successful and lasting cancer cure. Consequently it is of immense importance to develop specific and highly sensitive diagnosis tools and detection screens to identify neoplastic tissue and to initiate the tumor-directed therapy.
This work contributed to this research field by developing an *in vitro* screening tool on microarrays basis. The surface of these microarrays was covalently functionalized with tailor-made ligands **9a**, **9f** and **9g** to visualize hGal-1 binding and to detect elevated protein concentrations of tumor patients in the future (section 5.2.1). Further, an *N*-acetyllactosamine-based precursor molecule for conversion with the PET isotope ^{18}F was implemented which may serve for tracking hGal-1 associated tumors *in vivo* through positron emission tomography in the future (section 5.2.2).

5.2.1 Carbohydrate Microarrays

Microarray experiments were performed together with Elisabeth Memmel and experimental realization will be published in detail in her Ph.D. thesis.[323] Briefly, used microarrays are composed of a glass slide with a hydrophilic polymer coating. The polymer layer is elongated with long and flexible spacer units that carry reactive NHS-ester groups at the polymer termini for covalent attachment of carbohydrates, proteins or other biomolecules via an amine functionality. The three-dimensional arrangement

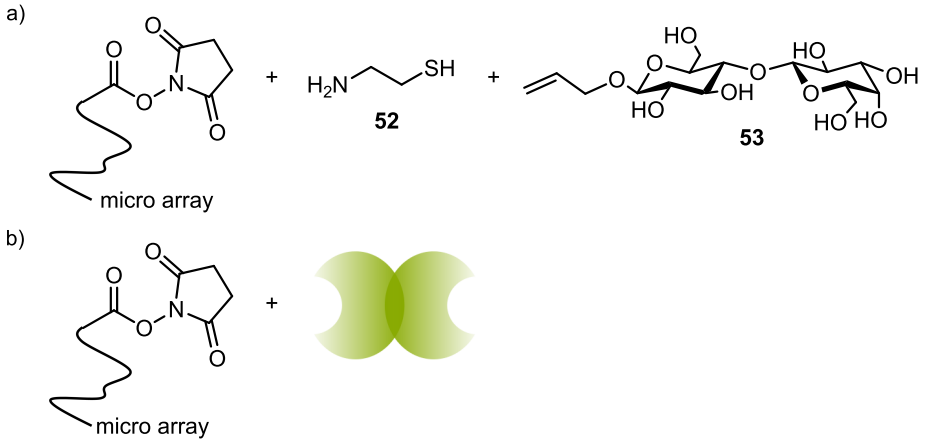

Fig. 5.30 Functionalization of the microarray surface with a) 1-*O*-allyl-modified disaccharides (1-*O*-allyl-β-D-lactose **53** is shown examplarily) in a two step reaction or b) galectins via a lysine side chain.

offers excellent accessibility of the binding partner to immobilized ligands in a quasi-liquid environment and the polymer is designed to exhibit very low intrinsic non-specific binding.[vii]

For carbohydrate immobilization microarrays were at first incubated with cysteamine (**52**) to functionalize the chip surface with thiol groups. Subsequently, carbohydrates were attached to the chip via their 1-*O*-allyl-modification in a photo reaction at 254 nm. Protein immobilization was realized by direct coupling of a lysine side chain to the NHS ester groups of the polymer (Fig. 5.30).

The binding event was either visualized by Alexa647 labeled hGal-1 or by a fluorophore labeled specific antibody.

Carbohydrate detection by Alexa647 labeled hGal-1

Carbohydrates **53**, **23**, **9a**, **9f** and **9g** were immobilized on the microarray and detected with Alexa647 labeled hGal-1 (labeling of hGal-1 was performed by Dr. Antonia Göhler)[324]. Fig. 5.31 a shows the result after incubation with the tagged hGal-1 for 3 h at 4 °C. Fig. 5.31 b presents a control experiment where the same disaccharides were incubated with the Alexa647 labeled β-galactoside binding plant lectin peanut agglutinin (PNA). hGal-1 binds selectively the click products and no signal is observed for lactose or LacNAc. The situation is vice versa for PNA that recognizes exclusively immobilized lactose. The array surface represents a multivalent network like the highly diverse and complex glycan structure of human cells and thus enables the investigation of the bivalent interaction with the homodimer hGal-1. In contrast, SPR affinity studies investigated the monovalent binding of immobilized hGal-1 on the gold chip and monomeric ligands in the

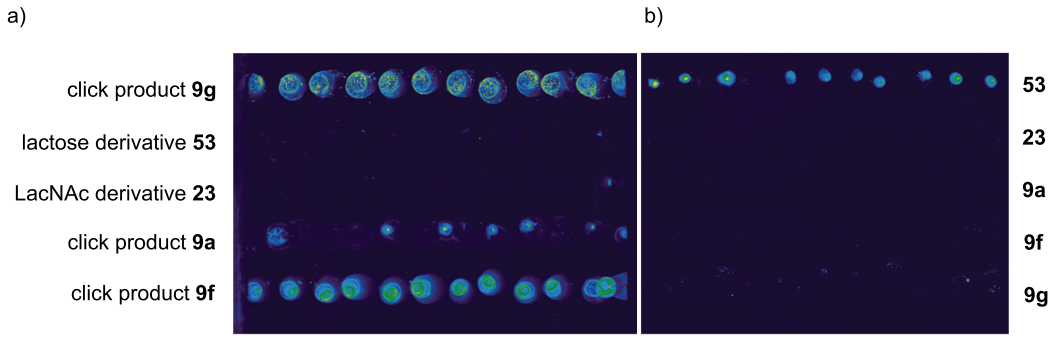

Fig. 5.31 Glyco chip with immobilized carbohydrates. a) Alexa647 labeled hGal-1 selectively recognizes disaccharides **9g**, **9a** and **9f** and no signal is observed for lactose or LacNAc). b) Alexa647 tagged PNA was incubated in a control experiment and exclusively binds lactose.

[vii] "Three-dimensional thin film coating- NEXTERION Slide H". *schott.com* SCHOTT AG. Web. 13 May 2014. <http://www.schott.com/nexterion/english/products/coated_slides/thin_film.html>

mobile phase. Evidently, the recognition process is affected by multivalent effects[325] and a discrimination between the natural binding motifs (lactose, LacNAc) and structurally optimized click products becomes possible. Riguera *et al*. discussed in detail how affinity is influenced by multivalent recognition processes by evaluating competitive studies in solution as well as SPR experiments of tetrameric Concanavalin A (ConA) and mannose dendrimers.[326]
The results of the microarray experiments show that small differences in affinity as determined by SPR can be potentiated by multivalent effects.

Carbohydrate detection by hGal-1, hGal-3 and labeled antibodies

It is known from literature that galectin-3, a further member of the galectin family, participates in various processes of tumor progression.[327] Recently, galectin-3 has been proposed as a promising cancer marker.[328–330] However, in contrast to galectin-1, the expression pattern of galectin-3 strongly depends on the cancer type and both up- and down-regulated protein production has been described for neoplastic tissue.[331,332] In this context it appeared extremely attractive to apply the microarray for detecting both tumor-associated galectins with novel triazole-based ligands via the highly conserved carbohydrate recognition domain (CRD). The subsequent incubation with labeled antibodies of different fluorophores should then allow a discrimination between hGal-1 and hGal-3 binding.
Galectin-3 belongs to chimeric galectins composed of a *C*-terminal CRD and an *N*-terminal collagen-like domain for self-aggregation into oligomeric structures (cf. section 2.2.1). To experimentally assess if the click products developed in Project I also target galectin-3 the protein was recombinantly expressed as full length protein (hGal-3FL,

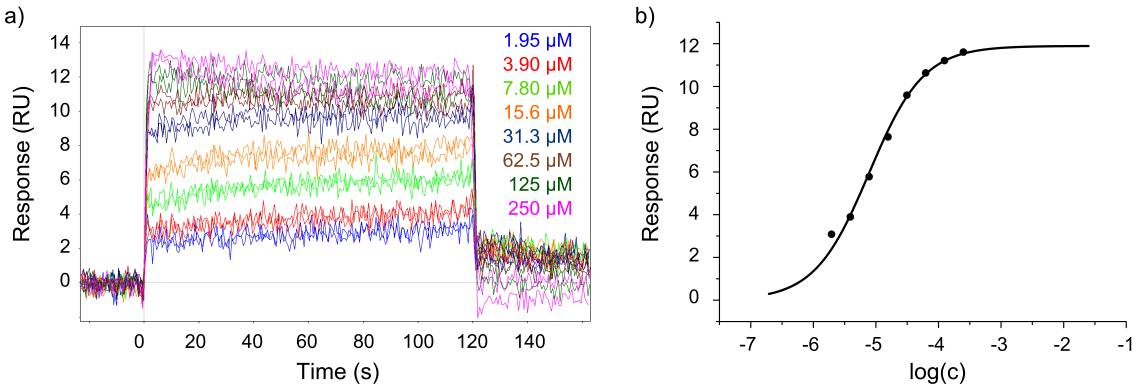

Fig. 5.32 SPR data for the interaction between hGal-3CRD and **9f**. a) Sensograms for concentrations from 1.95 μM to 250 μMb) Binding curve and sigmoidal fit.

Table 5.7 Results from SPR experiments with immobolized hGal-3 and various click products. a) K_d values were determined with runs in eight concentrations from $1.95 \cdot 10^{-6}$ to $2.50 \cdot 10^{-4}$ and measured in duplicates. [b] K_d values were estimated in a single-concentration screen (100 μM) and measured in duplicates. [c] K_d values were determined with runs in seven concentrations from $1.95 \cdot 10^{-6}$ to $1.25 \cdot 10^{-4}$ and measured in duplicates.

Ligand	hGal-3CRD K_d [μM]	hGal-3FL K_d [μM]
LacNAc	16[b]	26[b]
Alkyne **10**	29.3 ± 3.2[a]	34.2 ± 2.9[a]
9a	19.3 ± 1.1[a]	19.8 ± 2.0[a]
9b	25[b]	24[b]
9c	16.9 ± 1.37[a]	18.9 ± 2.0[a]
9d	41[b]	36[b]
9e	67[b]	62[b]
9f	7.77 ± 0.62[a]	8.29 ± 0.58[a]
9g	12.3 ± 0.81[c]	15.4 ± 0.6[c]
9h	37[b]	50[b]
9i	4.52 ± 0.32[a]	4.42 ± 0.35[a]
9j	28[b]	39[b]

250 amino acids) and as truncated version of the *C*-terminal CRD only (hGal-3CRD, 138 amino acids) and purified via lactosyl sepharose. Subsequent SPR experiments demonstrated that the triazoles **9** also comprise affine hGal-3 binders. Immobilization of the proteins on the SPR chip surface excluded multivalent effects and thus the affinity was expected to be similar for both proteins. Indeed, the binding activity of all measured ligands excellently agrees for hGal-3CRD and hGal-3FL (Table 5.7). Fig. 5.32 depicts experimental data of the SPR measure for hGal-3CRD and **9f**. Response units as a function of the concentration were fitted with a sigmoidal function to obtain a K_d value of 7.77 ± 0.62 μM.

As for hGal-1 an increase in affinity was observed for click products **9f** and **9i** while the affinity did not improve for **9a** and **9d** and resulted in the same range like the alkyne precursor **10**. Nilsson *et al.* synthesized a library of 3-*N*-extended LacNAc derivatives via amide bond formation and cocrystallized one of their ligands with hGal-3 (Fig. 5.33 a).[333] They found that Arg144 located adjacent to the CRD forms a cation-π interaction with the electron-deficient fluorinated benzyl substituent. In contrast, hGal-1 lacks an arginine in this position and strong interactions with the guanidinium group are

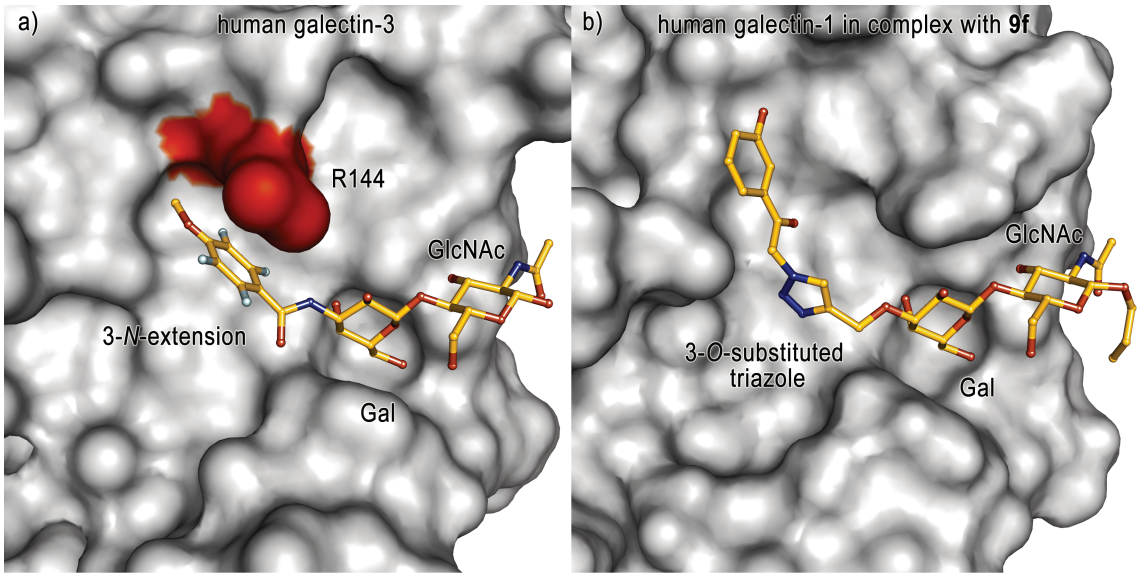

Fig. 5.33 X-ray data of hGal-3- and hGal-1-ligand complexes in comparison. a) hGal-3 in complex with a 3-*N*-extended LacNAc derivative by Nilsson *et al.*[333] Arg144 forms a cation-π interaction with the electron-deficient fluorinated benzyl substituent via the guanidinium group in the side chain. b) hGal-1 in complex with triazole **9f**. hGal-1 lacks an arginine adjacent to the CRD and strong interactions with the guanidinium group are not possible.

not possible (Fig. 5.33 b). Arg144 may also interact with the substituted triazoles of **9f** and **9i** and account for the observed affinities which are similar to the K_d values of the LacNAc based ligands by Nilsson *et al.*

With the successful confirmation of the binding between hGal-3 and click products a proof-of-concept experiment aimed at testing the specificity of fluorophore labeled antibodies. To this end the galectins were immobilized on the microarray surface and detected with commercially available polyclonal antibodies (Fig. 5.34 a and b). The hGal-1 antibody carried an Alexa647 tag and the hGal-3 antibody specific for the truncated as well as for the full length protein was equipped with an Alexa555 fluorophore to allow a two-colour detection. hGal-1, hGal-3CRD and hGal-3FL were spotted in concentrations of 1, 5, 10 and 25 μg/ml and incubated with antibody concentrations of 2, 10 and 100 μg/ml (1 h, 4 °C). Binding of hGal-3 was detected specifically with the minimal antibody concentration of 2 μg/ml and the varying protein concentrations during spotting are reflected in different signal intensities (Fig. 5.34 a). The fluorescence signal of the anti-hGal-3 antibody was observed upon excitation with λ_{exc} = 532 nm. For specific detection of hGal-1 binding an antibody concentration of 100 μg/ml was required to obtain adequate signal intensities at λ_{exc} = 635 nm (Fig. 5.34 b).
Next, carbohydrates were immobilized on a microarray and incubated with 100 μg/ml

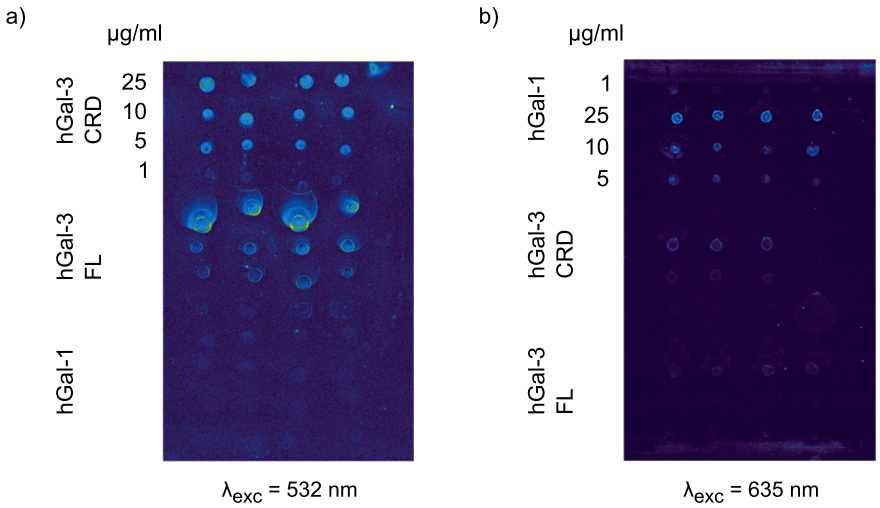

Fig. 5.34 Glyco chip with covalently linked hGal-1, hGal-3CRD and hGal-3FL. The galectins were spotted in concentrations from 25 to 1 μg/ml in the same order for three proteins (for reasons of comprehensibility only the topmost is marked). a) The glycochip was incubated with 2 μg/ml of the anti-hGal-3 antibody and binding visualized at λ_{exc} = 532 nm. b) The glycochip was incubated with 100 μg/ml of the anti-hGal-1 antibody and binding visualized at λ_{exc} = 635 nm.

hGal-1 and hGal-3CRD for 3 h at 4 °C, respectively. The hGal-3CRD protein was used in the study as this construct yielded a better spot morphology in the previous experiment. Ongoing experiments also include hGal-3FL to exploit multivalent effects of the pentameric structure. Following treatment with the specific antibodies (12 h, 4 °C) allowed the visualization of the binding event. Both, hGal-1 and hGal-3CRD recognized triazole-based ligands **9f** and **9g** and resulted in comparable signal intensities (Fig. 5.35 a and b). However, selective detection of hGal-1 or hGal-3CRD is a prerequisite to distuingish hGal-1- from hGal-3 associated tumors in a diagnostic application and prompted further studies. Hereby, immobilized carbohydrates were incubated with a 1:1 mixture of both galectins (each 100 μg/ml) to mimick their physiological coexistence and treated subsequently with a 1:1 mixture of the antibodies (each 100 μg/ml). Due to different excitation wavelengths of the antibody fluorophores the hGal-3CRD binding became visible at λ_{exc} = 532 nm and a resulting fluorescence detection at λ_{fl} = 575 $\pm$ 17.5 nm, while the hGal-1 interactions was detected at λ_{exc} = 635 nm with fluorescence emission at λ_{fl} = 670 $\pm$ 20 nm (Fig. 5.35 c).

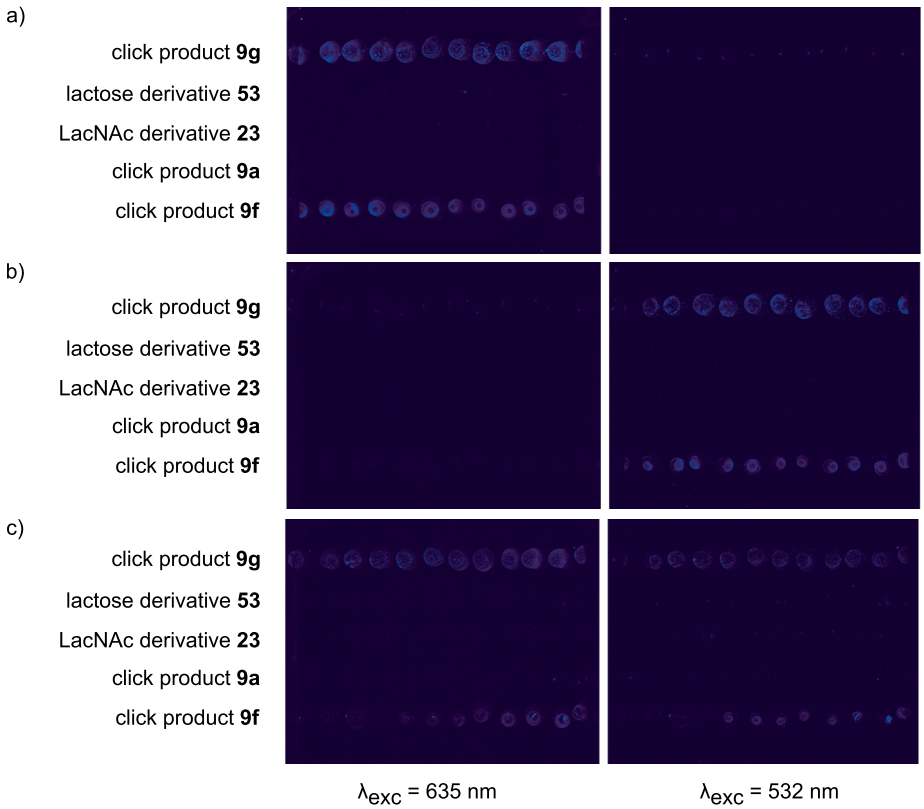

Fig. 5.35 a) Incubation with hGal-1 (100 μg/ml) and subsequent treatment with the hGal-1 antibody (100 μg/ml). Fluorescence signals at λ_{fl} = 670 $\pm$ 20 nm were observed for **9g** and **9f** after excitation with λ_{exc} = 635 nm but not after excitation with λ_{exc} = 532 nm. b) Incubation with hGal-3CRD (100 μg/ml) and subsequent treatment with the hGal-3 antibody (100 μg/ml). Fluorescence signals at λ_{fl} = 532 $\pm$ 17.5 nm were observed for **9g** and **9f**. c) Incubation with a 1:1 mixture of both galectins (each 100 μg/ml) and subsequent treatment with a 1:1 mixture of both antibodies (each 100 μg/ml). The binding of hGal-1 was visualized at λ_{fl} = 670$\pm$20 nm while the hGal-3 antibody emitted at λ_{fl} = 532$\pm$17.5 nm.

Conclusion

Results of the microarray experiments demonstrated that the lectins, either hGal-1 or hGal-3, can be detected selectively even in the presence of the other protein. This finding is of extreme importance as clinical studies of Saussez *et al.* confirmed that "the determination of the levels of circulating galectin-1 and -3 in HNSCC patients could be used to monitor tumor progression and/or responses to therapy".[334] The authors reported about a median galectin-3 level of 3.2 ng/ml in HNSCC (head and neck squamous cell carcinoma) patients and a value of 2.39 ng/ml for the healthy control group.[334] For galectin-1 they found a median level of 6.2 ng/ml in cancer patients and 5 ng/ml in healthy individuals. Further, levels of both galectins significantly decreased

after therapeutic treatment. In a different study levels of galectin-3 varied from a median value of 320 ng/ml in sera of patients with metastatic gastrointestinal cancer to 40 ng/ml for nonmetastatic breast cancer (62 ng/mg for healthy individuals).[335] Laurent *et al.* determined a significantly lower median galectin-3 level of 2.76 ng/ml in sera of patients with benign thyroid lesions and a comparable value for healthy individuals (2.22 ng/ml).[336] The same study resulted in a median galectin-1 value of 17.9 ng/ml for sera of patients with benign thyroid lesions and yielded a substantially lower value of 4.7 ng/ml for healthy controls. Elevated levels of both galectin-1 (277.7 ng/ml vs 236.7 ng/ml) and galectin-3 (8.31 ng/ml vs. 7.16 ng/ml) were also found in colorectal carcinoma.[330] The authors further observed a decrease of galectin-1 levels after successful tumor surgery.

Ongoing experiments with Prof. Dr. Jörg Wischhusen (Universitätsklinikum Würzburg) investigate the functionalized microarrays regarding their potential to detect elevated galectin concentrations of tumor cell lines and in blood sera of cancer patients. Current microarray experiments further address the aspect of sensitive detection of these rather low protein concentrations and probe signal intensities of galectin-abundant samples compared to control samples with normal galectin levels. Thus, functionalized microarrays with immobilized ligands deriving from this thesis may find a clinical application for selective diagnosis of hGal-1 and hGal-3 associated tumors in the future.

5.2.2 Synthesis and Evaluation of hGal-1 Ligands for PET

The PET technology permits to track malignant tissue due to physiological alterations such as increased metabolism rates or upregulated protein expression. However, the successful performance of a diagnostic screen essentially requires highly specific and

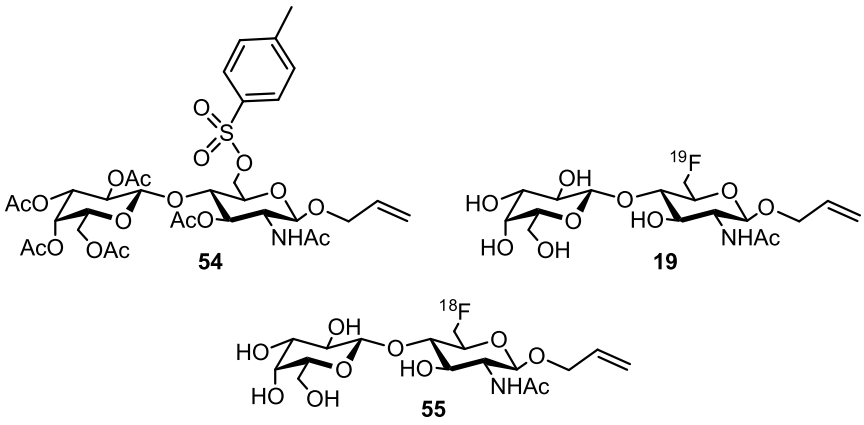

Fig. 5.36 PET precursor **54** for a bimolecular nucleophilic substitution of either $^{19}F^-$ or $^{18}F^-$ followed by basic deprotection to yield reference compound **19** and radiotracer **55**, respectively.

physiologically tolerated radiotracers. This project addressed this demand by developing a synthesis for a LacNAc-based and fluorine labeled PET tracer to detect galectin-associated tumors in the future. The position for functionalization was inspired by X-ray crystallography of hGal-1 in complex with LacNAc (Fig. 5.3). The structure proposes *O*-6 as this hydroxyl group is not involved in interactions with the protein and it is assumable that an OH/F exchange would not significantly influence the steric demand of the carbohydrate scaffold. The route to synthetic LacNAc derivatives considered the modification of *O*-6 at a late stage of the synthesis (Scheme 5.8), which is an essential criterion due to the half-life period of ^{18}F with $t_{1/2}$ = 110 min, and aimed at introducing the fluorine by a bimolecular nucleophilic substitution (S_N2) at an electrophilic *C*-6. Taking into consideration that the synthesis involved the preparation of an activated PET precursor and the ^{19}F reference compound while the ^{18}F radiotracer is formed locally before *in vivo* injection by Dr. Reik Löser, Helmholtz-Zentrum Dresden-Rossendorf, it was important to implement molecules that are stable for transport and storable for a certain period. In this context, triflates are highly reactive electrophiles but do not fulfill the latter requirement satisfactorily whereas tosylates are less reactive, in return they offer a better flexibility between activation of the ligand and conversion into the radiotracer. Thus, precursor of choice was tosylate **54** to yield ^{19}F reference **19** and radio tracer **55** (Fig. 5.36). For preparation of **55** [^{18}F]fluoride anions are produced in a cyclotron through proton irradiation of [^{18}O]H_2O leading to aqueous [^{18}F]HF in the ^{18}O(p,n)^{18}F nuclear reaction.[337] Aqueous [^{18}F]fluoric acid is neutralized by adsorption on an anion-exchange cartridge and converted to [^{18}F]KF by elution with Kryptofix 222 and K_2CO_3 in H_2O/CH_3CN followed by azeotropic distillation. [^{18}F]fluorine obtained by this procedure is "no-carrier-added" (NCA) which implies that the [^{18}F]F^- exhibits a high specific radioactivity.[215]

Synthesis of PET precursor 54 and ^{19}F-reference compound 19

Semi-deprotected disaccharide **40** permitted regioselective tosylation of the envisioned position *C*-6 and was realized in quantitative yield with an excess of *p*TsCl and pyridine acting as solvent as well as nucleophilic catalyst (Scheme 5.15). Following fluorination with the weak nucleophile F^- was performed according to the protocol of Chi *et al.*[338] The authors demonstrated that the use of sterically demanding protic *tert*-alcohols like *tert*-BuOH or *tert*-amylalcohol greatly increases the nucleophilicity of the fluoride while shorter linear alcohols lead to solvation of the anion, thereby drastically reducing the reactivity of the anion. CsF was preferred over its homolog KF as the latter reacts strongly basic in the presence of traces of H_2O and requires the use of a cryptand for complexing the cation and generating the naked anion. In contrast, the cesium cation is characterized by a large polarizability. Thus, the bond character is less ionic and the fluoride reactive

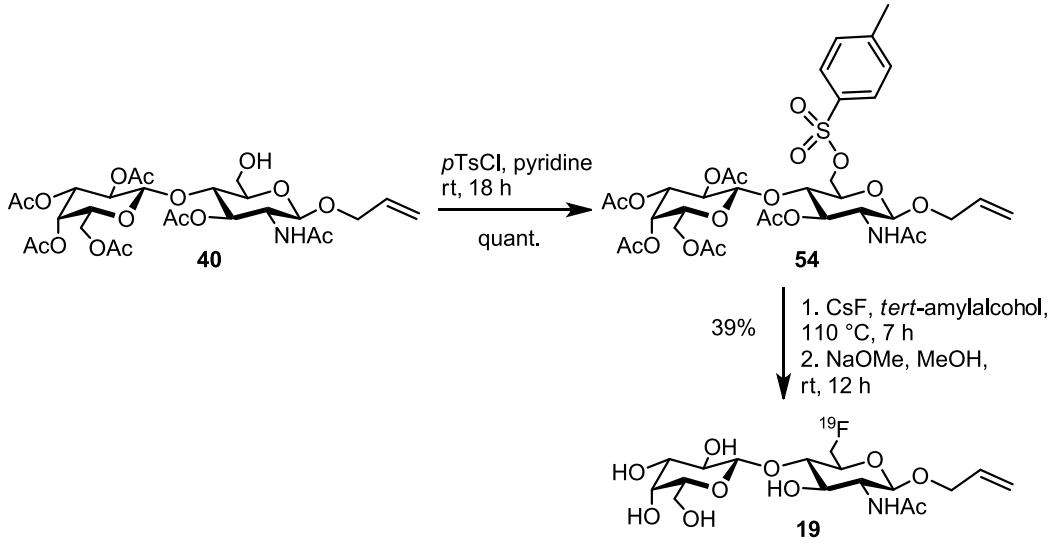

Scheme 5.15 Synthesis of PET reference compound **19** via tosylate **54**.

even in the absence of a cryptand. Still, the reaction yields were rather poor and product isolation by column chromatography impeded by unreacted starting material eluting at an almost identic R_f value.

Discussion of spectroscopic data

^{1}H and ^{13}C NMR spectroscopic data of the carbohydrate scaffold of **54**, peracetylated ^{19}F-compound **62** and **19** are similar to those of **40** and the following discussion will focus on striking differences provoked by the functional groups.

Protons of the tosyl group in **54** resonate in the ^{1}H NMR spectrum in two multiplets between δ = 7.81-7.79 ppm and δ = 7.38-7.36 ppm. For the *p*-positioned methyl group appears a singlet at δ = 2.46 ppm. Signals for protons *H*-6a and *H*-6b are low-field shifted compared to **40** due to the altered chemical environment and appear as a doublet of doublet at δ = 4.45 ppm and δ = 4.17 ppm, respectively. The ^{13}C NMR spectrum reflects the tosyl substituent with signals for aromatic carbons at δ = 145.42, 132.80, 130.10 and 128.17 ppm. The latter two signals were assigned to meta- and ortho-located carbons. The methyl group resonates high field shifted at δ = 21.81 ppm. Similar to the protons *H*-6 the carbon *C*-6 is shifted to low field in comparison to the free alcohol **54** and resonates at δ = 67.91 ppm.

Conversion of tosylate **54** to fluoride **62** and **19** can be traced unambiguously with NMR spectroscopy. The ^{1}H NMR spectrum no longer comprises signals for aromatic protons instead protons *H*-6a and *H*-6b resonate clearly low field shifted between δ = 4.83-4.66 ppm in a rather complicated multiplet including a large geminal ^{1}H-^{19}F, typically ^2J > 40 Hz, a geminal ^{1}H-^{1}H and a smaller vicinal coupling, respectively. The signal

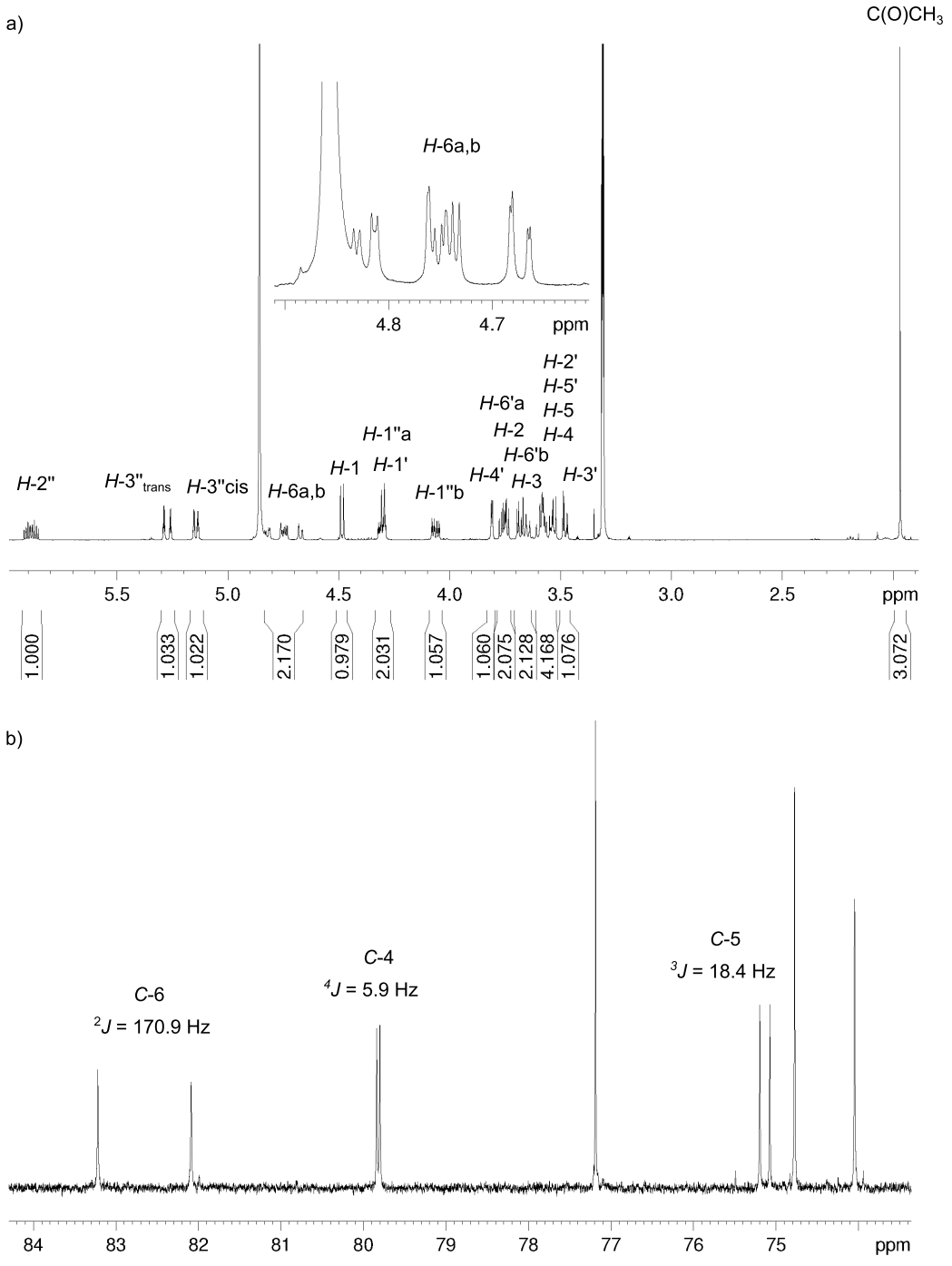

Fig. 5.37 a) ^{1}H-NMR spectrum of reference compound **19**. The cutout depicts signals for *H*-6 as a result of geminal and vicinal couplings with ^{19}F and *H*-5. b) Cutout of the ^{13}C-NMR spectrum of reference compound **19** is shown. Selected signals are assigned with the respective ^{19}F, ^{13}C couplings.

for proton *H*-5 is superposed by *H*-4, *H*-5' and *H*-2, all resonating in a multiplet between δ = 3.61-3.52 ppm, and thus, the vicinal coupling with fluorine, typically around 25 Hz, is not to determine (Fig. 5.37 a). In the ^{13}C NMR spectrum *C*-6 resonates significantly low field shifted (δ = 82.66 ppm) compared to **54** and splits into a doublet with a geminal coupling of ^{2}J = 170.9 Hz. Owing to the size of the ^{13}C-^{19}F couplings further the vicinal coupling of *C*-5 with fluorine of ^{3}J = 18.4 Hz and the long range coupling of *C*-4 with fluorine of ^{4}J = 5.9 Hz was ascertained to confirm the identity of **19** (Fig. 5.37 b). ESI mass spectrometry provided a basis peak of m/z = 448.15861 corresponding to the molecule mass and sodium and a second minor peak of m/z = 873.32814 for the double molecule mass and sodium.

Cocrystallization of hGal-1 and ^{19}F-reference compound 19

The introduction of a radiotracer for targeting and tracking a specific pathological biochemical process certainly demands for a detailed comprehension of the underlying binding event and prompted further studies for elucidating the interaction between hGal-1 and **19**. It is conceivable that the fluorine hinders the natural interactions due to electronic effects or constrains the carbohydrate in an alterated geometric orientation. Crystallographic experiments were performed to adress this issue and structure determination resulted in a complex of the protein with the ^{19}F reference compound **19** at a resolution of 1.35 Å. The electron density map contoured at a

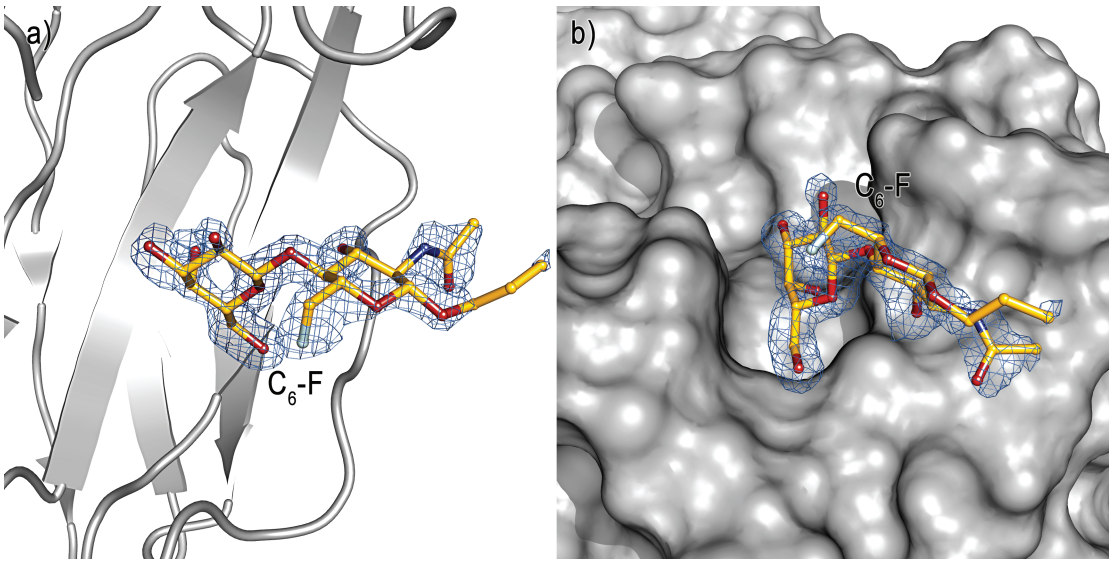

Fig. 5.38 Complex of hGal-1 and **19**. Electron density at a resolution of 1.35 Å is contoured at a level of 0.8 σ. The fluorine substituted disaccharide occupies the common binding mode and the halogen faces out of the CRD.

level of 0.8 σ unambiguously located the carbohydrate ligand within the CRD and demonstrates a conserved binding mode (Fig. 5.38). The fluorine substituent faces out of the binding pocket and neither disturbes established interactions nor forms novel. Indeed, the orientation of the halogen shows a high agreement with the substituted hydroxyl group of LacNAc and **23**. This finding substantiates the great power of rationally designing ligands for various purposes in a structure-based approach and promises that *C*-6-fluorinated *N*-acetyllactosamine-based ligands may find a clinical application for diagnosis of hGal-1 associated tumors in the future. *In vivo* studies are currently in progress in cooperation with Dr. R. Löser, Helmholtz-Zentrum Dresden-Rossendorf, to test physiological stability, distribution and accumulation.

5.3 Investigation of hGal-1 Communication Pathways on Cell Surfaces

High resolution fluorescence microscopy of hGal-1 networking with membrane-anchored glycoproteins of Neuroblastoma (SK-N-MC) cells was performed in cooperation with Prof. Dr. Markus Sauer, Department of Biotechnology and Biophysics, University of Würzburg. Experiments aimed at getting insights into hGal-1 mediated communication pathways responsible for various cell signaling processes. One approach involved the incubation of Neuroblastoma cells with different concentrations of Alexa647 labeled galectin-1 and analysis with the *d*STORM method (section 5.3.1). A second approach intends to compare those results with glycoengineered cell surfaces presenting covalently linked binding partner lactose. The second project is still in process and first results are presented in section 5.3.2.

5.3.1 Spatial Organization of hGal-1 on Neuroblastoma Cell Surfaces

*d*STORM experiments and following cluster analyses were performed by Dr. Antonia Göhler and experimental as well as analytic details are published in her Ph.D. thesis.[324] Incubation of Neuroblastoma cells with hGal-1 concentrations between 1 μM and 10 nM and investigation of the spatial organization by dSTORM provided high resolution images of the cell surface (Fig. 5.39 b-d) and give a far more precise idea than the respective far field fluorescence images (Fig. 5.39 a).[339] Resulting localization patterns include single localizations of an average diameter of approximately 25 nm corresponding to a single hGal-1 receptor interaction and larger cluster formations up to diameters of few hundreds nm (Fig. 5.39 d). The mean cluster diameter was determined to approximately 78 nm and is similar to the value of 76$\pm$42 nm for the C-type lectin DC-SIGN[340]. Interestingly,

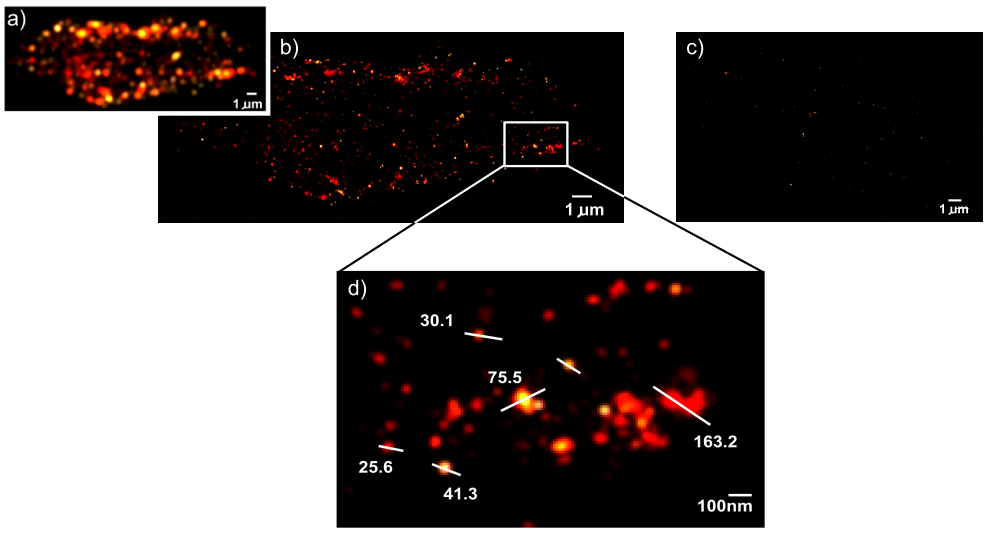

Fig. 5.39 Surface of Neuroblastoma cell incubated with Alexa647 labeled hGal-1 (1 μM). a) Far field fluorescence image. b) Reconstructed high resolution image (15000 single images, integration time 20 ms, power density 1-5 kW/cm^2 at 641 nm). c) *d*STORM image resulting from prior incubation of hGal-1 (1 μM) with 50 mM lactose. d) Magnified part of b) that shows single localizations and clusters of different size.

the average cluster diameter was constant for all hGal-1 concentration while the number of total localizations decreased with the protein concentration. Further, the ratio of single localizations to clustered localizations depended on the concentration of hGal-1. This finding indicates that hGal-1 induces cluster formation on cell surfaces and that a certain amount of the protein is necessary for this process. However, homodimeric hGal-1 itself is only capable of linking two glycoproteins and consequently, the observed results further

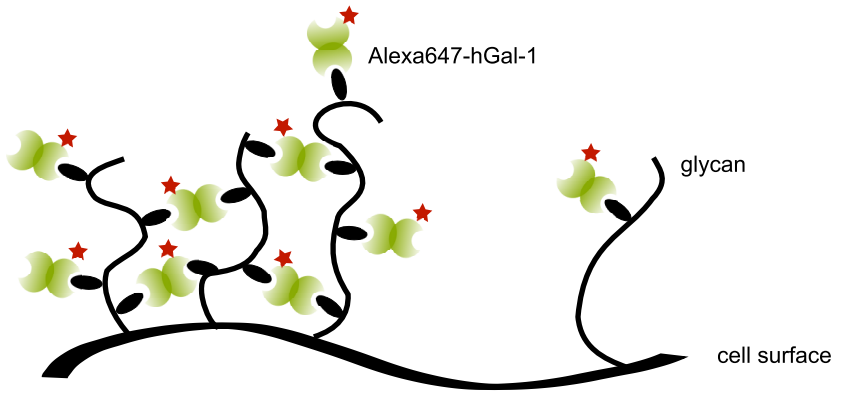

Fig. 5.40 Proposed mechanism of hGal-1 associated cluster formation on Neuroblastoma cell surfaces.

imply that those glycoproteins present more than one binding motif (Fig. 5.40). These considerations were corrobarated in a further experiment. The addition of 50 mM lactose to a protein sample of 1 μM hGal-1 prior to incubation on Neuroblastoma cells led to a decrease of the number of total localizations and the percentage arranged in clusters was significantly lower (Fig. 5.39 c). The outcome conforms with the localizations caused by a hGal-1 concentration of 10 nM and can be explained with saturated CRDs due to lactose binding. Recently, Bertozzi *et al.* demonstrated hGal-1-induced networking on surfaces of cells that are deficient in β-galactosides.[341] The authors introduced artificial lactose-bearing lipids into the cell membrane and monitored the hGal-1 interactions by the FRET technique. The *d*STORM experiments might provide for the first time a proof for hGal-1 induced clustering on human cells with high resolution.

5.3.2 Spatial Organization of hGal-1 on Glycoengineered Cells

High-resolution imaging of metabolically glycoengineered Neuroblastoma cells have gained valuable insights into the number and spatial distribution of glycan modifications.[342] In the experimental realization Neuroblastoma cells were grown in medium supplemented with an azide-tagged *N*-acetylglucosamine derivative[viii] and conversion with alkyne-functionalized Alexa647 proved a successful incorporation of the synthetic monosaccharide into membrane-anchored glycoproteins.
Ongoing experiments intend to covalently attach 1-*O*-propargyl-β-D-lactose, the binding motif of hGal-1, to azide-bearing cell surfaces and to incubate them with Alexa647 labeled protein. It is of great interest to study interactions of cells with an alternated glycoprotein cloak. First, the experiments will provide further insights into hGal-1's role in cluster formation and second, lactose-decorated cells will imitate receptors that are involved in hGal-1-mediated physiological interactions. It is well known that hGal-1 induces apoptosis in T-helper cells upon binding to surface glyco and confers immunity to the tumor cells.[138] It is conceivable that a tumor cell can be reprogrammed by a tailor-made carbohydrate cloak and to be opposed with its own weapon hGal-1. A confirmation of this idea would have major impacts on any kind of lectin-mediated pathological processes and only recently, Kim *et al.* published a way to translate metabolic glycoengineering into an *in vivo* application.[343] The authors showed that an injection of tetraacetylated *N*-azidoacetyl-D-mannosamine (Ac_4ManNAz) loaded nanoparticles to tumor-bearing mice led to an accumulation of the particles within the tumor tissue through the enhanced permeation and retention (EPR) effect and thus enabled cell surface modification of tumor cells predominantly. Nanoparticles with surface modifications of both a cyclic alkyne and a photosentisizer were intravenously administered afterwards and attached to the engioneered tumor cells through strain-

[viii] The *N*-acetylglucosamine derivative was synthesized and provided by E. Memmel.

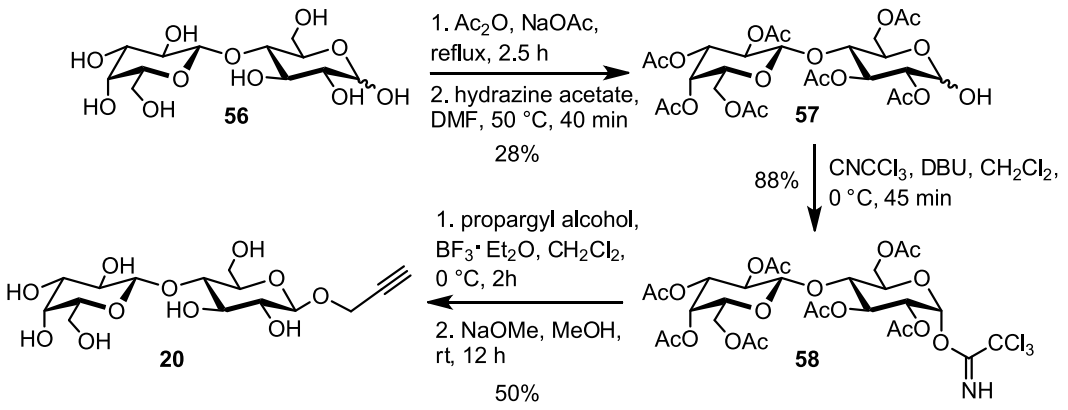

Scheme 5.16 Five step synthesis to alkyne modified lactose for covalent attachment of glyco engineered Neuroblastoma cells.

promoted click chemistry. This strategy greatly enhanced the therapeutic efficacy of laser irradiation for destructing tumors in infected A549 mice compared to the phototherapy without prior nanoparticle treatment.[343]

Initial experiments of this project included the synthesis of the lactose derivative. The propargyl functionality was introduced at *C*-1 of lactose in a five step (Scheme 5.16) synthesis as previously described by Tietze *et al.*[344] Synthetic manipulations included peracetylation of the disaccharide, regioselective deprotection of *C*-1 and activation with $CNCCl_3$, glycosylation of the glycosyl donor with propargyl alcohol as acceptor molecule and removal of the acetate protecting groups.

^{1}H,^{13}C NMR spectroscopy and mass spectrometry confirmed the identity of the alkyne modified lactose **20**. Diastereotopic protons *H*-1"a and *H*-1"b resonate at δ = 4.43 and 4.39 ppm in the ^{1}H NMR spectrum and split into a characteristic doublet of doublet, respectively, with a large geminal coupling of ^2J = 15.6 Hz and a small ^4J of 2.4 Hz for the long range coupling with the alkynyl proton *H*-3". The latter resonates high field shifted at δ = 2.86 Hz and the signal appears as a triplet-like doublet of doublet. Striking signals for the carbohydrate scaffold are two doublets at δ = 4.49 and 4.36 ppm for both anomeric protons that split with a large vicinal coupling of approximately ^3J = 7.7 Hz, indicative for β-configurations of the glycosidic bonds. Further carbohydrate protons resonate between δ = 3.92 and 3.25 ppm with the characteristic splitting patterns. The ^{13}C NMR spectrum gives rise to signals at low field at δ = 105.07 and 101.91 ppm for the anomeric carbons while further carbons of the carbohydrate scaffold resonate between δ = 77.07 and 61.81 ppm. Alkynyl carbons were assigned to signals at δ = 79.94 and 76.30 ppm and the methylene carbon *C*-1" resonates slightly high field shifted at δ = 56.67 ppm.

Further, an SPR affinity screen with immobilized hGal-1 was performed to evaluate the influence of the 1-*O*-propargyl extension on the binding affinity. Lactose was measured

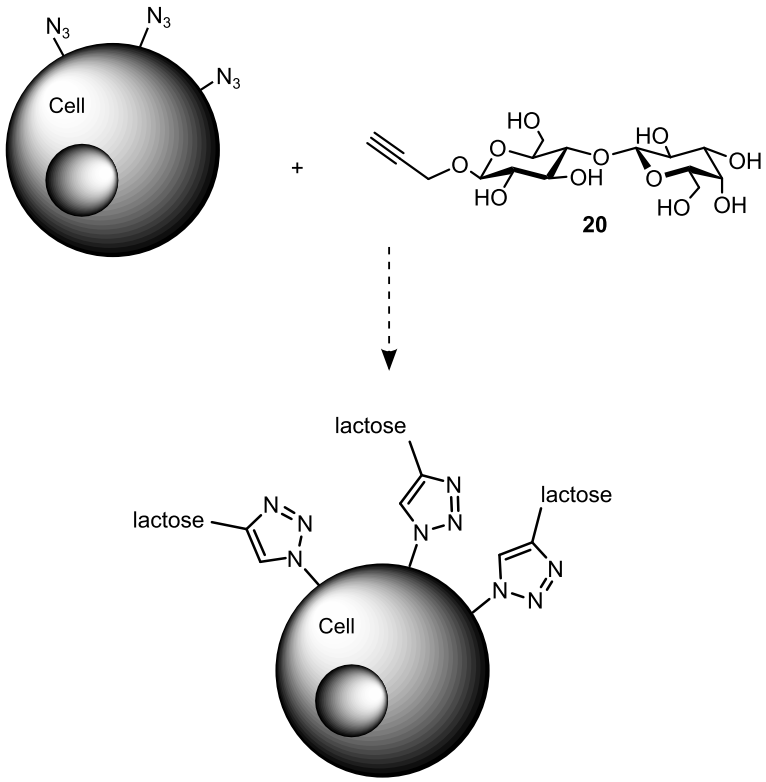

Scheme 5.17 Functionalization of metabolically glyconengineered cell surfaces with lactose is currently under investigation.

as reference compound. For alkyne-modified lactose **20** a K_d value of 274 $\pm$ 74 μM was determined and a similar value of 269 $\pm$ 41 μM was found for lactose. The K_d of lactose is in good agreement with a previous affinity determination.[74] Obviously, the 1-*O*-propargyl-modification does not significantly influence the interaction with hGal-1 as already observed for the LacNAc derivatives.

Functional lactose **20** is currently under investigation in *d*STORM experiments by Sebastian Letschert (Scheme 5.17).

Chapter 6

Summary

Cancer is one of the predominant health threats of our generation and claims millions of victims each year. Despite indisputable progress in cancer research over the past decades there is still a huge lack of therapies without adverse side effects and most of the physiological processes in cancer biology remain to be elucidated.

In this context, galectin-1 has evolved to a key player in tumor progression during the last years and is highly overexpressed by numerous cancer types. Previously conducted studies confirmed that the β-galactoside-binding protein mediates various molecular interactions associated with tumor growth, spread and survival. Upon interaction with carbohydrate-based binding epitopes of glycan structures on human cell surfaces galectin-1 induces proliferative, angiogenetic and migratory signals and modulates negative T cell regulation which essentially helps the tumor to evade the immune response. These findings attributed galectin-1 a pivotal role in tumor physiology and strongly suggest the protein as target for diagnostic and therapeutic applications.

The crystallographic data of human galectin-1 in complex with lactose[74] motivated a strategy for designing tailor-made galectin-1 ligands by functionalizing selected hydroxyl groups that are not involved in the sophisticated interplay between the disaccharide and the protein. Synthetic modifications intended to introduce chemical groups i) to

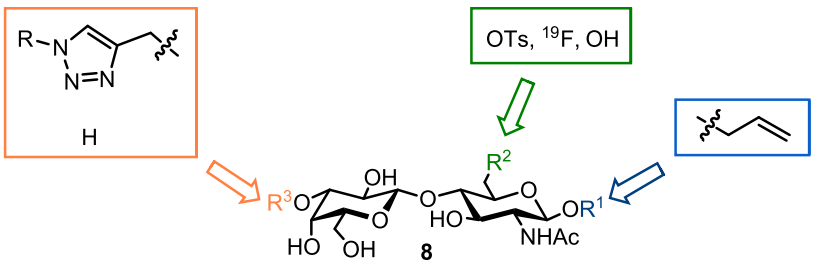

Fig. 6.1 Proposed LacNAc derivative **8**. Indicated synthetic modifications were inspired by the crystallographic data[74] of hGal-1 in complex with lactose.

address a potential binding site adjacent to the carbohydrate recognition domain (CRD) with extended hGal-1-ligand interactions (R^3), ii) to implement a tracer isotope (R^2) for diagnostic detection and iii) to install a linker unit (R^1) for immobilization on microarrays or drug loading (Fig. 6.1). Substitution of the hydroxyl group at *C*-2 with an *N*-acetyl moiety was integrated within the synthetic approach to exploit the inherently higher natural affinity of hGal-1 towards *N*-acetyllactosamine (LacNAc) versus lactose.
These preliminary structural analyses shaped the work of the three presented galectin-1 projects and guided the experimental performance from prediction to future drug candidates and diagnostic tools.

Project I: Rational ligand design for hGal-1 drug candidates and diagnostic tools

Initial experiments included the recombinant expression of homodimeric hGal-1 by *E. coli*. Following cocrystallization of hGal-1 and LacNAc in cooperation with Dr. Clemens Grimm provided a complex of high resolution (1.40 Å) and proved unambiguously the transferability of structural inspirations drawn from the complex hGal-1/lactose[74] (Fig. 6.2). Subsequently, precursor molecules **10** and **23** were synthesized in a convergent multi-step reaction depicted in Scheme 6.1. The allyl unit at *O*-1 (blue arrow) and the optional alkyne group at *O*-3' (orange arrow) were introduced at an

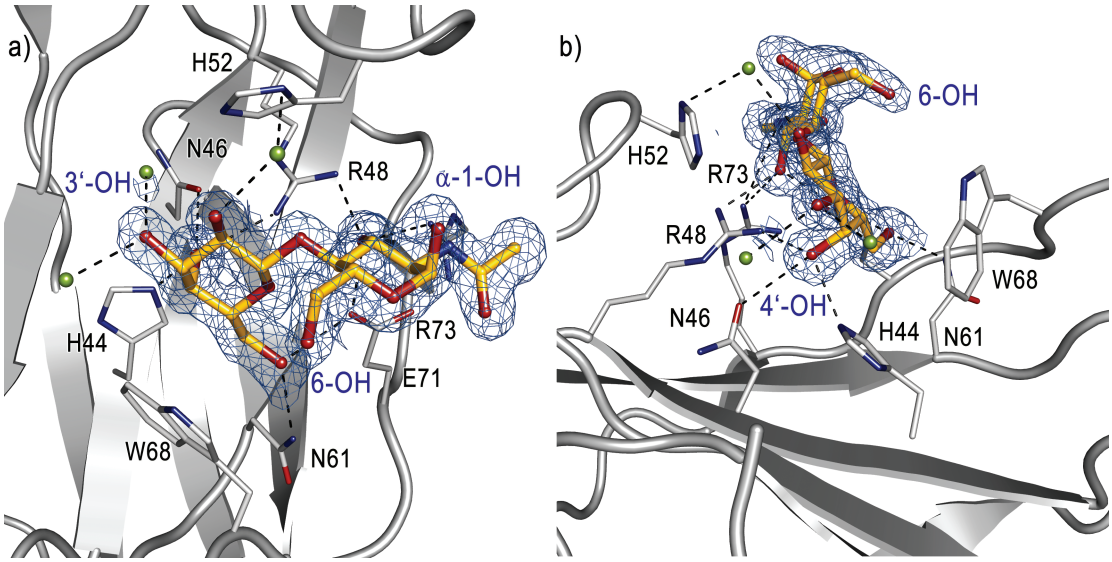

Fig. 6.2 Complex of hGal-1 and LacNAc. Electron density is presented as $2F_{obs}$-F_{calc} map and contoured to a σ-level of 1.0. a) The galactosyl moiety is involved in various interactions and is essential for the recognition process while the contribution of the *N*-acetylglucosamine unit is less pronounced. 3'-OH, 6-OH and 1-OH groups are not interacting with the protein and are suited for modifications. b) Different perspective to highlight the binding cleft of hGal-1 that is filled by the galactosyl moiety.

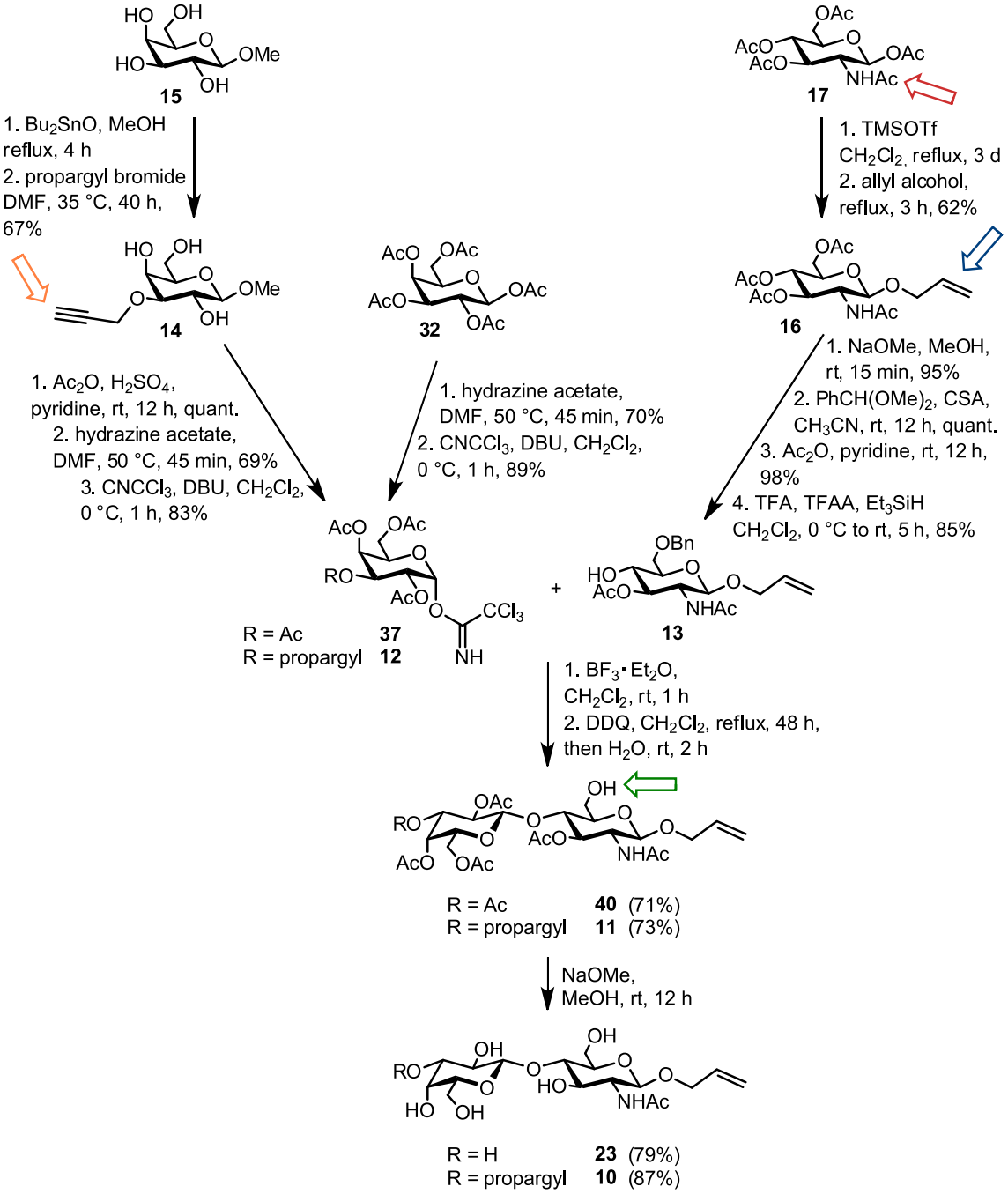

Scheme 6.1 Synthetic route to precursor molecules **10** and **23**.

early stage of the synthesis and chosen according to their reaction profile that allows conversion of the resulting disaccharides later on with organic azides in the popular Huisgen-Meldal-Sharpless click reaction or with thiols in a photochemical cycloaddition, respectively. The synthetic route comprised as key steps the regioselective protection to *N*-acetylglucosamine derivative **13** and activation of the galactosyl donors **12** and **37** with

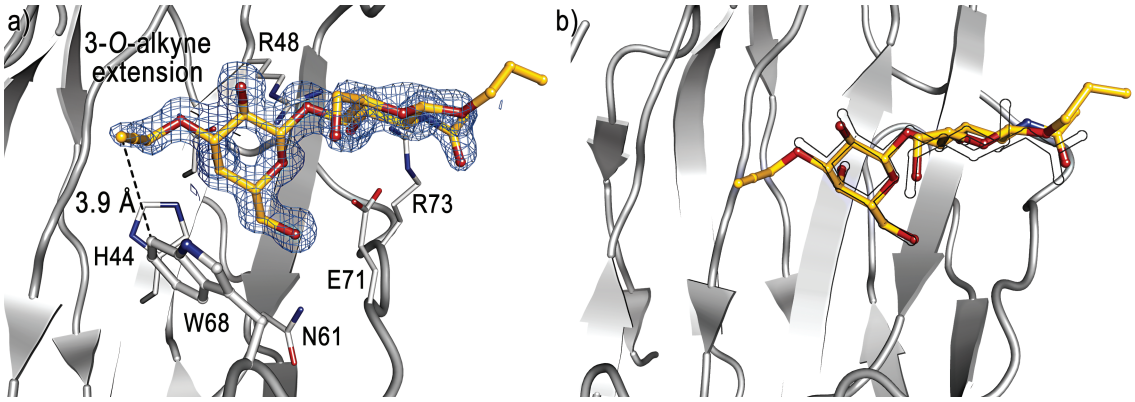

Fig. 6.3 a) Complex of hGal-1 and alkyne precursor **10**. Electron density is presented as $2F_{obs}$-F_{calc} map and contoured to a σ-level of 1.0. b) Superposition of **10** (yellow) and the natural disaccharide LacNAc (black line) in complex with hGal-1 shows a conserved binding mode of the carbohydrate scaffolds.

$CNCCl_3$. Protecting group manipulations carefully considered the discrimination of *C*-6 to functionalize this position with an isotopic PET tracer within the scope of Project II (position highlighted with a green arrow). Lewis-acidic promoted glycosylation and following stepwise deprotection led to disaccharides **10** and **23** in an overall yield of 12% and 17%, respectively.

Crystallization of hGal-1 in complex with both precursors demonstrated that neither the allyl unit at *O*-1 nor the alkyne group at *O*-3' influence the binding geometry of the carbohydrate scaffold or disturb natural interactions (Fig. 6.3), thus providing the anticipated reactive templates for the envisioned extension of protein ligand interactions and immobilization on microarrays. SPR experiments with covalently bound hGal-1 and LacNAc ($K_d = 91.4 \pm 4.62\ \mu M$), **10** ($K_d = 107 \pm 8.80\ \mu M$) and **23** ($K_d = 135 \pm 36.0\ \mu M$) confirmed the structural analyses and resulted in similar K_d values for the three disaccharides.

The crystallographic data enabled comprehensive computational studies in cooperation with Prof. Dr. Gisbert Schneider to predict promising click products for addressing the potential binding domain of hGal-1 rather than producing a library of triazoles. Topranked molecules were synthesized and converted with alkyne precursor **10** in the Cu(I)-catalyzed 1,3-dipolar cycloaddition to obtain click products **9a**-**9j** (Scheme 6.2). Surprisingly, the SPR assay with the triazoles resulted in only moderate increases in affinity (factor 2-3) for compounds **9a**, **9f** and **9d** while the affinity of further click products was in the same range of LacNAc and **10**. Complementary ITC experiments elucidated the thermodynamic nature of the interactions and revealed that the binding event is enthalpically driven and suffers from an enthalpy-entropy compensation. Structural characterization of the binding mode was indispensable at this point to probe the suggested rational ligand design

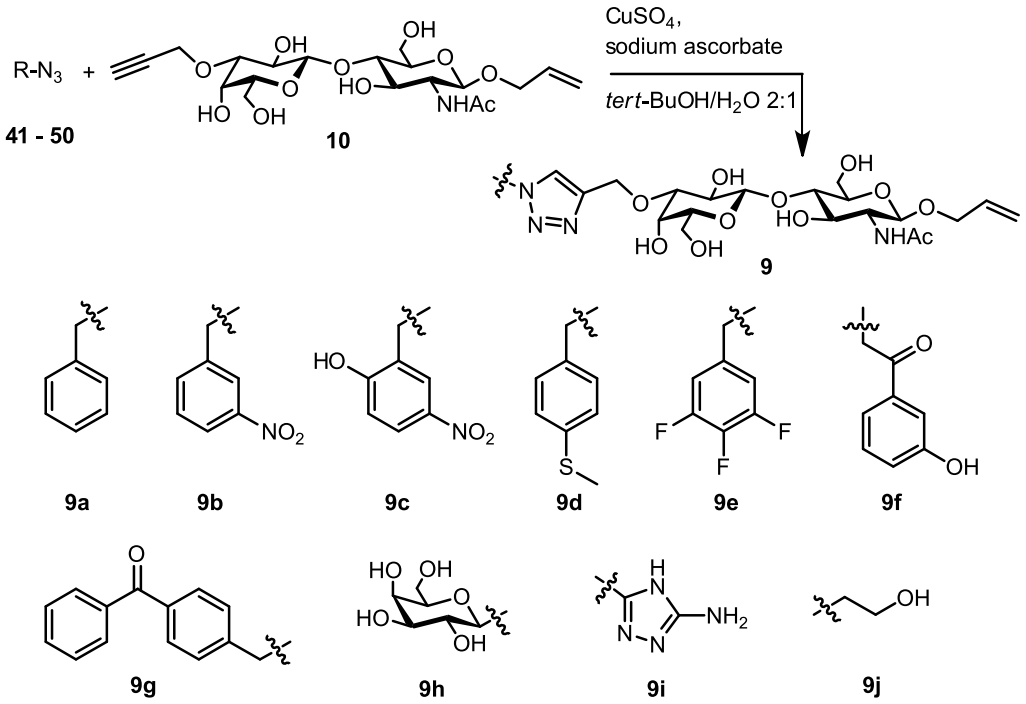

Scheme 6.2 Click reaction between alkyne precursor **10** and promising azides. Click product **9f** was synthesized *in situ* from **10**, bromide **51** and NaN_3.

including organic synthesis, biophysical affinity assays and computational predictions. Soaking experiments of hGal-1 crystals with the click products provided high resolution data for three hGal-1-ligand complexes. Remarkably, the carbohydrate scaffold of click

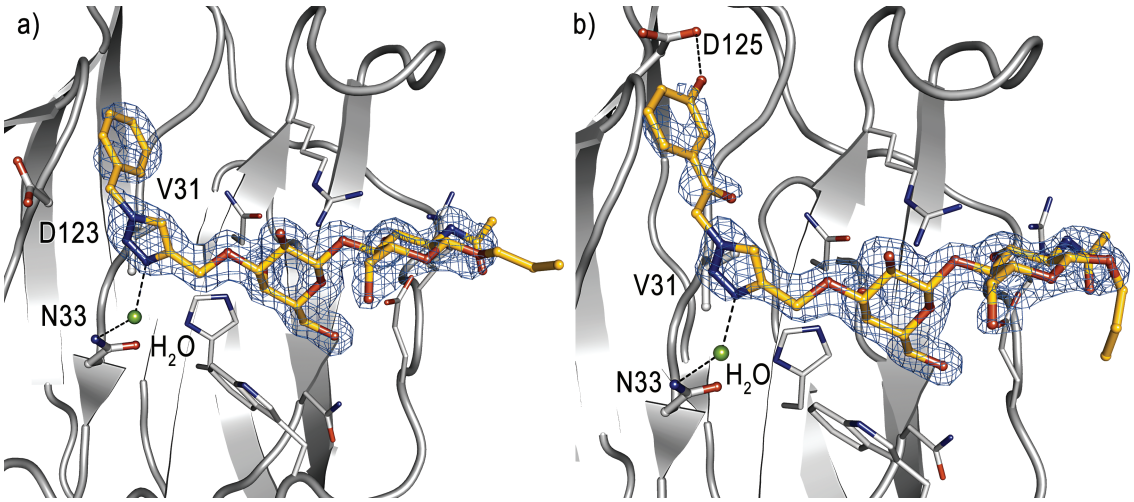

Fig. 6.4 Complexes of hGal-1 and click products a) **9a** and b) **9f**. The triazole acts as linker unit and forms a water-mediated interaction with Asn33. The substituents address the targeted protein area adjacent to the CRD, respectively.

products **9a**, **9f** and **9i** bound in a highly conserved way and the substituted triazoles addressed the targeted and defined protein area. The triazole clearly fulfilled its function as linker unit and showed a water-mediated key interaction with Asn33 in all complexes while the novel functional groups formed specific interactions as shown for **9a** and **9f** in Fig. 6.4. Evidently, an isolated interpretation of SPR and ITC results would have led to an underestimation of rationally obtained ligands and both techniques were not capable of unravelling binding geometry and distinct interactions, thus emphasizing the power of the chosen highly interdisciplinary strategy towards novel hGal-1 ligands. Selected click products were evaluated with regard to their diagnostic potential within the scope of Project II.

Project II: Development of diagnostic tools for tumor-associated hGal-1

The development of diagnostic tools is of immense importance as tumor diagnosis at an early stage of the disease greatly enhances the chances for a successful and lasting cancer cure. Carbohydrate microarrays have emerged as a powerful tool to trace lectin interactions *in vitro* while PET is a non-invasive *in vivo* technology for tracking physiological aberrancies. In the first part of Project II carbohydrate microarrays were used to visualize hGal-1 binding by "fishing" the protein from the incubation mixture via affine and specific interactions with an immobilized ligand. To this end, click products **9a**, **9f** and **9g** were covalently attached to the thiol-bearing chip surface (Fig. 6.5). 1-*O*-Allyl-β-D-lactose (**53**) and *N*-acetyl-1-*O*-allyl-β-D-lactosamine (**23**) served as reference compounds. In a proof-of-concept experiment the functionalized microarray was incubated with Alexa647 labeled hGal-1 and excitation with λ_{exc} = 635 nm

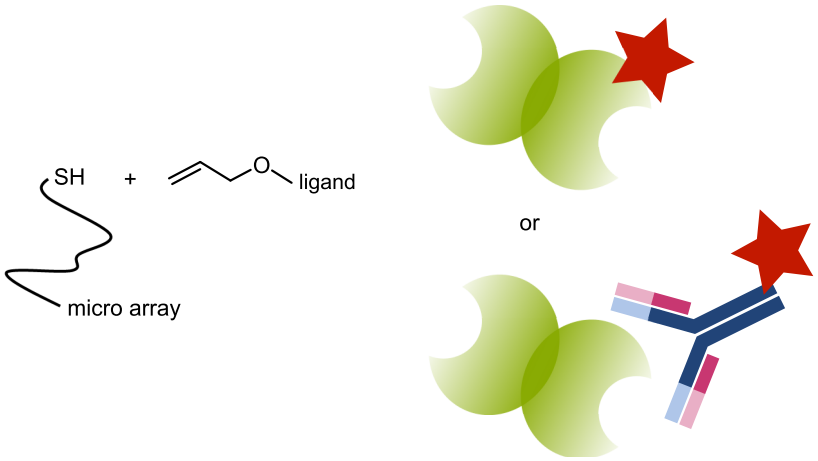

Fig. 6.5 Schematic illustration of the photochemical immobilization of allyl-linked ligands onto the thiol-bearing surface of the microarray. Detection occurred either by Alexa647 labeled hGal-1 or by sandwich formation with hGal-1 and fluorophore-labeled antibodies.

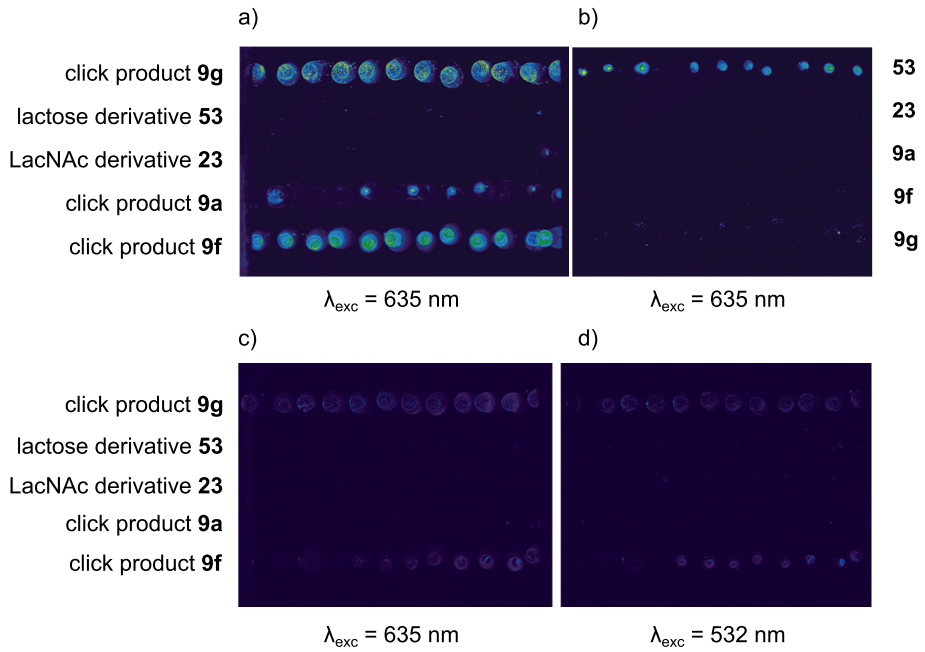

Fig. 6.6 Microarray with immobilized disaccharides. a) Alexa647 labeled hGal-1 selectively recognized click products **9a**, **9f** and **9g** and no signal was observed for lactose or LacNAc. b) Control experiment with Alexa647 labeled β-galactoside-binding peanut agglutinin (PNA) that binds exclusively lactose. c+d) Incubation with a 1:1 mixture of hGal-1 and hGal-3CRD (100 μg/ml each) followed by treatment with a 1:1 mixture of the anti-hGal-1 antibody and the anti-hGal-3 antibody (100 μg/ml each). Galectin-1 binding is selectively detected upon excitation at λ_{exc} = 635 nm and galectin-3 upon excitation at λ_{exc} = 532 nm.

resulted in fluorescence signals for spots with immobilized click products while no signal was observed for the reference compounds **53** and **23** (Fig. 6.6 a and b). The selective recognition of the click products versus LacNAc and lactose was attributed to multivalent effects which allowed a discrimination between the natural binding motifs and computationally predicted triazoles through an increased avidity. However, this approach is not adequate to display overexpressed galectin-1 in the clinic and to address this issue a second visualization strategy was investigated. Here, the microarray was first incubated with hGal-1 followed by addition of a fluorophore-labeled anti-hGal-1 antibody and again a clear fluorescence signal was detected for click products **9f** and **9g** (Fig. 6.6 c). It was further anticipated that galectin-3, a second member of the galectin family related to tumor progression, would recognize the immoblized click products due to the highly conserved carbohydrate recognition domain. In this regard the sandwich formation allowed to discriminate between hGal-1 and hGal-3 binding by employing antibodies conjugated to different Alexa-fluorophores (Fig. 6.6 c and d). This finding is highly promising as elevated levels of both galectins have been suggested for monitoring of tumor progression and therapeutic success.[328,330,331,334–336]

Ongoing experiments with Prof. Dr. Jörg Wischhusen (Universitätsklinikum Würzburg) examine the functionalized microarrays regarding their potential to detect increased galectin levels of tumor cell lines and in blood sera of cancer patients and may find a clinical application for selective diagnosis of hGal-1 and hGal-3 associated tumors in the future.

In the second part of Project II a LacNAc-based PET precursor was prepared by functionalizing *O*-6 of LacNAc within the synthetic approach presented in Scheme 6.1. The position was inspired by the crystallographic data of hGal-1 in complex with lactose[74] and LacNAc and converted to a tosylate acting as a good leaving group (Scheme 6.3). Substitution with nucleophilic $^{19}F^{-}$ and following deacetylation provided the reference compound **19** while the radioactive isotope ^{18}F will be introduced locally by Dr. Reik Löser, HZDR. To probe the influence of the fluorine molecule **19** was subjected to soaking experiments with hGal-1 crystals. High resolution data of the complex confirmed that the halogen is arranged analogously to the hydroxyl group in **23** and does not affect the binding mode of the carbohydrate scaffold (Fig. 6.7). Currently, the LacNAc derivatives are under investigation by the cooperation partner regarding physiological stability, distribution and accumulation.

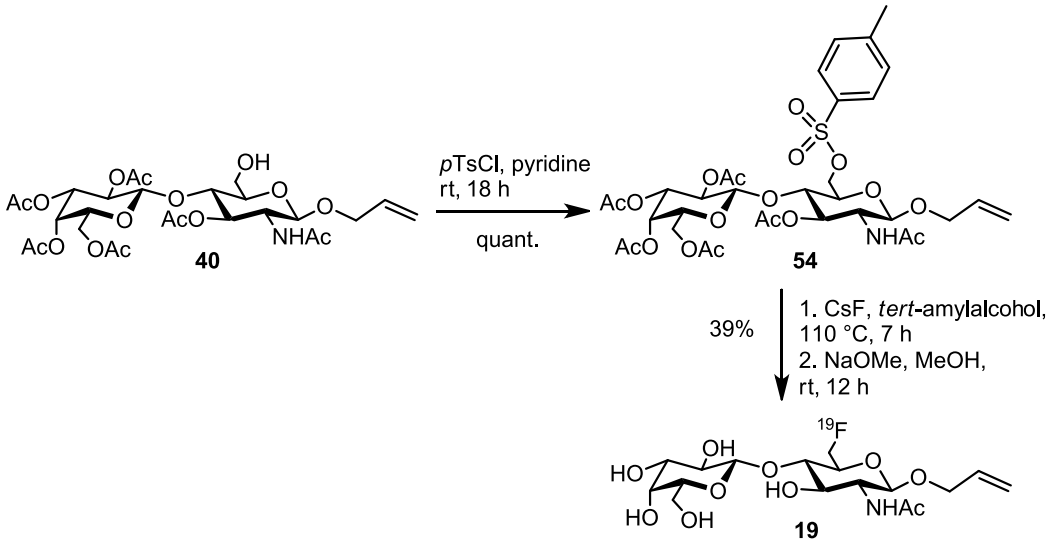

Scheme 6.3 Synthesis of PET reference compound **19** via tosylate **54**.

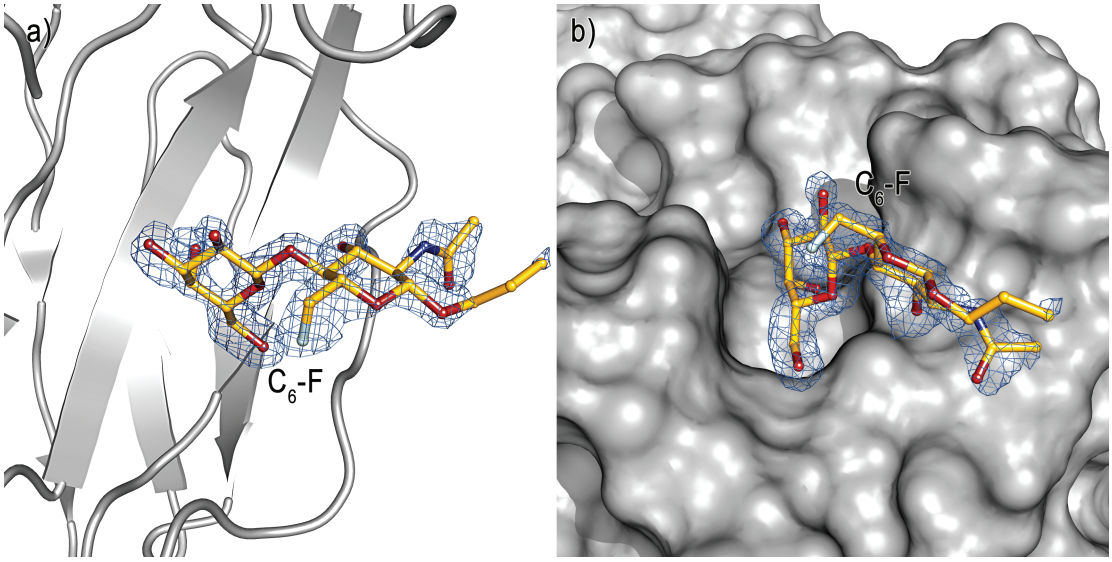

Fig. 6.7 Complex of hGal-1 and **19**. Electron density at a resolution of 1.35 Å is contoured at a level of 0.8 σ. The fluorine substituted disaccharide occupies the common binding mode and the halogen faces out of the CRD.

Project III: Investigation of hGal-1 communication pathways on human cell surfaces

High resolution microscopy in cooperation with Prof. Dr. Markus Sauer intended to better understand the highly complex communication pathways of hGal-1 on human cell surfaces that are associated with various cell signaling processes.
In the first part of Project III Neuroblastoma cells were incubated with Alexa647 labeled

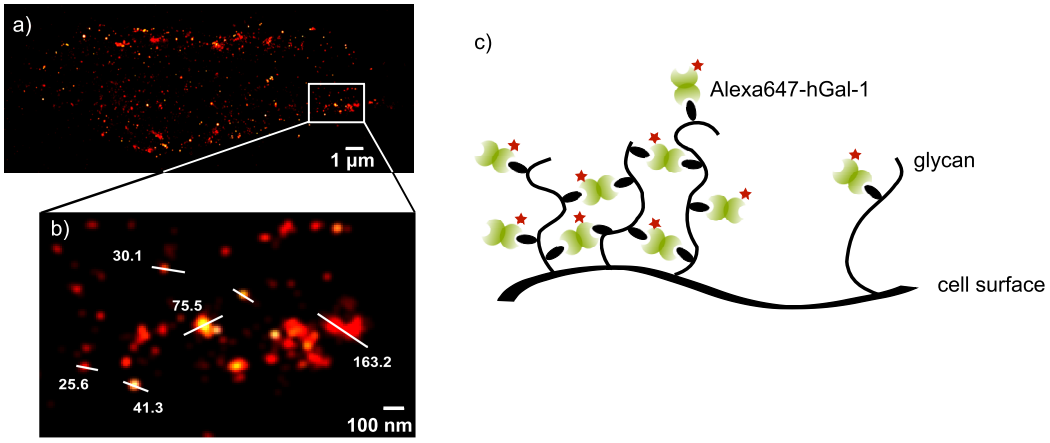

Fig. 6.8 a) Surface of Neuroblastoma cell incubated with Alexa647 labeled hGal-1 (1 μM). b) Enlarged part of a) that shows single localizations and clusters of different size. c) Proposed mechanism of hGal-1 associated cluster formation of Neuroblastoma cell surfaces.

hGal-1 of different concentrations (1 μM to 10 nM) to provide images with a resolution up to 20 nm. Cluster analyses showed that the average cluster size is independent of the protein concentration while the number of total localization decreased with the protein concentration. Further, the ratio of single localizations depended on the hGal-1 concentration. Prior incubation of hGal-1 (1 μM) with lactose (50 mM) reduced the number of localizations and led to results similar to those obtained for hGal-1 in a concentration of 10 nM. These findings strongly suggested that interactions via the CRD are responsible for cluster formation and that a certain concentration of (unbound) protein is required. The observed cluster effects further implied that glycan structures of cell surfaces present multivalent binding motifs as homodimeric hGal-1 is only capable of linking two β-galactosides (Fig. 6.8).

In the second part of Project III 1-*O*-propargyl-β-D-lactose was synthesized (Scheme 6.4) for increasing the presentation of hGal-1 binding motifs on Neuroblastoma cells by metabolic glycoengineering, currently under progress by Sebastian Letschert. An alterated glyco coat may provide precious information for evaluating hGal-1 cluster formation and bears the potential to reprogramm the tumor's microenvironment. hGal-1 induces apoptosis of T helper cells and it is of extreme impact to study if the same effect is observed in lactose-engineered tumor cells.

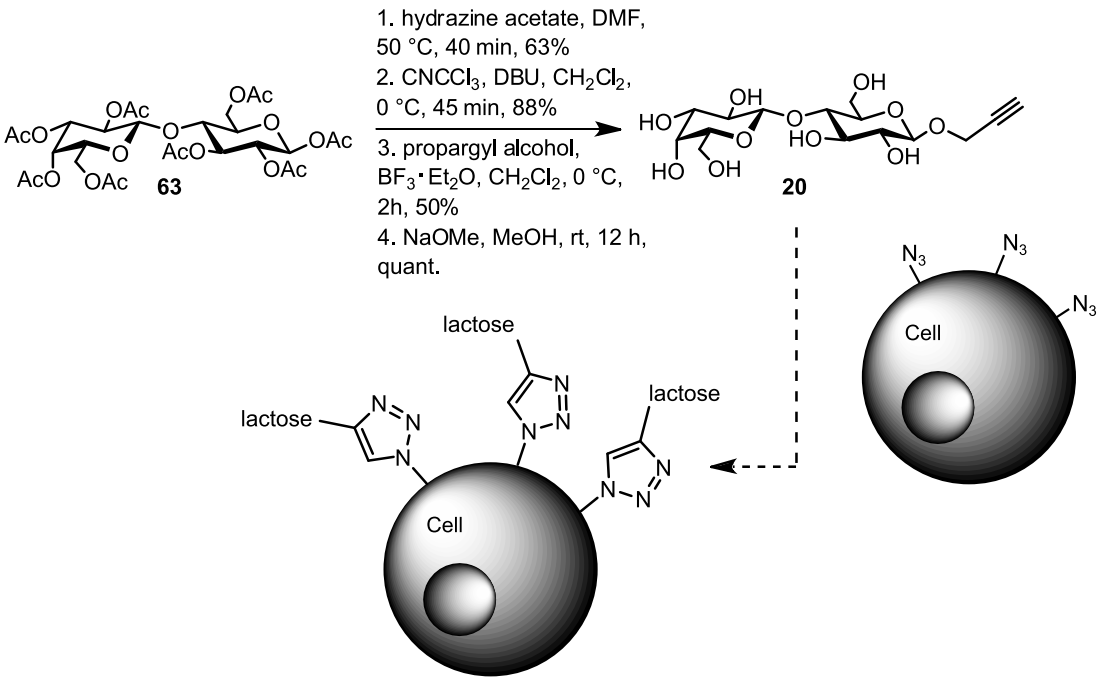

Scheme 6.4 Synthesis of alkyne-modified lactose **20** for labeling of glycoengineered cell surfaces to increase the presentation of hGal-1 binding motifs.

Conclusion and Outlook

The presented work contributes essentially to gain a deeper comprehension of hGal-1-ligand interactions on a molecular level and introduces first tailor-made binding partners by employing a highly interdisciplinary approach of organic synthesis, protein X-ray crystallography, biophysical affinity assays and computational prediction. Though the affinity of extended disaccharides is still characterized by K_d values in the micromolecular range, cocrystallization of hGal-1 and those structures elucidated a well-defined binding geometry and provided precious information about the involved interactions. X-ray data permit in an unrivaled manner to draw decisive conclusion for future structural modifications either to further increase the affinity or to attach functional groups for analytical or therapeutic purposes. In this context, a previously conducted study

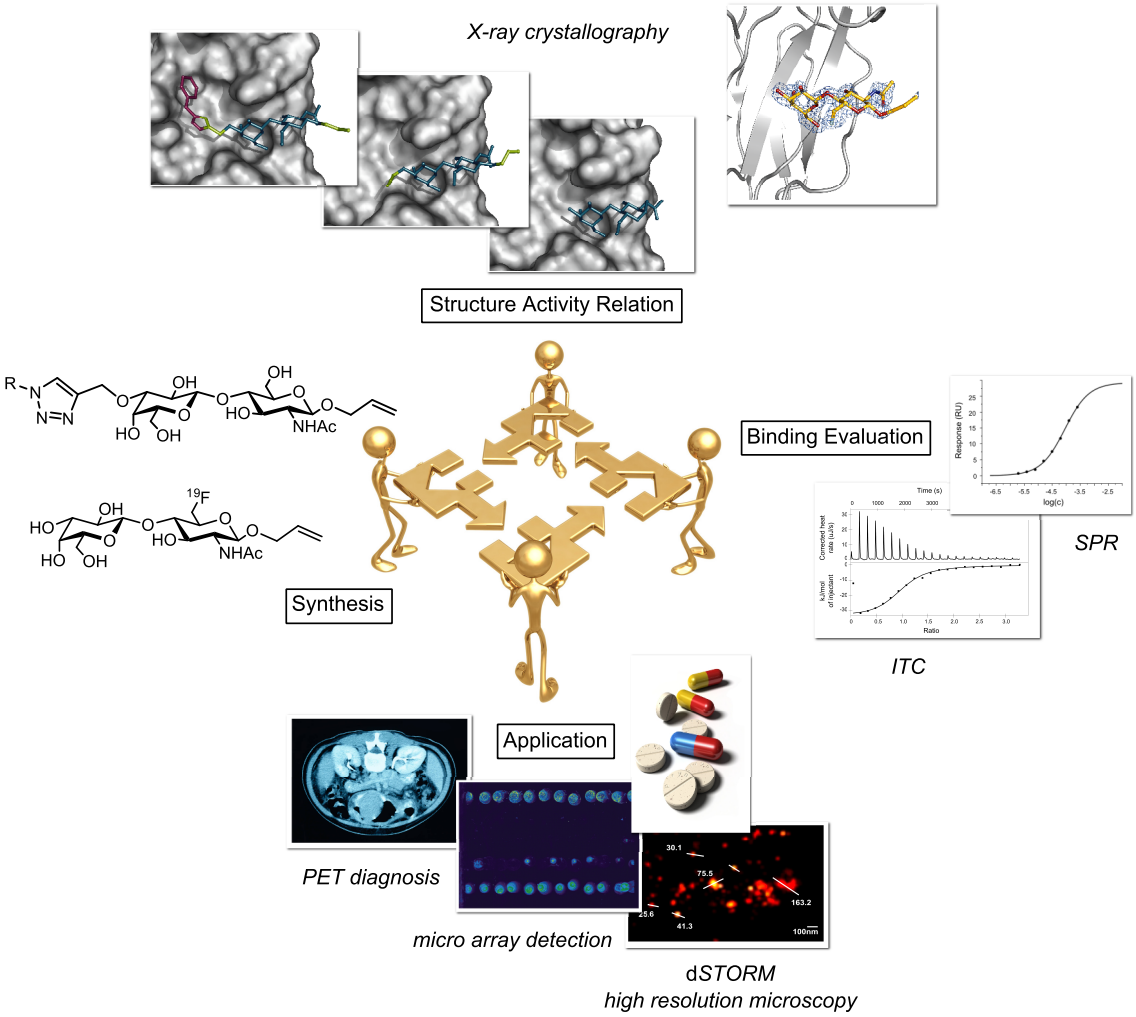

Fig. 6.9 Techniques of different disciplines that complemented and enriched the study of tumor-associated hGal-1 interactions in a cooperative way.

demonstrated that mutant mice deficient in both galectin-1 and galectin-3 lack strong phenotypic effects and developed without noticeable abnormalities.[172] Tribulatti *et al.* further reported about redundant and antagonistic functions between galectin members.[171] These findings strongly suggest that therapeutic cancer targeting with introduced triazoles will have a positive impact on tumor regression without expecting severe side effects.

Microarray experiments already demonstrate the potential of introduced ligands for an application in the medical diagnosis by exploiting the multivalent effect of immobilized carbohydrates. Additional interactions and higher affinities might be beneficial for a sensitive tracking of pathological elevated galectin concentrations of tumor patients in the future. The application-oriented focus of this work is further underpinned by the implementation of a precursor molecule for positron emission tomography. Findings about the physiological profile along with the integration of crystallographic inspired modifications of the natural binding partner LacNAc might lead to tracer molecules for selective diagnosis and localization of hGal-1 associated tumors in the future.

On a cellular level the investiagtion of hGal-1 recognition processes is of fundamental importance and high resolution microscopy of tumor cell surfaces has been proven to be a valuable tool for visualization of differences in protein clustering in presence and absence of CRD-binding ligands. The artificial modulation of the cell surface presentation by metabolic glycoengineering offers a different strategy for future cancer treatment. *d*STORM is a promising technique in this context to investigate the physiological interferences *in vitro* and to translate observations into *in vivo* strategies.

Chapter 7

Zusammenfassung

Krebserkrankungen zählen zu den vorherrschenden Gesundheitsbedrohungen unserer Generation und fordern Millionen von Todesopfern jährlich. Trotz unbestrittenem Fortschritt in der Krebsforschung in den vergangenen Jahrzehnten herrscht nach wie vor ein erheblicher Mangel an nebenwirkungsfreien Behandlungsmöglichkeiten und viele der physiologischen Prozesse in der Krebsbiologie sind ungeklärt.
In diesem Zusammenhang hat sich Galectin-1 zu einem Schlüsselelement in Tumorprogression im Laufe der letzten Jahre entwickelt, da es von zahlreichen Tumoren überexprimiert wird. Frühere Studien bestätigten, dass das β-Galactosid-bindende Protein verschiedene molekulare Wechselwirkungen vermittelt, welche in direktem Zusammenhang mit Tumorwachstum, -ausbreitung und -überleben stehen. Durch die Wechselwirkung mit Kohlenhydrat-basierenden Bindungsepitopen von Glykanstrukturen auf Zelloberflächen induziert Galectin-1 proliferative, angiogenetische und migratorische Signale und moduliert die negative Regulierung von T-Zellen, entscheidend für den Tumor, um der Immunantwort zu entkommen. Diese Beobachtungen schreiben Galectin-1 eine zentrale Rolle in der Tumorphysiologie zu, was dieses Protein zu einem attraktiven Target für diagnostische und therapeutische Anwendungen macht.
Die Kristallstruktur von humanem Galectin-1 im Komplex mit Lactose motivierte

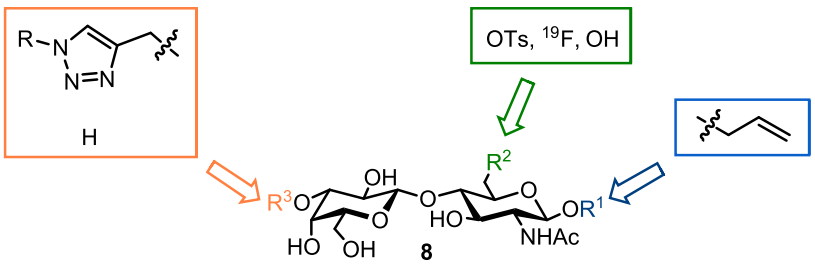

Abb. 7.1 Vorgeschlagenes LacNAc Derivat **8**. Angegebene synthetische Modifikationen wurden von der Kristallstruktur des hGal-1/Lactose Komplexes[74] inspiriert.

eine Strategie für das Design von maßgeschneiderten Galectin-1 Liganden, wobei ausgewählte Hydroxylgruppen, welche nicht an dem hochkomplexen Zusammenspiel zwischen Protein und Disaccharid beteiligt sind, funktionalisiert wurden. Synthetische Modifikationen beabsichtigten, chemische Gruppen einzuführen, um i) eine potentielle Bindungstasche in Nachbarschaft der Kohlenhydraterkennungsdomäne (CRD) zu adressieren (R^3), ii) einen Isotopenmarker (R^2) für die diagnostische Detektion zu implementieren und iii) eine Brückeneinheit (R^1) zu integrieren, welche einer späteren Immobilisierung auf Mikroarrays oder einer kovalenten Wirkstoffverknüpfung dient (Abb. 7.1). Zusätzlich wurde die Hydroxylgruppe an *C*-2 mit einer *N*-Acetyleinheit substituiert, um die inherente, höhere natürliche Affinität von Galectin-1 zu *N*-Acetyllactosamin versus Lactose auszunutzen.
Diese einleitenden strukturellen Analysen gestalteten maßgeblich die Arbeit der drei vorgestellten Galectin-1 Projekte und leiteten die experimentelle Durchführung von Vorhersage bis hin zu zukünftigen Wirkstoffkandidaten und diagnostischen Hilfsmitteln.

Projekt I: Rationales Ligandendesign für hGal-1 Wirkstoffkandidaten und diagnostische Hilfsmittel

Anfängliche Experimente umfassten die rekombinante Expression von homodimerem humanen Galectin-1 durch *E. coli*. Nachfolgende Kokristallisation von hGal-1 und

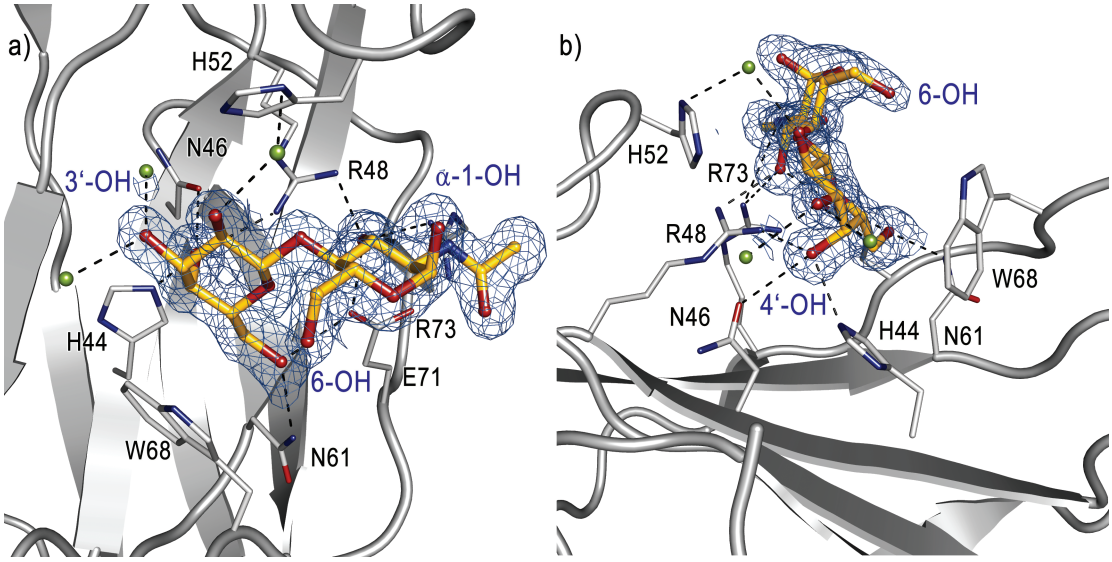

Abb. 7.2 Komplex aus hGal-1 und LacNAc. Die Elektronendichte ist als $2F_{obs}$-F_{calc}-Dichte dargestellt und auf ein σ-Level von 1.0 konturiert. a) Die Galactosyleinheit ist essentiell für den Erkennungsprozess. 3'-OH, 6-OH und 1-OH wechselwirken nicht mit dem Protein und eignen sich für Modifikationen. b) Andere Perspektive, um die Bindungstasche zu betonen, welche von LacNAc adressiert wird.

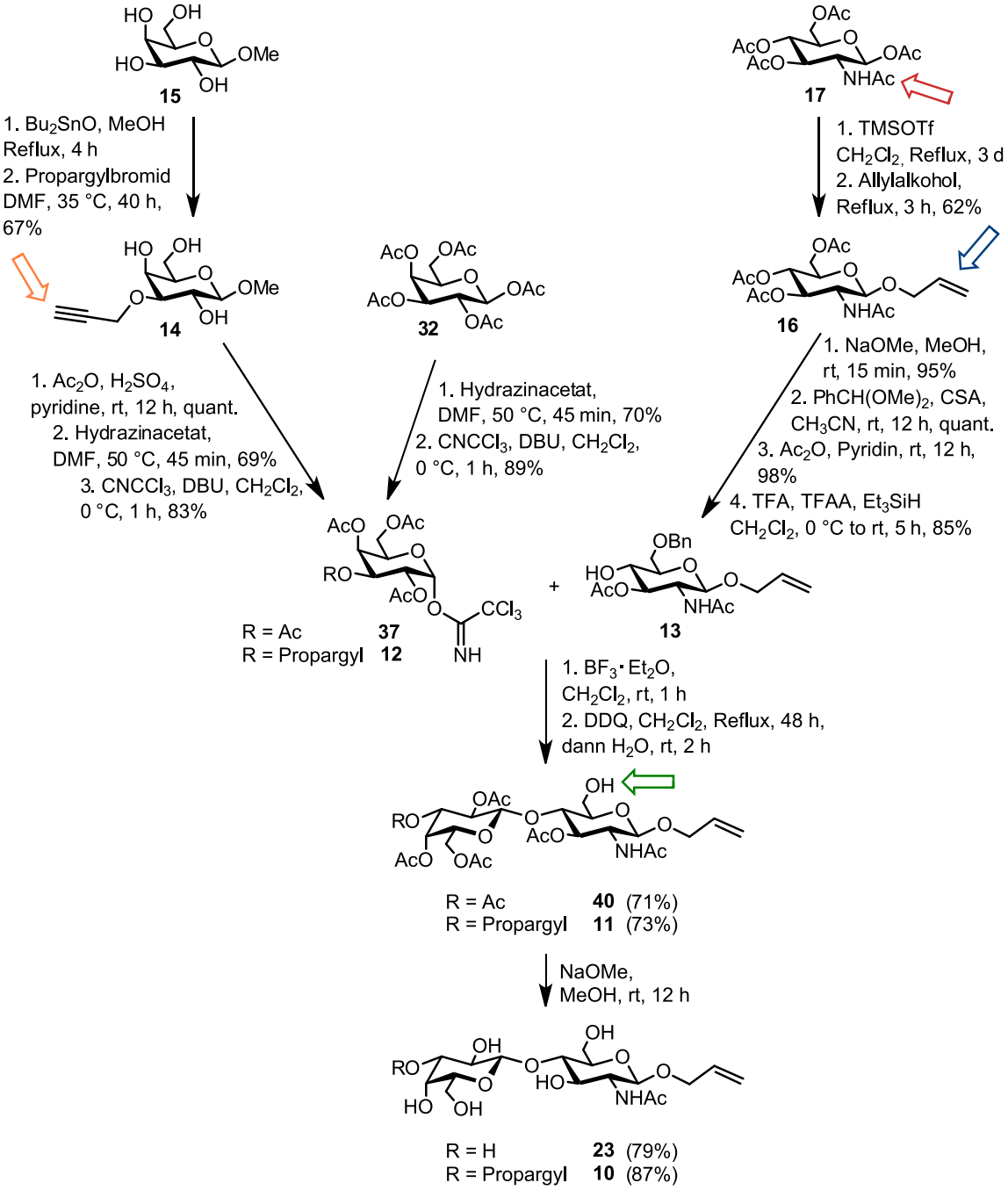

Schema 7.1 Syntheseroute zu Vorläufermolekülen **10** und **23**.

LacNAc in Kooperation mit Dr. Clemens Grimm lieferte einen hochaufgelösten Komplex (1.40 Å) und bestätigte eindeutig die Übertragbarkeit von strukturellen Inspirationen aus dem hGal-1-Komplex mit Lactose[74] (Abb. 7.2). Anschließend wurden Vorläufermoleküle **10** und **23** in einer konvergenten Mehrstufensynthese dargestellt wie in Schema 7.1 abgebildet. Die Allyleinheit an *O*-1 (blauer Pfeil) und

die optionale Alkingruppe an *C*-3' (orangener Pfeil) wurden jeweils zu einem frühen Zeitpunkt der Synthese eingeführt und nach ihrem Reaktionsprofil ausgewählt. Die Alkingruppe kann später in der bekannten Huisgen-Meldal-Sharpless Click-Reaktion mit organischen Aziden umgesetzt werden, während die Allylgruppe eine photochemische Reaktion mit Thiolen eingeht. Die synthetische Route beinhaltete als Schlüsselschritte die regioselektive Schützung zu *N*-Acetylglucosaminderivat **13** sowie die Aktivierung der Galactosyldonoren **12** und **37** mit $CNCCl_3$. Die Wahl der Schutzgruppen berücksichtigte eine Diskriminierung von *C*-6, um diese Position im Rahmen von Projekt II mit einem PET Isotopenmarker zu funktionalisieren (Position mit einem grünen Pfeil gekennzeichnet). Die Glykosylierungsreaktion erfolgte durch Aktivierung mittels einer Lewissäure und nachfolgende stufenweise Entschützung führte zu den beiden Disacchariden **10** and **23** mit einer entsprechenden Gesamtausbeute von 12% und 17%. Kristallstrukturen von hGal-1 im Komplex mit beiden Vorläufermolekülen demonstrierten, dass weder die Allyleinheit an *O*-1 noch die Alkingruppe an *O*-3' die Bindungsgeometrie des Kohlenhydratgrundgerüsts beeinflussen oder natürliche Wechselwirkungen stören (Abb. 7.3) und somit die vorhergesagten, reaktiven Template lieferten. SPR Experimente mit kovalent gebundenem hGal-1 und LacNAc (K_d = 91.4 ± 4.62 μM), **10** (K_d = 107 ± 8.80 μM) und **23** (K_d = 135 ± 36.0 μM) bestätigten die Strukturanalyse und ergaben ähnliche K_d-Werte für die drei Disaccharide. Die kristallographischen Ergebnisse ermöglichten umfangreiche *in silico*-Studien in Kooperation mit Prof. Dr. Gisbert Schneider, welche vielversprechende Clickprodukte aus zugänglichen Aziden und Alkin **10** vorhersagten, um die potentielle Bindungsdomäne von hGal-1 zu adressieren. Der rationale Ansatz und die Integration von rechnerischen Arbeiten wurden gegenüber der Produktion einer breit gefächerten Triazolbibliothek

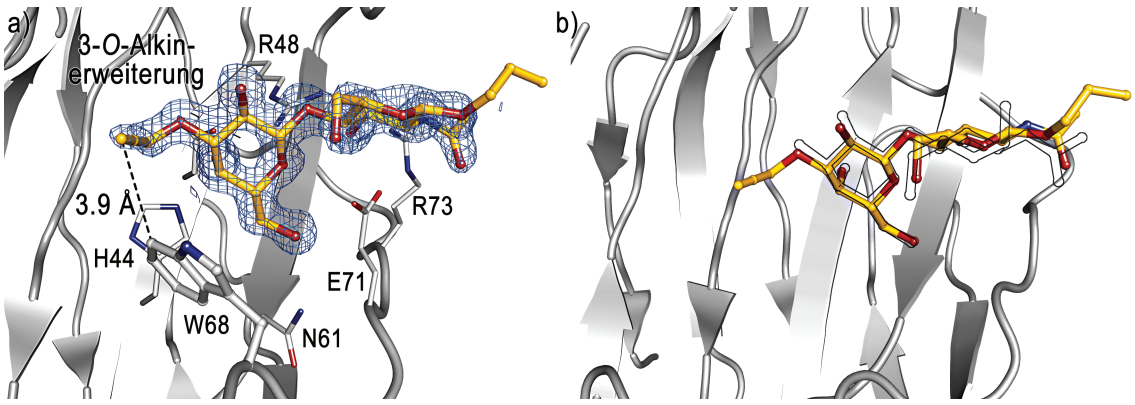

Abb. 7.3 a) Komplex zwischen hGal-1 und Alkinvorläufer **10**. Die Elektronendichte ist als $2F_{obs}$-F_{calc}-Dichte dargestellt und auf ein σ-Level von 1.0 konturiert. b) Überlagerung von **10** (gelb) und dem natürlichen Disaccharid LacNAc (schwarze Linie) in Komplex mit hGal-1 zeigt einen konservierten Bindungsmodus des Kohlenhydratgrundgerüsts.

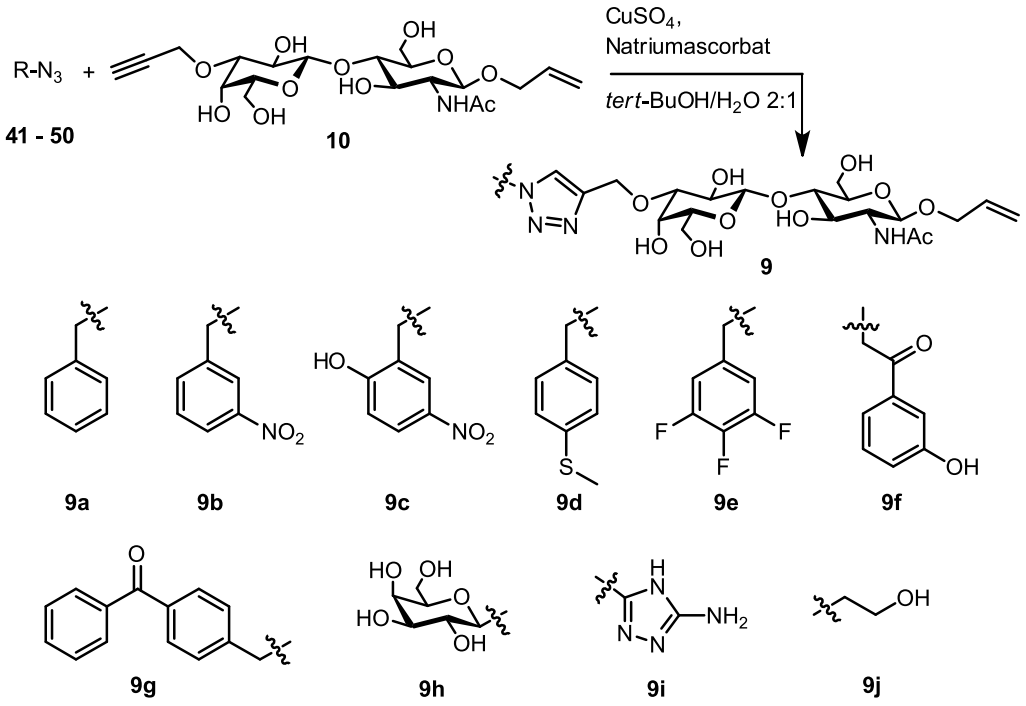

Schema 7.2 Clickreaktion zwischen Alkinvorläufer **10** und vielversprechenden Aziden. Clickprodukt **9f** wurde *in situ* aus **10**, Bromid **51** und NaN_3 dargestellt.

bevorzugt. Die bestbewerteten Moleküle wurden anschließend synthetisiert und mit Alkinvorläufer **10** in der Cu(I)-katalysierten 1,3-dipolaren Cycloaddition zu Clickprodukten **9a**-**9j** umgesetzt (Schema 7.2). Überraschenderweise resultierte der SPR-Assay in nur moderaten Affinitätszuwächsen (Faktor 2-3) für Verbindungen **9a**, **9f** und **9d**, während die Affinität der weiteren Clickprodukte ähnlich der von LacNAc und **10** war. Ergänzende ITC Experimente gaben Einblick in die thermodynamische Natur der Wechselwirkungen und zeigten, dass das Bindungsereignis enthalpisch getrieben ist und eine Enthalpie-Entropie-Kompensation auftritt. Eine strukturelle Charakterisierung der Bindungsmodi war an dieser Stelle zwingend erforderlich, um das vorgeschlagene rationale Ligandendesign zu überprüfen, welches organische Synthese, biophysikalische Affinitätsassays und *in silico*-Vorhersagen umschloss. Soakingexperimente mit hGal-1-Kristallen und den Clickprodukten lieferten hochaufgelöste Daten für drei hGal-1-Liganden Komplexe. Bemerkenswerterweise bindet das Kohlenhydratgrundgerüst der Clickprodukte **9a**, **9f** und **9i** hochkonserviert und die substituierten Triazole adressieren die angesteuerte und definierte Proteinfläche. Das Triazol erfüllt eindeutig seine Funktion als Brückeneinheit und weist eine Wasser-vermittelte Schlüsselwechselwirkung mit Asn33 in allen Komplexen auf, während die neu eingeführten funktionellen Gruppen spezifische Wechselwirkungen eingehen wie für **9a** und **9f** in Abb. 7.4 gezeigt. Offensichtlich hätte eine isolierte Interpretation der SPR- und ITC-Ergebnisse

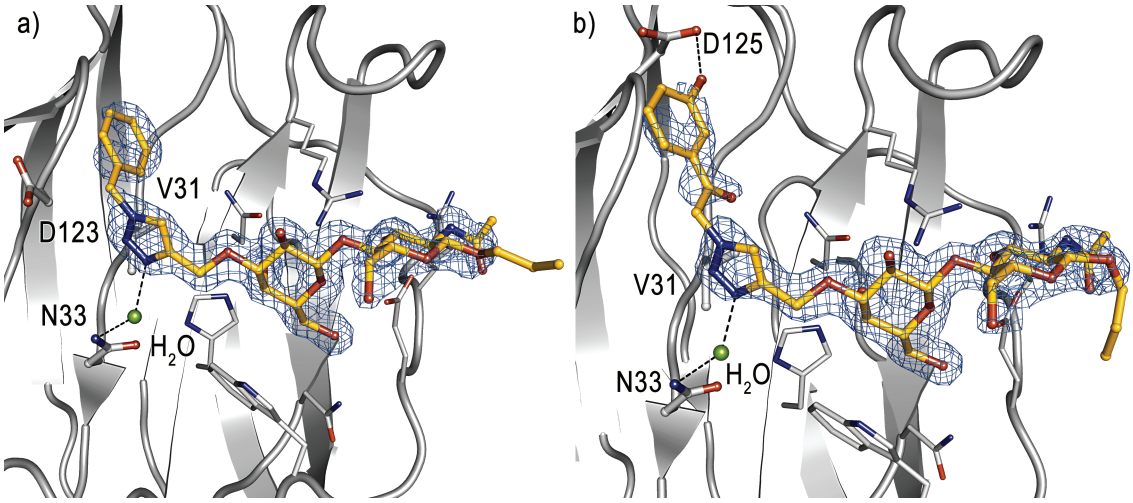

Abb. 7.4 Komplexe zwischen hGal-1 und Clickprodukt a) **9a** und b) **9f**. Das Triazol fungiert als Brückeneinheit und bildet eine Wasser-vermittelte Wechselwirkung mit Asn33 aus. Die Substituenten adressieren jeweils die angesteuerte Proteinfläche in Nachbarschaft zu der CRD.

möglicherweise zu einer Unterschätzung der rational entwickelten Liganden geführt und beide Techniken waren nicht in der Lage die Bindungsgeometrie sowie individuelle Wechselwirkungen aufzudecken, was die Stärke der gewählten hoch interdisziplinären Strategie zu neuartigen hGal-1 Liganden betont. Ausgewählte Clickprodukte wurden im Rahmen von Projekt II hinsichtlich ihres diagnostischen Potentials untersucht.

Projekt II: Entwicklung diagnostischer Hilfsmittel für tumor-assoziiertes hGal-1

Die Entwicklung diagnostischer Hilfsmittel ist von immenser Bedeutung, da eine Tumordiagnose zu einem frühen Stadium die Chancen auf eine erfolgreiche und dauerhafte Krebsheilung extrem erhöht. Kohlenhydratfunktionalisierte Mikroarrays haben sich zu einem mächtigen Werkzeug entwickelt, um Lectininteraktionen *in vitro* aufzuspüren, wohingegen PET eine nichtinvasive *in-vivo*-Technologie zur Verfolgung von physiologischen Abnormalitäten darstellt.
Im ersten Teil von Projekt II wurden Mikroarrays verwendet, um eine hGal-1-Bindung zu visualisieren, indem das Protein aus der Inkubationslösung über affine und spezifische Wechselwirkungen mit einem immobilisierten Liganden "gefischt" wurde. Hierfür wurden Clickprodukte **9a**, **9f** und **9g** kovalent auf der thiolmodifizierten Chipoberfläche gebunden (Abb. 7.5). 1-*O*-Allyl-β-D-lactose (**53**) und *N*-Acetyl-1-*O*-allyl-β-D-lactosamin (**23**) dienten als Referenzverbindungen. In einem Proof-of-Concept Experiment wurde der funktionalisierte Mikroarray mit Alexa647-markiertem hGal-1 inkubiert und eine Anregung mit λ_{exc} = 635 nm resultierte in Fluoreszenzsignalen für Spots mit immobilisierten Clickprodukten, wohingegen kein Signal für die

Abb. 7.5 Schematische Darstellung der photochemischen Immobilisierung der Allyl-funktionalisierten Liganden auf der Thiol-modifizierten Oberfläche des Mikroarrays. Die Detektion erfolgte entweder über Alexa657-markiertes hGal-1 oder über eine Sandwichformation mit hGal-1 und Fluorophor-markierten Antikörpern.

Referenzverbindungen **53** und **23** erhalten wurde (Abb. 7.6 a und b). Die selektive Erkennung der Clickprodukte gegenüber LacNAc und Lactose wurde multivalenten Effekten zugeschrieben, welche eine Diskriminierung zwischen den natürlichen schwachen Bindungsmotiven und rechnerisch vorhergesagten Triazolen

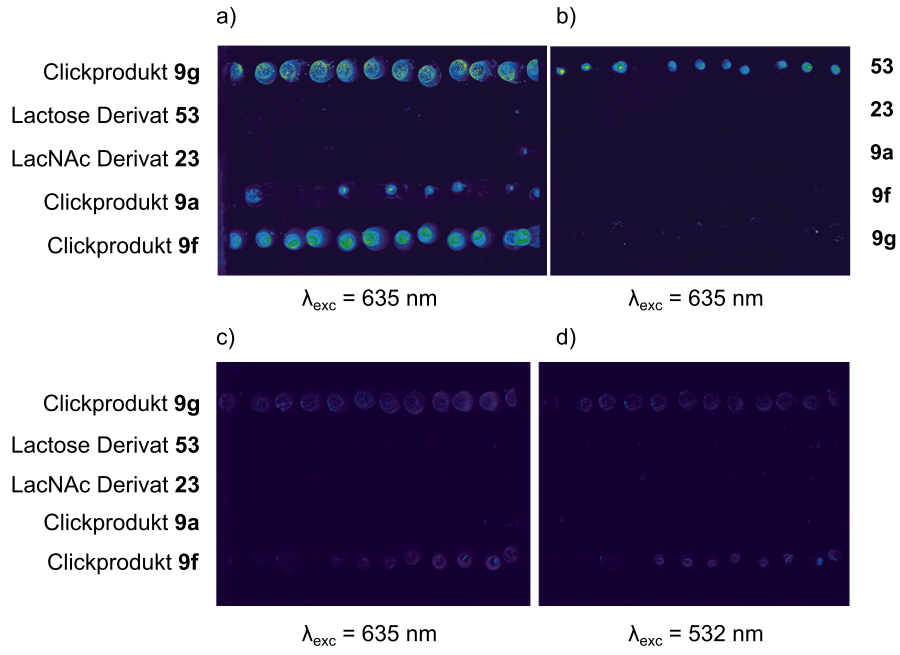

Abb. 7.6 Mikroarray mit immobilisierten Disacchariden. a) Alexa647-markiertes hGal-1 erkennt selektiv Clickprodukte **9a**, **9f** und **9g** und kein Signal wurde für Lactose oder LacNAc beobachtet. b) Kontrollexperiment mit Alexa647-markiertem Peanut Agglutinin (PNA), welches ausschließlich Lactose bindet. c+d) Inkubation mit einer 1:1 Mischung aus hGal-1 und hGal-3 (jeweils 100 μg/ml), gefolgt von einer Zugabe einer 1:1 Mischung aus anti-hGal-1 und anti-hGal-3 Antikörpern (jeweils 100 μg/ml). Die Galectin-1 Bindung wurde selektiv nach Anregung mit λ_{exc} = 635 nm und Galectin-3 nach Anregung mit λ_{exc} = 532 nm detektiert.

durch eine gesteigerte Avidität ermöglichten. Jedoch ist dieser Ansatz nicht geeignet, um überexprimiertes Galectin-1 in der Klinik nachzuweisen, sodass eine zweite Visualisierungsstrategie untersucht wurde. Hierbei wurde der Mikroarray zunächst mit hGal-1 inkubiert, gefolgt von einer Zugabe eines Fluorophor-markierten anti-hGal-1 Antikörpers. Wieder war ein deutliches Fluoreszenzsignal für Clickprodukte **9g** und **9f** zu erkennen (Abb. 7.6 c). Desweiteren wurde vermutet, dass Galectin-3, ein weiterer Vertreter der Galectinfamilie, der Tumorprogression begünstigt, aufgrund der hochkonservierten Kohlenhydraterkennungsdomäne die immobilisierten Clickprodukte erkennen würde. In diesem Kontext erlaubte die Sandwichbildung eine Diskriminierung von einer hGal-1- und einer hGal-3-Bindung, indem Antikörper mit verschiedenen Alexa-Fluorophorkonjugaten eingesetzt wurden (Abb. 7.6 c und d). Dieses Ergebnis ist äußerst vielversprechend, denn erhöhte Spiegel beider Galectine wurden als Marker für Tumorprogression und Therapieerfolg vorgeschlagen.[328,330,331,334–336]
Laufende Experimente mit Prof. Dr. Jörg Wischhusen (Universitätsklinikum Würzburg) untersuchen die funktionalisierten Mikroarrays bezüglich ihres Potentials erhöhte Galectinspiegel in Tumorzelllinien und Blutseren von Krebspatienten nachzuweisen und könnten zukünftig einen klinischen Einsatz zur selektiven Diagnose von hGal-1- und hGal-3-assoziierten Tumoren finden.

Im zweiten Teil von Projekt II wurde ein LacNAc-basierter PET-Vorläufer dargestellt. Die Position *O*-6 wurde von Kristallstrukturen der Komplexe hGal-1/Lactose[74] und hGal-1/LacNAc inspiriert und in der Syntheseroute, abgebildet in Schema 7.1, berücksichtigt. Reaktion von partiell geschütztem LacNAc Derivat **40** und Tosylchlorid lieferte den

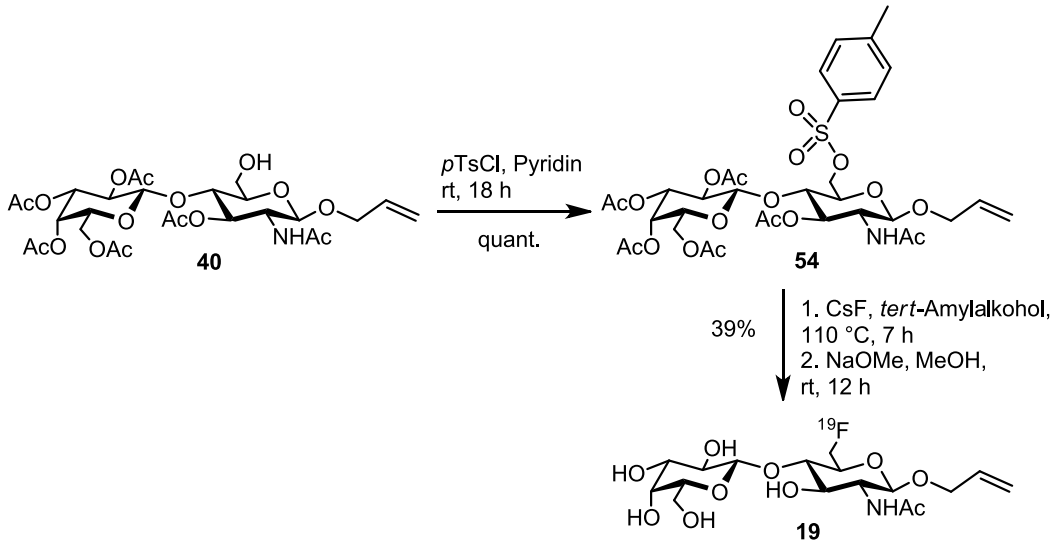

Schema 7.3 Synthese der PET-Referenzverbindung **19** via Tosylat **54**.

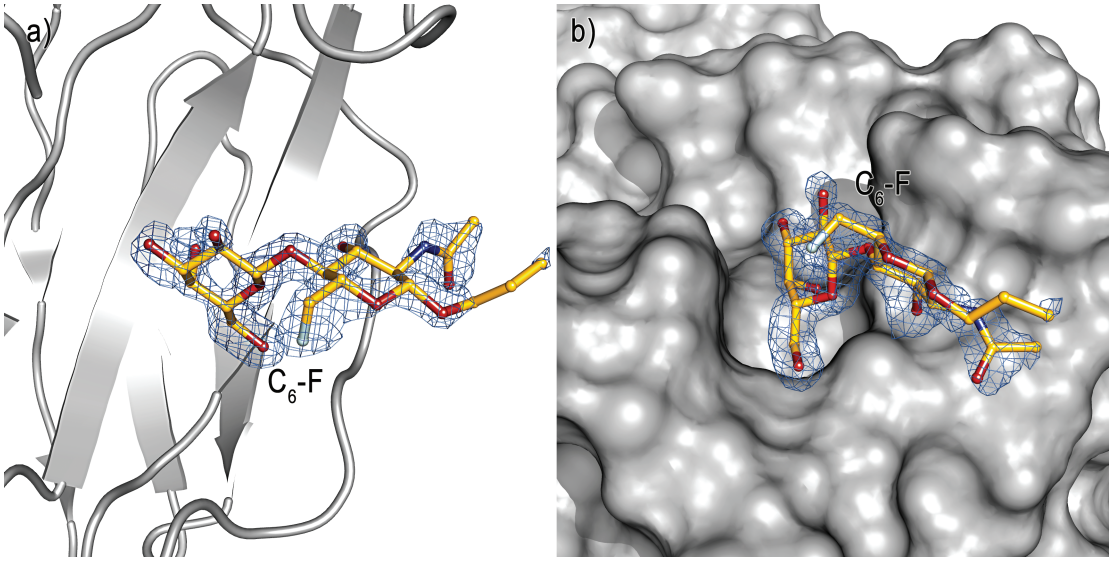

Abb. 7.7 Komplex aus hGal-1 und **19**. Die Elektronendichte bei einer Auflösung von 1.35 Å ist konturiert auf ein σ-Level von 0.8. Das fluorsubstituierte Disaccharid nimmt den gleichen Bindungsmodus wie die hydroxylierte Verbindung **23** ein und das Halogen weist aus der CRD heraus.

PET-Vorläufer **54**, welcher mit nukleophilem $^{19}F^-$ und nachfolgender Deacetylierung zu Referenzverbindung **19** umgesetzt wurde (Schema 7.3). Das radioaktive Isotop ^{18}F wird aufgrund seiner geringen Halbwertszeit von $t_{1/2}$ = 110 min lokal von Dr. Reik Löser, HZDR, eingeführt. Um den Einfluss des Fluors zu bewerten, wurde Molekül **19** Soakingexperimenten mit hGal-1-Kristallen unterzogen. Hochaufgelöste Daten des Komplexes bestätigten, dass das Halogen analog zu der Hydroxylgruppe in **23** angeordnet ist und den Bindungsmodus des Kohlenhydratgerüsts nicht beeinträchtigt (Abb. 7.7). Aktuell werden die LacNAc-Derivate von dem Kooperationspartner hinsichtlich physiologischer Stabilität, Verteilung und Anreicherung untersucht.

Projekt III: Untersuchung von hGal-1 Kommunikationswegen auf humanen Zelloberflächen

Hochauflösende Mikroskopie in Kooperation mit Prof. Dr. Markus Sauer zielte auf ein besseres Verständnis der hochkomplexen Kommunikationswege von hGal-1 auf humanen Zelloberflächen, welche in Zusammenhang mit verschiedenen Signaltransduktionsprozessen stehen.
Im ersten Teil von Projekt III wurden Neuroblastomazellen mit Alexa647-markiertem hGal-1 unterschiedlicher Konzentration (1 μM bis 10 nM) inkubiert und Bilder mit einer Auflösung bis zu 20 nm erhalten. Clusteranalysen zeigten, dass die durchschnittliche Clustergröße unabhängig von der Proteinkonzentration ist, während die Anzahl der

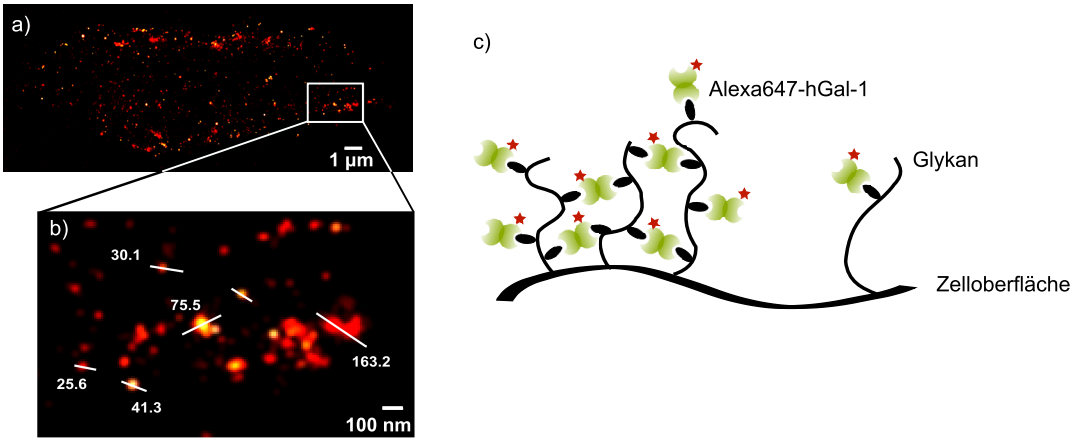

Abb. 7.8 a) Oberfläche einer Neuroblastomazelle, die mit Alexa647-markiertem hGal-1 inkubiert wurde (1 μM). b) Vergrößerter Ausschnitt von a), der einzelne Lokalisationen und Cluster verschiedener Größe zeigt. c) Vorgeschlagener Mechanismus der hGal-1-assoziierten Clusterbildung auf Neuroblastomazelloberflächen.

Gesamtlokalisationen mit der Proteinkonzentration abnimmt. Vorige Inkubation von hGal-1 (1 μM) mit Lactose (50 mM) reduzierte die Anzahl der Lokalisationen und ergab ähnliche Resultate wie für hGal-1 in einer Konzentration von 10 nM. Diese Ergebnisse lieferten wichtige Hinweise, dass die Interaktionen der CRD verantwortlich für die Clusterbildung sind und dass eine gewisse Schwellenkonzentration an (ungebundenem) Protein erforderlich ist. Desweiteren implizierten die beobachteten Clustereffekte, dass Glykanstrukturen auf der Zelloberfläche multivalente Bindungsmotive präsentieren, da homodimeres hGal-1 nur zwei β-Galactoside zu verknüpfen vermag (Abb. 7.8).
Im zweiten Teil von Projekt III wurde 1-*O*-Propargyl-β-D-lactose synthetisiert (Schema 7.4), um die Präsentation von hGal-1 Bindungsmotiven auf Neuroblastomazellen über metabolisches Glycoengineering zu erhöhen - aktuell in Arbeit von Sebastian Letschert. Ein künstlich veränderter Glykanmantel könnte wertvolle Informationen zur Evaluierung von hGal-1-Clustern liefern und birgt das Potential die Tumormikroumgebung umzuprogrammieren. hGal-1 induziert Apoptose in T-Helferzellen und es ist von großer Bedeutung zu untersuchen, ob der gleiche Effekt in Lactose-veränderten Tumorzellen beobachtet wird.

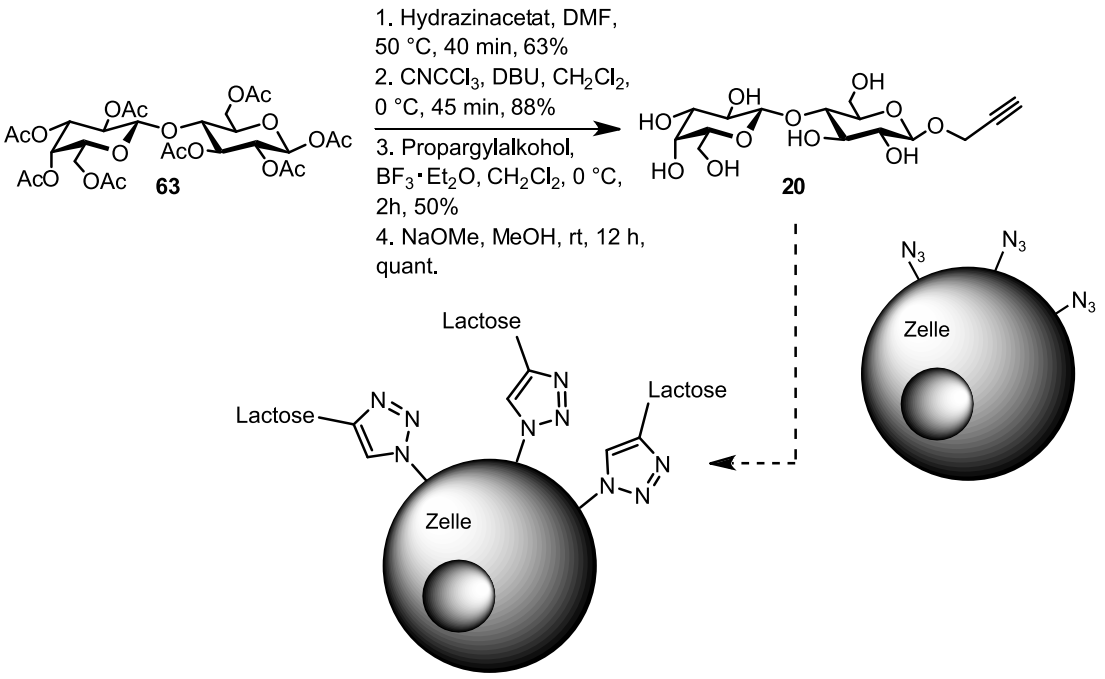

Schema 7.4 Synthese von Alkin-modifizierter Lactose **20**, um die Präsentation von hGal-1 Bindungsmotiven auf Tumorzelloberflächen über metabolisches Glycoengineering zu erhöhen.

Fazit und Ausblick

Die vorgestellte Arbeit trägt wesentlich zu einem tieferen Verständnis von Galectin-1-Liganden Wechselwirkungen auf molekularer Ebene bei und führt erste maßgeschneiderte Bindungspartner für hGal-1 ein. Das rationale Ligandendesign stellt einen hochinterdisziplinären Ansatz dar, welcher organische Synthese, Proteinröntgenstrukturanalysen, biophysikalische Affinitätsassays und *in silico*-Vorhersagen einschließt. Obwohl die Affinitäten der erweiterten Disaccharide sich noch im mikromolaren Bereich bewegen, konnte mit Hilfe von Kokristallisationsexperimenten eine wohldefinierte Bindungsgeometrie aufgedeckt und wertvolle Informationen über die beteiligten Interaktionen gewonnen werden. Die Röntgenstrukturen erlauben in unvergleichbarer Weise entscheidende Rückschlüsse für zukünftige strukturelle Modifikationen zu ziehen, um entweder die Affinität weiter zu steigern oder eine funktionelle Gruppe für analytische oder therapeutische Zwecke anzubinden. In diesem Zusammenhang zeigte eine frühere Studie, dass Mäuse mit simultaner Galectin-1 und -3 Defizienz keine ausgeprägten phenotypischen Erscheinungen aufweisen und sich ohne erkennbare Anomalien entwickeln.[172] Desweiteren berichteten Tribulatti *et al.* über redundante und antagonistische Funktionen unter Galectinvertretern.[171] Die Beobachtungen weisen darauf hin, dass ein therapeutischer Einsatz von eingeführten

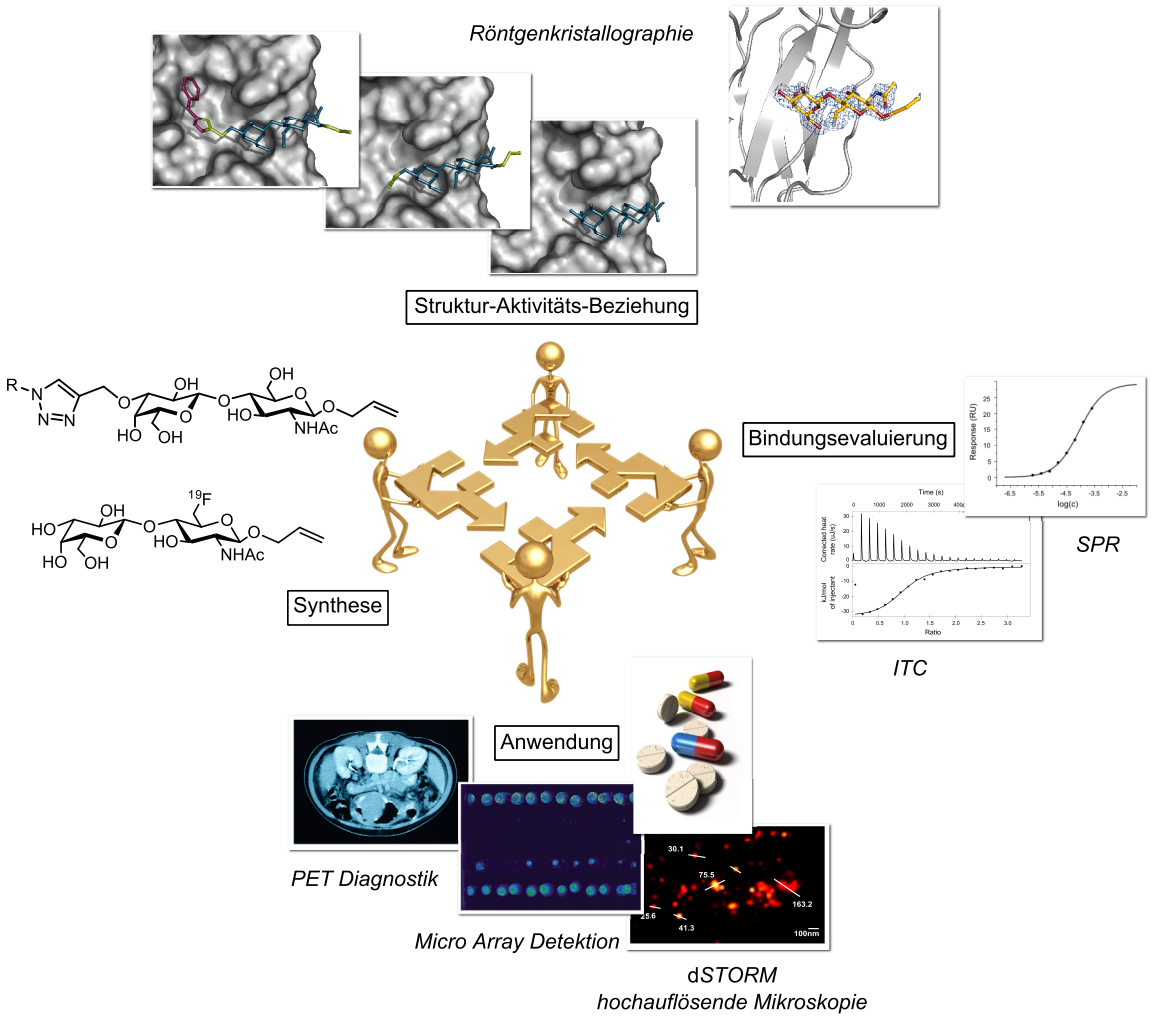

Abb. 7.9 Techniken verschiedener Disziplinen, die die Untersuchung von Wechselwirkungen des Tumor-assoziierten hGal-1 in kooperativer Weise ergänzt und bereichert haben.

Triazolen einen positiven Einfluss auf Tumorregression haben könnte, ohne dass schwere Nebenwirkungen zu erwarten sind.
Mikroarrays haben bereits das Potential der vorgestellten Liganden für eine Anwendung in der medizinischen Diagnostik aufgezeigt, indem der multivalente Effekt von immobilisierten Kohlenhydraten genutzt wurde. Zusätzliche Wechselwirkungen und höhere Affinitäten könnten zukünftig von Vorteil sein, um pathologisch erhöhte Galectinspiegel in Tumorpatienten sensitiv nachzuweisen. Der anwendungsorientierte Fokus der Arbeit wurde zusätzlich mit der Implementierung eines Vorläufermoleküls für die Positronen-Emissions-Tomographie gestützt und Ergebnisse über das physiologische Profil zusammen mit der Integration von kristallographisch motivierten Modifikationen des natürlichen Liganden LacNAc lassen auf Markermoleküle für eine selektive Diagnose und Lokalisierung von hGal-1-assoziierten Tumoren in der Zukunft hoffen.

Auf zellulärer Ebene ist die Untersuchung von hGal-1-Erkennungsprozessen von fundamentaler Bedeutung und hochauflösende Mikroskopie von Tumorzelloberflächen hat sich als Technologie der Wahl herausgestellt, um Unterschiede des Clusterverhaltens in An- und Abwesenheit von CRD-bindenden Liganden zu visualisieren. Die künstliche Modulierung der Zelloberflächenpräsentation über metabolisches Glycoengineering eröffnet eine weitere Strategie für eine zukünftige Krebsbehandlung. *d*STORM ist in diesem Zusammenhang eine vielversprechende Methode, um physiologische Interferenzen *in vitro* zu untersuchen und Beobachtungen in *in-vivo*-Strategien zu übersetzen.

Chapter 8

Experimental

8.1 Instruments & Materials for Biochemical Studies

Instrument	Type	Company
Autoclave	Varioklav	Thermo Scientific
Clean bench	SAFE2020	Thermo Scientific
Centrifuges	Ultracentrifuge Optima^{TM} L-90 K/L-80 XP	Beckman Coulter
	Fresco17	Heraeus
	Multifuge 1L-R	Heraeus
Centrifuge rotors	45Ti; Jla-8.1000	Beckman Coulter
Centrifuge beakers	Jla-8.1000 (1L, polypropylen)	Beckman Coulter
Electrophoresis device	power-phor-N	Anamed
pH-Meter	FiveGo^{TM}	Mettler Toledo
Thermomixer	Thermomixer comfort	Eppendorf AG
Incubator	MaxQ 8000	Thermo Scientific
Thermoblock	Duotherm	Biometra
Mastercycler	MasterCycler personal	Eppendorf AG
Sonotrode	Sonoplus	Bandelin
Vortexer	MS1 Minishaker	IKA
Fast Protein Liquid Chromatography (FPLC)	ÄKTA purifer	GE Healthcare

Instrument	Type	Company
FPLC column	Superdex 200	GE Healthcare
Microscope	SMZ1000	Nikon
Microscope object lens	WD45	Nikon
Ultra pure water device	Milli-Q Plus	Millipore
Photometer	BioPhotometer	Eppendorf AG
Biosensor (SPR)	SPR-2	Sierra Sensors GmbH
Calorimeter	nanoITC	TA Instruments
Array reader	GenePix Personal 4100A	Axon Instruments/Molecular Devices Corp.

Chemicals

All chemicals applied in biochemical experiments were purchased from commercial sources (*Sigma-Aldrich*, *Fluka*, *Carl Roth*, *Merck*, *Carbosynth*) and used without further purification.

LB-medium:

Peptone 10 g/l, yeast extract 5 g/l, NaCl 5 g/l

The medium was autoclaved at 120 °C and 1 bar overpressure for 20 min. LB-Agar plates contained additional 15 g/l Agar (added before sterilization). Antibiotics were added to LB-agar when media had cooled down to lower than 60 °C or prior to use.

Terrific Broth Medium (TB-medium):

Tryptone 12 g/l, yeast extract 21 g/l, glycerol 15%

The medium was autoclaved at 120 °C and 1 bar overpressure for 20 min. Before use a sterile solution of KH_2HPO_4 (c_{final} 17 mM)/K_2HPO_4 (c_{final} 72 mM)(pH 7) and antibiotics were added.

Buffers

Buffers were sterilized at 120 °C and 1 bar overpressure for 20 min if not indicated otherwise. 1 M imidazol stock solution was adjusted to pH 8 before use.

Basic buffers

Phosphate buffered saline pH 7.4 (20x PBS)	2.80 M NaCl, 54.0 mM KCl, 200 mM Na_2HPO_4, 36.0 mM KH_2PO_4 Prior to use 20x PBS was diluted to 1x.
Tris-acetate-EDTA buffer pH 8.0 (50x TAE)	2.00 M Tris, 1.00 M glacial acetic acid, 50 mM EDTA pH 8 Prior to use 50x TAE was diluted to 1x.
De-Ni-buffer pH 8.0	20 mM TrisHCl, 50 mM EDTA, 500 mM NaCl

Buffer for affinity assays

SPR buffer:	
Dialysis buffer	10 mM NaOAc pH 7.3, 1 mM TCEP
Immobilization buffer A	10 mM NaOAc pH 4.5, 1 mM TCEP
Immobilization buffer B	10 mM NaOAc pH 5.0
Running buffer	1x PBS pH 7.5, 0.005% Tween, 0.2 mM TCEP
ITC buffer	5 mM Na-phosphate, pH 7.2, 200 mM NaCl, 4 mM β-ME

Buffers for hGal-1 isolation and purification via IMAC (Ni-NTA)

Lysis buffer	1x PBS pH 7.4, 5 mM β-ME, 11 mM imidazole, 0.2 mM AP, 0.2 mM LIP, 0.2 mM PEP, 0.2 mM AEBSF, 0.2 mM LPMSF
Washing buffer	20 mM HEPES pH 7.5, 120 mM NaCl, 2 mM β-ME, 10 mM imidazole
Elution buffer	20 mM HEPES pH 7.5, 120 mM NaCl, 2 mM β-ME, 250 mM imidazole
Dialysis buffer	20 mM HEPES pH 7.5, 120 mM NaCl, 2 mM β-ME
Storage buffer	20 mM Na, K phosphate pH 7.0, 5 mM lactose, 1 mM TCEP

Buffers for TEV isolation and purification via IMAC (Ni-NTA)

Lysis buffer	60 mM Na-phosphate pH 8, 250 mM NaCl, 5 mM β-ME, 11 mM imidazole
Washing buffer	60 mM Na-phosphate pH 8
Elution buffer	60 mM Na-phosphate pH 8, 250 mM NaCl, 5 mM β-ME, 230 mM imidazole
Dialysis buffer	60 mM Na-phosphate pH 8, 250 mM NaCl, 5 mM β-ME
Storage buffer TEV	40 mM Tris pH 7.5, 50 mM NaCl, 1 mM EDTA, 5 mM β-ME

Buffers for hGal-3 isolation and purification via lactosyl sepharose

Lysis buffer	60 mM Na-phosphate pH 8, 250 mM NaCl, 5 mM β-ME, 11 mM imidazole
Washing buffer	1x PBS pH 7.4, 5 mM β-ME
Elution buffer	1x PBS pH 7.4, 5 mM β-ME, 300 mM lactose
Storage buffer	1x PBS pH 7.4, 0.2 mM TCEP

Buffers and solutions for SDS-PAGE

Loading buffer, 4x	0.2 M Tris pH 6.8, 8% SDS, 40% glycerol, 0.25% bromophenol blue, 0.1 M DTT
Denaturing Tris/glycine buffer, 10x	30.0 g/l Tris, 30.0 g/l SDS, 144 g/l glycine
Fixing solution	20% (w/v) trichloroacetic acid
Staining solution A	0.2% (w/v) Coomassie Blue in methanol
Staining solution B	20% (v/v) acetic acid
Decolouration solution	10% (v/v) acetic acid, 20% (v/v) methanol

SDS-PAGE

Running Gel, 15%: 0.40 M Tris pH 8.8, 15% acrylamide, 0.1% SDS, 0.1% APS, 0.08% TEMED.

Stacking Gel, 4%: 0.13 M Tris pH 6.8, 4% acrylamide, 0.1% SDS, 0.1% APS, 0.08% TEMED.

Bacterial strains & plasmids, DNA and oligonucleotides

Cloning experiments were performed with the *E. coli* TOP10 strain. For expression the *E. coli* BL21 Star^{TM} strain (both *Invitrogen*^{TM}) was used.

DNA sequences of hGal-1 (vector pANY) and hGal-3FL (vector pMA) were purchased from *GeneArt*®, *Life Technologies* and cloned into vector pET28a (*Novagen*). TEV protease was kindly provided as pET28a-TEV construct in BL21(DE3)plysS by Prof. Dr. Utz Fischer, Biocenter, University of Würzburg.

PCR primers were purchased from *Sigma* and designed regarding the required cloning and protease restiction site. Upon delivery primers were dissolved in stddH_2O to a final concentration of 100 μM and stored at -20 °C.

Biological kits and enzymes

Biological kits (peqGOLD Gel Extraction Kit, peqGOLD Plasmid Miniprep KitI, peqGOLD Cycle-Pure Kit) were ordered from *peqlab* and applied according to the

instructor's manual.

Restriction enzymes (*XhoI*, *EcoR*I, *Nco*I) and T4 Ligase were purchased from *Thermo Scientific*. Accupol DNA Polymerase was purchased from *Ampliqon*.

Crystallographic equipment

Crystallization screens were performed in 24 well plates with pregreased rim from *Crystalgene Inc.* and with circular cover slides (plain, 22 mm diameter) from *Jena Bioscience*. Crystals were mounted in loops (diameter depended on crystal size, typically 0.6-0.9 mm) from *Molecular Dimensions Ltd.*

Microarray equipment

Microarray experiments were performed with *SCHOTT* NEXTERION slide H and the print and incubation system of *Schleicher & Schuell* MicroCASTer (8-pin system) and *Schleicher & Schuell Bio Science* chip clip. Data extraction and evaluation was performed with GenePix Pro 4.1. Fluorophore labeled and polyclonal galectin specific antibodies were purchased from *antibodies – online GmbH*.

8.2 Biochemical Methods

The basic methods of molecular biology were carried out as described earlier.[174] hGal-1 crystallization experiments were performed in cooperation with Dr. Clemens Grimm (Biocenter, University of Würzburg). ITC, SPR and computational screenings were performed in cooperation with Dr. Michael Reutlinger and Dr. Petra Schneider (group of Prof. Dr. G. Schneider, Institute of Pharmaceutical Sciences, ETH Zürich).

8.2.1 General Biochemical Methods

Gel electrophoresis of DNA

Gel electrophoresis was applied for analytical and preparative purposes. The DNA sample was mixed with 6x loading buffer, applied to a 1% agarose gel and separated at 120 V (70 mA) for 75 min in 1x TAE with GeneRuler^{TM} 1 kb DNA ladder as reference. After preparative runs DNA bands were visualized under UV light and excised. DNA isolation was performed with the peqGOLD Gel Extraction Kit.

SDS-PAGE for protein analysis

The protein purity was analyzed by electrophoresis where proteins are separated by charge and molecular weight. To this end, the protein sample is denaturated with SDS and simultaneously negatively charged in proportion to its weight. Upon applying a potential the protein migrates through the polyacrylamide gel to the anode.
In detail, the protein sample was mixed in a ration of 1:4 with loading buffer and incubated for 5 min at 95 °C. Then, the sample was loaded on a 15% SDS-PAGE and separated at 120 V, 1 h.
The gel was stained according to the following Coomassie staining protocol: fixing solution (30 min), staining solution (60 min), decolouration solution (15 min), decolouration solution (overnight).

Regeneration of Ni-NTA

Ni-NTA was purchased by *Qiagen* and used without further treatment. After protein purification the column material was regenerated with De-Ni-buffer (2x column volumes), 6 M guanidin hydrochlorid (2x column volume), ddH_2O (10x column volume), 100 mM $NiCl_2 \cdot 6H_2O$, 20% EtOH (5x column volume) and stored at 4 °C.

Preparation of lactosyl sepharose

Lactosyl sepharose was prepared as previously described.[345] Briefly, sepharose 4B suspension was filled in *BioRad* mini-columns. The column material was washed with ddH_2O (2x column volume), 0.5 M Na_2CO_3 pH 11 (2x column volume) and resuspended in 0.5 M Na_2CO_3 pH 11 (1x column volume). After addition of divinylsulfone (1/10 of column volume) columns were rotated at rt for 70 min and washed with ddH_2O (2x column volume). Then, 0.5 M lactose in 0.5 M Na_2CO_3 pH 10 was added and sepharose incubated at 4 °C for 20 h. Again the sepharose was washed with ddH_2O (2x column volume) and suspended in 0.5 M Na_2CO_3 pH 8.5 (1x column volume) containing 2 v/v% β-ME. Columns were rotated at rt for 2 h, washed with ddH_2O (1x column volume) and equilibrated with PBS pH 7.4, 5 mM β-ME. After usage columns were extensively washed with elution buffer, washing buffer and stored at 4 °C over washing buffer containing 0.04% NaN_3.

Concentration of protein samples

Protein samples were concentrated at 13100 *g* and 4 °C with concentrators (Vivaspin 500) from *sartorius stedim biotech*. Concentrators are equipped with a membrane of different pore sizes, respectively, and were chosen according to the protein mass. During

centrifugation buffer permeates through the membrane and the protein sample gets concentrated.

Determination of protein concentration

Protein concentrations were determined according to their absorption at 280 nm. The specific extinction coefficient was considered as follows:

$$c_{obs} = c_{re} \cdot \varepsilon_{280\ nm} \tag{8.1}$$

c_{obs}:	measured protein concentration
c_{re}:	real protein concentration
$\varepsilon_{280\ nm}$(hGal-1):	0.576
$\varepsilon_{280\ nm}$(hGal-3FL):	1.368
$\varepsilon_{280\ nm}$(hGal-3CRD):	0.632

Exctinction coefficients $\varepsilon_{280\ nm}$ were predicted with the *ExPASy ProtParam* online tool.

Dialysis of protein samples

For buffer exchange protein samples were subjected to dialysis with dialysis cups (Slide-A-Lyzer MINI Dialysis Units, *Thermo Scientific* for V < 100 μl and dialysis tubes (*ZelluTrans Roth*) for V > 100 μl. Dialysis devices are equipped with a semi-permeable membrane. The pore size of these membranes allows permeation of small molecules (salts, additives etc.) and keeps macromolecules within the cup or tube. Dialysis was performed either with the 20000-fold of protein volume or in 2-3 steps with the 1000-fold of protein volume. The dialysis buffer was stirred slowly to support diffusion.

Protection of hGal-1 with IAA

hGal-1 was slightly mixed with 100 mM IAA in PBS at 4 °C overnight before dialyzed against PBS at 4 °C overnight.[282]

8.2.2 Cloning of Galectins

PCR:

DNA template (0.2 μg), forward primer (0.2 μM), reverse primer (0.2 μM), Accupol buffer with 15 mM $MgCl_2$ (1x), dNTP mix (0.2 μM each) and Accupol (2.5 units per reaction) were pipetted on ice and treated according to the PCR protocol. The PCR product was purified by the peqGOLD Cycle-Pure Kit or gel electrophoresis.

PCR primer

	forward primer	**reverse primer**
hGal-1	5'-TATAGAATTCGAAAAC CTGTACTTCCAGGGTATG GCTTGTGGTCTGGTT-3'	5'-TATACTCGAGTCAGTC GAACGCCACACATTTG-3'
hGal-3FL	5'-TATACCATGGCAGATAA CTTTAGCCTG-3'	5'-TATACTCGAGTTAGATC ATGGTATAGCTTGCG-3'
hGal3-CRD	5'-TATACCATGGGACCGC TGATTGTTCCGTATAA	5'-TATACTCGAGTTAGATC ATGGTATAGCTTGCG-3'

PCR protocol

hGal-1	**hGal-3**
Lid 105 °C	Lid 105 °C
T_1 = 95.0 °C (2 min)	T_1 = 95.0 °C (2 min)
T_2 = 95.0 °C (30 sec)	T_2 = 95.0 °C (30 sec)
T_3 = 60.0 °C (30 sec)	T_3 = 63.0 °C (30 sec)
T_4 = 72.0 °C (1 min)	T_4 = 72.0 °C (1 min)
repeat T_2-T_4 30 times	repeat T_2-T_4 35 times
T_5 = 72.0 °C (4 min)	T_5 = 72.0 °C (4 min)
T_6 = 10.0 °C (hold)	T_6 = 10.0 °C (hold)

Digestion with restriction enzymes:

Purified PCR products and cloning vectors were digested with the respective restriction enzymes in recommended buffer at 37 °C, 0 rpm overnight. The digestion reaction was

purified by gel electrophoresis, separated DNA cut off and extracted with the peqGOLD Gel Extraction Kit. The DNA concentration was determined via the absorption at 260 nm.

Digestion conditions

Template	Restriction enzymes	Buffer
hGal-1	*Eco*RI, *Xho*I	Tango 2X
hGal-3FL	*Nco*I, *Xho*I	Tango 2X
hGal-3CRD	*Nco*I, *Xho*I	Tango 2X

Ligation of galectin DNA with the cloning vector:

Ligation reactions were performed according to Eq. 8.2 with 25 ng of vector DNA. Vector, insert (= galectin DNA), T4 ligase (2.5 Weiss units) and T4 ligase buffer (1x, containing 1 mM ATP) were pipetted on ice and incubated at 22 °C for 25 min.

$$m(insert) = 5 \cdot m(vector) \cdot \frac{bp\ of\ insert}{bp\ of\ vector} \tag{8.2}$$

Transformation in chemo competent cells:

The ligation product (10 μl) and ccTOP10 cells (50 μl) were slightly mixed, incubated on ice (30 min), warmed at 42 °C (40 sec) and again incubated on ice (2 min). LB medium (500 μl) was added and cells grown for 1 h at 37 °C, 1400 rpm. Then, cells were spread on LB Kan plates (c(Kan) = 50 μg/ml) and grown at 37 °C overnight. Single colonies were picked and grown in LB Kan medium (5 ml, c(Kan) = 50 μg/ml) at 37 °C, 240 rpm overnight. The plasmid DNA was isolated with the peqGOLD Plasmid Miniprep Kit I and galectin sequence confirmed by sequencing analysis (*GATC Biotech*). For protein expression the plasmid was heat-transformed into ccBL21 Star^{TM} cells following the same protocol.

8.2.3 Protein Expression & Purification

hGal-1: BL21 Star^{TM} cells transformed with plasmid pET28a-hGal1 were grown at 37 °C, 160 rpm in TB medium containing 50 μg/ml kanamycin until the OD_{600} reached approximately 0.2. The medium was then cooled to 18 °C and at an OD_{600} of approximately 0.8 expression was induced by addition of IPTG to a final concentration of 0.5 mM. After 20 h cells were harvested by centrifugation at 4500 *g* and 4 °C for 15 min. For cell lysis, cell pellets were resuspended in lysis buffer and lysed by sonification. The

lysate was cleared by centrifugation at 45000 *g* at 2 °C and incubated for 2 h at 4 °C with Ni-NTA sepharose resin equilibrated with washing buffer. After 4 extensive washes with washing buffers, the bound His_6-hGal-1 protein was eluted with elution buffer. Pass-through fraction and protein containing washing fractions were incubated again on regenerated Ni-NTA resin. Combined hGal-1 fractions were dialysed against dialysis buffer and digested with the TEV protease for 12 h at 16 °C. The sample was then concentrated and purified by FPLC using storage buffer as running buffer. hGal-1 eluted as a single gaussian peak. Peak fractions were pooled, concentrated to approximately 40 mg/ml and stored at -80 °C. The yield was typically 70 mg per liter cell culture.

hGal-3: BL21 Star^{TM} cells transformed with plasmids pET28a-hGal-3FL and pET28a-hGal-3CRD were grown at 37 °C, 160 rpm in LB medium containing 50 μg/ml kanamycin until the OD_{600} reached approximately 0.2, respectively. The medium was then cooled to 18 °C and at an OD_{600} of approximately 0.6 expression was induced by addition of IPTG to a final concentration of 0.5 mM. After 20 h cells were harvested by centrifugation at 5000 *g* and 4 °C for 20 min. For cell lysis, cell pellets were washed with washing buffer, resuspended in lysis buffer and lysed by sonification. The lysate was cleared by centrifugation at 16000 *g* and 2 °C and the clear lysate was incubated for 2 h at 4 °C with lactosyl sepharose resin equilibrated with washing buffer. The following steps were the same as for hGal-1 with the respective buffers. The yield of hGal-3CRD and hGal-3FL were 2 mg and 15 mg per liter cell culture, respectively.

TEV protease: BL21(DE3)pLysS cells transformed with plasmid pET28a-TEV were grown at 37 °C, 190 rpm in LB medium containing kanamycin and chloramphenicol (each 50 μg/ml) until the OD_{600} reached approximately 0.2. The medium was then cooled to 30 °C and at an OD_{600} of approximately 0.3, the medium was cooled to 18 °C. At an OD_{600} of approximately 0.7 expression was induced by addition of IPTG to a final concentration of 0.5 mM. After 20 h cells were harvested by centrifugation at 7000 *g* and 4 °C for 20 min. For cell lysis, cell pellets were washed with washing buffer, resuspended in lysis buffer and lysed by sonification. The lysate was cleared by centrifugation at 16000 *g* and 2 °C and treated according to the purification protocol of hGal-1. However, washing and elution steps were performed at 4 °C. Protein-containing elution fractions were combined, desalted in storage buffer and 50% glycerol added before storage at -80 °C. The yield was 10 mg per liter cell culture.

8.2.4 Crystallization of hGal-1

Crystallization of hGal-1 was previously described[74,78,279–281] and screening conditions containing $(NH_4)_2SO_4$ and PEG 4000 as precipitant were tested.
Both, the initial $(NH_4)_2SO_4$ and PEG 4000 screens consisted of 24 different conditions with the general composition of the precipitating buffers:

$(NH_4)_2SO_4$		**PEG 4000**	
x.x M	$(NH_4)_2SO_4$	y%	PEG 4000
100 μM	buffer	100 μM	buffer
1%	β-ME	0.2 M	$(NH_4)_2SO_4$
		1%	β-ME

$(NH_4)_2SO_4$ was used in the concentrations of x.x = 1.6 M, 1.8 M, 2.0 M, 2.2 M, 2.4 M and 2.6 M. The pH was varied from 4.6 with sodium citrate, 5.0, 5.5 to 6.0 with BisTris, respectively. Additionally, a screening plate without β-ME was prepared.
PEG was added in the concentrations of y = 24%, 27%, 30% and 33%. The pH ranged from 4.6 (sodium citrate), 5.0 (BisTris), 6.5 (HEPES), 7.5 (HEPES), 8.5 (TrisHCl), 8.8 (TrisHCl). Again, a screening plate without β-ME was prepared.

Crystallization experiments were performed in 24-well plates with pregreased well rims and ligand-free crystals of hGal-1 were yielded by the hanging-drop vapor-diffusion method. A 1-4 μl drop of hGal-1 (20 mg/ml in storage buffer) was pipetted on a glass cover slide and mixed with an equal volume of precipitating buffer. The cover silde was placed on the respective well to generate a closed crystallization atmosphere. First crystals appeared after a few days of growth at 16 °C and grew to a full size of 0.5-0.8 mm within a period of 3-4 weeks.

Crystals grew best in 2.0 M $(NH_4)_2SO_4$ at pH 5 and 27% PEG at pH 5.0 with 1% β-ME, respectively, thus these conditions were applied for crystal production.

Soaking with carbohydrate ligands

Soaking experiments were performed with hGal-1 crystals grown in 2.0 M $(NH_4)_2SO_4$ at pH 5. The cover slide was taken off the well and growth buffer removed carefully under the microscope. Soaking buffer (2.2 M $(NH_4)_2SO_4$, 100 μM BisTris pH 5.0, 1% β-ME)

Table 8.2 Exact conditions for the generation of hGal-1/disaccharide complexes that were solved at the ESRF, Grenoble. All protein crystals were grown in 2.0 M $(NH_4)_2SO_4$, 100 μM BisTris pH 5.0, 1% β-ME at 16 °C. Ligands were dissolved to the indicated concentration in 2.2 M $(NH_4)_2SO_4$, 100 μM BisTris pH 5.0, 1% β-ME for soaking experiments.

Ligand	Concentration	Method
LacNAc	12.5 mM	recrystallization of seeded crystal
10	20 mM	soaking (24 h)
23	20 mM	soaking (24 h)
9a	<10 mM (saturated solution)	soaking (24 h)
9f	<10 mM (saturated solution)	soaking (24 h)
9i	<10 mM (saturated solution)	soaking (24 h)
19	10 mM	soaking (24 h)

was supplemented with the respective disaccharide (different concentrations, Table 8.2) and added to the crystals. To avoid damage of the protein crystals by osmotic pressure removal of growth buffer and addition of soaking buffer was accomplished stepwise. Alternatively, a 2 μl drop of soaking buffer was placed on a fresh cover slide and crystals transferred into soaking buffer before crystals were harvested after several hours of soaking duration.
The complex of hGal1 and natural *N*-acetyllactosamine was obtained by seeding an $(NH_4)_2SO_4$ crystal into a drop of the mother liquor supplemented with 12.5 mM LacNAc. Crystals dissolved within hours and reappeared after several days with a different shape. Those were harvested for structure determination.
Table 8.2 summarizes individual conditions that yielded hGal-1 ligand complexes.

Harvesting & Freezing of crystals

For transport and data collection crystals were transferred into soaking buffer supplemented with 25% glycerol. Buffer exchange was performed stepwise (see above). Loops for crystal harvesting were selected according to the size of the crystal (typically 0.6-0.8 mm) and attached to stainless steel pins that held magnetically to the end of a 'cryo-pen'. Crystals were captured within the loop and frozen immediately in liquid

nitrogen (-196 °C). All following manipulations until storage were performed with the crystal immersed in nitrogen. The pin-loop assembly was transferred to a cryogenic vial and placed in a 10-well aluminium revolver "puck" for automated sample loading. Until data collection protein crystals were stored in dewars at -196 °C.

8.2.5 Data Collection, Structure Solution and Refinement

Crystal testing was performed on a RIGAKU rotating X-ray source to prove successful soaking. Datasets with high resolution were collected at cryogenic temperatures on beamlines ID14-4 and ID23-1 of the European Synchrotron Radiation Facility, Grenoble, France (ESRF) and on beamline BL 14.2 at BESY, Berlin.
Two different crystal structures (one for hGal-1/LacNAc and one for the ligand-free hGal-1 and all other complexes) were solved by molecular replacement. Symmetry and cell parameters differ significantly from those of hGal-1 structures so far deposited with the PDB. For molecular replacement the program PHASER[346] and coordinates from PDB entry 3T2T were used. In the dataset of the complex hGal-1/LacNAc two hGal-1 dimers were located in the asymmetric unit, for the other structures a single dimer was found. Refinement of the solutions was performed with PHENIX[347] and the models subjected to a cycle of manual rebuilding. Coordinates of the respective ligand were positioned in the allocated electron density. The PRODRG server[348] was used to generate coordinate and restraint files of the ligands. Automated refinement and manual rebuilding included manual water building. After a maximum of two further cycles R and R_{free} factors converged in all data. The difference electron density $2F_{obs}$-F_{calc} was determined with the phases obtained from the model, with disaccharide ligands omitted to prevent model bias.

8.2.6 Affinity Assays

SPR

SPR experiments were performed by Dr. Michael Reutlinger on a SPR-2 instrument from *Sierra Sensors GmbH* with a temperature stabilized light source. Interactions were investigated at 25 °C with a flow rate of 25 μl/min. hGal-1 in SPR dialysis buffer was diluted with immobilization buffer A to a final concentration of 50 μg/ml. A BSA solution of 1.7 mg/ml was prepared in immobilization buffer B and further diluted to a final concentration of 20 μg/ml. Protein immobilization on sensor chips with a carboxymethyl dextran matrix (SPR-2 Amine HC-E, *Sierra Sensors*) was performed according to the following protocol: The chip surface was activated by injecting the activation solution (200 mM EDC and 50 mM NHS) for 5 min. Protein samples were injected on the corresponding spots on the chip surface for 8 min. To inactivate remaining reactive sites

1 M ethanolamine at pH 8.5 was injected for 5 min. Sensor chip I was prepared with hGal-1 on spot 2, at a level of 4707 RU, and BSA as reference on spot 1, at a level of 7523 RU. After immobilization blank buffered was injected until the baseline had been stabilized. For affinity measures 2 mM stock solutions of the ligands were prepared and serially diluted twofold to yield the indicated concentrations. One-concentration-screens were performed with ligand solutions of 100 μM. Samples were injected for 2 min over each spot and reference measures performed with blank buffer after every second injection. Each concentration was measured at least in duplicate. The recorded data were evaluated with Scrubber2 software (version 2.0c, BioLogic Software) and measured raw data double-referenced.

ITC

ITC experiments for thermal characterization of hGal-1 ligand interaction were carried out by Dr. Petra Schneider on a high-sensitivity nanoITC instrument. The instrument comprises a reference and measuring cell with a volume of 177 μl and a syringe for ligand addition with a volume 50 μl. hGal-1 and ligand samples were prepared in the identic buffer to yield the indicated concentrations. The protein solution (V = 300 μl) was degassed prior to use and filled in the measuring cell. The syringe was filled with 50 μl of ligand solution. Data were recorded by NanoAnalyze computer software from TA Instruments. Titration was started with addition of 1 μl ligand solution and data omitted from data analysis. For data acquirement 20 aliquots of 2.5 μl were titrated to the measuring cell with buffered hGal-1. The recorded data were corrected for heat of dilution of the titrated ligand sample and analyzed with the "independent" model of the software.

8.3 Instruments & Materials for Organic Synthesis

Instruments

Nuclear Magnetic Resonance Spectroscopy: Proton nuclear magnetic resonance (^{1}H-NMR) spectra were measured on a *BRUKER AVANCE 400 FT-NMR* or a *BRUKER AVANCE DMX 600 FT-NMR* spectrometer at 25 °C. Proton chemical shifts (δ scale) are expressed in parts per million (ppm) and were determined relative to a residual protic solvent as an internal reference ($CDCl_3$: δ = 7.26 ppm, MeOD: δ = 3.31 ppm, d_6-acetone: δ = 2.05 ppm). Data for ^{1}H-NMR spectra are listed as follows: chemical shift (δ ppm) (multiplicity, integration, coupling constants (Hz), assigned proton). Couplings are indicated as: s = singlet, d = doublet, t = triplet, m = mulitplet. Carbon nuclear magnetic resonance (^{13}C-NMR) spectra were recorded with the same *BRUKER* spectrometers at 100.9 and 150.9 MHz, respectively. Carbon chemical shifts (δ scale) are indicated in parts per million (ppm) as well and calibrated to the carbon resonance of the respective solvent ($CDCl_3$: δ = 77.16 ppm, MeOD: δ = 49.00 ppm, d_6-acetone: δ = 206.26 ppm). For interpretation of ^{1}H- and ^{13}C-spectra a selection of 2D-NMR experiments (COSY, HSQC, HMBC) were considered as appropriate. The numbering of proton and carbon atoms in the assignment of NMR signals in the following characterizations does not conform to the IUPAC nomenclature.

Mass spectrometry: Mass spectrometry (MS) measurements were performed on a *BRUKER Daltonics-Microflex MALDI TOF-MS* (matrix-assisted laser desorption ionization, MALDI) or on a *BRUKER Daltonics autoflex II* (electronspray ionization, ESI) instrument.

Optical rotation polarimetry: Optical rotations were determined at the given temperature (T in [°C]) on a *Jasco P1020* polarimeter with a sodium lamp (λ = 589 nm, D-line) and measured in a cell with a path length (l) of 10 cm. Concentrations are indicated in g/100 ml. Specific optical rotations ($[\alpha]_D{}^T$) were calculated according the equation $[\alpha]_D{}^T = 1000 \cdot \alpha/(c \cdot l)$ and are listed in $^\circ 10^{-1} cm^2 g^{-1}$.

High-pressure microwave apparatus: Reactions with microwaves were performed in a *µCHEMIST ATC-FO 300* microwave apparatus by *MLS*.

Mixing instrument: Small volume reactions were carried out in an *Eppendorf Thermomixer comfort* device as indicated.

Balances: Chemicals were weighed on the laboratory scale *ALS 220-4* by

Kern & Sohn GmbH and on the micro scale *MC 5* by *Sartorius AG*.

Materials

Solvents: All solvents were distilled prior to use. Anhydrous solvents were prepared as follows: CH_2Cl_2 and DMF were distilled over calcium hydride, MeOH over magnesium methoxide and pyridine over KOH. Anhydrous solvents were distilled freshly before use or stored over molecular sieves for short periods.

Reagents: All reagents were purchased from commercial sources (*Merck*, *Sigma-Aldrich*, *Fluka*, *Carbosynth*) and applied without further purification unless specified otherwise.

Inert gas: Reactions with anhydrous conditions were carried out under an atmosphere of nitrogen (99.996%) by *Linde* without further treatment and in oven-dried glassware (180 °C oven temperature).

Thin layer chromatography (tlc): Tlc was performed with pre-coated silica gel sheets (*POLYGRAM®SIL G/UV254*) from *MACHEREY-NAGEL GmbH & Co. KG* and reaction process visualized by exposure to ultraviolet light (UV, 254 nm, *BRENDA NU-6KL 2x6 W*) or by staining with an acidic solution of *N*-(1-naphthyl)-ethylenediamine in MeOH (0.3% (m/v) *N*-(1-naphthyl)-ethylenediamine, 5.0% (v/v) conc. sulfuric acid, 94.7% (v/v) MeOH).

Column chromatography: Flash column chromatography was carried out with silica gel of *MACHEREY-NAGEL GmbH & Co. KG* (particle size 0.032-0.062 mm). Solvent composition is expressed in volume parts (v/v).

8.4 Syntheses towards Novel hGal-1 Ligands

8.4.1 *N*-Acetyl-1-*O*-allyl-β-D-lactosamine (23)

2-Acetamido-3,4,6-tri-*O*-acetyl-1-*O*-allyl-2-deoxy-β-D-glucopyranoside (16)

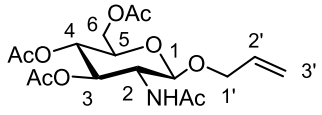

16

TMSOTf (2.70 ml, 14.9 mmol) was added to a solution of **17** (4.90 g, 12.6 mmol) in anhydrous CH_2Cl_2 (60 ml) and refluxed for 3 d. Allyl alcohol (2.57 ml, 37.8 mmol) was added and after 3 h at 45 °C the reaction was cooled down and quenched with NEt_3 (2.5 ml, 17.9 mmol). The mixture was filtered off, concentrated and purified by column chromatography (EE/Cy 5:2 $\rightarrow$ EE/Cy 4:1) to obtain a colorless solid (3.02 g, 7.80 mmol, 62%).

Formular : $C_{17}H_{25}NO_9$ (387.38 g/mol)

$\boldsymbol{R_f}$: 0.13 (EE/Cy 4:1)

^{1}**H** (**600 MHz**, **CDCl$_3$**) : δ = 5.89-5.83 (m, 1H, H-2'); 5.45 (d, 1H, ^3J = 8.8 Hz, N*H*); 5.29 (dd, 1H, ^3J = 10.6, 9.2 Hz, *H*-3); 5.27 (dddd, 1H, ^3J = 17.2 Hz, ^2J = 1.6 Hz, ^4J = 1.3 Hz, *H*-3'$_{trans}$); 5.20 (dddd, 1H, ^3J = 10.4 Hz, ^2J = 1.6 Hz, ^4J = 1.3 Hz, *H*-3'$_{cis}$); 5.08 (dd, 1H, ^3J = 9.8, 9.2 Hz, *H*-4); 4.71 (d, 1H, ^3J = 8.3 Hz, *H*-1); 4.34 (dddd, 1H, ^2J = 13.0 Hz, ^3J = 5.0 Hz, ^4J = 1.3 Hz, *H*-1'a); 4.26 (dd, 1H, ^2J = 12.3 Hz, ^3J = 4.8 Hz, *H*-6a); 4.14 (dd, 1H, ^2J = 12.3 Hz, ^3J = 2.5 Hz, *H*-6b); 4.09 (dddd, 1H, ^2J = 13.0 Hz, ^3J = 6.3 Hz, ^4J = 1.3 Hz, *H*-1'b); 3.90-3.85 (m, 1H, *H*-2); 3.69 (ddd, 1H, ^3J = 9.8, 4.8, 2.5 Hz, *H*-5); 2.09, 2.03, 2.02, 1.95 (s, 12 H, 4 x C(O)C*H*$_3$) ppm.

^{13}**C** (**150.9 MHz**, **CDCl$_3$**) : δ = 170.91, 170.72, 170.13, 169.39 (4 x *C*(O)CH$_3$); 133.49 (*C*-2'); 117.88 (*C*-3'); 99.61 (*C*-1); 72.30 (*C*-3); 71.81 (*C*-5); 69.95 (*C*-1'); 68.59 (*C*-4); 62.11 (*C*-6); 54.81 (*C*-2); 23.37, 20.75, 20.69, 20.63 (4 x C(O)*C*H$_3$) ppm.

HRMS (**ESI**, $\mathbf{m/z}$) : calcd. for $C_{17}H_{25}N_9O$ $[M+Na]^+$ 410.14215, found 410.14176, Δppm: 0.95.

$[\alpha]_{\mathbf{D}}^{\mathbf{22}}$: -14.4 (c = 0.5, $CHCl_3$).

2-Acetamido-1-*O*-allyl-2-deoxy-β-D-glucopyranoside (25)

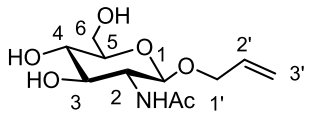

25

16 (2.66 g, 6.87 mmol) was suspended in anhydrous MeOH (10 ml). The addition of NaOMe (13.7 ml, 0.5 M in MeOH, 6.87 mmol) yielded a clear solution that was stirred for 15 min at rt. The mixture was neutralized with Amberlite® IR 125, the cation exchanger filtered off and the solvent evaporated. The product was isolated as a colorless solid (1.71 g, 6.54 mmol, 95%).

Formular : $C_{11}H_{19}NO_6$ (261.27 g/mol)

^{1}H (600 MHz, MeOD) : δ = 5.93-5.86 (m, 1H, *H*-2'); 5.28 (dddd, 1H, ^3J = 17.2 Hz, ^2J = 1.8 Hz, ^4J = 1.8 Hz, *H*-3'$_{trans}$); 5.14 (dddd, 1H, ^3J = 10.6 Hz, ^2J = 1.8 Hz, ^4J = 1.5 Hz, *H*-3'$_{cis}$); 4.44 (d, 1H, ^3J = 8.4 Hz, *H*-1); 4.34 (dddd, 1H, ^2J = 13.3 Hz, ^3J = 4.9 Hz, ^4J = 1.8 Hz, *H*-1'a); 4.08 (dddd, 1H, ^2J = 13.3 Hz, ^3J = 5.8 Hz, ^4J = 1.5 Hz, *H*-1'b); 3.89 (dd, 1H, ^2J = 11.9 Hz, ^3J = 2.3 Hz, *H*-6a); 3.69 (dd, 1H, ^2J = 11.9 Hz, ^3J = 6.0 Hz, *H*-6b); 3.68 (dd, ^3J = 10.3, 8.4 Hz, *H*-2); 3.45 (dd, 1H, ^3J = 10.3, 8.6 Hz, *H*-3); 3.34-3.31 (m, 1H, *H*-4); 3.26 (ddd, 1H, ^3J = 9.7, 6.0, 2.3 Hz, *H*-5); 1.98 (s, 3H, C(O)CH_3) ppm.

^{13}C (150.9 MHz, MeOD) : δ = 173.75 (*C*(O)CH$_3$); 135.61 (*C*-2'); 116.91 (*C*-3'); 101.86 (*C*-1); 78.02 (*C*-5); 76.10 (*C*-3); 72.15 (*C*-4); 70.69 (*C*-1'); 62.81 (*C*-6); 57.34 (*C*-2); 22.92 (C(O)*C*H$_3$) ppm.

HRMS (ESI, m/z) : calcd. for $C_{11}H_{19}NO_6$ $[M+Na]^+$ 284.11049, found 284.11062, Δppm: 0.39.

$[\alpha]_D^{21}$: -34.0 (c = 0.5, MeOH).

2-Acetamido-1-*O*-allyl-4,6-*O*-benzylidene-2-deoxy-β-D-glucopyranoside (59)

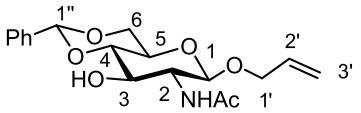

59

Benzaldehyde dimethylacetal (1.45 ml, 9.72 mmol) and CSA (51.0 mg, 219 μmol) were added to a suspension of **25** (1.27 g, 4.86 mmol) in anhydrous CH_3CN (20 ml). The suspension was stirred at rt for 12 h, neutralized with NEt_3 (0.76 ml, 5.47 mmol) and concentrated. The crude product was purified by column chromatography (CH_2Cl_2/MeOH 20:1) to yield a colorless solid (1.70 g, 4.86 mmol, quant.).

Formular : $C_{18}H_{23}NO_6$ (349.38 g/mol)

$\boldsymbol{R_f}$: 0.28 (CH_2Cl_2/MeOH 15:1)

^{1}H (600 MHz, MeOD) : δ = 7.51-7.49 (m, 2H, H_{arom}); 7.36-7.34 (m, 3H, H_{arom}); 5.92-5.86 (m, 1H, *H*-2'); 5.61 (s, 1H, *H*-1"); 5.28 (dddd, 1H, ^3J = 17.2 Hz, ^4J = 1.8 Hz, ^2J = 1.7 Hz, *H*-3'$_{trans}$); 5.16 (dddd, 1H, ^3J = 10.5 Hz, ^2J = 1.7 Hz, ^4J = 1.5 Hz, *H*-3'$_{cis}$); 4.58 (d, 1H, ^3J = 8.2 Hz, *H*-1); 4.32-4.28 (m, 2H, *H*-1'a, *H*-6a); 4.07 (dddd, 1H, ^2J = 13.4 Hz, ^3J = 5.8 Hz, ^4J = 1.5 Hz, *H*-1'b); 3.83-3.75 (m, 3H, *H*-2, *H*-4, *H*-6b); 3.56-3.53 (m, 1H, *H*-3); 3.45-3.41 (m, 1H, *H*-5); 1.99 (s, 3H, C(O)CH_3) ppm.

^{13}C (150.9 MHz, MeOD) : δ = 173.74 (*C*(O)CH_3); 139.11 ($C_{arom,\ quart}$); 135.42 (*C*-2'); 129.94 ($C_{arom,\ p}$); 129.04, 127.51 (4 x C, $C_{arom,\ o}$, $C_{arom,\ m}$); 117.07 (*C*-3'); 102.94 (*C*-1"); 102.54 (*C*-1); 82.88 (*C*-3); 72.57 (*C*-4); 71.07 (*C*-1'); 69.66 (*C*-6); 67.68 (*C*-5); 57.99 (*C*-2); 22.94 (C(O)*C*H_3) ppm.

HRMS (ESI, m/z) : calcd. for $C_{18}H_{23}NO_6$ $[M+Na]^+$ 372.14176, found 372.14140, Δppm: 0.97.

$[\alpha]_D^{21}$: -84.5 (c = 0.5, MeOH).

2-Acetamido-3-*O*-acetyl-1-*O*-allyl-4,6-*O*-benzylidene-2-deoxy-β-D-glucopyranoside (26)

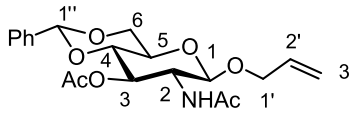

26

59 (375 mg, 1.07 mmol) was dissolved in anhydrous pyridine (5 ml), acetic anhydride (0.51 ml, 5.37 mmol) was added and the mixture stirred at rt for 12 h. Tlc (CH_2Cl_2/MeOH 20:1) monitored complete conversion of the educt. The mixture was concentrated and coevaporated with toluene to obtain the product as a colorless solid (412 mg, 1.05 mmol, 98%).

Formular : $C_{20}H_{25}NO_7$ (391.42 g/mol)

$\boldsymbol{R_f}$: 0.49 (CH_2Cl_2/MeOH 20:1)

^{1}**H** (**600 MHz**, **CDCl$_3$**) : δ = 7.45-7.43 (m, 2H, H_{arom}); 7.37-7.34 (m, 3H, H_{arom}); 5.87-5.80 (m, 1H, *H*-2'); 5.63 (d, 1H, ^3J = 9.4 Hz, N*H*); 5.51 (s, 1H, *H*-1"); 5.28-5.24 (m, 2H, *H*-3'$_{trans}$, *H*-3); 5.19 (dddd, 1H, ^3J = 10.5 Hz, ^2J = 1.4 Hz, ^4J = 1.4 Hz, *H*-3'$_{cis}$); 4.55 (d, 1H, ^3J = 8.4 Hz, *H*-1); 4.34 (dd, 1H, ^2J = 10.5 Hz, ^3J = 5.0 Hz, *H*-6a); 4.31 (dddd, 1H, ^2J = 13.1 Hz, ^3J = 5.0 Hz, ^4J = 1.5 Hz, *H*-1'a); 4.13-4.09 (m, 1H, *H*-2); 4.02 (dddd, 1H, ^2J = 13.1 Hz, ^3J = 6.1 Hz, ^4J = 1.4 Hz, *H*-1'b); 3.81 (dd, 1H, ^2J = 10.5 Hz, ^3J = 10.3 Hz, *H*-6b); 3.71 (dd, ^3J = 9.5 Hz, *H*-4); 3.54-3.50 (m, 1H, *H*-5); 2.08, 1.92 (s, 6H, 2 x C(O)CH_3) ppm.

^{13}**C** (**150.9 MHz**, **CDCl$_3$**) : δ = 171.33, 170.13 (2 x *C*(O)CH$_3$), 136.92 ($C_{arom,\ quart}$); 133.49 (*C*-2'); 129.12 ($C_{arom,\ p}$), 128.24, 126.12 (4 x C, $C_{arom,\ o}$, $C_{arom,\ m}$), 117.62 (*C*-3'); 101.42 (*C*-1"); 101.00 (*C*-1); 78.61 (*C*-4); 71. 80 (*C*-3); 70.02 (*C*-1'); 68.63 (*C*-6); 66.46 (*C*-5); 54.64 (*C*-2); 23.34, 20.89 (2 x C(O)*C*H$_3$) ppm.

HRMS (**ESI**, $\mathbf{m/z}$) : calcd. for $C_{20}H_{25}NO_7$ $[M+Na]^+$ 414.15232, found 414.15197, Δppm: 0.85.

$[\alpha]_{\mathbf{D}}^{\mathbf{22}}$: -86.0 (c = 0.5, $CHCl_3$).

2-Acetamido-3-*O*-acetyl-1-*O*-allyl-6-*O*-benzyl-2-deoxy-β-D-glucopyranoside (13)

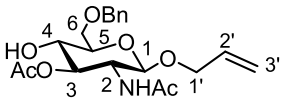

13

26 (300 mg, 766 μmol) was dissolved in anhydrous CH_2Cl_2 (10 ml), cooled to 0 °C and treated with TFAA (107 μl, 766 μmol) and Et_3SiH (735 μl, 4.60 mmol). After 10 min TFA (293 μl, 3.83 mmol) was added dropwise and the mixture was stirred for 2 h at 0 °C before it was warmed to rt in 3 h and quenched with NEt_3 (1.07 ml, 7.66 mmol). The mixture was diluted with CH_2Cl_2 (10 ml) and washed with sat. $NaHCO_3$ solution (2 x 10 ml) and H_2O (10 ml). The combined aqueous phases were extracted once with CH_2Cl_2 (10 ml), the combined organic phases dried over Na_2SO_4 and concentrated under reduced pressure. Column chromatography (CH_2Cl_2/MeOH 20:1) afforded a colorless solid (255 mg, 648 μmol, 85%).

Formular : $C_{20}H_{27}NO_7$ (393.43 g/mol)

$\boldsymbol{R_f}$: 0.19 (CH_2Cl_2/MeOH 30:1)

^{1}**H** (**600 MHz**, $\mathbf{CDCl_3}$) : δ = 7.37-7.28 (m, 5H, H_{arom}); 5.88-5.81 (m, 1H, *H*-2'); 5.52 (d, 1H, ^3J = 8.9 Hz, N*H*); 5.26 (dddd, 1H, ^3J = 17.2 Hz, ^2J = 1.5 Hz, ^4J = 1.4 Hz, *H*-3'$_{trans}$); 5.17 (dddd, 1H, ^3J = 10.7 Hz, ^2J = 1.5 Hz, ^4J = 1.4 Hz, *H*-3'$_{cis}$); 5.04 (dd, 1H, ^3J = 10.7, 9.1 Hz, *H*-3); 4.62 (d, 1H, ^2J = 11.9 Hz, -OCH_2Ph); 4.57 (d, 1H, ^2J = 11.9 Hz, -OCH_2Ph); 4.52 (d, 1H, ^3J = 8.4 Hz, *H*-1); 4.32 (dddd, 1H, ^2J = 13.1 Hz, ^3J = 4.9 Hz, ^4J = 1.4 Hz, *H*-1'a); 4.06 (dddd, 1H, ^2J = 13.1 Hz, ^3J = 6.2 Hz, ^4J = 1.4 Hz, *H*-1'b); 3.96 (m, 1H, *H*-2); 3.81 (dd, 1H, ^2J = 10.2 Hz, ^3J = 5.1 Hz, *H*-6a); 3.78-3.73 (m, 2H, *H*-6b, *H*-4); 3.55-3.52 (m, 1H, *H*-5); 2.10, 1.95 (s, 6H, C(O)CH_3) ppm.

^{13}**C** (**150.9 MHz**, $\mathbf{CDCl_3}$) : δ = 171.96 (-OC(O)CH_3); 170.16 (-NHC(O)CH_3); 137.48 ($C_{arom,\ quart}$); 133.70 (*C*-2'); 128.51 (2C, $C_{arom,\ m}$, $C_{arom,\ o}$); 127.94 ($C_{arom,\ p}$); 127.76 (2C, $C_{arom,\ m}$, $C_{arom,\ o}$); 117.49 (*C*-3'); 100.08 (*C*-1); 75.34 (*C*-3); 73.80 (2C, *C*-5, -OCH_2Ph); 71.00 (*C*-4); 70.51 (*C*-6); 69.62 (*C*-1'); 54.02 (*C*-2); 23.36 (-OC(O)CH_3); 20.94 (NHC(O)CH_3) ppm.

HRMS (**ESI**, $\mathbf{m/z}$) : calcd. for $C_{20}H_{27}NO_7$ $[M+Na]^+$ 416.16797, found 416.16816, Δppm: 0.46.

$[\alpha]_D^{22}$: -55.7 (c = 0.5, $CHCl_3$).

2-Acetamido-4-*O*-acetyl-1-*O*-allyl-6-*O*-benzyl-2-deoxy-β-D-glucopyranoside (29)

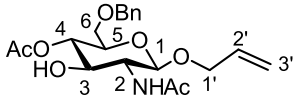

29

29 appeared as side product in few reactions to **13**.

Formular : $C_{20}H_{27}NO_7$ (393.43 g/mol)

$\boldsymbol{R_f}$: 0.13 (CH_2Cl_2/MeOH 30:1)

^{1}H (400 MHz, $CDCl_3$) : δ = 7.36-7.27 (m, 5H, H_{arom}); 5.96-5.86 (m, 1H, *H*-2'); 5.73 (d, 1H, ^3J = 4.6 Hz, N*H*); 5.30 (dddd, 1H, ^3J = 17.1 Hz, ^2J = 1.6 Hz, ^4J = 1.4 Hz, *H*-3'$_{trans}$); 5.24 (dddd, 1H, ^3J = 10.4 Hz, ^2J = 1.6 Hz, ^4J = 1.4 Hz, *H*-3'$_{cis}$); 4.90 (dd, 1H, ^3J = 9.1 Hz, *H*-4); 4.62 (d, 1H, ^3J = 8.3 Hz, *H*-1); 4.57 (d, 1H, ^2J = 12.0 Hz, -OCH_2Ph); 4.52 (d, 1H, ^2J = 11.9 Hz, -OCH_2Ph); 4.38 (dddd, 1H, ^2J = 12.7 Hz, ^3J = 5.2 Hz, ^4J = 1.6 Hz, *H*-1'a); 4.10 (dddd, 1H, ^2J = 12.7 Hz, ^3J = 6.5 Hz, ^4J = 1.4 Hz, *H*-1'b); 3.95 (dd, 1H, ^3J = 9.9, 9.1 Hz, *H*-3); 3.64-3.56 (m, 3H, *H*-6a, *H*-6b, *H*-5); 3.50-3.44 (m, 1H, *H*-2); 2.04, 2.01 (s, 6H, C(O)CH_3) ppm.

^{13}C (100.6 MHz, $CDCl_3$) : δ = 172.19 (-NC(O)CH_3); 170.55 (-OHC(O)CH_3); 137.85 ($C_{arom,\ quart}$); 133.44 (*C*-2); 128.37, 127.80, 127.72 (5C, C_{arom}); 118.26 (*C*-3'); 99.99 (*C*-1); 73.61 (*C*-5); 73.57 (-OCH_2Ph); 73.02 (*C*-3); 72.33 (*C*-4); 69.90 (*C*-1'); 69.28 (*C*-6); 58.83 (*C*-2); 25.56 (-NHC(O)CH_3); 20.89 (-OC(O)CH_3) ppm.

HRMS (ESI, m/z) : calcd. for $C_{20}H_{27}NO_7$ $[M+Na]^+$ 416.16797, found 416.797, Δppm: 2.50.

1,2,3,4,6-Penta-*O*-acetyl-β-D-galactopyranoside (32)

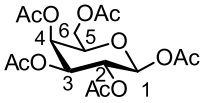

32

A suspension of sodium acetate (4.76 g, 58.1 mmol) in acetic anhydride (100 ml, 1.06 mol) was heated to reflux at 150 °C . D-Galactose (5.23 g, 29.0 mmol) was added

and the mixture refluxed for 2.5 h. The cooled mixture was then poured on ice water (600 ml) and kept at 4 °C overnight to form a yellowish viscous oil. The aqueous supernatant was removed, the residue kept at 4 °C for further 24 h and then filtered off to obtain the product as a colorless solid (3.18 g, 8.17 mmol, 28%).

Formular : $C_{16}H_{22}O_{11}$ (390.34 g/mol)

$\boldsymbol{R_f}$: 0.1 (EE/Cy 3:1)

$^{\mathbf{1}}\mathbf{H}$ $(\mathbf{400\ MHz}, \mathbf{CDCl_3})$: δ = 5.70 (d, 1H, ^3J = 8.3 Hz, *H*-1); 5.43 (dd, 1H, ^3J = 3.4, 1.0 Hz, *H*-4); 5.33 (dd, 1H, ^3J = 10.5, 8.3 Hz, *H*-2); 5.08 (dd, 1H, ^3J = 10.5, 3.4 Hz, *H*-3); 4.19-4.10 (m, 2H, *H*-6a, *H*-6b); 4.07-4.03 (m, 1H, *H*-5); 2.16, 2.12, 2.04, 2.00 (s, 15H, 5 x C(O)CH_3) ppm.

$^{\mathbf{13}}\mathbf{C}$ $(\mathbf{100.6\ MHz}, \mathbf{CDCl_3})$: δ = 170.31, 170.09, 169.93, 169.34, 168.94 (5 x *C*(O)CH_3); 92.18 (*C*-1); 71.72 (*C*-5); 70.84 (*C*-3); 67.85 (*C*-2); 66.80 (*C*-4) 61.01 (*C*-6); 20.79, 20.62, 20.60, 20.51 (5 x C(O)*C*H_3) ppm.

MS $(\mathbf{MALDI},\ \mathbf{m/z})$: calcd. for $C_{16}H_{22}O_{11}$ $[M+Na]^+$ 413.12, found 413.12.

$[\alpha]_{\mathbf{D}}^{\mathbf{22}}$: 20.87 (c = 0.1, $CHCl_3$).

2,3,4,6-Tetra-*O*-acetyl-D-galactopyranose (35)

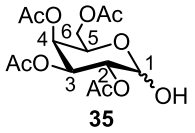

35

A solution of **32** (5.00 g, 12.8 mmol) in anhydrous DMF (15 ml) was heated to 50 °C before hydrazine acetate (1.48 g, 16.0 mmol) was added. The mixture was stirred for 45 min at 50 °C, diluted with EE (80 ml) and washed with H_2O (3 x 20 ml), 0.1 M HCl (20 ml), sat. $NaHCO_3$ solution (20 ml) and H_2O (20 ml). The aqueous phase was reextracted once with EE (20 ml), the combined organic phases dried over Na_2SO_4 and concentrated. The crude product was purified by column chromatography (CH_2Cl_2 $\rightarrow$ CH_2Cl_2/MeOH 30:1) to obtain the product as a colorless oil (3.13 g, 8.99 mmol, 70%) in an anomeric mixture of α/β 2.7/1.

Formular : $C_{14}H_{20}O_{10}$ (348.30 g/mol)

$\boldsymbol{R_f}$: 0.35 (CH_2Cl_2/MeOH 30:1)

^{1}H (400 MHz, $CDCl_3$) : δ = 5.50 (d, 1H, ^3J = 3.5 Hz, *H*-1α); 5.46 (dd, 1H, ^3J = 3.4, 1.3 Hz, *H*-4α); 5.42-5.38 (m, 2H, *H*-3α, *H*-4β); 5.14 (dd, 1H, ^3J = 10.8, 3.5 Hz, *H*-2α); 5.07-5.03 (m, 2H, *H*-2β, *H*-3β); 4.69 (d, 1H, ^3J = 7.8 Hz, *H*-1β); 4.46 (ddd, 1H, ^3J = 6.8, 1.3 Hz, *H*-5α); 4.18-4.03 (m, 4H, *H*-6α a/b, *H*-6β a/b); 3.95 (ddd, 1H, ^3J = 6.4, 1.2 Hz, *H*-5β); 2.14 (β), 2.13 (α), 2.09 (β), 2.08 (α), 2.04 (α), 2.04 (β), 1.98 (β), 1.98 (α) (s, 24 H, 4 x C(O)CH_3,α, 4 x C(O)CH_3,β) ppm.

^{13}C (100.6 MHz, $CDCl_3$) : δ = 171.06 (β), 170.53 (α), 170.48 (β), 170.37 (α), 170.23 (α), 170.15 (β), 170.04 (α), 170.01 (β) (4 x *C*(O)CH_3(α), 4 x *C*(O)CH_3(β)), 95.95 (*C*-1β); 90.62 (*C*-1α); 71.00, 70.97, 70.37 (*C*-5β, *C*-3β, *C*-2β); 68.34 (*C*-2α); 68.19 (*C*-4α); 67.24 (*C*-3α); 67.13 (*C*-4β); 66.15 (*C*-5α); 61.77 (*C*-6α); 61.43 (*C*-6β); 20.77 (β, α), 20.66 (α), 20.64 (β), 20.61 (α), 20.59 (α), 20.56 (β), 20.50 (β) (4 x C(O)*C*H_3(α), 4 x C(O)*C*H_3(β) ppm.

HRMS (ESI, m/z) : calcd. for $C_{14}H_{20}O_{10}$ $[M+Na]^+$ 371.09487, found 371.09467, Δppm: 0.54.

2,3,4,6-Tetra-*O*-acetyl-1-*O*-trichloroacetimido-α-D-galactopyranoside (37)

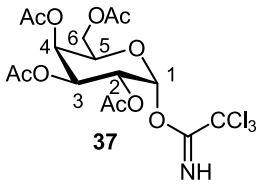

37

35 (2.16 g, 6.20 mmol) was dissolved in anhydrous CH_2Cl_2 (40 ml), cooled to 0 °C and treated with $CNCCl_3$ (9.32 ml, 93.0 mmol) and DBU (0.926 ml, 6.20 mmol). Both reagents were dried over mol sieves before usage. After the solution was stirred for 1 h at 0 °C charcoal was added and the mixture filtered over Celite®. Column chromatography (Cy/EE 5:1→Cy/EE 2:1) afforded exclusively the α-anomer as a light yellow sticky solid (2.71 g, 5.50 mmol, 89%).

Formular : $C_{16}H_{20}Cl_3NO_{10}$ (492.69 g/mol)

$\boldsymbol{R_f}$: 0.44 (EE/Cy 1:1)

^{1}H (600 MHz, $CDCl_3$) : δ = 8.67 (s, 1H, N*H*); 6.60 (d, 1H, ^3J = 3.6 Hz, *H*-1); 5.56 (dd, 1H, ^3J = 3.2, 1.1 Hz, *H*-4); 5.43 (dd, 1H, ^3J = 10.8, 3.2 Hz, *H*-3); 5.37 (dd, 1H, ^3J = 10.8, 3.6 Hz, *H*-2); 4.45-4.43 (m, 1H, *H*-5); 4.17 (dd, 1H, ^2J = 11.4 Hz, ^3J = 6.8 Hz, *H*-6a); 4.09 (dd, 1H, ^2J = 11.4 Hz, ^3J = 6.7 Hz, *H*-6b); 2.17, 2.03, 2.02 (s, 12H, 4 x C(O)CH_3) ppm.

^{13}C (150.9 MHz, $CDCl_3$) : δ = 170.29, 170.09, 170.07, 169.97 (4 x *C*(O)CH_3), 160.95 (*C*=NH); 93.53 (*C*-1); 90.76 (*C*Cl_3); 68.98 (*C*-5); 67.50 (*C*-3); 67.36 (*C*-4); 66.90 (*C*-2); 61.25 (*C*-6); 20.66, 20.63, 20.60, 20.54 (4 x C(O)*C*H_3) ppm.

HRMS (ESI, m/z) : calcd. for $C_{16}H_{20}Cl_3NO_{10}$ $[M+Na]^+$ 514.00450, found 514.00417, Δppm: 0.64.

$[\alpha]_D^{22}$: 109.7 (c = 0.2, $CHCl_3$).

2,3,4,6-Tetra-*O*-acetyl-β-D-galactopyranosyl-(1$\rightarrow$4)-2-acetamido-3-*O*-acetyl-1-*O*-allyl-6-*O*-benzyl-2-deoxy-β-D-glucopyranoside (38)

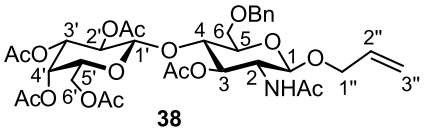

38

To a solution of **13** (1.06 g, 2.69 mmol) in anhydrous CH_2Cl_2 (10 ml) **37** (1.99 g, 4.04 mmol) and $BF_3{\cdot}Et_2O$ (512 μl, 4.04 mmol) were added at rt. After 1 h the reaction was quenched with NEt_3 (638 μl, 4.58 mmol), diluted with CH_2Cl_2 (10 ml), washed with sat. $NaHCO_3$ solution (5 ml) and H_2O (5 ml). The aqueous phase was reextracted once with CH_2Cl_2 (5 ml) and the combined organic phases were dried over Na_2SO_4 and concentrated. The crude product was purified by column chromatography (CH_2Cl_2/MeOH 80:1 $\rightarrow$ CH_2Cl_2/MeOH 50:1) to obtain a colorless solid (1.54 g, 2.13 mmol, 79%).

Formular : $C_{34}H_{45}NO_{16}$ (723.72 g/mol)

R_f : 0.18 (CH_2Cl_2/MeOH 30:1)

^{1}H (600 MHz, $CDCl_3$) : δ = 7.40-7.31 (m, 5H, Ph); 5.88-5.82 (m, 1H, *H*-2"); 5.54 (d, 1H, ^3J = 9.4 Hz, N*H*); 5.30 (dd, 1H, ^3J = 3.5, 1.0 Hz, *H*-4'); 5.26 (dddd, 1H, ^3J = 17.3 Hz, ^4J = 1.7 Hz, ^2J = 1.6 Hz, *H*-3"$_{trans}$); 5.18 (dddd, 1H, ^3J = 5.2 Hz,

^2J = 1.6 Hz, ^4J = 1.5 Hz, *H*-3"$_{cis}$); 5.05-5.01 (m, 2H, *H*-2', *H*-3); 4.86 (dd, 1H, ^3J = 10.4, 3.5 Hz, *H*-3'); 4.73 (d, 1H, ^2J = 12.1 Hz, -CH_2Ph); 4.50 (d, 1H, ^2J = 12.1 Hz, -CH_2Ph); 4.45 (d, 1H, ^3J = 8.0 Hz, *H*-1 or *H*-1') 4.45 (d, 1H, ^3J = 7.6 Hz, *H*-1 or *H*-1'); 4.33 (dddd, 1H, ^2J = 13.2 Hz, ^3J = 4.9 Hz, ^4J = 1.5 Hz, *H*-1"a); 4.09-4.03 (m, 4H, *H*-1"b, *H*-2, *H*-6'a, *H*-6'b); 3.95 (dd, ^3J = 8.4 Hz, *H*-4); 3.74-3.73 (m, 2H, *H*-6a, *H*-6a); 3.71-3.69 (m, 1H, *H*-5'); 3.48 (ddd, 1H, ^3J = 8.4, 3.1 Hz, *H*-5); 2.13, 2.06, 2.03, 1.96 (s, 18H, 6 x C(O)CH_3) ppm.

^{13}C (**150.9 MHz, $CDCl_3$**) : δ = 170.88, 179.37, 170.188, 170.34, 169.16 (6 x *C*(O)CH_3); 137.81 ($C_{arom,\ quart}$); 133.71 ($C_{arom,\ p}$); 128.58 ($C_{arom,\ m}$, $C_{arom,\ o}$); 128.02 (*C*-2"); 127.97 ($C_{arom,\ m}$, $C_{arom,\ o}$); 117.37 (*C*-3"); 100.35 (*C*-1'); 100.05 (*C*-1); 74.71 (*C*-5); 74.49 (*C*-4); 73.66 (*C*H_2Ph); 72.47 (*C*-3); 70.83 (*C*-3'); 70.55 (*C*-5'); 69.48 (*C*-1"); 69.11 (*C*-2'); 67.66 (*C*-6); 66.80 (*C*-4'); 60.95 (*C*-6'); 53.24 (*C*-2); 20.83, 20.73, 20.67, 20.64, 20.54 (6 x C(O)*C*H_3) ppm.

HRMS (**ESI**, **m/z**) : calcd. for $C_{34}H_{45}NO_{16}$ $[M+Na]^+$ 746.26306, found 746.26329, Δppm: 0.31.

$[\alpha]_D^{22}$: -25.0 (c = 0.5, $CHCl_3$).

2,3,4,6-Tetra-*O*-acetyl-β-D-galactopyranosyl-(1→4)-2-acetamido-3-*O*-acetyl-1-*O*-allyl-2-deoxy-β-D-glucopyranoside (40)

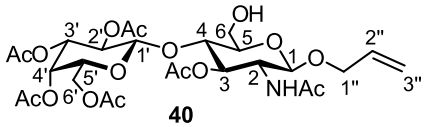

40

DDQ (665 mg, 2.93 mmol) was added to a solution of **38** (424 mg, 586 μmol) in anhydrous CH_2Cl_2 (30 ml) and heated to 45 °C. The mixture was stirred for 48 h at this temperature before H_2O (7 ml) was added. After 2 h at rt the mixture was diluted with CH_2Cl_2 (40 ml) and washed with sat. $NaHCO_3$ solution (40 ml) and brine (40 ml). The combined organic phases were dried over Na_2SO_4 and concentrated. The crude product was purified by column chromatography (CH_2Cl_2/MeOH 100:1 → 20:1) to obtain a light rose solid (333 mg, 526 μmol, 90%).

Formular : $C_{27}H_{39}NO_{16}$ (633.60 g/mol)

R_f : 0.19 (CH_2Cl_2/MeOH 20:1)

^{1}H (600 MHz, $CDCl_3$) : δ = 5.88-5.81 (m, 1H, *H*-2"); 5.55 (d, 1H, ^3J = 9.4 Hz, N*H*); 5.35 (dd, 1H, ^3J = 3.4, 1.0 Hz, *H*-4'); 5.26 (dddd, 1H, ^3J = 17.2 Hz, ^4J = 1.6 Hz, ^2J = 1.5 Hz, *H*-3"$_{trans}$); 5.19 (dddd, 1H, ^3J = 10.5 Hz, ^2J = 1.5 Hz, ^4J = 1.4 Hz, *H*-3"$_{cis}$); 5.11 (dd, 1H, ^3J = 10.5, 8.0 Hz, *H*-2'); 5.07 (dd, 1H, ^3J = 10.5, 9.0 Hz, *H*-3); 4.99 (dd, 1H, ^3J = 10.5, 3.4 Hz, *H*-3'); 4.62 (d, 1H, ^3J = 8.0 Hz, *H*-1'); 4.48 (d, 1H, ^3J = 8.2 Hz, *H*-1); 4.31 (dddd, 1H, ^2J = 13.2 Hz, ^3J = 4.9 Hz, ^4J = 1.6 Hz, *H*-1"a); 4.13-4.00 (m, 4H, *H*-6'a, *H*-6'b, *H*-2, *H*-1"b); 3.94-3.87 (m, 3H, *H*-5', *H*-4, *H*-6a); 3.75-3.72 (m, 1H, *H*-6b); 3.37 (ddd, 1H, ^3J = 9.4, 2.7 Hz, *H*-5); 2.14, 2.07, 2.06, 2.05, 1.96, 1.95 (s, 18H, 6 x C(O)CH_3) ppm.

^{13}C (150.9 MHz, $CDCl_3$) : δ = 171.19, 170.54, 170.32, 170.29, 170.20, 169.45 (6 x *C*(O)CH_3); 133.69 (*C*-2"); 117.77 (*C*-3"); 101.15 (*C*-1'); 100.45 (*C*-1); 75.07 (*C*-5); 74.98 (*C*-4); 73.21 (*C*-3); 71.04 (*C*-3'); 70.75 (*C*-5'); 70.13 (*C*-1"); 69.34 (*C*-2'); 66.91 (*C*-4'); 61.04 (*C*-6'); 60.69 (*C*-6); 54.05 (*C*-2); 23.46, 21.00, 20.86, 20.80, 20.79, 20.68 (6 x C(O)*C*H_3) ppm.

HRMS (ESI, m/z) : calcd. for $C_{27}H_{39}NO_{16}$ $[M+H]^+$ 634.23416, found 634.23433, Δppm: 0.27.

$[\alpha]_D^{22}$: -27.3 (c = 0.2, $CHCl_3$).

β-D-Galactopyranosyl-(1$\rightarrow$4)-2-acetamido-1-*O*-allyl-2-deoxy-β-D-glucopyranoside (23)

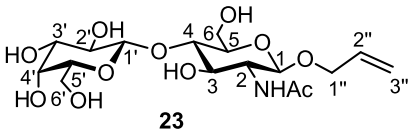

23

40 (40.0 mg, 0.063 mmol) was dissolved in anhydrous MeOH (5 ml) and treated with NaOMe (0.5 M in MeOH, 126 μl, 0.063 mmol). The mixture was stirred for 12 h at rt, neutralized with Amberlite® IR 125, the cation exchanger filtered off and the solvent evaporated. The product was isolated as a colorless solid (21.0 mg, 50.0 μmol, 79%).

Formular : $C_{17}H_{29}NO_{11}$ (423.41g/mol)

R_f : 0.40 (CH_2Cl_2/MeOH 3:1)

^{1}H (600 MHz, MeOD) : δ = 5.91-5.85 (m, 1H, *H*-2"); 5.26 (dddd, 1H, ^3J = 17.2 Hz,

^2J = 1.7 Hz, ^4J = 1.6 Hz, *H*-3"$_{trans}$); 5.13 (dddd, 1H, ^3J = 10.5 Hz, ^2J = 1.7 Hz, ^4J = 1.6 Hz, *H*-3"$_{cis}$); 4.44 (d, 1H, ^3J = 8.4 Hz, *H*-1); 4.37 (d, 1H, ^3J = 7.6 Hz, *H*-1'); 4.32 (dddd, 1H, ^2J = 13.3 H, ^3J = 4.8 Hz, ^4J = 1.6 Hz, *H*-1"a); 4.06 (dddd, 1H, ^2J = 13.3 Hz, ^3J = 5.8 Hz, ^4J = 1.6 Hz, *H*-1"b); 3.91 (dd, 1H, ^2J = 12.2 Hz, ^3J = 2.5 Hz, *H*-6a); 3.85 (dd, 1H, ^2J = 12.2 Hz, ^3J = 4.4 Hz, *H*-6b); 3.81-3.80 (m, 1H, *H*-4'); 3.77-3.74 (m, 2H, *H*-2, *H*-6'a); 3.68 (dd, 1H, ^2J = 11.6 Hz, ^3J = 4.6 Hz, *H*-6'b); 3.63-3.60 (m, 2H, *H*-3, *H*-4); 3.59-3.57 (m, 1H, *H*-5'); 3.53 (dd, 1H, ^3J = 9.8 Hz, 7.6 Hz, *H*-2'); 3.48 (dd, 1H, ^3J = 9.8, 3.2 Hz, *H*-3'); 3.40-3.37 (m, 1H, *H*-5); 1.96 (s, 3H, C((O)CH_3) ppm.

^{13}C (150.9 MHz, MeOD) : δ = 173.56 (*C*(OCH$_3$); 135.54 (*C*-2"); 116.95 (*C*-3"); 105.10 (*C*-1'); 101.88 (*C*-1); 80.94 (*C*-4); 77.15 (*C*-5'); 76.59 (*C*-5); 74.83 (*C*-3'); 74.23 (*C*-3); 72.60 (*C*-2'); 70.75 (*C*-1"); 70.33 (*C*-4'); 62.52 (*C*-6'); 61.94 (*C*-6); 56.63 (*C*-2); 22.90 (C(O)*C*H$_3$) ppm.

HRMS (**ESI**, **m/z**) : calcd. for $C_{17}H_{29}NO_{11}$ $[M+Na]^+$ 446.16302, found 446.16328, Δppm: 0.58.

$[\alpha]_D^{21}$: -28.7 (c = 0.2, MeOH).

8.4.2 *N*-Acetyl-1-*O*-allyl-3'-*O*-propargyl-β-D-lactosamine (10)

2,3,4,6-Tetra-*O*-acetyl-1-bromo-α-D-galactopyranoside (33)

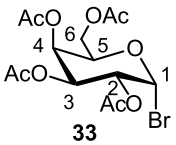

33

A solution of **32** (1.00 g, 2.56 mmol) in anhydrous CH_2Cl_2 (20 ml) was cooled to 0 °C. HBr (33% in CH_3CO_2H, 1.33 ml, 7.69 mmol) was added dropwise and the reaction stirred for 4 h at rt. The mixture was then diluted with CH_2Cl_2 (20 ml) and washed with ice water (2 x 20 ml) and sat. $NaHCO_3$ solution (20 ml). The combined organic phases were dried over Na_2SO_4 and the solvent evaporated to obtain the product as a yellow oil (1.08 g, 2.63 mmol, quant.). For reaction with NaN_3 the bromide was further purified by flash chromatography with Cy/EE 4:1, reducing the yield to 62%.

Formular : $C_{14}H_{19}BrO_9$ (411.20 g/mol)

R_f : 0.35 (CH_2Cl_2/MeOH 80:1)

^{1}H (400 MHz, $CDCl_3$) : δ = 6.69 (d, 1H, ^3J = 4.0 Hz, *H*-1); 5.51 (dd, 1H, ^3J = 3.4, 1.4 Hz, *H*-4); 5.40 (dd, 1H, ^3J = 10.8, 3.4 Hz, *H*-3); 5.05 (dd, 1H, ^3J = 10.8, 4.0 Hz, *H*-2); 4.50-4.46 (m, 1H, *H*-5); 4.18 (dd, 1H, ^2J = 11.4 Hz, ^3J = 6.4 Hz, *H*-6a); 4.10 (dd, 1H, ^2J = 11.4 Hz, ^3J = 6.8 Hz, *H*-6b); 2.15, 2.11, 2.05, 2.01 (s, 12H, 4 x C(O)CH_3) ppm.

^{13}C (100.6 MHz, $CDCl_3$) : δ = 170.26, 170.02, 169.85, 169.70 (4 x *C*(O)CH_3); 88.11 (*C*-1); 71.06 (*C*-5); 67.98 (*C*-3); 67.77 (*C*-2); 66.97 (*C*-4) 60.80 (*C*-6); 20.71, 20.60, 20.54, 20.51 (4 x C(O)*C*H_3) ppm.

MS (MALDI, m/z) : calcd. for $C_{14}H_{19}BrO_9$ $[M+Na]^+$ 433.01, found 433.03.

$[\alpha]_D^{20}$: 220.1 (c = 0.1, $CHCl_3$).

2,3,4,6-Tetra-*O*-acetyl-1-*O*-methyl-β-D-galactopyranoside (60)

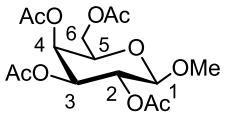

60

33 (500 mg, 1.22 mmol) was dissolved in anhydrous Et_2O (10 ml) and treated with MeOH (62.0 μl, 1.52 mmol) and Ag_2CO_3 (587 mg, 2.13 mmol). The mixture was stirred at rt for 12 h, filtered over Celite® and washed with sat. $FeSO_4 \cdot 7H_2O$ solution (20 ml) and H_2O (2 x 20 ml). The combined organic layers were dried over Na_2SO_4 and the solvent evaporated to yield the product as a yellow oil (300 mg, 828 μmol, 68%).

Formular : $C_{15}H_{22}O_{10}$ (362.33 g/mol)

R_f : 0.8 (CH_2Cl_2/MeOH 20:1)

^{1}H (400 MHz, $CDCl_3$) : δ = 5.39 (dd, 1H, ^3J = 3.4, 1.1 Hz, *H*-4); 5.20 (dd, 1H, ^3J = 10.6, 7.9 Hz, *H*-2); 5.02 (dd, 1H, ^3J = 10.6, 3.4 Hz, *H*-3); 4.40 (d, 1H, ^3J = 7.9 Hz, *H*-1); 4.21 (dd, 1H, ^2J = 11.2 Hz, ^3J = 6.5 Hz, *H*-6a); 4.14 (dd, 1H, ^2J = 11.2 Hz, ^3J = 6.9 Hz, *H*-6b); 3.91 (ddd, 1H, ^3J = 6.9, 6.5, 1.1 Hz, *H*-5); 3.52 (s, 3H, -OCH_3); 2.15, 2.06, 2.05, 1.98 (s, 12H, 4 x C(O)CH_3) ppm.

^{13}C (**100.6 MHz**, **$CDCl_3$**) : δ = 170.38, 170.25, 170.15, 169.47 (4 x *C*(O)CH_3); 102.09 (*C*-1); 70.98 (*C*-3); 70.65 (*C*-5); 68.82 (*C*-2); 67.07 (*C*-4) 61.28 (*C*-6); 56.97 (-O*C*H_3); 20.79, 20.66, 20.56 (4 x C(O)*C*H_3) ppm.

MS (**MALDI**, $\mathbf{m/z}$) : calcd. for $C_{15}H_{22}O_{10}$ $[M+Na]^+$ 385.11, found 385.13.

$[\alpha]_D^{22}$: 127.5 (c = 0.05, $CHCl_3$).

1-*O*-Methyl-β-D-galactopyranoside (15)

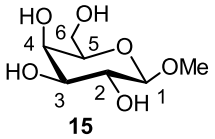

15

60 (118 mg, 326 μmol) was dissolved in anhydrous MeOH (5 ml) and treated with NaOMe (0.5 M in MeOH, 651 μl, 326 μmol). The mixture was stirred for 10 min at rt, neutralized with Amberlite® IR 120, the cation exchanger filtered off and the solvent evaporated. The product was isolated as a colorless solid (46.8 mg, 241 μmol, 74%).

Formular : $C_7H_{14}O_6$ (194.18 g/mol)

$\boldsymbol{R_f}$: 0.1 (CH_2Cl_2/MeOH 10:1)

^{1}H (**400 MHz**, **MeOD**) : δ = 4.18 (d, 1H, ^3J = 7.0 Hz, *H*-1); 3.89 (dd, 1H, ^3J = 3.0, 0.8 Hz, *H*-4); 3.84- 3.76 (m, 2H, *H*-6a, *H*-6b); 3.58 (s, 3H, -OCH_3); 3.58- 3.50 (m, 3H, *H*-5, *H*-2, *H*-3) ppm.

^{13}C (**100.6 MHz**, **MeOD**) : δ = 106.02 (*C*-1); 76.65 (*C*-5); 75.00 (*C*-2); 72.51 (*C*-3); 70.31 (*C*-4); 62.49 (*C*-6); 57.24 (-O*C*H_3) ppm.

MS (**MALDI**, $\mathbf{m/z}$) : calcd. for $C_{10}H_{16}O_6$ $[M+Na]^+$ 217.07, found 217.07.

$[\alpha]_D^{21}$: 11.8 (c = 0.05, CH_3CN).

1-*O*-Methyl-3-*O*-propargyl-β-D-galactopyranoside (14)

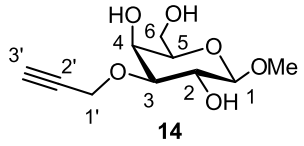

14

To a solution of **15** (2.00 g, 10.3 mmol) in anhydrous MeOH (30.0 ml) was added Bu_2SnO (3.33 g, 13.4 mmol). The suspension was refluxed until it became a clear yellowish solution (4 h). Then the solvent was removed and the colorless residue dried under vacuum for 2 h before it was resuspended in anhydrous DMF (30.0 ml) and treated with propargyl bromide (2.22 ml, 20.6 mmol). The mixture was stirred for 40 h at 35 °C, concentrated and coevaporated with toluene. Column chromatography (CH_2Cl_2/MeOH 10:1) yielded a yellowish sticky solid (1.60 g, 67%).

Formular : $C_{10}H_{16}O_6$ (232.23 g/mol)

$\boldsymbol{R_f}$: 0.22 (CH_2Cl_2/MeOH 10:1)

^{1}**H (600 MHz, *d*-acetone):** δ = 4.40 (dd, 1H, ^2J = 15.8 Hz, ^4J = 2.4 Hz, *H*-1'a); 4.35 (dd, 1H, ^2J = 15.8 Hz, ^4J = 2.5 Hz, *H*-1'b); 4.15 (d, 1H, ^3J = 7.7 Hz, *H*-1); 4.14-4.13 (m, 1H, O*H*-2); 4.11-4.10 (m, 1H, O*H*-4); 3.91 (dd, 1H, ^3J = 5.9 Hz, O*H*-6); 3.79-3.72 (m, 3H, *H*-6a,*H*-6b, *H*-4); 3.64-3.61 (m, 1H, *H*-2); 3.52-3.48 (m, 2H, *H*-5, *H*-3); 3.43 (s, 3H, -OC*H*3); 2.94 (dd, 1H, ^4J = 2.5, 2.4 Hz, *H*-3') ppm.

^{13}**C (150.9 MHz, *d*-acetone):** δ = 105.58 (*C*-1); 81.54 (*C*-3), 81.31 (*C*-2'); 75.85 (*C*-5); 75.66 (*C*-3'); 71.42 (*C*-2); 67.10 (*C*-4); 62.08 (*C*-6); 57.62 (*C*-1'); 56.63 (-O*C*H_3) ppm.

HRMS (**ESI**, $\mathbf{m/z}$) : calcd. for $C_{10}H_{16}NO_6$ $[M+Na]^+$ 255.08391, found 255.08391, Δppm: 0.55.

$[\alpha]_{\mathbf{D}}^{\mathbf{21}}$: 8.8 (c = 0.5, MeOH).

1,2,4,6-Tetra-*O*-acetyl-3-*O*-propargyl-D-galactopyranoside (34)

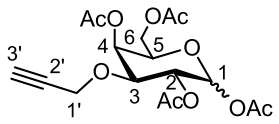

34

14 (300 mg, 1.29 mmol) was dissolved in acetic anhydride (5.00 ml, 52.9 mmol) and treated with cat. amounts of conc. H_2SO_4. The mixture was stirred for 12 h at rt, before it was diluted with CH_2Cl_2 (10 ml) and washed with H_2O (10 ml), sat. $NaHCO_3$ solution (10 ml) and brine (10 ml). Organic phases were dried over Na_2SO_4 and the solvent evaporated in vacuum to yield the product as a yellowish oil in an anomeric mixture of α/β 3.3:1 (500 mg, 1.29 mmol, quant.).

Formular : $C_{17}H_{22}O_{10}$ (386.35 g/mol)

$\boldsymbol{R_f}$: 0.67 (CH_2Cl_2/MeOH 10:1)

^{1}**H** (**600 MHz**, **$CDCl_3$**) : δ = 6.34 (d, 1H, ^3J = 3.7 Hz, *H*-1α); 5.69 (d, 1H, ^3J = 8.4 Hz, *H*-1β); 5.51 (dd, 1H, ^3J = 3.4, 1.3 Hz, *H*-4α); 5.42 (dd, 1H, ^3J = 3.5, 1.1 Hz, *H*-4β); 5.22 (dd, 1H, ^3J = 10.4, 3.7 Hz, *H*-2α); 5.19 (dd, 1H, ^3J = 10.0, 8.4 Hz, *H*-2β); 4.29-4.27 (m, 1H, *H*-5α); 4.26-4.17 (m, 5H, *H*-1'αa, *H*-1'αb, *H*-1'βa, *H*-1'βb, *H*-6βa); 4.15-4.04 (m, 4H, *H*-6βb, *H*-6αa, *H*-6αb, *H*-3α); 3.99-3.97 (m, 1H, *H*-5β); 3.89 (dd, 1H, ^3J = 10.0, 3.5 Hz, *H*-3β); 2.47-2.44 (m, 2H, *H*-3'α, *H*-3'β); 2.16 (α), 2.15 (α,β), 2.12 (β), 2.08 (β), 2.06 (α,β), 2.05 (α) (s, 24H, 4 x C(O)C$H_3\alpha$, 4 x C(O)C$H_3\beta$) ppm.

^{13}**C** (**150.9 MHz**, **$CDCl_3$**) : δ = 170.49 (α), 170.45 (β), 170.29 (β), 170.25 (α), 169.98 (α), 169.57 (β), 169.18 (β), 168.92 (α) (4 x *C*(O)C$H_3\alpha$, 4 x *C*(O)C$H_3\beta$); 92.11 (*C*-1β); 89.95 (*C*-1α); 78.95 (*C*-2'α or *C*-3'α); 78.82 (*C*-2'β or *C*-3'β); 75.66 (*C*-3β); 75.30 (*C*-2'β or *C*-3'β); 75.04 (*C*-2'α or *C*-3'α); 71.95 (*C*-3α); 71.85 (*C*-5β); 69.00 (*C*-5α); 68.88 (*C*-2β); 67.71 (*C*-2α); 66.36 (*C*-4α); 65.26 (*C*-4β); 61.84 (*C*-6α); 61.56 (*C*-6β); 56.86 (*C*-1'α); 56.66 (*C*-1'β); 20.92 (α), 20.85 (β), 20.80 (β), 20.73 (β), 20.71 (α, α,β), 20.68 (α) (4 x C(O)*C*$H_3\alpha$, 4 x C(O)*C*$H_3\beta$) ppm.

HRMS (**ESI**, $\mathbf{m/z}$) : calcd. for $C_{17}H_{22}O_{10}$ $[M+Na]^+$ 409.11052, found 409.11065, Δppm: 0.32.

$[\alpha]_{\mathbf{D}}^{\mathbf{21}}$: 82.4 (c = 0.25, $CHCl_3$).

2,4,6-Tri-*O*-acetyl-3-*O*-propargyl-D-galactopyranose (36)

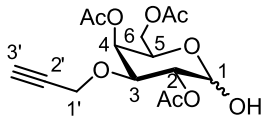

36

34 (2.80 g, 7.25 mmol) was dissolved in anhydrous DMF (30 ml) and heated to 50 °C. Hydrazine acetate (834 mg, 9.06 mmol) was added and the mixture stirred at this temperature. When tlc monitored complete conversion of the educt (after ca. 45 min) the mixture was diluted with EE (80 ml) and washed with H_2O (3 x 30 ml), 0.1 M HCl (1 x 30 ml), and sat. $NaHCO_3$ solution (1 x 30 ml). The combined aqueous phases were reextracted with EE (30 ml) and the combined organic phases dried over Na_2SO_4. The crude product was subjected to colum chromatography (CH_2Cl_2/MeOH 100:1 $\rightarrow$ CH_2Cl_2/MeOH 50:1) to obtain the product as a clear viscous oil in an anomeric mixture of α/β 2.4:1 that contained traces of DMF (1.73 g, 5.02 mmol, 69%).

Formular : $C_{15}H_{20}O_9$ (344.31 g/mol)

$\boldsymbol{R_f}$: 0.22 (CH_2Cl_2/MeOH 30:1)

^{1}**H** (**600 MHz**, $\mathbf{CDCl_3}$) : δ = 5.49-5.48 (m, 2H, *H*-1α, *H*-4α); 5.41 (dd, 1H, ^3J = 3.5, 1.0 Hz, *H*-4β); 5.07 (dd, 1H, ^3J = 10.4, 3.6 Hz, *H*-2α); 4.92 (dd, 1H, ^3J = 10.0, 8.1 Hz, *H*-2β); 4.65 (d, 1H, ^3J = 8.1 Hz, *H*-1β); 4.41-4.39 (m, 1H, *H*-5α); 4.22-4.20 (m, 4H, *H*-1'αa, *H*-1'αb, *H*-1'βa, *H*-1'βb); 4.18- 4.13 (m, 4H, *H*-6βa, *H*-6βb, *H*-6αa, *H*-3α); 4.06 (dd. 1H, ^2J = 11.5 Hz, ^3J = 7.0 Hz, *H*-6αb); 3.89-3.87 (m, 1H, *H*-5β); 3.85 (dd, 1H, ^3J = 10.0, 3.5 Hz, *H*-3β); 2.46-2.45 (m, 2H, *H*-3'α,β); 2.14 (β), 2.14 (β), 2.13 (α), 2.13 (α), 2.07 (α,β) (s, 18H, 3 x C(O)C$H_3\alpha$, 3 x C(O)C$H_3\beta$) ppm.

^{13}**C** (**150.9 MHz**, $\mathbf{CDCl_3}$) : δ = 171.55 (β), 170.60 (β), 170.58 (α), 170.48 (α), 170.38 (α), 170.31 (β) (3 x *C*(O)C$H_3\alpha$, 3 x *C*(O)C$H_3\beta$); 95.47 (*C*-1β); 90.85 (*C*-1α); 79.09 (*C*-2'α); 79.06 (*C*-2'β); 75.23 (*C*-3β); 74.97 (*C*-3'α, *C*-3'β); 72.58 (*C*-2β); 71.23 (*C*-3α); 71.17 (*C*-5β); 69.57 (*C*-2α); 67.09 (*C*-4α); 66.60 (*C*-5α); 65.77 (*C*-4β); 62.36 (*C*-6'α); 62.00 (*C*-6'β); 56.89 (*C*-1'α); 56.85 (*C*-1'β); 20.97 (α), 20.94 (β), 20.76 (α), 20.75 (β), 20.74 (α), 20.71 (β) (3 x C(O)*C*$H_3\alpha$, 3 x C(O)*C*$H_3\beta$) ppm.

HRMS (**ESI**, $\mathbf{m/z}$) : calcd. for $C_{15}H_{20}O_9$ $[M+Na]^+$ 367.09995, found 367.09974, Δppm: 0.57.

2,4,6-Tri-*O*-acetyl-1-*O*-trichloroacetimido-3-*O*-propargyl-α-D-galactopyranoside (12)

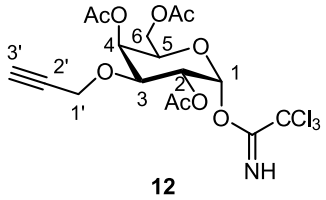

12

36 (170 mg, 494 μmol) were dissolved in anhydrous CH_2Cl_2 (5 ml), cooled to 0 °C and treated with $CNCCl_3$ (990 μl, 9.87 mmol) and DBU (74.0 μl, 494 μmol). Both reagents were dried over mol sieves before usage. After the solution was stirred for 1 h at 0 °C charcoal was added and the mixture filtered over Celite®. Column chromatography (Cy/EE 5:1 $\rightarrow$ Cy/EE 2:1) afforded exclusively the α-anomer as a colorless solid (0.200 g, 0.409 mmol, 83%).

Formular : $C_{17}H_{20}Cl_3NO_9$ (488.70 g/mol)

$\boldsymbol{R_f}$: 0.5 (Cy/EE 1:1)

^{1}**H** (**600 MHz**, **CDCl$_3$**) : δ = 8.64 (s, 1H, N*H*); 6.57 (d, 1H, ^3J = 3.6 Hz, *H*-1); 5.56 (dd, 1H, ^3J = 3.3, 1.3 Hz, *H*-4); 5.25 (dd, 1H, ^3J = 10.4, 3.6 Hz, *H*-2); 4.39-4.37 (m, 1H, *H*-5); 4.26 (dd, 1H, ^2J = 10.4 Hz, ^3J = 3.3 Hz, *H*-3); 4.25-4.24 (m, 2H, *H*-1'a, *H*-1'b); 4.20 (dd, 1H, ^2J = 11.5 Hz, ^3J = 6.2 Hz, *H*-6a); 4.06 (dd, 1H, ^2J = 11.5 Hz,^3J = 7.0 Hz, *H*-6b); 2.44 (dd, 1H, ^4J = 2.4 Hz, *H*-3'); 2.16, 2.05, 2.04 (3 x C(O)CH_3) ppm.

^{13}**C** (**150.9 MHz**, **CDCl$_3$**) : δ = 170.41, 170.26, 170.20 (3 x *C*(O)CH3); 160.82 (*C*=NH); 93.90 (*C*-1); 90.93 (*C*Cl_3); 78.82, 75.11 (*C*-2', *C*-3'); 71.90 (*C*-3); 69.45 (*C*-5); 68.25 (*C*-2); 66.37 (*C*-4); 61.86 (*C*-6); 56.96 (*C*-1'); 20.71, 20.68, 20.66 (3 x C(O)*C*H_3) ppm.

HRMS (**ESI**, $\mathbf{m/z}$) : calcd. for $C_{17}H_{20}Cl_3NO_9$ $[M+Na]^+$ 510.00959, found 510.00926, Δppm: 0.65.

2,4,6-Tri-*O*-acetyl-3-*O*-propargyl-β-D-galactopyranosyl-(1$\rightarrow$4)-2-acetamido-3-*O*-acetyl-1-*O*-allyl-6-*O*-benzyl-2-deoxy-β-D-glucopyranoside (39)

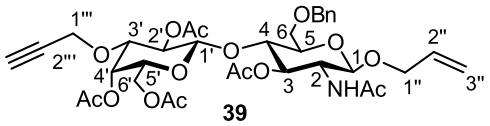

39

To a solution of **12** (1.18 g, 2.42 mmol) in anhydrous CH_2Cl_2 (30 ml) was added **13** (650 mg, 1.65 mmol) and $BF_3{\cdot}Et_2O$ (314 μl, 2.48 mmol). The mixture was stirred at rt until tlc monitored complete consumption of **12** (ca. 1 h). Then NEt_3 (530 μl, 3.80 mmol) was added and the solution was diluted with CH_2Cl_2 (20 ml) and washed with sat. $NaHCO_3$ solution (20 ml) and H_2O (20 ml). The aqueous phase was reextracted once with CH_2Cl_2 (20 ml) and the combined organic phases were dried over Na_2SO_4 and concentrated. The crude product was purified by column chromatography (CH_2Cl_2/MeOH 70:1 $\rightarrow$ CH_2Cl_2/MeOH 10:1) to obtain a colorless solid (1.05 g, 1.45 mmol, 88%).

Formular : $C_{35}H_{45}NO_{15}$ (719.73 g/mol)

$\boldsymbol{R_f}$: 0.13 (CH_2Cl_2/MeOH 30:1)

^{1}**H** (**600 MHz, CDCl$_3$**) : δ = 7.39-7.30 (m, 5H, H_{arom}); 5.88-5.82 (m, 1H, *H*-2"); 5.58 (d, 1H, ^3J = 9.3 Hz, N*H*); 5.31 (dd, 1H, ^3J = 3.5, 1.0 Hz, *H*-4'); 5.26 (dddd, 1H, ^3J = 17.3 Hz, ^4J = 1.7 Hz, ^2J = 1.6 Hz, *H*-3"$_{trans}$); 5.17 (dddd, 1H, ^3J = 10.5 Hz, ^2J = 1.6 Hz, ^4J = 1.5 Hz, *H*-3"$_{cis}$); 5.01 (dd, 1H, ^3J = 9.4, 8.2 Hz, *H*-3); 4.92 (dd, 1H, ^3J = 9.9, 8.1 Hz, *H*-2'); 4.71 (d, 1H, ^2J = 12.0 Hz, -CH_2-Ph); 4.53 (d, 1H, ^2J = 12.0 Hz, -CH_2-Ph); 4.47 (d, 1H, ^3J = 8.1 Hz, *H*-1'); 4.42 (d, 1H, ^3J = 7.5 Hz, *H*-1); 4.32 (dddd, 1H, ^2J = 13.2 Hz, ^3J = 4.8 Hz, ^4J = 1.5 Hz, *H*-1"a); 4.16-4.15 (m, 2H, *H*-1"'); 4.13-4.03 (m, 4H, *H*-2, *H*-6'a, *H*-6'b, *H*-1"b); 3.94 (dd, 1H, ^3J = 8.3, 8.2 Hz, *H*-4); 3.77-3.76 (m, 2H, *H*-6a, *H*-6b); 3.67-3.64 (m, 2H, *H*-5', *H*-3'); 3.51 (ddd, 1H, ^3J = 8.3, 3.5 Hz, *H*-5); 2.45 (dd, 1H, ^4J = 2.4 Hz, *H*-3"'); 2.12, 2.08, 2.03, 2.03, 1.96 (s, 15H, 5 x C(O)CH_3) ppm.

^{13}**C** (**150.9 MHz, CDCl$_3$**) : δ = 170.85, 170.47, 170.34, 170.04, 169.43 (5 x *C*(O)CH3); 138.04 ($C_{arom,\ quart}$); 133.72 (*C*-2"); 128.50, 127.85 (5 x C_{arom}); 117.31 (*C*-3"); 100.52 (*C*-1'); 100.10 (*C*-1); 79.14 (*C*-2"'); 75.79 (*C*-3'); 75.01 (*C*-3"'); 74.78 (*C*-5); 74.55 (*C*-4); 73.61 (-*C*H_2-Ph); 72.58 (*C*-3); 70.68 (*C*-5'); 70.27 (*C*-2'); 69.45 (*C*-1"); 67.97 (*C*-6); 65.23 (*C*-4'); 61.48 (*C*-6'); 56.55 (*C*-1"'); 53.06 (*C*-2); 23.31, 20.95, 20.82, 20.76, 20.72 (5 x C(O)*C*H_3) ppm.

HRMS (**ESI**, $\mathbf{m/z}$) : calcd. for $C_{35}H_{45}NO_{15}$ $[M+Na]^+$ 742.26814, found 742.26836, Δppm: 0.30.

$[\alpha]_{\mathbf{D}}^{\mathbf{22}}$: -5.9 (c = 0.5, $CHCl_3$).

2,4,6-Tri-*O*-acetyl-3-*O*-propargyl-β-D-galactopyranosyl-(1→4)-2-acetamido-3-*O*-acetyl-1-*O*-allyl-2-deoxy-β-D-glucopyranoside (11)

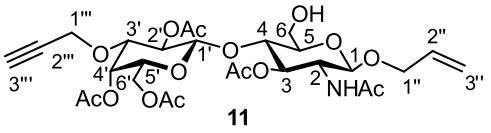

11

39 (200 mg, 278 μmol) was dissolved in anhydrous CH_2Cl_2 (10 ml), treated with DDQ (315 mg, 1.39 mmol) and refluxed for 48 h. After addition of H_2O (3 ml) the mixture was stirred for further 2 h at rt, diluted with CH_2Cl_2 and washed with sat. $NaHCO_3$ solution (10 ml), brine (10 ml) and H_2O (3 x 10 ml). Organic phases were combined, dried over Na_2SO_4 and concentrated. The crude product was subjected to column chromatography (CH_2Cl_2/MeOH 50:1) to yield the product as a colorless solid (0.146 g, 0.232 mmol, 83%).

Formular : $C_{28}H_{39}NO_{15}$ (629.61 g/mol)

$\boldsymbol{R_f}$: 0.42 (CH_2Cl_2/MeOH 15:1)

^{1}**H** (**600 MHz**, **$CDCl_3$**) : δ = 5.87-5.81 (m, 1H, *H*-2"); 5.51 (d, 1H, ^3J = 9.4 Hz, N*H*); 5.35 (m, 1H, *H*-4'); 5.26 (dddd, 1H, ^3J = 17.2 Hz, ^4J = 1.7 Hz, ^2J = 1.5 Hz, *H*-3"$_{trans}$); 5.19 (dddd, 1H, ^3J = 10.4 Hz,^2J = 1.5 Hz, ^4J = 1.4 Hz, *H*-3"$_{cis}$); 5.04 (dd, 1H, ^3J = 10.5, 9.0 Hz, *H*-3); 4.97 (dd, 1H, ^3J = 10.0, 8.0 Hz, *H*-2'); 4.58 (d, 1H, ^3J = 8.0 Hz, *H*-1'); 4.45 (d, 1H, ^3J = 8.3 Hz, *H*-1); 4.32 (dddd, 1H, ^2J = 13.2 Hz, ^3J = 4.9 Hz, ^4J = 1.4 Hz, *H*-1"a); 4.17-4.16 (m, 2H, *H*-1"'); 4.11-4.10 (m, 2H, *H*-6'a, *H*-6'b); 4.08-4.03 (m, 2H, *H*-1"b, *H*-2); 3.93-3.88 (m, 2H, *H*-4, *H*-6a); 3.85-3.82 (m, 1H, *H*-5'); 3.80-3.76 (m, 2H, *H*-3', *H*-6b); 3.38 (ddd, 1H, ^3J = 9.6, 2.6 Hz, *H*-5); 2.44 (dd, 1H, ^4J = 2.4 Hz, *H*-3"'); 2.12, 2.10, 2.08, 2.07, 1.96 (s, 15H, 5 x C(O)CH_3) ppm.

^{13}**C** (**150.9 MHz**, **$CDCl_3$**) : δ = 171.09, 170.48, 170.33, 170.13, 169.53 (5 x *C*(O)CH_3); 133.52 (*C*-2"); 117.61 (*C*-3"); 101.18 (*C*-1'); 100.38 (*C*-1); 78.99 (*C*-2"'); 75.69 (*C*-3'); 75.18 (*C*-3"'); 74.91 (*C*-5); 74.82 (*C*-4); 73.15 (*C*-3); 70.72 (*C*-5'); 70.29 (*C*-2'); 69.98 (*C*-1"); 65.08 (*C*-4'); 61.44 (*C*-6'); 60.56 (*C*-6); 56.46 (*C*-1"'); 53.84 (*C*-2); 23.32,

20.91, 20.83, 20.76, 20.71 (5 x C(O)CH_3) ppm.

HRMS (**ESI**, $\mathbf{m/z}$) : calcd. for $C_{28}H_{39}NO_{15}$ [M+Na]+ 652.22119, found 652.22131, Δppm: 0.18.

3-*O*-Propargyl-β-D-galactopyranosyl-(1→4)-2-acetamido-1-*O*-allyl-2-deoxy-β-D-glucopyranoside (10)

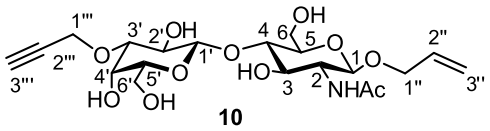

10

To a solution of **11** (146 mg, 232 μmol) in anhydrous MeOH (10 ml) was added NaOMe (0.5 M in MeOH, 464 μl, 0.232 mmol). The mixture was stirred for 12 h at rt, neutralized with Amberlite® IR 125, the cation exchanger filtered off and the solvent evaporated. The product was isolated as a colorless solid (93.0 mg, 202 μmol, 87%).

Formular : $C_{20}H_{31}NO_{11}$ (461.46 g/mol)

$\boldsymbol{R_f}$: 0.44 (CH_2Cl_2/MeOH 5:1)

^{1}H (600 MHz, MeOD) : δ = 5.92-5.85 (m, 1H, *H*-2"); 5.27 (dddd, ^3J = 17.2 Hz, ^4J = 1.8 Hz, ^2J = 1.7 Hz, *H*-3"$_{trans}$); 5.13 (dddd, ^3J = 10.5 Hz, ^2J = 1.7 Hz, ^4J = 1.4 Hz, *H*-3"$_{cis}$); 4.45 (d, 1H, ^3J = 8.4 Hz, *H*-1); 4.42 (d, 1H, ^3J = 7.8 Hz, *H*-1'); 4.39 (dd, 1H, ^2J = 15.9 Hz, ^4J = 2.4 Hz, *H*-1"'a); 4.38-4.31 (m, 3H, *H*-1"'b, *H*-1"a); 4.08-4.05 (m, 2H, *H*-1"b, *H*-4'); 3.92 (dd, 1H, ^2J = 12.2 Hz, ^3J = 2.5 Hz, *H*-6a); 3.85 (dd, 1H, ^2J = 12.2 Hz, ^3J = 4.4 Hz, *H*-6b); 3.78-3.74 (m, 2H, *H*-2, *H*-6'a); 3.70-3.67 (m, 1H, *H*-6'b); 3.64-3.60 (m, 3H, *H*-3, *H*-4, *H*-2'); 3.59-3.56 (m, 1H, *H*-5'); 3.52 (dd, 1H, ^3J = 9.7, 3.2 Hz, *H*-3'); 3.40-3.37 (m, 1H, *H*-5); 2.87 (dd, 1H, ^4J = 2.4 Hz, *H*-3"'); 1.97 (s, 3H, C(O)CH_3) ppm.

^{13}C (150.9 MHz, MeOD) : δ = 173.52 (*C*(O)CH_3); 135.54 (*C*-2"); 116.94 (*C*-3"); 104.96 (*C*-1'); 101.90 (*C*-1); 81.62 (*C*-3'); 80.99 (*C*-4); 80.86 (*C*-2"'); 76.94 (*C*-5'); 76.57 (*C*-5); 76.10 (*C*-3"'); 74.21 (*C*-3); 71.73 (*C*-2'); 70.74 (*C*-1"); 67.21 (*C*-4'); 62.44 (*C*-6'); 61.93 (*C*-6); 57.91 (*C*-1"'); 56.60 (*C*-2); 22.91 (C(O)*C*H_3) ppm.

HRMS (**ESI**, $\mathbf{m/z}$) : calcd. for $C_{20}H_{31}NO_{11}$ $[M+Na]^+$ 484.17893, found 484.17848, Δppm: 0.93.

$[\alpha]_{\mathbf{D}}^{\mathbf{20}}$: -33.1 (c = 0.1, MeOH).

8.4.3 Synthesis of Organic Azides

General procedure for the synthesis of benzyl azides (A)

Derivatives of benzyl bromide and NaN_3 (2 eq.) were mixed in H_2O and heated in the microwave oven at 110 °C for 60 min. The mixture was diluted with sat. $NaHCO_3$ solution and the benzyl azide extracted with EE. Organic layers were combined, dried over Na_2SO_4 and the solvent evaporated. In ^{1}H-, ^{13}C-NMR spectra appeared signals for the product and for the starting material in varying amounts. The azide was used in the Cu(I)-catalyzed alkyne azide cycloaddition without further purification and characterization.

Benzyl azide (41)

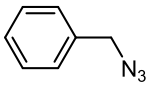

41

Benzyl bromide (340 mg, 1.99 mmol) and NaN_3 (258 mg, 3.98 mmol) were reacted according to the general procedure A for 30 min. The resulting colorless oil (166 mg, (*195 mg*), 1.25 mmol, 63%) contained 15% benzyl bromide.

Formular : $C_7H_7N_3$ (133.15 g/mol)

^{1}**H** (**400 MHz**, **CDCl$_3$**) : δ = 7.42-7.30 (m, 5H, H_{arom}); 4.35 (s, 2H, CH_2) ppm.

^{13}**C** (**100.6 MHz**, **CDCl$_3$**) : δ = 129.16 - 128.35 (6 x C, C_{arom}); 54.96 (CH$_2$) ppm.

3-Nitrobenzyl azide (42)

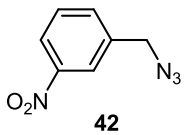

42

3-Nitrobenzyl bromide (400 mg, 1.85 mmol) and NaN_3 (241 mg, 3.70 mmol) were reacted according to the general procedure A. The resulting brown oil (321 mg,

1.80 mmol, 97%) contained no starting material.

Formular : $C_7H_6N_4O_2$ (178.15 g/mol)

^{1}H (**400 MHz, $CDCl_3$**) : δ = 8.22-8.19 (m, 2H, H_{arom}); 7.68-7.65 (m, 1H, H_{arom}); 7.60-7.56 (m, 1H, H_{arom}); 4.51 (s, 2H, CH_2) ppm.

^{13}C (**100.6 MHz, $CDCl_3$**) : δ = 137.80, 133.96, 130.03, 123.38, 123.01 (6 x C, C_{arom}); 53.91 (CH_2) ppm.

2-Hydroxy-5-nitrobenzyl azide (43)

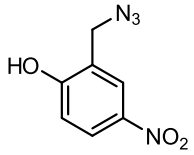

43

2-Hydroxy-5-nitrobenzyl bromide (400 mg, 1.72 mmol) and NaN_3 (224 mg, 3.45 mmol) were reacted according to the general procedure A and diluted with H_2O before extraction. The resulting viscous red oil contained no starting material (288 mg, 14.8 mmol, 86%).

Formular : $C_7H_6N_4O_3$ (178.15 g/mol)

^{1}H (**400 MHz, $CDCl_3$**) : δ = 8.17-8.14 (m, 2H, H_{arom}); 6.98-6.95 (m, 1H, H_{arom}); 4.53 (s, 2H, CH_2) ppm.

^{13}C (**100.6 MHz, $CDCl_3$**) : δ = 126.11, 125.84, 116.60 (6 x C, C_{arom}); 50.80 (CH_2) ppm.

4-(Methylthio)benzyl azide (44)

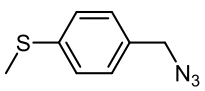

44

4-(Methylthio)benzyl bromide (400 mg, 1.84 mmol) and NaN_3 (240 mg, 3.68 mmol) were reacted according to the general procedure A. The resulting yellow oil (275 mg,

(*306 mg*), 1.52 mmol, 83%) contained 10% of starting material.

Formular : $C_8H_9N_3S$ (179.24 g/mol)

^{1}H (**400 MHz**, **$CDCl_3$**) : δ = 7.31-7.19 (m, 4H, H_{arom}); 4.30 (s, 2H, CH_2); 2.50 (s, 3H, CH_3) ppm.

^{13}C (**100.6 MHz**, **$CDCl_3$**) : δ = 128.92-126.93 (6 x C, C_{arom}); 54.56 (CH_2); 15.86 (CH_3) ppm.

3,4,5-Trifluorobenzyl azide (45)

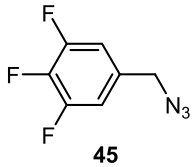

45

3,4,5-Trifluorobenzyl bromide (300 mg, 1.33 mmol) and NaN_3 (173 mg, 2.67 mmol) were reacted according to the general procedure A. The resulting yellow oil (218 mg (*232 mg*), 1.17 mmol, 87%) contained 6% of starting material.

Formular : $C_7H_4F_3N_3S$ (187.12 g/mol)

^{1}H (**400 MHz**, **$CDCl_3$**) : δ = 7.04-6.92 (m, 2H, H_{arom}); 4.32 (s, 2H, CH_2) ppm.

^{13}C (**100.6 MHz**, **$CDCl_3$**) : δ = 112.27, 112.21, 112.12, 112.06 (6 x C, C_{arom}); 53.58 (CH_2) ppm.

4-(Azidomethyl)benzophenone (47)

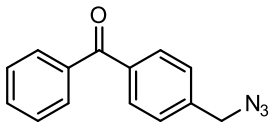

47

4-(Bromomethyl)benzophenone (300 mg, 1.09 mmol) and NaN_3 (142 mg, 2.18 mmol) were reacted according to the general procedure A to obtain the product as a yellow oil

in quantitative yield (255 mg, 1.07 mmol, 99%).

Formular : $C_{14}H_{11}N_3O$ (237.26 g/mol)

^{1}H (400 MHz, $CDCl_3$) : δ = 7.85-7.80 (m, 4H, H_{arom}); 7.63-7.59 (m, 1H, H_{arom}); 7.52-7.43 (m, 4H, H_{arom}); 4.45 (s, 2H, CH_2) ppm.

^{13}C (100.6 MHz, $CDCl_3$) : δ= 196.21 (*C*O); 140.05, 137.59, 137.56 (3 x C, $C_{arom,\ quart}$); 132.67 ($C_{arom,\ p}$); 130.70, 130.13, 128.47, 127.97 (8 x C, $C_{arom,\ m}$, $C_{arom,\ o}$); 54.45 (*C*H_2) ppm.

2,3,4,6-Tetra-*O*-acetyl-1-azido-β-D-galactopyranoside (61)

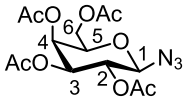

61

33 (1.31 g, 3.19 mmol) was dissolved in anhydrous CH_2Cl_2 (10 ml) and layered with sat. $NaHCO_3$ solution (10 ml). NaN_3 (700 mg, 10.8 mmol) and TBAHS (1.08 g, 3.19 mmol) were added and the two phase system stirred vigorously for 50 min at rt. Subsequently, the reaction was diluted with EE (110 ml) and washed with sat. $NaHCO_3$ solution (25 ml), H_2O (2 x 25 ml) and brine (25 ml). The organic layer was dried over Na_2SO_4 and the solvent removed in vacuum to yield the product as a colorless solid (1.14 g, 3.05 mmol, 96%).

Formular : $C_{14}H_{19}N_3O_9$ (373.32 g/mol)

R_f : 0.27 (CH_2Cl_2/MeOH 80:1)

^{1}H (400 MHz, $CDCl_3$) : δ = 5.42 (dd, 1H, ^3J = 3.4 Hz, 1.1 Hz, *H*-4); 5.17 (dd, 1H, ^3J = 10.4, 8.7 Hz, *H*-2); 5.04 (dd, 1 H, ^3J = 10.4, 3.4 Hz, *H*-3); 4.59 (d, 1H, ^3J = 8.7 Hz, *H*-1); 4.21-4.13 (m, 2H, *H*-6); 4.03-3.99 (m, 1H, *H*-5); 2.17, 2.09, 2.06, 1.99 (s, 4 x C(O)CH_3) ppm.

^{13}C (100.6 MHz, $CDCl_3$) : δ = 170.34, 170.09, 169.97, 169.34 (*C*(O)CH_3); 88.32 (*C*-1); 72.90 (*C*-5); 70.74 (*C*-3); 68.09 (*C*-2); 66.86 (*C*-4); 61.22 (*C*-6); 20.66, 20.64, 20.60, 20.50 (4 x C(O)*C*H_3) ppm.

HRMS (**ESI**, $\mathbf{m/z}$) : calcd. for $C_{14}H_{19}N_3O_9$ $[M+Na]^+$ 396.10135, found 396.10121, Δppm: 0.35.

$[\alpha]_{\mathbf{D}}^{\mathbf{21}}$: -23.6 (c = 0.25, $CHCl_3$).

IR : $\tilde{\nu}$ = 2130 (-N_3), 1360 (-N_3).

1-Azido-β-D-galactopyranoside (48)

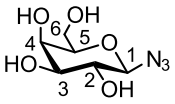

48

61 (1.03 g, 2.76 mmol) was dissolved in anhydrous MeOH (20 ml) and stirred at rt. NaOMe (0.5 M, 5.52 ml, 2.76 mmol) was added dropwise and after 20 min the mixture was neutralized with Amberlite® IR 125, the cation exchanger filtered off and the solvent evaporated to obtain the product as a colorless solid (545 mg, 2.66 mmol, 96%).

Formular : $C_6H_{11}N_3O_5$ (205.17 g/mol)

$\boldsymbol{R_f}$: 0.43 (CH_2Cl_2/MeOH 4:1)

$^{\mathbf{1}}$**H** (**400 MHz**, **MeOD**) : δ = 4.49-4.47 (m, 1H, *H*-1); 3.92 (dd, 1H, ^3J = 2.9, 1.2 Hz, *H*-4); 3.84 (dd, 1 H, ^2J = 11.4 Hz, ^3J = 6.9 Hz, *H*-6a); 3.78 (dd, 1H, ^2J = 11.4 Hz, ^3J = 5.1 Hz, *H*-6b); 3.67 (ddd, 1H, ^3J = 6.9, 5.1, 1.2 Hz, *H*-5); 3.58 - 3.51 (m, 2H, *H*-2, *H*-3) ppm.

$^{\mathbf{13}}$**C** (**100.6 MHz**, **MeOD**) : δ = 92.62 (*C*-1); 78.94 (*C*-5); 74.99 (*C*-3); 72.01 (*C*-2); 70.24 (*C*-4); 62.47 (*C*-6) ppm.

HRMS (**ESI**, $\mathbf{m/z}$) : calcd. for $C_6H_{11}N_3O_5$ $[M+Na]^+$ 228.05909, found 228.05925, Δppm: 0.70.

$[\alpha]_{\mathbf{D}}^{\mathbf{21}}$: -5.1 (c = 0.5, MeOH).

IR : $\tilde{\nu}$ = 2125 (-N_3), 1350 (-N_3).

8.4.4 Synthesis of Triazole-based hGal-1 Ligands by Click Chemistry

3-*O*-[2-(3'-Hydroxyacetophenone)-1*H*-1,2,3-triazol-4-yl]methyl-β-D-galactopyranosyl-(1$\rightarrow$4)-2-acetamido-1-*O*-allyl-2-deoxy-β-D-glucopyranoside (9f)

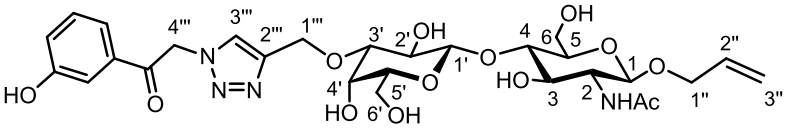

9f

NaN_3 (15.0 mg, 233 μmol) was solved in H_2O (500 μl), 2-bromo-3'-hydroxyacetophenone (**51**) (50.0 mg, 233 μmol) added and after 2 h at 40 °C, 1200 rpm the crude azide was treated with **10** (15.5 mg, 33.0 μmol), sodium ascorbate (6.54 mg, 33.0 μmol), $CuSO_4$ (527 μg, 3.30 μmol)and *tert*-butanol (250 μl) at 40 °C, 1200 rpm for 24 h. Then, the mixture was concentrated and subjected to flash chromatography using a gradient elution CH_2Cl_2/MeOH 30:1 $\rightarrow$ 6:1 to yield a colorless solid (16.0 mg, 25.0 μmol, 76%).

Formular : $C_{28}H_{38}N_4O_{13}$ (638.62 g/mol)

$\boldsymbol{R_f}$: 0.30 (CH_2Cl_2/MeOH 5:1)

^{1}**H (600 MHz, MeOD)** : δ = 8.03 (s, 1H, *H*-3'''); 7.58-7.56 (m, 1H, Ph); 7.45-7.44 (m, 1H, Ph); 7.41-7.39 (m, 1H, Ph); 7.13-7.11 (m, 1H, Ph); 5.91-5.85 (m, 1H, *H*-2"); 5.27 (dddd, 1H, ^3J = 17.3 Hz, ^2J = 1.8 Hz, ^4J = 1.8 Hz, *H*-3"$_{trans}$); 5.13 (dddd, 1H, ^3J = 10.5 Hz, ^2J = 1.8 Hz, ^4J = 1.6 Hz, *H*-3"$_{cis}$); 4.89 (d, 1H, ^2J = 12.5 Hz, *H*-1'''a); 4.826 (d, 1H, ^2J = 12.5 Hz, *H*-1'''b); 4.45 (d, 1H, ^3J = 8.5 Hz, *H*-1); 4.43 (d, 1H, ^3J = 8.0 Hz, *H*-1'); 4.33 (dddd, 1H, ^2J = 13.3 Hz, ^3J = 4.9 Hz, ^4J = 1.6 Hz, *H*-1"a); 4.09-4.05 (m, 2H, *H*-4', *H*-1"b); 3.93 (dd, 1H, ^2J = 12.2 Hz, ^3J = 2.5 Hz, *H*-6a); 3.87 (dd, 1H, ^3J = 12.2 Hz, ^3J = 4.4 Hz, *H*-6b); 3.81-3.75 (m, 2H, *H*-2, *H*-6'a); 3.71 (dd, 1H, ^2J = 11.6 Hz, ^3J = 4.5 Hz, *H*-6'b); 3.68 (dd, 1H, ^3J = 9.5, 7.9 Hz, *H*-2'); 3.63-3.58 (m, 3H, *H*-3, *H*-4, *H*-5'); 3.46 (dd, 1H, ^3J = 9.6, 3.2 Hz, *H*-3'); 3.41-3.38 (m, 1H, *H*-5); 1.97 (s, 3H, C(O)CH_3) ppm.

No signal for *H*-4''' appeared in the ^{1}H-NMR spectrum.

^{13}C (150.9 MHz, MeOD) : δ = 192.80 (*C*O); 173.54 (*C*(O)CH_3); 159.41 (C_{Ph}); 146.20 (*C*-2"'); 136.91 (C_{Ph}); 135.54 (*C*-2"); 131.23 (C_{Ph}); 126.91 (*C*-3"'); 122.58, 120.50 (2 x C_{Ph}); 116.95 (*C*-3"); 115.36 (C_{Ph}); 105.00 (*C*-1'); 101.91 (*C*-1); 82.77 (*C*-3'); 81.06 (*C*-2'); 76.99 (*C*-5'); 76.58 (*C*-5); 74.26 (*C*-3); 71.79 (*C*-4); 70.77 (*C*-1"); 67.05 (*C*-4'); 3.71 (*C*-1"'); 62.60 (*C*-6'); 61.98 (*C*-6); 56.57 (*C*-2); 22.91 (C(O)*C*H_3) ppm.

No signal for *C*-4"' appeared in the ^{13}C-NMR spectrum.

HRMS (ESI, m/z) : calcd. for $C_{28}H_{38}N_4O_{13}$ $[M+Na]^+$ 661.23276, found 661.23300, Δppm: 0.36.

$[\alpha]_D^{21}$: -6.5 (c = 0.05, MeOH).

General procedure for the Cu(I)-catalyzed alkyne azide cycloaddition (B)

The alkyne **10** was solved to a final concentration of 0.1 M in *tert*-butano/H_2O 2:1 and treated with an excess of the corrsponding azide (5 eq.). $CuSO_4$ (0.1 M, 0.1 eq) and sodium ascorbate (1 M, 1 eq) were added and the reaction mixed thoroughly at 1440 rpm and 25 °C/ 40 °C until tlc showed complete consumption of the alkyne. The reaction was then concentrated and the 1,4-substituted triazole was purified by flash chromatography.

3-*O*-[1-(2-Hydroxyethyl)-1*H*-1,2,3-triazol-4-yl]methyl-β-D-galactopyranosyl-(1→4)-2-acetamido-1-*O*-allyl-2-deoxy-β-D-glucopyranoside (9j)

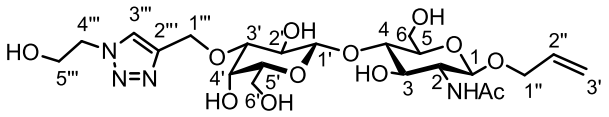

9j

10 (24.0 mg, 52.0 μmol) and 2-azidoethanol (**50**) (23.0 mg, 260 μmol) were treated according to the general procedure B at 25 °C for 12 h. The crude product was purified by flash chromatography using a gradient elution CH_2Cl_2/MeOH 5:1 → 1:1 to yield a colorless solid (20.0 mg, 36.0 μmol, 70%).

Formular : $C_{22}H_{36}N_4O_{12}$ (548.54 g/mol)

R_f : 0.14 (CH_2Cl_2/MeOH 4:1)

^{1}H (600 MHz, D_2O/MeOD 3 : 1) : δ = 8.09 (s, 1H, *H*-3"'); 5.93-5.86 (m, 1H, *H*-2"); 5.31-5.28 (m, 1H, *H*-3"$_{trans}$); 5.25-5.24 (m, 1H, *H*-3"$_{cis}$); 4.85 (d, 1H, ^2J = 12.4 Hz, *H*-1"'a, partly covered by H_2O); 4.75 (d, 1H, ^2J = 12.4 Hz, *H*-1"'b); 4.57-4.55 (m, 3H, *H*-1, *H*-4"'a, *H*-4"'b); 4.47 (d, 1H, ^3J = 7.1 Hz, *H*-1'); 4.35-4.31 (m, 1H, *H*-1"a); 4.16-4.13 (m, 2H, *H*-1"b, *H*-4'); 4.00-3.95 (m, 3H, *H*-5"', *H*-6a); 3.82 (dd, 1H, ^2J = 12.4 Hz, ^3J = 5.2 Hz, *H*-6b); 3.78 (dd, 1H, ^2J = 11.9 Hz, ^3J = 3.8 Hz, *H*-6'a); 3.75-3.66 (m, 5H, *H*-6'b, *H*-2, *H*-3, *H*-4, *H*-5'); 3.61-3.54 (m, 3H, *H*-2', *H*-3', *H*-5); 2.02 (s, 3H, C(O)CH_3) ppm.

^{13}C (150.9 MHz, D_2O/MeOD 3 : 1) : δ = 175.28 (*C*(O)CH_3); 134.34 (*C*-2"); 126.51 (*C*-3"'); 118.91 (*C*-3"); 103.97 (*C*-1'); 103.79 (*C*-1); 81.21 (*C*-3'); 79.43 (*C*-2'); 76.22 (*C*-5'); 75.79 (*C*-5); 73.49 (*C*-3); 71.38 (*C*-1"); 71.04 (*C*-4); 66.03 (*C*-4'); 62.67 (*C*-1"'); 62.04 (*C*-6'); 61.09 (2C, *C*-6, *C*-5"'); 56.07 (*C*-2); 53.55 (*C*-4"'); 23.08 (C(O)*C*H_3) ppm.

No signal for *C*-2"' appeared in the ^{13}C-NMR spectrum.

HRMS (ESI, m/z) : calcd. for $C_{22}H_{36}NO_{12}$ $[M+Na]^+$ 571.22219, found 571.22181, Δppm: 0.67.

$[\alpha]_D^{21}$: -11.5 (c = 0.05, MeOH).

3-*O*-[1-(1-*N*-β-D-Galactopyranosyl)-1*H*-1,2,3-triazol-4-yl]methyl-β-D-galactopyranosyl-(1→4)-2-acetamido-1-*O*-allyl-2-deoxy-β-D-glucopyranoside (9h)

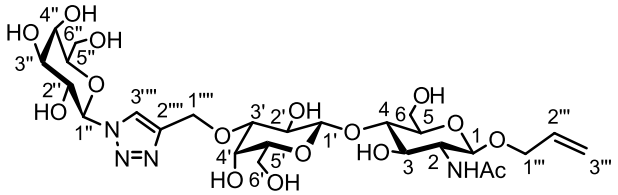

9h

10 (22.0 mg, 48.0 μmol) and **48** (37.0 mg, 180 μmol) were treated according to the general procedure B at 40 °C for 48 h. The crude product was purified by flash chromatography using a gradient elution CH_2Cl_2/MeOH 5:1 → 2:1 to yield a colorless solid (25.0 mg, 38.0 μmol, 79%).

Formular : $C_{26}H_{42}N_4O_{16}$ (666.63 g/mol)

$\boldsymbol{R_f}$: 0.10 (CH_2Cl_2/MeOH 3:1)

^{1}H (**600 MHz**, **MeOD**) : δ = 8.24 (s, 1H, *H*-3””); 5.92 - 5.85 (m, 1H, *H*-2”’); 5.57 (d, 1H, ^3J = 9.3 Hz, *H*-1”); 5.27 (dddd, 1H, ^3J = 17.2 Hz, ^4J = 1.8 Hz, ^2J = 1.8 Hz, *H*-3”’$_{trans}$); 5.13 (dddd, 1H, ^3J = 10.5 Hz, ^2J = 1.8 Hz, ^4J = 1.6 Hz, *H*-3”’$_{cis}$); 4.86 (d, 1H, ^2J = 12.4 Hz, *H*-1””a); 4.78 (d, 1H, ^2J = 12.4 Hz, *H*-1””b); 4.45 (d, 1H, ^3J = 8.4 Hz, *H*-1); 4.42 (d, 1H, ^3J = 7.8 Hz, *H*-1’); 4.33 (dddd, 1H, ^2J = 13.4 Hz,^3J = 4.9 Hz, ^4J = 1.6 Hz, *H*-1”’a); 4.15 (dd, 1H, ^3J = 9.3 Hz, *H*-2”); 4.09 - 4.05 (m, 2H, *H*-4’, H-1”’b); 3.99 (dd, 1H, ^3J = 3.3, 0.8 Hz, *H*-4”); 3.92 (dd, 1H, ^2J = 12.2 Hz, ^3J = 2.6 Hz*H*-6a); 3.87-3.83 (m, 2H, *H*-6b, *H*-5”); 3.78-3.74 (m, 4H, *H*-2, *H*-6”a, *H*-6”b, *H*-6’a); 3.72-3.69 (m, 2H, *H*-6’b, *H*-3”); 3.67-3.61 (m, 3H, *H*-2’, *H*-3, *H*-4); 3.60 - 3.57 (m, 1H, *H*-5’); 3.44 (dd, 1H, ^3J = 9.7, 3.2 Hz, *H*-3’); 3.41-3.38 (m, 1H, *H*-5); 1.97 (s, 3H, CH_3) ppm.

^{13}C (**150.9 MHz**, **MeOD**) : δ = 173.54 (*C*OCH_3); 146.37 (*C*-2””); 133.54 (*C*-2”’); 123.85 (*C*-3””); 116.95 (*C*-3”’); 104.96 (*C*-1‘); 101.92 (*C*-1); 90.26 (*C*-1”); 82.71 (*C*-3‘); 81.05 (*C*-2’); 79.94 (*C*-5”); 76.94 (*C*-5’); 76.56 (*C*-5); 75.26 (*C*-3”); 74.23 (*C*-3); 71.77 (*C*-4); 71.48 (*C*-2”); 70.76 (*C*-1”’); 70.34 (*C*-4”); 66.88 (*C*-4’); 63.54 (*C*-1””); 62.54 (*C*-6’); 62.40 (*C*-6”); 61.98 (*C*-6); 56.57 (*C*-2); 22.91 (C(O)*C*H_3) ppm.

HRMS (**ESI**, **m/z**) : calcd. for $C_{26}H_{42}N_4O_{16}$ $[M+Na]^+$ 689.24880, found 689.24897, Δppm: 0.25.

$[\alpha]_{\mathbf{D}}^{\mathbf{21}}$: 2.8 (c = 0.05, MeOH).

3-*O*-[1-Benzyl-1*H*-1,2,3-triazol-4-yl]methyl-β-D-galactopyranosyl-(1→4)-2-acetamido-1-*O*-allyl-2-deoxy-β-D-glucopyranoside (9a)

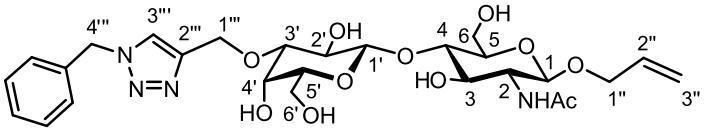

9a

10 (24.0 mg, 52.0 μmol) and **41** (35.0 mg, 217 μmol) were treated according to the general procedure B at 25 °C for 17 h and 3 h at 40 °C. The crude product was purified by flash chromatography using a gradient elution CH_2Cl_2/MeOH 20:1 → 7:1 to yield a greenish solid (26.0 mg, 44.0 μmol, 84%).

Formular : $C_{27}H_{38}N_4O_{11}$ (594.61 g/mol)

R_f : 0.25 (CH_2Cl_2/MeOH 5:1)

^{1}H (600 MHz, MeOD) : δ = 8.00 (s, 1H, *H*-3"'); 7.39-7.32 (m, 5H, H_{arom}); 5.91-5.85 (m, 1H, *H*-2"); 5.60 (s, 2H, *H*-4"'); 5.27 (dddd, 1H, ^3J = 17.3 Hz, ^2J = 1.7 Hz, ^4J = 1.6 Hz, *H*-3"$_{trans}$); 5.13 (dddd, 1H, ^3J = 10.5 Hz, ^2J = 1.7 Hz, ^4J = 1.5 Hz, *H*-3"$_{cis}$); 4.81 (d, 1H, ^2J = 12.1 Hz, *H*-1"'a); 4.72 (d, 1H, ^2J = 12.1 Hz, *H*-1"'b); 4.44 (d, 1H, ^3J = 8.5 Hz, *H*-1); 4.40 (d, 1H, ^3J = 7.8 Hz, *H*-1'); 4.32 (dddd, 1H, ^2J = 13.4 Hz, ^3J = 4.8 Hz, ^4J = 1.6 Hz, *H*-1"a); 4.06 (dddd, 1H, ^2J = 13.4 Hz, ^3J = 5.7 Hz, ^4J = 1.5 Hz, *H*-1"b); 4.03-4.02 (m, 1H, *H*-4'); 3.92 (dd, 1H, ^2J = 12.2 Hz, ^3J = 2.5 Hz, *H*-6a); 3.85 (dd, 1H, ^2J = 12.2 Hz, ^3J = 4.4 Hz, *H*-6b); 3.78-3.74 (m, 2H, *H*-2, *H*-6'a); 3.68 (dd, 1H, ^2J = 11.5 Hz, ^3J = 4.5 Hz, *H*-6'b); 3.65-3.60 (m, 3H, *H*-2', *H*-3, *H*-4); 3.57-3.55 (m, 1H, *H*-5'); 3.41-3.37 (m, 2H, *H*-3', *H*-5); 1.96 (s, 3H, C(O)CH_3) ppm.

^{13}C (150.9 MHz, MeOD) : δ = 173.53 (*C*(O)CH$_3$); 136.74 ($C_{arom,\ quart}$); 135.54 (*C*-2"); 130.04 (2C, $C_{arom,\ m}$, $C_{arom,\ o}$); 129.62 ($C_{arom,\ p}$); 129.16 (2C, $C_{arom,\ m}$, $C_{arom,\ o}$); 116.93 (*C*-3"); 104.98 (*C*-1'); 101.92 (*C*-1); 82.82 (*C*-3'); 81.08 (*C*-2'); 76.94 (*C*-5'); 76.57 (*C*-5); 74.22 (*C*-3); 71.70 (*C*-4); 70.75 (*C*-1"); 66.87 (*C*-4'); 63.64 (*C*-1"'); 62.53 (*C*-6'); 61.99 (*C*-6); 56.58 (*C*-2); 55.00 (*C*-4"'); 22.91 (C(O)*C*H$_3$) ppm.

No signal for *C*-2"' and *C*-3"' appeared in the ^{13}C-NMR spectrum.

HRMS (ESI, m/z) : calcd. for $C_{27}H_{38}N_4O_{11}$ $[M+Na]^+$ 617.24293, found 617.24328, Δppm: 0.57.

$[\alpha]_D^{21}$: -25.3 (c = 0.1, MeOH).

3-*O*-[1-(3-Nitrobenzyl)-1*H*-1,2,3-triazol-4-yl]methyl-β-D-galactopyranosyl-(1→4)-2-acetamido-1-*O*-allyl-2-deoxy-β-D-glucopyranoside (9b)

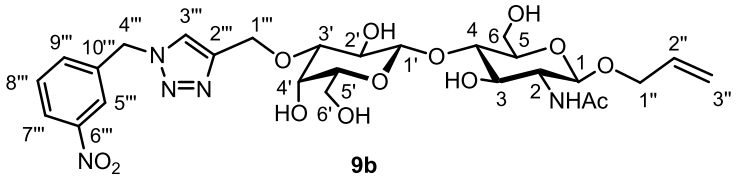

9b

10 (20.0 mg, 43.0 μmol) and **42** (39.0 mg, 217 μmol) were treated according to the general procedure B at 25 °C for 7 d. The crude product was purified by flash chromatography using a gradient elution CH_2Cl_2/MeOH 20:1 → 9:1 to yield a brownish solid (10.0 mg, 16.0 μmol, 36%).

Formular : $C_{27}H_{37}N_5O_{13}$ (639.61 g/mol)

$\boldsymbol{R_f}$: 0.33 (CH_2Cl_2/MeOH 5:1)

^{1}**H** (**600 MHz**, **MeOD**) : δ = 8.24-8.22 (m, 2H, Ph); 8.09 (s, 1H, *H*-3"'); 7.74-7.72 (m, 1H, Ph); 7.66-7.63 (m, 1H, Ph); 5.91-5.85 (m, 1H, *H*-2"); 5.77 (s, 2H, *H*-4"'); 5.28-5.25 (m, 1H, *H*-3"$_{trans}$); 5.14-5.12 (m, 1H, *H*-3"$_{cis}$); 4.84 (d, 1H, ^{2}J = 12.4 Hz, *H*-1"'a, partly covered by H_2O); 4.75 (d, 1H, ^{2}J = 12.4 Hz, *H*-1"'b); 4.44 (d, 1H, ^{3}J = 8.4 Hz, *H*-1); 4.40 (d, 1H, ^{3}J = 7.7 Hz, *H*-1'); 4.32 (dddd, 1H, ^{2}J = 13.3 Hz, ^{3}J = 4.8 Hz, ^{4}J = 1.6 Hz, *H*-1"a); 4.08-4.04 (m, 2H, *H*-1"b, *H*-4'); 3.91 (dd, 1H, ^{2}J = 12.2 Hz, ^{3}J = 2.4 Hz, *H*-6a); 3.84 (dd, 1H, ^{2}J = 12.2 Hz, ^{3}J = 4.4 Hz, *H*-6b); 3.78-3.74 (m, 2H, *H*-2, *H*-6'a); 3.69 (dd, 1H, ^{2}J = 11.5 Hz, ^{3}J = 4.6 Hz, *H*-6'b); 3.65-3.60 (m, 3H, *H*-2', *H*-3, *H*-4); 3.57-3.55 (m, 1H, *H*-5'); 3.42 (dd, 1H, ^{3}J = 9.6, 3.2 Hz, *H*-3'); 3.39-3.37 (m, 1H, *H*-5); 1.96 (s, 3H, C(O)CH_3) ppm.

^{13}**C** (**150.9 MHz**, **MeOD**) : δ = 173.52 (*C*(O)CH_3); 149.93 (*C*-7"'); 146.89 (*C*-2"'); 139.06 (*C*-5"') 135.54 (*C*-2"); 135.32 (*C*-10"'; 131.39 (*C*-9"'); 125.36 (*C*-3"'); 124.40 (*C*-8"'); 123.94 (*C*-6"'); 116.94 (*C*-3"); 104.97 (*C*-1'); 101.91 (*C*-1); 82.79 (*C*-3'); 81.07 (*C*-2'); 76.93 (*C*-5'); 76.57 (*C*-5); 74.22 (*C*-3); 71.70 (*C*-4); 70.75 (*C*-1"); 66.86 (*C*-4'); 63.56 (*C*-1"'); 62.52 (*C*-6'); 61.99 (*C*-6); 56.59 (*C*-2); 53.84 (*C*-4"'); 22.91 (C(O)*C*H_3) ppm.

HRMS (**ESI**, $\mathbf{m/z}$) : calcd. for $C_{27}H_{37}N_5O_{13}$ $[M+Na]^+$ 662.22801, found 662.22828, Δppm: 0.41.

$[\alpha]_{\mathbf{D}}^{\mathbf{21}}$: -20.3 (c = 0.05, MeOH).

3-*O*-[1-(4-Methylthio)benzyl)-1*H*-1,2,3-triazol-4-yl]methyl-β-D-galactopyranosyl-(1→4)-2-acetamido-1-*O*-allyl-2-deoxy-β-D-glucopyranoside (9d)

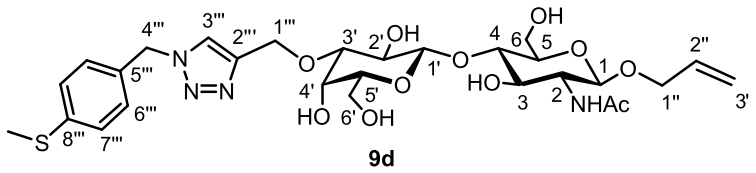

9d

10 (20.0 mg, 43.0 μmol) and **44** (39.0 mg, 217 μmol) were treated according to the general procedure B at 25 °C for 7 d. The crude product was purified by flash chromatography using a gradient elution CH_2Cl_2/MeOH 20:1 → 9:1 to yield a brownish solid (21.0 mg, 33.0 μmol, 76%).

Formular : $C_{28}H_{40}N_4O_{11}S$ (640.70 g/mol)

R_f : 0.29 (CH_2Cl_2/MeOH 5:1)

^{1}**H** (**600 MHz**, **MeOD**) : δ = 7.97 (s, 1H, *H*-3'''); 7.27 (s, 4H, H_{arom}); 5.91-5.85 (m, 1H, *H*-2"); 5.55 (s, 2H, *H*-4'''); 5.28-5.25 (m, 1H, *H*-3"$_{trans}$); 5.14-5.12 (m, 1H, *H*-3"$_{cis}$); 4.81 (d, 1H, ^2J = 12.2 Hz, *H*-1'''a); 4.72 (d, 1H, ^2J = 12.2 Hz, *H*-1'''b); 4.44 (d, 1H, ^3J = 8.4 Hz, *H*-1); 4.40 (d, 1H, ^3J = 7.8 Hz, *H*-1'); 4.32 (dddd, 1H, ^2J = 13.4 Hz, ^3J = 4.8 Hz, ^4J = 1.6 Hz, *H*-1"a); 4.06 (dddd, 1H, ^2J = 13.4 Hz, ^3J = 5.7 Hz, ^4J = 1.5 Hz, *H*-1"b); 4.02-4.02 (m, 1H, *H*-4'); 3.92 (dd, 1H, ^2J = 12.1 Hz, ^3J = 2.5 Hz, *H*-6a); 3.85 (dd, 1H, ^2J = 12.1 Hz, ^3J = 4.4 Hz, *H*-6b); 3.78-3.74 (m, 2H, *H*-2, *H*-6'a); 3.68 (dd, 1H, ^2J = 11.5 Hz, ^3J = 4.5 Hz, *H*-6'b); 3.64-3.59 (m, 3H, *H*-2', *H*-3, *H*-4); 3.57-3.55 (m, 1H, *H*-5'); 3.41-3.37 (m, 2H, *H*-3', *H*-5); 2.46 (s, 3H, S-CH_3); 1.96 (s, 3H, C(O)CH_3) ppm.

^{13}**C** (**150.9 MHz**, **MeOD**) : δ = 173.51 (*C*(O)CH$_3$); 146.62 (*C*-2'''); 141.06 (*C*-8'''); 135.55 (*C*-2"); 133.20 (*C*-5'''); 129.77, 127.69 (4C, *C*-6''', *C*-7'''); 124.92 (*C*-3'''); 116.93 (*C*-3"); 104.97 (*C*-1'); 101.92 (*C*-1); 82.80 (*C*-3'); 81.09 (*C*-2'); 76.93 (*C*-5'); 76.58 (*C*-5); 74.21 (*C*-3); 71.70 (*C*-4); 70.74 (*C*-1"); 66.86 (*C*-4'); 63.59 (*C*-1'''); 62.52 (*C*-6'); 62.00 (*C*-6); 56.59 (*C*-2); 54.54 (*C*-4'''); 22.90 (C(O)*C*H$_3$); 15.41 (S-*C*H$_3$) ppm.

HRMS (**ESI**, **m/z**) : calcd. for $C_{28}H_{40}N_4O_{11}S$ [M+Na]$^+$ 663.23065, found 663.23023, Δppm: 0.63.

$[\alpha]_D^{21}$: -7.5 (c = 0.05, MeOH).

3-*O*-[1-(3,4,5-Trifluorobenzyl)-1*H*-1,2,3-triazol-4-yl]methyl-β-D-galactopyranosyl-(1$\rightarrow$4)-2-acetamido-1-*O*-allyl-2-deoxy-β-D-glucopyranoside (9e)

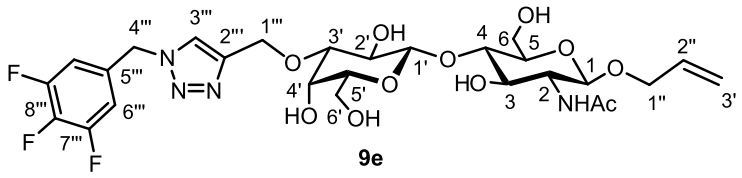

9e

10 (23.0 mg, 50.0 μmol) and **45** (47.0 mg, 249 μmol) were treated according to the general procedure B at 40 °C for 3 d. The crude product was purified by flash chromatography using a gradient elution CH_2Cl_2/MeOH 20:1 $\rightarrow$ 9:1 to yield a brownish solid (32.0 mg, 49.0 μmol, 99%).

Formular : $C_{27}H_{35}F_3N_4O_{11}$ (648.58 g/mol)

$\boldsymbol{R_f}$: 0.22 (CH_2Cl_2/MeOH 5:1)

^{1}**H** (**600 MHz**, **MeOD**) : δ = 8.11 (s, 1H, *H*-3"'); 7.16-7.11 (m, 2H, H_{arom}); 5.91-5.85 (m, 1H, *H*-2"); 5.60 (s, 2H, *H*-4"'); 5.27 (dddd, 1H, ^3J = 17.2 Hz, ^2J = 1.6 Hz, ^4J = 1.7 Hz, *H*-3"$_{trans}$); 5.13 (dddd, 1H, ^3J = 10.5 Hz, ^2J = 1.6 Hz, ^4J = 1.6 Hz, *H*-3"$_{cis}$); 4.83 (d, 1H, ^2J = 11.9 Hz, *H*-1"'a); 4.74 (d, 1H, ^2J = 11.9 Hz, *H*-1"'b); 4.44 (d, 1H, ^3J = 8.4 Hz, *H*-1); 4.41 (d, 1H, ^3J = 7.7 Hz, *H*-1'); 4.32 (dddd, 1H, ^2J = 13.3 Hz, ^3J = 4.7 Hz, ^4J = 1.6 Hz, *H*-1"a); 4.08-4.04 (m, 2H, *H*-4', *H*-1"b); 3.92 (dd, 1H, ^2J = 12.1 Hz, ^3J = 2.3 Hz, *H*-6a); 3.85 (dd, 1H,^2J = 12.1 Hz, ^3J = 4.3 Hz, *H*-6b); 3.79-3.73 (m, 2H, *H*-2, *H*-6'a); 3.69 (dd, 1H, ^2J = 11.5 Hz, ^3J = 4.4 Hz, *H*-6'b); 3.66-3.61 (m, 3H, *H*-2', *H*-3, *H*-4); 3.59-3.56 (m, 1H, *H*-5'); 3.44-3.42 (m, 1H, *H*-3'); 3.40-3.36 (m, 1H, *H*-5); 1.96 (s, 3H, C(O)CH_3) ppm.

^{13}**C** (**150.9 MHz**, **MeOD**) : δ = 173.55 (*C*(O)CH$_3$); 152.50 (ddd, 2C, ^2J = 249.6 Hz, ^3J = 10.0 Hz, ^4J = 3.8 Hz, *C*-7"'); 140.85 (dt, 1C, ^2J = 250.9 Hz, ^3J = 17.5 Hz, *C*-8"'); 135.53 (*C*-2"); 13.87-133.47 (m, 1C, *C*-5"'); 116.93 (*C*-3"); 113.75 (dd, 2C, ^3J = 17.5 Hz, ^4J = 4.7 Hz, *C*-6"'); 104.99 (*C*-1'); 101.92 (*C*-1); 82.88 (*C*-3'); 81.05 (*C*-2'); 76.94 (*C*-5'); 76.57 (*C*-5); 74.23 (*C*-3); 71.71 (*C*-4); 70.75 (*C*-1"); 66.86 (*C*-4'); 63.67 (*C*-1"'); 62.52 (*C*-6'); 61.98 (*C*-6); 56.59 (*C*-2); 53.48 (*C*-4"'); 22.91 (C(O)*C*H$_3$) ppm.

No signal for *C*-2"' and *C*-3"' appeared in the ^{13}C-NMR spectrum.

HRMS (**ESI**, $\mathbf{m/z}$) : calcd. for $C_{27}H_{35}F_3N_4O_{11}$ $[M+Na]^+$ 671.21466, found 671.21430, Δppm: 0.54.

$[\alpha]_{\mathbf{D}}^{\mathbf{21}}$: -3.1 (c = 0.1, MeOH).

3-*O*-[4-Methylbenzophenone-1*H*-1,2,3-triazol-4-yl]methyl-β-D-galactopyranosyl-(1→4)-2-acetamido-1-*O*-allyl-2-deoxy-β-D-glucopyranoside (9g)

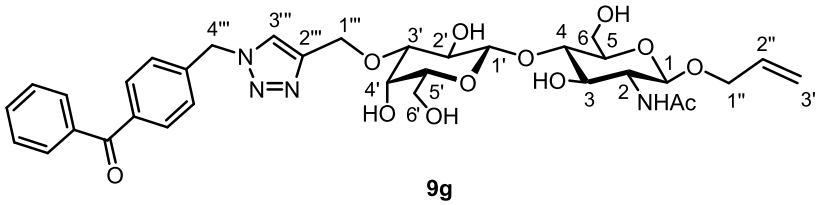

9g

10 (20.5 mg, 44.0 μmol) and **9g** (51.0 mg, 217 μmol) were treated according to the general procedure B at 40 °C for 1 d. The crude product was purified by flash chromatography using a gradient elution CH_2Cl_2/MeOH 30:1 → 15:1 to yield a colorless solid (27.0 mg, 39.0 μmol, 88%).

Formular : $C_{34}H_{42}N_4O_{12}$ (698.72 g/mol)

$\boldsymbol{R_f}$: 0.60 (CH_2Cl_2/MeOH 3:1)

^{1}**H** (**600 MHz**, **MeOD**) : δ = 8.08 (s, 1H, *H*-3"'); 7.80-7.78 (m, 2H, H_{arom}); 7.77-7.75 (m, 2H, H_{arom}); 7.66-7.63 (m, 1H, H_{arom}); 7.54-7.52 (m, 2H, H_{arom}); 7.48-7.46 (m, 2H, H_{arom}); 5.91-5.85 (m, 1H, *H*-2"); 5.73 (s, 2H, *H*-4"'); 5.27 (dddd, 1H, ^3J = 17.2 Hz, ^4J = 1.8 Hz, ^2J = 1.7 Hz, *H*-3"$_{trans}$); 5.13 (dddd, 1H, ^3J = 10.5 Hz, ^2J = 1.7 Hz, ^4J = 1.6 Hz, *H*-3"$_{cis}$); 4.84 (d, 1H, ^2J = 12.4 Hz, *H*-1"'a); 4.76 (d, 1H, ^2J = 12.4 Hz, *H*-1"'b); 4.44 (d, 1H, ^3J = 8.4 Hz, *H*-1); 4.41 (d, 1H, ^3J = 7.7 Hz, *H*-1'); 4.32 (dddd, 1H, ^2J = 13.3 Hz, ^3J = 4.8 Hz, ^4J = 1.6 Hz, *H*-1"a); 4.08-4.04 (m, 2H, *H*-4, *H*-1"b); 3.90 (dd, 1H, ^2J = 12.2 Hz, ^3J = 2.5 Hz, *H*-6a); 3.84 (dd, 1H, ^2J = 12.2 Hz, ^3J = 4.4 Hz, *H*-6b); 3.79-3.74 (m, 2H, *H*-2, H-6'a); 3.70-3.68 (m, 1H, *H*-6'b); 3.65-3.59 (m, 3H, *H*-2', *H*-3, *H*-4); 3.58-3.55 (m, 1H, *H*-5'); 3.42 (dd, 1H, ^3J = 9.6, 3.2 Hz, *H*-3'); 3.39-3.36 (m, 1H, *H*-5); 1.96 (s, 3H, C(O)CH_3) ppm.

^{13}**C** (**150.9 MHz**, **MeOD**) : δ = 197.86 (*C*O); 173.52 (*C*(O)CH_3); 146.79 (*C*-2"'); 141.49 ($C_{arom,\ quart}$-CO); 138.89 ($C_{arom,\ quart}$-CO); 138.61 ($C_{arom,\ quart}$); 135.54 (*C*-2"); 133.97, 131.62, 130.99, 129.59, 129.05 (9 x C_{arom}); 125.38 (*C*-3"'); 116.94 (*C*-3");

104.98 (*C*-1); 101.91 (*C*-1'); 82.82 (*C*-3'); 81.05 (*C*-2'); 76.93 (*C*-5'); 76.56 (*C*-5); 74.23 (*C*-3); 71.70 (*C*-4); 70.76 (*C*-1"); 66.88 (*C*-4'); 63.59 (*C*-1"'); 62.52 (*C*-6'); 61.97 (*C*-6); 56.58 (*C*-2); 54.43 (*C*-4"'); 22.91 (C(O)*C*H_3) ppm.

HRMS (**ESI**, $\mathbf{m/z}$) : calcd. for $C_{34}H_{42}N_4O_{12}$ $[M+Na]^+$ 721.26914, found 721.26868, Δppm: 0.64.

$[\alpha]_{\mathbf{D}}^{\mathbf{21}}$: -14.4 (c = 0.05, MeOH).

3-*O*-[1-(2-Hydroxy-5-nitrobenzyl)-1*H*-1,2,3-triazol-4-yl]methyl-β-D-galactopyranosyl-(1→4)-2-acetamido-1-*O*-allyl-2-deoxy-β-D-glucopyranoside (9c)

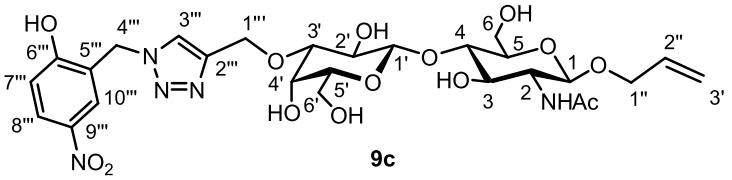

9c

10 (20.0 mg, 43.0 μmol) and **43** (42.0 mg, 217 μmol) were treated according to the general procedure B at 40 °C for 24 h. The crude product was purified by flash chromatography using a gradient elution CH_2Cl_2/MeOH 20:1 → 9:1 to yield a yellowish solid (20.0 mg, 31.0 μmol, 70%).

Formular : $C_{27}H_{37}N_5O_{14}$ (655.61 g/mol)

$\boldsymbol{R_f}$: 0.30 (CH_2Cl_2/MeOH 5:1)

^{1}H (600 MHz, MeOD) : δ = 8.00 (s, 1H, *H*-3"'); 7.99-7.96 (m, 2H, *H*-7"', *H*-8"'); 6.55 (d, 1H, ^4J = 9.1 Hz, *H*-10"'); 5.91-5.85 (m, 1H, *H*-2"); 5.50 (s, 2H, *H*-4"'); 5.27 (dddd, 1H, ^3J = 17.3 Hz, ^4J = 1.7 Hz, ^2J = 1.6 Hz, *H*-3"$_{trans}$); 5.13 (dddd, 1H, ^3J = 10.5 Hz, ^2J = 1.6 Hz, ^4J = 1.5 Hz, *H*-3"$_{cis}$); 4.81 (d, 1H, ^2J = 12.3 Hz, *H*-1"'a); 4.73 (d, 1H, ^2J = 12.3 Hz, *H*-1"'b); 4.43 (d, 1H, ^3J = 8.5 Hz, *H*-1); 4.40 (d, 1H, ^3J = 7.8 Hz, *H*-1'); 4.32 (dddd, 1H, ^2J = 13.3 Hz, ^3J = 4.9 Hz, ^4J = 1.7 Hz, *H*-1"a); 4.06 (dddd, 1H, ^2J = 13.3 Hz, ^3J = 5.8 Hz, ^4J = 1.5 Hz, *H*-1"b); 4.02-4.02 (m, 1H, *H*-4'); 3.91 (dd, 1H, ^2J = 12.1 Hz, ^3J = 2.5 Hz, *H*-6a); 3.85 (dd, 1H, ^2J = 12.1 Hz, ^3J = 4.4 Hz, *H*-6b); 3.78-3.74 (m, 2H, H-2, *H*-6'a); 3.68 (dd, 1H, ^2J = 11.6 Hz, ^3J = 4.4 Hz, *H*-6'b); 3.64-3.59 (m, 3H, *H*-2', *H*-3, *H*-4); 3.58-3.55 (m, 1H, *H*-5'); 3.41-3.37 (m, 2H, *H*-3', *H*-5); 1.97 (C(O)CH_3) ppm.

^{13}C (150.9 MHz, MeOD) : δ = 173.55 (*C*(O)CH_3); 146.07 (*C*-2"'); 135.54 (*C*-2"); 129.81, 128.12, 127.97, 126.97 (4C, C_{arom}); 125.29 (*C*-3"'); 124.79, 120.12 (2C, C_{arom}); 116.96 (*C*-3"); 104.92 (*C*-1'); 101.92 (*C*-1); 82.77 (*C*-3'); 81.08 (*C*-2'); 76.94 (*C*-5'); 76.58 (*C*-5); 74.27 (*C*-3); 71.74 (*C*-4); 70.76 (*C*-1"); 66.91 (*C*-4'); 63.69 (*C*-1"'); 62.59 (*C*-6'); 61.97 (*C*-6); 56.52 (*C*-2); 50.91 (*C*-4"'); 22.90 (C(O)*C*H_3) ppm.

HRMS (ESI, m/z) : calcd. for $C_{27}H_{37}N_5O_{14}$ $[M+Na]^+$ 678.22292, found 678.22267, Δppm: 0.37.

$[\alpha]_D^{21}$: 9.7 (c = 0.05, MeOH).

3-*O*-[1-(5-Amino-4*H*-1,2,4-triazol-3-yl)-1*H*-1,2,3-triazol-4-yl]methyl-β-D-galactopyranosyl-(1→4)-2-acetamido-1-*O*-allyl-2-deoxy-β-D-glucopyranoside (9i)

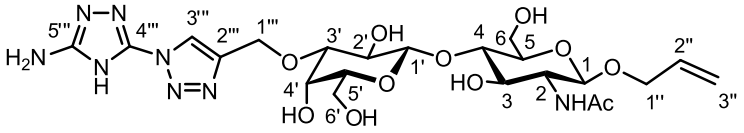

9i

10 (25.0 mg, 54.0 μmol) and 2-azido-5-amino-4*H*-1,2,4-triazole (**49**) (32.0 mg, 256 μmol) were treated according to the general procedure B at 40 °C for 12 h. The crude product was purified by flash chromatography using a gradient elution CH_2Cl_2/MeOH 20:1 → 2:1 to yield a colorless solid (13.0 mg, 22.0 μmol, 41%).

Formular : $C_{22}H_{34}N_85O_{11}$ (586.55 g/mol)

R_f : 0.10 (CH_2Cl_2/MeOH 5:1)

^{1}H (600 MHz, MeOD) : δ = 8.49 (s, 1H, *H*-3"'); 8.45 (s, 1H, N*H*); 5.92-5.86 (m, 1H, *H*-2"); 5.29 (dddd, 1H, ^3J = 17.3 Hz, ^4J = 1.6 Hz, ^2J = 1.5 Hz, *H*-3"$_{trans}$); 5.24 (dddd, 1H, ^3J = 10.4 Hz, ^2J = 1.5 Hz, ^4J = 1.4 Hz, *H*-3"$_{cis}$); 4.94-4.77 (2 H, covered by H_2O, H-1"'a, H-1"'b); 4.54 (d, 1H, ^3J = 8.3 Hz, *H*-1); 4.48 (d, 1H, ^3J = 7.3 Hz, *H*-1'); 4.34-4.31 (m, 1H, *H*-1"a); 4.17-4.17 (m, 1H, *H*-4') 4.15-4.12 (m, 1H, *H*-1"b); 3.96 (dd, 1H, ^2J = 12.3 Hz, ^3J = 2.0 Hz, *H*-6a); 3.82 (dd, 1H, ^2J = 12.4 Hz, ^3J = 5.0 Hz, *H*-6b); 3.79-3.73 (m, 3H, *H*-2, *H*-6'a, *H*-6'b); 3.69-3.65 (m, 3H, *H*-3, *H*-4, *H*-5'); 3.64-3.58 (m, 2H, *H*-2', *H*-3'); 3.55-3.52 (m, 1H, *H*-5); 2.02 (s, 3H, C(O)CH_3) ppm.

^{13}C (150.9 MHz, MeOD) : δ = 175.09 (*C*(O)CH_3); 171.47, 158.15 (2C, *C*-4"', *C*-5"'); 145.62 (*C*-2"'); 134.42 (*C*-2"); 124.10 (*C*-3"'); 118.74 (*C*-3"); 103.88 (*C*-1'); 101.18 (*C*-1); 81.57 (*C*-3'); 79.58 (*C*-2'); 76.28 (*C*-5'); 75.85 (*C*-5); 73.54 (*C*-3); 71.32 (*C*-1"); 71.14 (*C*-4); 66.18 (*C*-4'); 62. 61 (*C*-1"'); 62.07 (*C*-6'); 61.12 (*C*-6); 56.11 (*C*-2); 23.07 (C(O)*C*H_3) ppm.

HRMS (ESI, m/z) : calcd. for $C_{22}H_{34}N_8O_{11}$ $[M+Na]^+$ 609.22393, found 609.22400, Δppm: 0.11.

$[\alpha]_D^{21}$: 5.0 (c = 0.05, H_2O).

8.5 Syntheses towards a hGal-1 PET Tracer

8.5.1 *N*-Acetyl-1-*O*-allyl-6-*O*-tosyl-β-D-lactosamine (54)

2,3,4,6-Tetra-*O*-acetyl-β-D-galactopyranosyl-(1→4)-2-acetamido-3-*O*-acetyl-1-*O*-allyl-2-deoxy-6-*O*-tosyl-β-D-glucopyranoside (54)

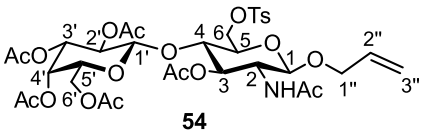

54

40 (195 mg, 308 μmol) was solved in anhydrous pyridine (5 ml) and treated with *p*-TsCl (176 mg, 923 μmol) at rt. After 6 h additional *p*-TsCl (120 mg, 160 μmol) was added and the reaction stirred for further 12 h. Then the solution was diluted with CH_2Cl_2 (10 ml), poured on ice water and the organic layer was washed with 10 ml of 0.1 M HCl, sat. $NaHCO_3$ solution, H_2O, dried over Na_2SO_4 and concentrated. The crude product was purified by flash column chromatography (CH_2Cl_2/MeOH 100:1→80:1) to obtain a colorless solid (242 mg, 308 μmol, quant.).

Formular : $C_{34}H_{45}NO_{18}S$ (787.78 g/mol)

R_f : 0.21 (CH_2Cl_2/MeOH 20:1)

^{1}H (600 MHz, $CDCl_3$) : δ = 7.81-7.79 (m, 2H, Ph); 7.38-7.36 (m, 2H, Ph); 5.81-5.74 (m, 2H, H-2", N*H*); 5.37 (dd, 1H, ^3J = 3.4, 0.9 Hz, *H*-4'); 5.21 (dddd, 1H, ^3J = 17.3 Hz, ^4J = 1.7 Hz, ^2J = 1.6 Hz, *H*-3"$_{trans}$); 5.18 (dddd, 1H, ^3J = 10.5 Hz,

^2J = 1.6 Hz, ^4J = 1.4 Hz, *H*-3"$_{cis}$); 5.11 (dd, 1H, ^3J = 10.5, 7.9 Hz, *H*-2'); 5.04 (dd, 1H, ^3J = 8.0, 7.2 Hz, *H*-3); 4.98 (dd, 1H, ^3J = 10.5, 3.4 Hz, *H*-3'); 4.50 (d, 1H, ^3J = 7.9 Hz, *H*-1'); 4.45 (d, 1H, ^3J = 6.4 Hz, *H*-1); 4.43 (dd, 1H, ^2J = 10.6 Hz, ^3J = 4.4 Hz, *H*-6a); 4.17 (dd, 1H, ^2J = 10.6 Hz, ^3J = 4.6 Hz, *H*-6b); 4.14 (dddd, 1H, ^2J = 13.2 Hz, ^3J = 4.9 Hz, ^4J = 1.7 Hz, *H*-1"a); 4.12-4.11 (m, 2H, *H*-6'a, *H*-6'b); 4.01 (ddd, 1H, ^3J = 9.3, 8.0, 6.4 Hz, *H*-2); 3.91 (dddd, 1H, ^2J = 13.2 Hz, ^3J = 5.9 Hz, ^4J = 1.4 Hz, *H*-1"b); 3.88 (ddd, 1H, ^3J = 7.7, 6.6, 0.9 Hz, *H*-5'); 3.81 (dd, 1H, ^3J = 7.2 Hz, *H*-4); 3.67-3.64 (m, 1H, *H*-5); 2.46 (s, 3H, Ph-CH_3); 2.15, 2.07, 2.06, 2.04, 2.00, 1.97 (s, 18 H, 6 x C(O)CH_3) ppm.

^{13}C (150.9 MHz, MeOD) : δ = 170.52, 170.41, 170.25, 170.13, 170.09, 169.82 (6 x *C*(O)CH$_3$); 145.42 (C_{arom}-CH$_3$); 133.49 (*C*-2"); 132.80 (C_{arom}-S); 130.10, 128.17 (4C, $C_{arom,\ m}$, $C_{arom,\ o}$); 117.49 (*C*-3"); 100.63 (*C*-1'); 99.52 (*C*-1); 74.03 (*C*-4); 72.33 (*C*-5); 71.18 (*C*-3); 71.02 (*C*-5'); 70.81 (*C*-3'); 69.47 (*C*-1"); 69.15 (*C*-2'); 67.91 (*C*-6); 66.82 (*C*-4'); 60.98 (*C*-6'); 51.86 (*C*-2); 23.34 (NHC(O)*C*H$_3$); 21.81 (CPh-*C*H$_3$); 20.91, 20.89, 20.79, 20.78, 20.67 (6 x C(O)*C*H$_3$) ppm.

HRMS (ESI, m/z) : calcd. for $C_{34}H_{45}NO_{18}S$ $[M+H]^+$ 661.23276, found 661.23300, Δppm: 0.36.

$[\alpha]_D^{21}$: -27.9 (c = 0.25, $CHCl_3$).

8.5.2 *N*-Acetyl-1-*O*-allyl-6-*O*-fluoro-β-D-lactosamine (19)

2,3,4,6-Tetra-*O*-acetyl-β-D-galactopyranosyl-(1→4)-2-acetamido-3-*O*-acetyl-1-*O*-allyl-2-deoxy-6-fluoro-β-D-glucopyranoside (62)

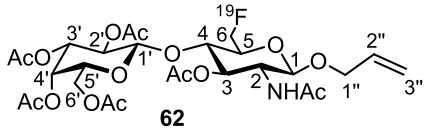

62

54 (100 mg, 127 μmol) in *tert*-amylalcohol (4 ml) was treated with CsF (96.0 mg, 635 μmol) and heated to 110 °C. After 7 h unreacted starting material was quenched with β-ME (17.3 μl, 254 μmol) for 1.5 h at 110 °C before the mixture was concentrated. The crude product was subjected to flash column chromatography (CH_2Cl_2/MeOH 100:1→80:1) to obtain a colorless solid (38.0 mg). ^{1}H-NMR showed impurities in the aliphatic region, however, mass spectrometry confirmed successful conversion of the tosylate. The solid was deprotected without further characterization and purification.

Formular : $C_{27}H_{38}FNO_{15}$ (635.59 g/mol)

$\boldsymbol{R_f}$: 0.21 (CH_2Cl_2/MeOH 20:1)

^{1}**H** (**400 MHz**, **CDCl$_3$**) : δ = 5.89-5.80 (m, 1H); 5.58 (d, 1H, *J* = 9.2 Hz); 5.36 (dd, 1H, *J* = 3.4, 1.0 Hz); 5.26 (dddd, 1H, *J* = 17.3, 1.6 Hz); 5.20-5.12 (m, 3H); 5.00 (dd, 1H, *J* = 10.5, 3.4 Hz); 4.69 (ddd, 1H, *J* = 21.7, 10.3, 2.8 Hz); 4.62-4.48 (m, 3H); 4.32 (dddd, 1H, *J* = 13.1, 4.9, 1.5 Hz); 4.16-4.00 (m, 4H); 3.93-3.86 (m, 2H); 3.60-3.50 (m, 1H); 2.15, 2.09, 2.06, 2.05, 1.97, 1.96 (6s, 18H) ppm.

MS(**MALDI**, **m**/**z**) : calcd for $C_{27}H_{38}FNO_{15}$ $[M+Na]^+$ 658.212, found 658.221.

19 (300 μg, 705 nmol) was dissolved in pyridine (30.0 μl) and treated with acetic anhydride (3.50 μl, 42.0 μmol) at rt for 12 h. TLC showed complete peracetylation, the mixture was coevaporated with toluene and mass spectrometry confirmed the structure.

$\boldsymbol{R_f}$: 0.21 (CH_2Cl_2/MeOH 20:1)

HRMS (**ESI**, **m**/**z**) : calcd. for $C_{27}H_{38}FNO_{15}$ $[M+Na]^+$ 636.22982, found 636.23004, Δppm: 0.35.

β-D-Galactopyranosyl-(1$\rightarrow$4)-2-acetamido-1-*O*-allyl-2-deoxy-6-fluoro-β-D-glucopyranoside (19)

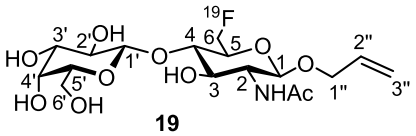

19

To a solution of **62** (38.0 mg, 60.0 μmol) in anhydrous MeOH (3 ml) was added NaOMe (239 μl, 0.5 M in MeOH, 120 μmol). After stirring at rt for 12 h the mixture was neutralized with Amberlite® IR125, the cation exchanger filtered off and the soultion concentrated. Flash column chromatography (CH_2Cl_2/MeOH 20:1$\rightarrow$2:1) provided the desired product as a colorless solid (10.0 mg, 24.0 μmol, 39%).

Formular : $C_{17}H_{28}FNO_{10}$ (425.40 g/mol)

$\boldsymbol{R_f}$: 0.33 (CH_2Cl_2/MeOH 3:1)

^{1}H (600 MHz, MeOD) : δ = 5.93-5.85 (m, 1H, *H*-2"); 5.27 (dddd, 1H, ^3J = 17.3 Hz, ^4J = 1.8 Hz, ^2J = 1.7 Hz, *H*-3"$_{trans}$); 5.14 (dddd, 1H, ^3J = 10.5 Hz, ^2J = 1.7 Hz, ^4J = 1.6 Hz, *H*-3"$_{cis}$); 4.83-4.66 (m, 2H, *H*-6a, *H*-6b); 4.49 (d, 1H, ^3J = 8.4 Hz, *H*-1); 4.32-4.29 (m, 2H, *H*-1', *H*-1"a); 4.06 (dddd, 1H, ^2J = 13.3 Hz, ^3J = 5.8 Hz, ^4J = 1.6 Hz, *H*-1"b); 3.81 (dd, 1H, ^3J = 3.3, 0.8 Hz, *H*-4'); 3.78-3.73 (m, 2H, *H*-2, *H*-6'a); 3.70-3.64 (m, 2H, *H*-3, *H*-6'b); 3.61-3.52 (m, 4H, *H*-4, *H*-5', *H*-5, *H*-2'); 3.48 (dd, 1H, ^3J = 9.7, 3.3 Hz, *H*-3'); 1.97 (s, 3H, NHC(O)CH_3) ppm.

^{13}C (150.9 MHz, MeOD) : δ = 173.54 (NH*C*(O)CH$_3$); 135.43 (*C*-2"); 117.11 (*C*-3"); 105.16 (*C*-1'); 101.85 (*C*-1); 82.66 (d, ^2J = 170.9 Hz, *C*-6); 79.82 (d, ^4J = 5.9 Hz, *C*-4); 77.19 (*C*-5'); 75.14 (d, ^3J = 18.4 Hz, *C*-5); 74.78 (*C*-3'); 74.05 (*C*-3); 72.53 (*C*-2'); 70.89 (*C*-1"); 70.31 (*C*-4'); 62.54 (*C*-6'); 56.55 (*C*-2); 22.90 (NHC(O)*C*H$_3$) ppm.

HRMS (ESI, m/z) : calcd. for $C_{17}H_{18}FNO_{10}$ $[M+Na]^+$ 448.15895, found 448.15861, Δppm: 0.83.

8.6 Lactose Derivatives for Microarrays & Metabolic Glycoengineering

8.6.1 1-*O*-Propargyl-β-D-lactose (20)

2,3,4,6-Tetra-*O*-acetyl-β-D-galactopyranosyl-(1$\rightarrow$4)-1,2,3,6-tetra-*O*-acetyl-β-D-glucopyranoside (63)

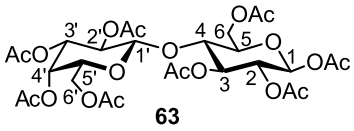

63

β-D-Galactopyranosyl-(1$\rightarrow$4)-D-glucopyranoside (**56**) (5.00 g, 14.6 mmol) was added to a refluxing mixture of sodium acetate (5.00 g, 61.1 mmol) and acetic anhydride (100 ml). The mixture was refluxed for further 2.5 h and poured on ice water (600 ml) under vigorously stirring. The brownish oil was filtered off and recrystallized in MeOH to obtain a colorless solid (4.45 g, 6.55 mmol, 45%).

Formular : $C_{28}H_{38}O_{19}$ (678.59 g/mol)

R_f : 0.30 (CH_2Cl_2/MeOH 30:1)

^{1}H (**400 MHz**, **$CDCl_3$**) : δ = 5.67 (d, 1H, ^3J = 8.2 Hz, *H*-1); 5.35 (dd, 1H, ^3J = 3.5, 1.1 Hz, *H*-4'); 5.24 (dd, 1H, ^3J = 9.4. 8.9 Hz, *H*-3); 5.11 (dd, 1H, ^3J = 10.5, 7.9 Hz, *H*-2'); 5.04 (dd, 1H, ^3J = 9.4, 8.2 Hz, *H*-2); 4.95 (dd, 1H, ^3J = 10.5, 3.5 Hz, *H*-3'); 4.48 (d, 1H, ^3J = 7.9 Hz, *H*-1'); 4.45 (dd, 1H, ^2J = 12.0 Hz, ^3J = 2.0 Hz, *H*-6a); 4.16-4.05 (m, 3H, *H*-6b, *H*-6a', *H*-6b'); 3.89-3.82 (m, 2H, *H*-4, *H*-5'); 3.76 (ddd, 1H, ^3J = 9.9, 4.8, 2.0 Hz, *H*-5); 2.15, 2.12, 2.10, 2.07, 2.05, 2.04, 2.03, 1.96 (8s, 24 H, 8 x C(O)CH_3) ppm.

^{13}C (**100.6 MHz**, **$CDCl_3$**) : δ = 170.32, 170.28, 170.10, 170.03, 169.58, 169.53, 168.98, 168.82 (8 x *C*(O)CH_3); 100.95 (*C*-1'); 91.55 (*C*-1); 75.67 (*C*-4); 73.52 (*C*-5); 72.64 (*C*-3); 70.96 (*C*-3'); 70.77 (*C*-5'); 70.54 (*C*-2); 69.03 (*C*-2'); 66.61 (*C*-4'); 61.75 (*C*-6); 60.84 (*C*-6'); 20.81, 20.79, 20.73, 20.61, 20.59, 20.48 (8 x C(O)*C*H_3) ppm.

MS (**MALDI**, **m/z**) : calcd. for $C_{28}H_{38}O_{19}$ $[M+Na]^+$ 701.190, found 701.157.

2,3,4,6-Tetra-*O*-acetyl-β-D-galactopyranosyl-(1$\rightarrow$4)-2,3,6-tri-*O*-acetyl-D-glucopyranoside (57)

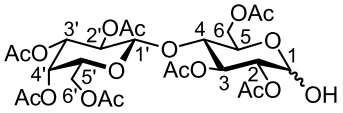

57

63 (1.00 g, 1.47 mmol) was dissolved in anhydrous DMF (12 ml) and heated to 50 °C before hydrazine acetate (0.170 g, 1.84 mmol) was added. The mixture was stirred at this temperature until tlc showed complete consumption of the starting material (40 min), diluted with EE (40 ml), washed with H_2O (3 x 10 ml), 0.1 M HCl (10 ml), sat. NaHCO3 solution (10 ml) and H_2O (10 ml). The organic phase was dried over Na_2SO_4, the solvent coevaporated with toluene and the crude product purified by flash chromatography ($CH_2Cl_2\rightarrow CH_2Cl_2$/MeOH 100:1$\rightarrow$50:1) to obtain a colorless solid as an anomeric mixture α/β 2:1 (0.590 g, 0.927 mmol, 63%).

Formular : $C_{26}H_{36}O_{18}$ (636.55 g/mol)

R_f : 0.17 (CH_2Cl_2/MeOH 30:1)

^{1}H (**600 MHz**, **$CDCl_3$**) : δ = 5.52 (dd, 1H, ^3J = 10.1, 9.4 Hz, *H*-3α); 5.38 (dd, 1H, ^3J = 3.6 Hz, *H*-1α); 5.36-5.35 (m, 2H, *H*-4'α, *H*-4'β); 5.25 (dd, 1H, ^3J = 9.6, 9.1 Hz, *H*-3β); 5.14-5.09 (m, 2H, *H*-2'α, *H*-2'β); 4.98-4.94 (m, 2H, *H*-3'α, *H*-3'β); 4.84 (dddd, 1H, ^3J = 10.1, 3.6, 0.9 Hz, *H*-2α); 4.79 (dd, 1H, ^3J = 9.6, 8.0 Hz, *H*-2β);

4.72 (dd, 1H, ^3J = 8.2, 8.0 Hz, *H*-1β); 4.52-4.47 (m, 4H, *H*-1'α, *H*-1'β, *H*-6αa, *H*-6βa); 41.9-4.06 (m, 7H, *H*-5α, *H*-6αb, *H*-6βb, *H*-6'αa, *H*-6'αb, *H*-6'βa, *H*-6'βb); 3.89-3.86 (m, 2H, *H*-5'α, *H*-5'β); 3.80-3.75 (m, 2H, *H*-4β, *H*-4α); 3.66 (ddd, 1H, ^3J = 9.9, 5.2, 2.1 Hz, *H*-5β); 3.37 (d, 1H, ^3J = 8.2 Hz, O*H*β); 2.88 (dd, 1H, ^3J = 3.6 Hz, ^4J = 0.9 Hz, O*H*α); 2.16 (α), 2.16 (β), 2.13 (α), 2.13 (β), 2.09 (β), 2.08 (α), 2.06 (β), 2.06 (α), 2.06 (β), 2.06 (α), 2.05 (α, β), 1.97 (α), 1.96 (β) (13s, 42H, 14 x C(O)*C*H$_3$) ppm.

^{13}C (**100.6 MHz, $CDCl_3$**) : δ = 171.26 (β), 170.61 (α), 170.56 (β), 170.52 (α), 170.50 (β), 170.41 (α), 170.35 (α), 170.29 (β), 170.26 (α), 170.22 (β), 169.72 (α), 169.71 (β), 169.22 (β), 169.16(α) (14 x *C*(O)CH$_3$); 101.26 (*C*-1'β); 101.18 (*C*-1'α); 95.49 (*C*-1β); 90.34 (*C*-1α); 76.45 (*C*-4α); 76.39 (*C*-4β); 73.71 (*C*-2β); 73.15 (*C*-5β); 72.10 (*C*-3β); 71.39 (*C*-2α); 71.21 (*C*-3'α); 71.13 (*C*-3'β); 70.88 (*C*-5'β); 70.82 (*C*-5'α); 69.67 (*C*-3α); 69.29 (*C*-2'α); 69.23 (*C*-2'β); 68.51 (*C*-5α);66.79 (*C*-4'α); 66.75 (*C*-4'β); 62.16 (*C*-6β); 61.99 (*C*-6α); 60.98 (*C*-6'α); 60.96 (*C*-6'β); 21.06 (α), 21.03 (α), 21.02 (β), 20.94 (β), 20.91 (α), 20.91 (β), 20.81 (α), 20.80 (α, α), 20.80 (β, β), 20.78 (β), 20.68 (α), 20.66 (β) (14 x C(O)*C*H$_3$ppm.

MS (**MALDI**, **m/z**) : calcd. for $C_{26}H_{38}O_{18}$ $[M+Na]^+$ 659.179, found 659.111.

$[\alpha]_D^{21}$: 23.1 (c = 0.25, $CHCl_3$).

2,3,4,6-Tetra-*O*-acetyl-β-D-galactopyranosyl-(1$\rightarrow$4)-2,3,6-tri-*O*-acetyl-1-*O*-trichloroacetimido-α-D-glucopyranoside (58)

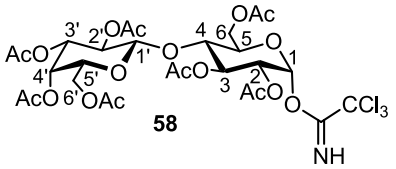

58

57 (200 mg, 314 μmol) was dissolved in anhydrous CH_2Cl_2, cooled to 0 °C and treated with $CNCCl_3$ (630 μl, 6.28 mmol) and DBU (47.0 μl, 314 μmol). Both reagents were dried over molecular sieves before usage. After stirring at 0 °C for 45 min charcoal was added and the mixture filtered over cellite. The solvent was evaporated in vacuum and flash chromatography (EE/Cy 1:1) afforded exclusively the α-anomer as a colorless solid (215 mg, 275 μmol, 88%).

Formular : $C_{28}H_{36}Cl_3NO_{18}$ (780.94 g/mol)

R_f : 0.24 (EE/Cy 1:1)

^{1}H (400 MHz, $CDCl_3$) : δ = 8.65 (s, 1H, N*H*); 6.48 (d, 1H, ^3J = 3.9 Hz, *H*-1); 5.56 (dd, 1H, ^3J = 9.9, 9.5 Hz, *H*-3); 5.35 (dd, 1H, ^3J = 3.4, 1.0 Hz, *H*-4'); 5.12 (dd, 1H, ^3J = 10.3, 7.8 Hz, *H*-2'); 5.06 (dd, 1H, ^3J = 9.9, 3.9 Hz, *H*-2); 4.96 (dd, 1H, ^3J = 10.3, 3.4 Hz, *H*-3'); 4.52 (d, 1H, ^3J = 7.8 Hz, *H*-1'); 4.50-4.46 (m, 1H, *H*-6'a); 4.17-4.06 (m, 4H, *H*-6'b, *H*-6a, *H*-6b, *H*-5'); 3.90-3.84 (m, 2H, *H*-4, *H*-5); 2.15, 2.11, 2.06, 2.04, 2.00, 1.96 (7s, 21H, 7 x C(O)CH_3) ppm.

^{13}C (100.6 MHz, $CDCl_3$) : δ = 170.29, 170.20, 170.10, 170.05, 170.03, 169.31, 169.02 (7 x *C*(O)CH_3), 161.00 (*C*=NH); 101.22 (*C*-1'); 92.92 (*C*-1); 90.71 (*C*Cl_3); 75.91 (*C*-4); 71.13 (*C*-3'); 70.93 (*C*-5); 70.74 (*C*-5'); 69.98 (*C*-2); 69.59 (*C*-3); 69.16 (*C*-2'); 66.61 (*C*-4'); 61.52 (*C*-6'); 60.77 (*C*-6); 20.85, 20.78, 20.64, 20.62, 20.48, 20.45 (7 x C(O)*C*H_3) ppm.

MS (MALDI, m/z) : calcd. for $C_{28}H_{36}Cl_3NO_{18}$ $[M+Na]^+$ 804.087, found 804.102.

2,3,4,6-Tetra-*O*-acetyl-β-D-galactopyranosyl-(1→4)-1-*O*-propargyl-2,3,6-tri-*O*-acetyl-β-D-glucopyranoside (64)

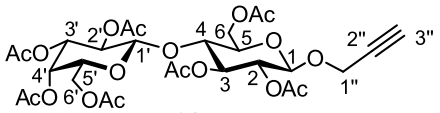

64

To a solution of **58** (1.00 g, 1.28 mmol) in anhydrous CH_2Cl_2 (15 ml) was added propargyl alcohol (224 μl, 3.84 mmol) and $BF_3{\cdot}Et_2O$ (49.0 μl, 384 μmol) at 0 °C. After 2 h the mixture was diluted with CH_2Cl_2 (10 ml), washed with H_2O (10 ml), sat. $NaHCO_3$ solution (10 ml) and brine (10 ml). Combined aqueous phases were reextracted with CH_2Cl_2 (20 ml), combined organic phases dried over $NaSO_4$ and concentrated. Flash chromatography (PE/EE 2:1→3:2) afforded the product as a colorless solid (430 mg, 637 μmol, 50%).

Formular : $C_{29}H_{38}O_{18}$ (674.60 g/mol)

R_f : 0.24 (EE/Cy 1:1)

^{1}H (600 MHz, $CDCl_3$) : δ = 5.34 (dd, 1H, ^3J = 3.5, 1.1 Hz, *H*-4'); 5.22 (dd, 1H, ^3J = 9.3 Hz, *H*-3); 5.10 (dd, 1H, ^3J = 10.5, 7.9 Hz, *H*-2'); 4.95 (dd, 1H, ^3J = 10.5, 3.5 Hz,

H-3'); 4.91 (dd, 1H, ^3J = 9.3, 7.9 Hz, *H*-2); 4.74 (d, 1H, ^3J = 7.9 Hz, *H*-1); 4.50 (dd, 1H, ^2J = 12.0 Hz, ^3J = 2.1 Hz, *H*-6a); 4.48 (d, 1H, ^3J = 7.9 Hz, *H*-1'); 4.34-4.33 (m, 2H, *H*-1"a, *H*-1"b); 4.14-4.06 (m, 3H, *H*-6b, *H*-6'a, *H*-6'b); 3.88-3.86 (m, 1H, *H*-5'); 3.81 (dd, 1H, ^3J = 9.9, 9.3 Hz, *H*-4); 3.63 (ddd, 1H, ^3J = 9.9, 4.9, 2.1 Hz, *H*-5); 2.45 (dd, 1H, ^4J = 2.4 Hz, *H*-3"); 2.15, 2.12, 2.06, 2.05, 2.04, 2.04, 1.96 (7s, 21H, 7 x C(O)CH_3 ppm.

^{13}C (150.9 MHz, $CDCl_3$) : δ = 170.49, 170.29, 170.21, 169.89, 169.88, 169.18 (7 x *C*(O)CH_3), 101.18 (*C*-1'); 98.00 (*C*-1); 78.21 (*C*-2"); 76.27 (*C*-4); 75.60 (*C*-3"); 72.89 (*C*-5), 72.81 (*C*-3); 71.44 (*C*-2); 71.12 (*C*-3'); 70.84 (*C*-5'); 69.22 (*C*-2'); 66.74 (*C*-4'); 61.95 (*C*-6); 60.95 (*C*-6'); 56.01 (*C*-1"); 21.00, 20.94, 20.87, 20.79, 20.78, 20.77, 20.65 (7 x C(O)*C*H_3) ppm.

HRMS (ESI, m/z) : calcd. for $C_{29}H_{38}O_{18}$ $[M+Na]^+$ 692.23964, found 692.24011, Δppm: 0.67.

β-D-Galactopyranosyl-(1→4)-1-*O*-propargyl-β-D-glucopyranoside (20)

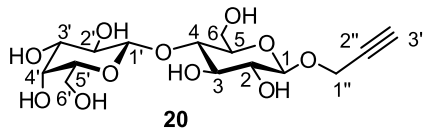

20

64 (50.0 mg, 74.0 μmol) was dissolved in anhydrous MeOH (2 ml) and treated with NaOMe (296 μl, 0.5 M in MeOH, 148 μmol) for 12 h at rt. The mixture was neutralized with Amberlite® IR125, the cation exchanger filtered off and the solvent evaporated in vacuum to yield a colorless solid (28.0 mg, 74.0 μmol, quant.).

Formular : $C_{15}H_{24}O_{11}$ (380.34 g/mol)

^{1}H (600 MHz, MeOD) : δ = 4.49 (d, 1H, ^3J = 7.8 Hz, *H*-1); 4.43 (dd, 1H, ^2J = 15.6 Hz, ^3J = 2.4 Hz, *H*-1"a); 4.39 (dd, 1H, ^2J = 15.6 Hz, ^3J = 2.5 Hz, *H*-1"b); 4.36 (d, 1H, ^3J = 7.6 Hz, *H*-1'); 3.90 (dd, 1H, ^2J = 12.1 Hz, ^3J = 2.4 Hz, *H*-6a); 3.84 (dd, 1H, ^2J = 12.1 Hz, ^3J = 4.4 Hz, *H*-6b); 3.81 (dd, 1H, ^3J = 3.2, 0.9 Hz, *H*-4'); 3.77 (dd, 1H, ^2J = 11.5 Hz, ^3J = 7.5 Hz, *H*-6'a); 3.69 (dd, 1H, ^2J = 11.5 Hz, ^3J = 4.7 Hz, *H*-6'b); 3.59-3.52 (m, 4H, *H*-4, *H*-5', *H*-2', *H*-3); 3.48 (dd, 1H, ^3J = 9.7, 3.2 Hz, *H*-3'); 3.41 (ddd, 1H, ^3J = 9.4, 4.4, 2.4 Hz, *H*-5); 3.27 (dd, ^3J = 9.0, 7.8 Hz, *H*-2); 2.87 (dd, 1H, ^4J = 2.5, 2.4 Hz, *H*-3") ppm.

^{13}C (150.9 MHz, MeOD) : δ = 105.07 (*C*-1'); 101.91 (*C*-1); 80.47 (*C*-4); 79.94

(*C*-2"); 77.07 (*C*-5'); 76.56 (*C*-5); 76.35 (*C*-3); 76.30 (*C*-3"; 74.79 (*C*-3'); 74.50 (*C*-2); 72.53 (*C*-2'); 70.29 (*C*-4'); 62.48 (*C*-6'); 61.81 (*C*-6); 56.57 (*C*-1") ppm.

HRMS (**ESI**, $\mathbf{m/z}$) : calcd. for $C_{15}H_{24}O_{11}$ $[M+Na]^+$ 403.12108, found 403.12121, Δppm: 0.32.

$[\alpha]_{\mathbf{D}}^{\mathbf{21}}$: 35.5 (c = 0.05, MeOH).

8.6.2 1-*O*-Allyl-β-D-lactose (53)

2,3,4,6-Tetra-*O*-acetyl-β-D-galactopyranosyl-(1→4)-1-*O*-allyl-2,3,6-tri-*O*-acetyl-β-D-glucopyranoside (65)

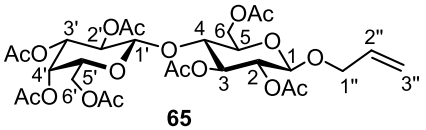

65

To a solution of **58** (1.07 g, 1.37 mmol) in anhydrous CH_2Cl_2 (20 ml) was added allyl alcohol (280 μl, 4.11 mmol) and $BF_3{\cdot}Et_2O$ (52.0 μl, 411 μmol) at 0 °C. After 2 h the mixture was diluted with CH_2Cl_2 (10 ml), washed with H_2O (10 ml), sat. $NaHCO_3$ solution (10 ml) and brine (10 ml). Combined aqueous phases were reextracted with CH_2Cl_2 (20 ml), combined organic phases dried over Na_2SO_4 and concentrated. Flash chromatography (PE/EE 2:1→3:2) afforded the product as a colorless solid (80 mg, 118 μmol, 9%).

Formular : $C_{29}H_{40}O_{18}$ (676.62 g/mol)

$\boldsymbol{R_f}$: 0.22 (EE/Cy 1:1)

^{1}H (**600 MHz**, **$CDCl_3$**) : δ = 5.86-5.77 (m, 1H, *H*-2"); 5.32 (dd, 1H, ^3J = 3.5, 1.1 Hz, *H*-4'); 5.23 (dddd, 1H, ^3J = 17.3 Hz, ^2J = 1.6 Hz. ^4J = 1.6 Hz, *H*-3"$_{trans}$); 5.20-5.15 (m, 2H, H-3, *H*-3"$_{cis}$); 5.08 (dd, 1H, ^3J = 10.5, 7.8 Hz, *H*-2'); 4.95-4.88 (m, 2H, *H*-2, *H*-3'); 4.51-4.45 (m, 3H, *H*-1, *H*-1', *H*-6'a); 4.28 (dddd, 1H, ^2J = 13.2 Hz, ^3J = 4.9 Hz, ^4J = 1.5 Hz, *H*-1"a); 4.13-4.02 (m, 4H, *H*-6'b, *H*-6a, *H*-6b, *H*-1"b); 3.87-3.84 (m, 1H, *H*-5'); 3.79 (dd, 1H, ^3J = 9.9, 9.2 Hz, *H*-4); 3.58 (ddd, 1H, ^3J = 9.9, 5.1, 2.1 Hz, *H*-5); 2.13, 2.10, 2.04, 2.02, 1.94 (7 x C(O)CH_3) ppm.

^{13}C (**150.9 MHz**, **$CDCl_3$**) : δ = 170.29, 170.26, 170.08, 169.97, 169.71, 169.55,

168.99 (7 x *C*(O)CH_3), 133.30 (*C*-2"); 117.54 (*C*-3"); 101.00 (*C*-1'); 99.26 (*C*-1); 76.24 (*C*-4); 72.80 (*C*-3); 72.58 (*C*-5); 71.63 (*C*-2); 70.94 (*C*-3'); 70.64 (*C*-5'); 69.94 (*C*-1"); 69.08 (*C*-2'); 66.59 (*C*-4'); 61.98 (*C*-6'); 60.78 (*C*-6); 20.78, 20.73, 20.63, 20.55, 20.42 (7 x C(O)*C*H_3) ppm.

HRMS (**ESI**, **m/z**) : calcd. for $C_{29}H_{40}O_{18}$ $[M+NH_4]^+$ 694.25529, found 694.25591, Δppm: 0.89.

β-D-Galactopyranosyl-(1→4)-1-*O*-allyl-β-D-glucopyranoside (53)

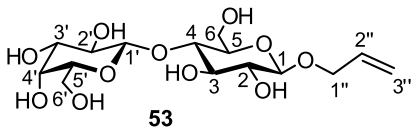

53

65 (75.0 mg, 111 μmol) was dissolved in anhydrous MeOH (8 ml) and treated with NaOMe (443 μl, 0.5 M in MeOH, 222 μmol) for 12 h at rt. The mixture was neutralized with Amberlit®e IR125, the cation exchanger filtered off and the solvent evaporated in vacuum to yield a colorless solid (40.0 mg, 105 μmol, 94%).

Formular : $C_{15}H_{26}O_{11}$ (382.36 g/mol)

^{1}H (**600 MHz**, **MeOD**) : δ = 6.00-5.93 (m, 1H, *H*-2"); 5.33 (dddd, ^3J = 17.3 Hz, ^2J = 1.7 Hz, ^4J = 1.7 Hz, *H*-3"$_{trans}$); 5.17 (dddd, ^3J = 10.4 Hz, ^2J = 1.7 Hz, ^4J = 1.3 Hz, *H*-3"$_{cis}$); 4.38-4.35 (m, 2H, *H*-1"a, *H*-1'); 4.34 (d, 1H, ^3J = 7.9 Hz, *H*-1); 4.15 (dddd, 1H, ^2J = 12.9 Hz, ^3J = 6.0 Hz, ^4J = 1.3 Hz, *H*-1"b); 3.90 (dd, 1H, ^2J = 12.1 Hz, ^3J = 2.5 Hz, *H*-6a); 3.84 (dd, 1H, ^2J = 12.1 Hz, ^3J = 4.3 Hz, *H*-6b); 3.81 (dd, 1H, ^3J = 3.3, 0.8 Hz, *H*-4'); 3.78 (dd, 1H, ^2J = 11.5 Hz, ^3J = 7.5 Hz, *H*-6'a); 3.79 (dd, 1H, ^2J = 11.5 Hz, ^3J = 4.7 Hz, *H*-6'b); 3.60-3.58 (m, 1H, *H*-5'); 3.58-3.51 (m, 3H, *H*-4, *H*-2', *H*-3); 3.48 (dd, 1H, ^3J = 9.8, 3.3 Hz, *H*-3'); 3.39 (ddd, 1H, ^3J = 9.7, 4.3, 2.5 Hz, *H*-5); 3.27 (dd, 1H, ^3J = 9.1, 7.9 Hz, *H*-2) ppm.

^{13}C (**150.9 MHz**, **MeOD**) : δ = 135.70 (*C*-2"); 117.47 (*C*-3"); 105.09 (*C*-1'); 103.25 (*C*-1); 80.59 (*C*-4); 77.09 (*C*-5');76.48, 76.46 (*C*-5, *C*-3);74.82 (*C*-3'); 74.73 (*C*-2); 72.56 (*C*-2'); 71.11 (*C*-1"); 70.30 (*C*-4'); 62.49 (*C*-6'); 61.90 (*C*-6) ppm.

HRMS(**ESI**, **m/z**) : calcd for $C_{15}H_{26}O_{11}$ $[M+Na]^+$ 405.13673, found 405.13665, Δppm: 0.20.

Bibliography

[1] Y. Yan, M. Björnmalm, F. Caruso, *ACS Nano* **2013**, *7*, 9512–9517.

[2] D. Hanahan, R. A. Weinberg, *Cell* **2011**, *144*, 646–674.

[3] L. Astorgues-Xerri, M. E. Riveiro, A. Tijeras-Raballand, M. Serova, C. Neuzillet, S. Albert, E. Raymond, S. Faivre, *Cancer Treat. Rev.* **2014**, *40*, 307–319.

[4] R. A. Weinberg, *Sci. Am.* **1996**, *275*, 62–70.

[5] N. Rubinstein, M. Alvarez, N. W. Zwirner, M. A. Toscano, J. M. Ilarregui, A. Bravo, J. Mordoh, L. Fainboim, O. L. Podhajcer, G. A. Rabinovich, *Cancer Cell* **2004**, *5*, 241–251.

[6] F. W. Sertürner, *Gilbert's Annalen d. Physik* **1817**, *25*, 56–89.

[7] P. Ehrlich, *Gesammelte Werke*, Vol. 3, Ed.: F. Himmelweit, Springer-Verlag, Berlin, **1957**.

[8] P. Ehrlich, A. Bertheim, *Ber. Dtsch. Chem. Ges.* **1912**, *45*, 756–766.

[9] A. Fleming, *Brit. J. Exp. Pathol.* **1929**, *10*, 226–236.

[10] J. Drews, *Science* **2000**, *287*, 1960–1964.

[11] H. van de Waterbeemd, E. Gifford, *Nat. Rev. Drug Discov.* **2003**, *2*, 192–204.

[12] J. Bajorath, *Nat. Rev. Drug Discov.* **2002**, *1*, 1474–1776.

[13] D. E. Scott, A. G. Coyne, S. A. Hudson, C. Abell, *Biochemistry* **2012**, *51*, 4990–5003.

[14] J. W. H. Li, J. C. Vederas, *Science* **2009**, *325*, 161–165.

[15] F. E. Koehn, G. T. Carter, *Nat. Rev. Drug Discov.* **2005**, *4*, 206–220.

[16] S. J. Projan, *Curr. Opin. Pharmacol.* **2003**, *3*, 457–458.

[17] B. E. Kirsop, *J. Ind. Microbiol. Biotechnol.* **1996**, *17*, 505–511.

[18] P. Gribbon, A. Sewing, *Drug Discov. Today* **2005**, *10*, 17–22.

[19] D. C. Rees, M. Congreve, C. W. Murray, R. Carr, *Nat. Rev. Drug Discov.* **2004**, *3*, 660–672.

[20] S. L. Dixon, H. O. Villar, *J. Chem. Inf. Comput. Sci.* **1998**, *38*, 1192–1203.

[21] M. A. Koch, A. Schuffenhauer, M. Scheck, S. Wetzel, M. Casaulta, A. Odermatt, P. Ertl, H. Waldmann, *Proc. Natl. Acad. Sci. U. S. A.* **2005**, *102*, 17272–17277.

[22] S. B. Shuker, P. J. Hajduk, R. P. Meadows, S. W. Fesik, *Science* **1996**, *274*, 1531–1534.

[23] C. W. Murray, T. L. Blundell, *Curr. Opin. Struct. Biol.* **2010**, *20*, 497–507.

[24] M. Congreve, C. W. Murray, T. L. Blundell, *Drug Discov. Today* **2005**, *10*, 895–907.

[25] W. P. Jencks, *P. Natl. Acad. Sci. Biol.* **1981**, *78*, 4046–4050.

[26] I. Jabeen, K. Pleban, U. Rinner, P. Chiba, G. F. Ecker, *J. Med. Chem.* **2012**, *55*, 3261–3273.

[27] C. W. Murray, D. C. Rees, *Nature Chem.* **2009**, *1*, 187–192.

[28] C. A. Lipinski, F. Lombardo, B. W. Dominy, P. J. Feeney, *Adv. Drug Delivery Rev.* **2001**, *46*, 3–26.

[29] F. H. Niesen, H. Berglund, M. Vedadi, *Nat. Protoc.* **2007**, *2*, 2212–2221.

[30] J. K. Kranz, C. Schalk-Hihi, *Methods Enzymol.* **2011**, *493*, 277–298.

[31] B. Ganem, Y. T. Li, J. D. Henion, *J. Am. Chem. Soc.* **1991**, *113*, 6294–6296.

[32] R. T. Aplin, C. V. Robinson, C. J. Schofield, N. J. Westwood, *J. Chem. Soc. Chem. Commun.* **1994**, 2415–2417.

[33] S. A. Hofstadler, K. A. Sannes-Lowery, *Nat. Rev. Drug Discov.* **2006**, *5*, 585–595.

[34] V. V. Hannah, C. Atmanene, D. Zeyer, A. Van Dorsselaer, S. Sanglier-Cianferani, *Future Med. Chem.* **2010**, *2*, 35–50.

[35] R. H. Griffey, K. A. Sannes-Lowery, J. J. Drader, V. Mohan, E. E. Swayze, S. A. Hofstadler, *J. Am. Chem. Soc.* **2000**, *122*, 9933–9938.

[36] R. H. Griffey, S. A. Hofstadler, K. A. Sannes-Lowery, D. J. Ecker, S. T. Crooke, *Proc. Natl. Acad. Sci. U. S. A.* **1999**, *96*, 10129–10133.

[37] K. A. Sannes-Lowery, R. H. Griffey, S. A. Hofstadler, *Anal. Biochem.* **2000**, *280*, 264–271.

[38] T. S. G. Olsson, M. A. Williams, W. R. Pitt, J. E. Ladbury, *J. Mol. Biol.* **2008**, *384*, 1002–1017.

[39] W. B. Turnbull, A. H. Daranas, *J. Am. Chem. Soc.* **2003**, *125*, 14859–14866.

[40] S. Núñez, J. Venhorst, C. G. Kruse, *Drug Discov. Today* **2012**, *17*, 10–22.

[41] U. Jönsson, L. Fagerstam, B. Ivarsson, B. Johnsson, R. Karlsson, K. Lundh, S. Lofas, B. Persson, H. Roos, I. Ronnberg, S. Sjolander, E. Stenberg, R. Stahlberg, C. Urbaniczky, H. Ostlin, M. Malmqvist, *BioTechniques* **1991**, *11*, 620–627.

[42] U. H. Danielson, *Curr. Top. Med. Chem.* **2009**, *9*, 1725–1735.

[43] T. Neumann, H. D. Junker, K. Schmidt, R. Sekul, *Curr. Top. Med. Chem.* **2007**, *7*, 1630–1642.

[44] M. Pellecchia, D. S. Sem, K. Wüthrich, *Nat. Rev. Drug Discov.* **2002**, *1*, 211–219.

[45] C. Dalvit, P. Pevarello, M. Tatò, M. Veronesi, A. Vulpetti, M. Sundström, *J. Biomol. NMR* **2000**, *18*, 65–68.

[46] C. Dalvit, G. Fogliatto, A. Stewart, M. Veronesi, B. Stockman, *J. Biomol. NMR* **2001**, *21*, 349–359.

[47] M. Mayer, B. Meyer, *Angew. Chem. Int. Ed.* **1999**, *38*, 1784–1788.

[48] T. Oltersdorf, S. W. Elmore, A. R. Shoemaker, R. C. Armstrong, D. J. Augeri, B. A. Belli, M. Bruncko, T. L. Deckwerth, J. Dinges, P. J. Hajduk, M. K. Joseph, S. Kitada, S. J. Korsmeyer, A. R. Kunzer, A. Letai, C. Li, M. J. Mitten, D. G. Nettesheim, S. Ng, P. M. Nimmer, J. M. O'Connor, A. Oleksijew, A. M. Petros, J. C. Reed, W. Shen, S. K. Tahir, C. B. Thompson, K. J. Tomaselli, B. L. Wang, M. D. Wendt, H. C. Zhang, S. W. Fesik, S. H. Rosenberg, *Nature* **2005**, *435*, 677–681.

[49] C.-M. Park, M. Bruncko, J. Adickes, J. Bauch, H. Ding, A. Kunzer, K. C. Marsh, P. Nimmer, A. R. Shoemaker, X. Song, S. K. Tahir, C. Tse, X. Wang, M. D. Wendt, X. Yang, H. Zhang, S. W. Fesik, S. H. Rosenberg, S. W. Elmore, *J. Med. Chem.* **2008**, *51*, 6902–6915.

[50] P. G. Wyatt, A. J. Woodhead, V. Berdini, J. A. Boulstridge, M. G. Carr, D. M. Cross, D. J. Davis, L. A. Devine, T. R. Early, R. E. Feltell, E. J. Lewis, R. L. McMenamin, E. F. Navarro, M. A. O'Brien, M. O'Reilly, M. Reule, G. Saxty, L. C. A. Seavers, D.-M. Smith, M. S. Squires, G. Trewartha, M. T. Walker, A. J. A. Woolford, *J. Med. Chem.* **2008**, *51*, 4986–4999.

[51] C. M. Rudin, C. L. Hann, E. B. Garon, M. R. de Oliveira, P. D. Bonomi, D. R. Camidge, Q. Chu, G. Giaccone, D. Khaira, S. S. Ramalingam, M. R. Ranson, C. Dive, E. M. McKeegan, B. J. Chyla, B. L. Dowell, A. Chakravartty, C. E. Nolan, N. Rudersdorf, T. A. Busman, M. H. Mabry, A. P. Krivoshik, R. A. Humerickhouse, G. I. Shapiro, L. Gandhi, *Clin. Cancer Res.* **2012**, *18*, 3163–3169.

[52] T. L. Blundell, H. Jhoti, C. Abell, *Nat. Rev. Drug Discov.* **2002**, *1*, 45–54.

[53] M. Malumbres, M. Barbacid, *Nat. Rev. Cancer* **2001**, *1*, 222–231.

[54] S. van den Heuvel, E. Harlow, *Science* **1993**, *262*, 2050–2054.

[55] D. N. W. Cooper, S. H. Barondes, *Glycobiology* **1999**, *9*, 979–984.

[56] R. J. Pieters, *ChemBioChem* **2006**, *7*, 721–728.

[57] J. Smetana, K., S. André, H. Kaltner, J. Kopitz, H.-J. Gabius, *Expert Opin. Ther. Targets* **2013**, *17*, 379–392.

[58] V. L. Thijssen, F. Poirier, L. G. Baum, A. W. Griffioen, *Blood* **2007**, *110*, 2819–2827.

[59] M. Salatino, D. O. Croci, G. A. Bianco, J. M. Ilarregui, M. A. Toscano, G. A. Rabinovich, *Expert Opin. Biol. Th.* **2008**, *8*, 45–57.

[60] G. A. Rabinovich, M. A. Toscano, *Nat. Rev. Immunol.* **2009**, *9*, 338–352.

[61] G. A. Rabinovich, *Br. J. Cancer* **2005**, *92*, 1188–1192.

[62] F. T. Liu, *Clin. Immunol.* **2000**, *97*, 79–88.

[63] F. T. Liu, G. A. Rabinovich, *Nat. Rev. Cancer* **2005**, *5*, 29–41.

[64] J. J. Shen, M. D. Person, J. J. Zhu, J. L. Abbruzzese, D. H. Li, *Cancer Res.* **2004**, *64*, 9018–9026.

[65] D. Demydenko, I. Berest, *Exp. Oncol.* **2009**, *31*, 74–79.

[66] J. Ouyang, A. Plütschow, E. P. von Strandmann, K. S. Reiners, S. Ponader, G. A. Rabinovich, D. Neuberg, A. Engert, M. A. Shipp, *Blood* **2013**, *121*, 3431–3433.

[67] S. H. Barondes, D. N. W. Cooper, M. A. Gitt, H. Leffler, *J. Biol. Chem.* **1994**, *269*, 20807–20810.

[68] K. Kasai, J. Hirabayashi, *J. Biochem.* **1996**, *119*, 1–8.

[69] V. I. Teichberg, I. Silman, D. D. Beitsch, G. Resheff, *Proc. Natl. Acad. Sci. U. S. A.* **1975**, *72*, 1383–1387.

[70] K. Drickamer, *J. Biol. Chem.* **1988**, *263*, 9557–9560.

[71] S. H. Barondes, V. Castronovo, D. N. W. Cooper, R. D. Cummings, K. Drickamer, T. Feizi, M. A. Gitt, J. Hirabayashi, C. Hughes, K. Kasai, H. Leffler, F. T. Liu, R. Lotan, A. M. Mercurio, M. Monsigny, S. Pillai, F. Poirer, A. Raz, P. W. J. Rigby, J. M. Rini, J. L. Wang, *Cell* **1994**, *76*, 597–598.

[72] Y. D. Lobsanov, M. A. Gitt, H. Leffler, S. H. Barondes, J. M. Rini, *J. Biol. Chem.* **1993**, *268*, 27034–27038.

[73] R. D. Cummings, F. T. Liu, *Essentials of Glycobiology*, 2^{nd} ed., pp. 475-489, Eds: A. Varki, R. D. Cummings, J. D. Esko, H. H. Freeze, P. Stanley, C. R. Bertozzi, G. W. Hart M. E. Etzler, Cold Spring Harbor Laboratory Press, New York, **2009**.

[74] M. F. López-Lucendo, D. Solís, S. André, J. Hirabayashi, K. Kasai, H. Kaltner, H. J. Gabius, A. Romero, *J. Mol. Biol.* **2004**, *343*, 957–970.

[75] K. Saraboji, M. Håkansson, S. Genheden, C. Diehl, J. Qvist, U. Weininger, U. J. Nilsson, H. Leffler, U. Ryde, M. Akke, D. T. Logan, *Biochemistry* **2012**, *51*, 296–306.

[76] D. D. Leonidas, E. H. Vatzaki, H. Vorum, J. E. Celis, P. Madsen, K. R. Acharya, *Biochemistry* **1998**, *37*, 13930–13940.

[77] S. A. Scott, K. Scott, H. Blanchard, *Acta Crystallogr. F* **2007**, *63*, 967–971.

[78] P. M. Collins, C. T. Öberg, H. Leffler, U. J. Nilsson, H. Blanchard, *Chem. Biol. Drug Des.* **2012**, *79*, 339–346.

[79] J. Seetharaman, A. Kanigsberg, R. Slaaby, H. Leffler, S. H. Barondes, J. M. Rini, *J. Biol. Chem.* **1998**, *273*, 13047–13052.

[80] G. Masuyer, T. Jabeen, C. T. Öberg, H. Leffler, U. J. Nilsson, K. R. Acharya, *FEBS J.* **2012**, *279*, 193–202.

[81] H. Ideo, T. Matsuzaka, T. Nonaka, A. Seko, K. Yamashita, *J. Biol. Chem.* **2011**, *286*, 11346–11355.

[82] H. Yoshida, M. Teraoka, N. Nishi, S.-i. Nakakita, T. Nakamura, M. Hirashima, S. Kamitori, *J. Biol. Chem.* **2010**, *285*, 36969–36976.

[83] J. S. Richardson, *Adv. Protein Chem.* **1981**, *34*, 167–339.

[84] M. J. Cho, R. D. Cummings, *J. Biol. Chem.* **1995**, *270*, 5198–5206.

[85] Y. Inagaki, Y. Sohma, H. Horie, R. Nozawa, T. Kadoya, *Eur. J. Biochem.* **2000**, *267*, 2955–2964.

[86] A. H. Pande, R. K. Gupta, Sumati, K. Hajela, *Protein Pept. Lett.* **2003**, *10*, 265–275.

[87] G. Levi, V. I. Teichberg, *J. Biol. Chem.* **1981**, *256*, 5735–5740.

[88] S. R. Stowell, M. Cho, C. L. Feasley, C. M. Arthur, X. Song, J. K. Colucci, S. Karmakar, P. Mehta, M. Dias-Baruffi, R. P. McEver, R. D. Cummings, *J. Biol. Chem.* **2009**, *284*, 4989–4999.

[89] T. Kadoya, K. Oyanagi, E. Kawakami, M. Hasegawa, Y. Inagaki, Y. Sohma, H. Horie, *Neurosci. Lett.* **2005**, *380*, 284–288.

[90] D. N. W. Cooper, S. H. Barondes, *J. Cell Biol.* **1990**, *110*, 1681–1691.

[91] R. C. Hughes, *Biochim. Biophys. Acta Gen. Subj.* **1999**, *1473*, 172–185.

[92] W. Nickel, *Eur. J. Biochem.* **2003**, *270*, 2109–2119.

[93] I. Camby, M. Le Mercier, F. Lefranc, R. Kiss, *Glycobiology* **2006**, *16*, 137R–157R.

[94] A. Muesch, E. Hartmann, K. Rohde, A. Rubartelli, R. Sitia, T. A. Rapoport, *Trends Biochem. Sci.* **1990**, *15*, 86–88.

[95] C. Seelenmeyer, S. Wegehingel, I. Tews, M. Künzler, M. Aebi, W. Nickel, *J. Cell Biol.* **2005**, *171*, 373–381.

[96] T. Schäfer, H. Zentgraf, C. Zehe, B. Brügger, J. Bernhagen, W. Nickel, *J. Biol. Chem.* **2004**, *279*, 6244–6251.

[97] W. Nickel, *Traffic* **2005**, *6*, 607–614.

[98] A. Satelli, P. S. Rao, P. K. Gupta, P. R. Lockman, K. S. Srivenugopal, U. S. Rao, *Oncol. Rep.* **2008**, *19*, 587–594.

[99] S. Di Lella, V. Sundblad, J. P. Cerliani, C. M. Guardia, D. A. Estrin, G. R. Vasta, G. A. Rabinovich, *Biochemistry* **2011**, *50*, 7842–7857.

[100] A. W. Stitt, C. McGoldrick, A. Rice-McCaldin, D. R. McCance, J. V. Glenn, D. K. Hsu, F. T. Liu, S. R. Thorpe, T. A. Gardiner, *Diabetes* **2005**, *54*, 785–794.

[101] G. R. Vasta, *Nat. Rev. Microbiol.* **2009**, *7*, 424–438.

[102] S. R. Stowell, C. M. Arthur, R. McBride, O. Berger, N. Razi, J. Heimburg-Molinaro, L. C. Rodrigues, J.-P. Gourdine, A. J. Noll, S. van Gunten, D. F. Smith, Y. A. Knirel, J. C. Paulson, R. D. Cummings, *Nat. Chem. Biol.* **2014**, *10*, 470–478.

[103] A. Danguy, I. Camby, R. Kiss, *Biochim. Biophys. Acta Gen. Subj.* **2002**, *1572*, 285–293.

[104] V. Balan, P. Nangia-Makker, A. Raz, *Cancers* **2010**, *2*, 592–610.

[105] D. O. Croci, M. Salatino, N. Rubinstein, J. P. Cerliani, L. E. Cavallin, H. J. Leung, J. Ouyang, J. M. Ilarregui, M. A. Toscano, C. I. Domaica, M. C. Croci, M. A. Shipp, E. A. Mesri, A. Albini, G. A. Rabinovich, *J. Exp. Med.* **2012**, *209*, 1985–2000.

[106] V. L. Thijssen, B. Barkan, H. Shoji, I. M. Aries, V. Mathieu, L. Deltour, T. M. Hackeng, R. Kiss, Y. Kloog, F. Poirier, A. W. Griffioen, *Cancer Res.* **2010**, *70*, 6216–6224.

[107] T. Dalotto-Moreno, D. O. Croci, J. P. Cerliani, V. C. Martinez-Allo, S. Dergan-Dylon, S. P. Mendez-Huergo, J. C. Stupirski, D. Mazal, E. Osinaga, M. A. Toscano, V. Sundblad, G. A. Rabinovich, M. Salatino, *Cancer Res.* **2013**, *73*, 1107–1117.

[108] H. Barrow, J. M. Rhodes, L.-G. Yu, *Int. J. Cancer* **2011**, *129*, 1–8.

[109] D. J. Laderach, L. D. Gentilini, L. Giribaldi, V. C. Delgado, L. Nugnes, D. O. Croci, N. Al Nakouzi, P. Sacca, G. Casas, O. Mazza, M. A. Shipp, E. Vazquez, A. Chauchereau, J. L. Kutok, S. J. Rodig, M. T. Elola, D. Compagno, G. A. Rabinovich, *Cancer Res.* **2013**, *73*, 86–96.

[110] J. Chen, S.-J. Zhou, Y. Zhang, G.-Q. Zhang, T.-Z. Zha, Y.-Z. Feng, K. Zhang, *World J. Gastroentero.* **2013**, *19*, 2073–2079.

[111] E.-J. Jung, H.-G. Moon, B. I. Cho, C.-Y. Jeong, Y.-T. Joo, Y.-J. Lee, S.-C. Hong, S.-K. Choi, W.-S. Ha, J. W. Kim, C.-W. Lee, J. S. Lee, S.-T. Park, *Int. J. Cancer* **2007**, *120*, 2331–2338.

[112] S. N. Chow, R. J. Chen, C. H. Chen, T. C. Chang, L. C. Chen, W. J. Lee, J. Shen, L. P. Chow, *Eur. J. Gynaecol. Oncol.* **2010**, *31*, 55–62.

[113] S. Saussez, I. Camby, G. Toubeau, R. Kiss, *Head Neck, J. Sci. Spec.* **2007**, *29*, 874–884.

[114] J. C. Chung, M. J. Oh, S. H. Choi, C. D. Bae, *Anz J. Surg.* **2008**, *78*, 245–251.

[115] T. Szöke, K. Kayser, J. D. Baumhäkel, I. Trojan, J. Furak, L. Tiszlavicz, A. Horvath, K. Szluha, H. J. Gabius, S. André, *Oncology* **2005**, *69*, 167–174.

[116] S. Rorive, N. Belot, C. Decaestecker, F. Lefranc, L. Gordower, S. Micik, C. A. Maurage, H. Kaltner, M. M. Ruchoux, A. Danguy, H. J. Gabius, I. Salmon, R. Kiss, I. Camby, *Glia* **2001**, *33*, 241–255.

[117] S. M. Koopmans, F. J. Bot, H. C. Schouten, J. Janssen, A. M. van Marion, *Am. J. Blood Res.* **2012**, *2*, 119–127.

[118] N. D'Haene, C. Maris, F. Sandras, M. F. Dehou, M. Remmelink, C. Decaestecker, I. Salmon, *Int. J. Immunopath. Ph.* **2005**, *18*, 431–443.

[119] M. J. Cho, R. D. Cummings, *J. Biol. Chem.* **1995**, *270*, 5207–5212.

[120] V. L. Thijssen, S. Hulsmans, A. W. Griffioen, *Am. J. Pathol.* **2008**, *172*, 545–553.

[121] X. Sanjuan, P. L. Fernandez, A. Castells, V. Castronovo, F. VandenBrule, F. T. Liu, A. Cardesa, E. Campo, *Gastroenterology* **1997**, *113*, 1906–1915.

[122] E. P. Moiseeva, E. L. Spring, J. H. Baron, D. P. de Bono, *J. Vasc. Res.* **1999**, *36*, 47–58.

[123] H.-J. Kim, H.-K. Jeon, Y. J. Cho, Y. A. Park, J.-J. Choi, I.-G. Do, S. Y. Song, Y.-Y. Lee, C. H. Choi, T.-J. Kim, D.-S. Bae, J.-W. Lee, B.-G. Kim, *Eur. J. Cancer* **2012**, *48*, 1914–1921.

[124] D. Spano, R. Russo, V. Di Maso, N. Rosso, L. M. Terracciano, M. Roncalli, L. Tornillo, M. Capasso, C. Tiribelli, A. Iolasconu, *Mol. Med.* **2010**, *16*, 102–115.

[125] A. B. Al-Mehdi, K. Tozawa, A. B. Fisher, L. Shientag, A. Lee, R. J. Muschel, *Nat. Med.* **2000**, *6*, 100–102.

[126] K. Ito, S. J. Ralph, *Clin. Exp. Metastas.* **2012**, *29*, 561–572.

[127] C. Fischer, H. Sanchez-Ruderisch, M. Welzel, B. Wiedenmann, T. Sakai, S. André, H. J. Gabius, L. Khachigian, K. M. Detjen, S. Rosewicz, *J. Biol. Chem.* **2005**, *280*, 37266–37277.

[128] A. Banh, J. Zhang, H. Cao, D. M. Bouley, S. Kwok, C. Kong, A. J. Giaccia, A. C. Koong, Q.-T. Le, *Cancer Res.* **2011**, *71*, 4423–4431.

[129] K. Yamaoka, K. Mishima, Y. Nagashima, A. Asai, Y. Sanai, T. Kirino, *J. Neurosci. Res.* **2000**, *59*, 722–730.

[130] H.-J. Kim, I.-G. Do, H.-K. Jeon, Y. J. Cho, Y. A. Park, J.-J. Choi, C. O. Sung, Y.-Y. Lee, C. H. Choi, T.-J. Kim, B.-G. Kim, J.-W. Lee, D.-S. Bae, *Hum. Pathol.* **2013**, *44*, 62–68.

[131] H. Li, Y. Wang, F. Zhou, *Clin. Invest. Med.* **2010**, *33*, E280–E289.

[132] V. L. Thijssen, R. Postel, R. J. M. G. E. Brandwijk, R. P. M. Dings, I. Nesmelova, S. Satijn, N. Verhofstad, Y. Nakabeppu, L. G. Baum, J. Bakkers, K. H. Mayo, F. Poirier, A. W. Griffioen, *Proc. Natl. Acad. Sci. U. S. A.* **2006**, *103*, 15975–15980.

[133] V. L. Thijssen, A. W. Griffioen, *Glycobiology* **2014**, doi:10.1093/glycob/cwu048.

[134] A. W. Griffioen, G. Molema, *Pharmcol. Rev.* **2000**, *52*, 237–268.

[135] S. H. Hsieh, N. W. Ying, M. H. Wu, W. F. Chiang, C. L. Hsu, T. Y. Wong, Y. T. Jin, T. M. Hong, Y. L. Chen, *Oncogene* **2008**, *27*, 3746–3753.

[136] M. Le Mercier, V. Mathieu, B. Haibe-Kains, G. Bontempi, T. Mijatovic, C. Decaestecker, R. Kiss, F. Lefranc, *J. Neuropath. Exp. Neur.* **2008**, *67*, 456–469.

[137] X.-Y. Zhao, T.-T. Chen, L. Xia, M. Guo, Y. Xu, F. Yue, Y. Jiang, G.-Q. Chen, K.-W. Zhao, *Carcinogenesis* **2010**, *31*, 1367–1375.

[138] N. L. Perillo, K. E. Pace, J. J. Seilhamer, L. G. Baum, *Nature* **1995**, *378*, 736–739.

[139] R. J. Patterson, W. Wang, J. L. Wang, *Glycoconjugate J.* **2004**, *19*, 499–506.

[140] J. W. Park, P. G. Voss, S. Grabski, J. L. Wang, R. J. Patterson, *Nucleic Acids Res.* **2001**, *29*, 3595–3602.

[141] A. Paz, R. Haklai, G. Elad-Sfadia, E. Ballan, Y. Kloog, *Oncogene* **2001**, *20*, 7486–7493.

[142] I. A. Prior, C. Muncke, R. G. Parton, J. F. Hancock, *J. Cell Biol.* **2003**, *160*, 165–170.

[143] B. Rotblat, L. Belanis, H. Liang, R. Haklai, G. Elad-Zefadia, J. F. Hancock, Y. Kloog, S. J. Plowman, *PLoS One* **2010**, *5*, doi: 10.1371/journal.pone.0011991.

[144] G. Elad-Sfadia, R. Haklai, E. Ballan, H. J. Gabius, Y. Kloog, *J. Biol. Chem.* **2002**, *277*, 37169–37175.

[145] B. Rotblat, H. Niv, S. Andre, H. Kaltner, H. J. Gabius, Y. Kloog, *Cancer Res.* **2004**, *64*, 3112–3118.

[146] S. André, R. J. Pieters, I. Vrasidas, H. Kaltner, L. Kuwabara, F. T. Liu, R. M. J. Liskamp, H. J. Gabius, *ChemBioChem* **2001**, *2*, 822–830.

[147] G. A. Rabinovich, A. Cumashi, G. A. Bianco, D. Ciavardelli, I. Iurisci, M. D'Egidio, E. Piccolo, N. Tinari, N. Nifantiev, S. Iacobelli, *Glycobiology* **2006**, *16*, 210–220.

[148] I. Vrasidas, S. Andre, P. Valentini, C. Bock, M. Lensch, H. Kaltner, R. M. J. Liskamp, H. J. Gabius, R. J. Pieters, *Org. Biomol. Chem.* **2003**, *1*, 803–810.

[149] J. Tejler, E. Tullberg, T. Frejd, H. Leffler, U. J. Nilsson, *Carbohydr. Res.* **2006**, *341*, 1353–1362.

[150] A. Nelson, J. M. Belitsky, S. Vidal, C. S. Joiner, L. G. Baum, J. F. Stoddart, *J. Am. Chem. Soc.* **2004**, *126*, 11914–11922.

[151] J. M. Belitsky, A. Nelson, J. D. Hernandez, L. G. Baum, J. F. Stoddart, *Chem. Biol.* **2007**, *14*, 1140–1151.

[152] M. C. Miller, A. Klyosov, K. H. Mayo, *Glycobiology* **2009**, *19*, 1034–1045.

[153] M. C. Miller, A. Klyosov, D. Platt, K. H. Mayo, *Carbohydr. Res.* **2009**, *344*, 1205–1212.

[154] M. C. Miller, A. A. Klyosov, K. H. Mayo, *Glycobiology* **2012**, *22*, 543–551.

[155] N. Demotte, R. Bigirimana, G. Wieërs, V. Stroobant, J.-L. Squiffflet, J. Carrasco, K. Thielemans, J.-F. Baurain, P. van der Smissen, P. J. Courtoy, P. van der Bruggen, *Clin. Cancer Res.* **2014**, *20*, 1823–1833.

[156] K. Ito, S. A. Scott, S. Cutler, L.-F. Dong, J. Neuzil, H. Blanchard, S. J. Ralph, *Angiogenesis* **2011**, *14*, 293–307.

[157] T. Delaine, I. Cumpstey, L. Ingragsia, M. Le Mercier, P. Okcchukwu, H. Leffler, R. Kiss, U. J. Nilsson, *J. Med. Chem.* **2008**, *51*, 8109–8114.

[158] H. van Hattum, H. M. Branderhorst, E. E. Moret, U. J. Nilsson, H. Leffler, R. J. Pieters, *J. Med. Chem.* **2013**, *56*, 1350–1354.

[159] A. W. Griffioen, D. W. J. van der Schaft, A. F. Barendsz-Janson, A. Cox, H. Boudier, H. F. P. Hillen, K. H. Mayo, *Biochem. J.* **2001**, *354*, 233–242.

[160] J. B. Wang, M. D. Wang, E. X. Li, D. F. Dong, *Peptides* **2012**, *38*, 457–462.

[161] R. P. M. Dings, B. W. Williams, C. W. Song, A. W. Griffioen, K. H. Mayo, R. J. Griffin, *Int. J. Cancer* **2005**, *115*, 312–319.

[162] R. P. M. Dings, M. Loren, H. Heun, E. McNiel, A. W. Griffioen, K. H. Mayo, R. J. Griffin, *Clin. Cancer Res.* **2007**, *13*, 3395–3402.

[163] R. P. M. Dings, E. S. Van Laar, J. Webber, Y. Zhang, R. J. Griffin, S. J. Waters, J. R. MacDonald, K. H. Mayo, *Cancer Lett.* **2008**, *265*, 270–280.

[164] R. P. M. Dings, M. M. Arroyo, N. A. Lockwood, L. I. Van Eijk, J. R. Haseman, A. W. Griffioen, K. H. Mayo, *Biochem. J.* **2003**, *373*, 281–288.

[165] R. J. Griffin, N. A. Koonce, R. P. M. Dings, E. Siegel, E. G. Moros, E. Braeuer-Krisch, P. M. Corry, *Radiat. Res.* **2012**, *177*, 804–812.

[166] M. Amano, M. Suzuki, S. Andoh, H. Monzen, K. Terai, B. Williams, C. W. Song, K. H. Mayo, T. Hasegawa, R. P. M. Dings, R. J. Griffin, *Int. J. Clin. Oncol.* **2007**, *12*, 42–47.

[167] R. P. M. Dings, Y. Yokoyama, S. Ramakrishnan, A. W. Griffioen, K. H. Mayo, *Cancer Res.* **2003**, *63*, 382–385.

[168] R. P. M. Dings, M. C. Miller, I. Nesmelova, L. Astorgues-Xerri, N. Kumar, M. Serova, X. Chen, E. Raymond, T. R. Hoye, K. H. Mayo, *J. Med. Chem.* **2012**, *55*, 5121–5129.

[169] J. McGraw, A. D. Gaudet, L. W. Oschipok, J. D. Steeves, F. Poirier, W. Tetzlaff, M. S. Ramer, *Pain* **2005**, *114*, 7–18.

[170] J. McGraw, L. T. McPhail, L. W. Oschipok, H. Horie, F. Poirier, J. D. Steeves, M. S. Ramer, W. Tetzlaff, *Eur. J. Neurosci.* **2004**, *20*, 2872–2880.

[171] V. M. Tribulatti, G. M. Figini, J. Carabelli, V. Cattaneo, O. Campetella, *J. Immunol.* **2012**, *188*, 2991–2999.

[172] C. Colnot, D. Fowlis, M. A. Ripoche, I. Bouchaert, F. Poirier, *Dev. Dyn.* **1998**, *211*, 306–313.

[173] L. A. Allison, *Fundamental Molecular Biology*, Blackwell Publishing, Oxford, **2006**.

[174] J. Sambrook, D. W. Russel, *MOLECULAR CLONING A Laboratory Manual*, 3rd ed., Cold Spring Harbor Laboratory Press, New York, **2001**.

[175] S. Knecht, D. Ricklin, A. N. Eberle, B. Ernst, *J. Mol. Recognit.* **2009**, *22*, 270–279.

[176] C. L. Young, Z. T. Britton, A. S. Robinson, *Biotechnol. J.* **2012**, *7*, 620–634.

[177] K. Terpe, *Appl. Microbiol. Biotechnol.* **2003**, *60*, 523–533.

[178] E. Hochuli, H. Döbeli, A. Schacher, *J. Chromatogr.* **1987**, *411*, 177–184.

[179] T. G. M. Schmidt, A. Skerra, *Protein Eng.* **1993**, *6*, 109–122.

[180] A. Pähler, W. A. Hendrickson, M. A. Kolks, C. E. Argaraña, C. R. Cantor, *J. Biol. Chem.* **1987**, *262*, 13933–13937.

[181] S. Voss, A. Skerra, *Protein Eng.* **1997**, *10*, 975–982.

[182] I. P. Korndörfer, A. Skerra, *Protein Sci.* **2002**, *11*, 883–893.

[183] S. I. Choi, H. W. Song, J. W. Moon, B. L. Seong, *Biotechnol. Bioeng.* **2001**, *75*, 718–724.

[184] M. P. Malakhov, M. R. Mattern, O. A. Malakhova, M. Drinker, S. D. Weeks, T. R. Butt, *J. Struct. Funct. Genomics* **2004**, *5*, 75–86.

[185] T. D. Parks, K. K. Leuther, E. D. Howard, S. A. Johnston, W. G. Dougherty, *Anal. Biochem.* **1994**, *216*, 413–417.

[186] U. C. Vothknecht, C. G. Kannangara, D. von Wettstein, *Proc. Natl. Acad. Sci. U. S. A.* **1996**, *93*, 9287–9291.

[187] L. Pauling, C. Niemann, *J. Am. Chem. Soc.* **1939**, *61*, 1860–1867.

[188] J. D. Bernal, D. Crowfoot, *Nature* **1934**, *133*, 794–795.

[189] J. C. Kendrew, R. E. Dickerson, B. E. Strandberg, R. G. Hart, D. R. Davies, D. C. Phillips, V. C. Shore, *Nature* **1960**, *185*, 422–427.

[190] M. F. Perutz, M. G. Rossmann, A. F. Cullis, H. Muirhead, G. Will, A. C. T. North, *Nature* **1960**, *185*, 416–422.

[191] B. Rupp, *BIOMOLECULAR CRYSTALLOGRAPHY Principles, Practice, and Application to Structural Biology*, Garland Science, New York, **2010**.

[192] G. Rhodes, *Chrystallography Made Crystal Clear*, 3rd ed., Elsevier Academic Press, London, **2006**.

[193] B. W. Low, C. C. H. Chen, J. E. Berger, L. Singman, J. F. Pletcher, *Proc. Natl. Acad. Sci. U. S. A.* **1966**, *56*, 1746–1750.

[194] E. Garman, C. Nave, *J. Synchrotron Radiat.* **2002**, *9*, 327–328.

[195] D. Ricklin, Dissertation, Universität Basel, **2005**.

[196] T. Turbadar, *Proc. Phys. Soc. (London)* **1959**, *73*, 40–44.

[197] R. P. H. Kooyman, H. Kolkman, J. Vangent, J. Greve, *Anal. Chim. Acta* **1988**, *213*, 35–45.

[198] E. Kretschmann, *Z. Phys.* **1971**, *241*, 313–324.

[199] B. Liedberg, C. Nylander, I. Lundstrom, *Sensors Actuators* **1983**, *4*, 299–304.

[200] H. Meyer, *BIOspektrum* **2002**, *Sonderausgabe 8. Jahrgang*, 532–535.

[201] E. Stenberg, B. Persson, H. Roos, C. Urbaniczky, *J. Colloid Interface Sci.* **1991**, *143*, 513–526.

[202] Y. Rossez, B. Coddeville, E. Elass, J.-F. Quinchon, O. Vidal, A. P. Corfield, P. Gosset, J.-M. Lacroix, J.-C. Michalski, C. Robbe-Masselot, *Biochimie* **2011**, *93*, 593–603.

[203] F. Debierre-Grockiego, S. Niehus, B. Coddeville, E. Elass, F. Poirier, R. Weingart, R. R. Schmidt, J. Mazurier, Y. Guérardel, R. T. Schwarz, *J. Biol. Chem.* **2010**, *285*, 32744–32750.

[204] F. Javier Muñoz, J. Pérez, A. Rumbero, J. Ignacio Santos, F. Javier Cañada, S. André, H.-J. Gabius, J. Jiménez-Barbero, J. V. Sinisterra, M. J. Hernáiz, *Bioconjugate Chem.* **2009**, *20*, 673–682.

[205] F. Javier Muñoz, J. Ignacio Santos, A. Ardá, S. Andrá, H.-J. Gabius, J. V. Sinisterra, J. Jiménez-Barbero, M. J. Hernáiz, *Org. Biomol. Chem.* **2010**, *8*, 2986–2992.

[206] S. W. Homans, *Drug Discov. Today* **2007**, *12*, 534–539.

[207] A. J. Ruben, Y. Kiso, E. Freire, *Chem. Biol. Drug Des.* **2006**, *67*, 2–4.

[208] J. B. Chaires, *Ann. Rev. Biophys.* **2008**, *37*, 135–151.

[209] G. A. Holdgate, W. H. J. Ward, *Drug Discov. Today* **2005**, *10*, 1543–1550.

[210] T. Wiseman, S. Williston, J. F. Brandts, L. N. Lin, *Anal. Biochem.* **1989**, *179*, 131–137.

[211] C. A. Anderson, *Phys. Rev.* **1933**, *43*, 491–494.

[212] P. A. M. Dirac, *Proc. R. Soc. Lond. A* **1028**, *117*, 610–624.

[213] M. Bauser, L. Lehmann, *Chem. unserer Zeit* **2012**, *46*, 80–99.

[214] T. Liang, C. N. Neumann, T. Ritter, *Angew. Chem. Int. Ed.* **2013**, *52*, 8214–8264.

[215] L. Cai, S. Lu, V. W. Pike, *Eur. J. Org. Chem.* **2008**, 2853–2873.

[216] K. Hamacher, H. H. Coenen, G. Stöcklin, *J. Nucl. Med.* **1986**, *27*, 235–238.

[217] T. Ido, C. N. Wan, V. Casella, J. S. Fowler, A. P. Wolf, M. Reivich, D. E. Kuhl, *J. Labelled Compd. Radiopharm.* **1978**, *14*, 175–183.

[218] P. Som, H. L. Atkins, D. Bandoypadhyay, J. S. Fowler, R. R. Macgregor, K. Matsui, Z. H. Oster, D. F. Sacker, C. Y. Shiue, H. Turner, C. N. Wan, A. P. Wolf, S. V. Zabinski, *J. Nucl. Med.* **1980**, *21*, 670–675.

[219] T. A. D. Smith, *Nucl. Med. Biol.* **2001**, *28*, 1–4.

[220] T. D. Poeppel, B. J. Krause, T. A. Heusner, C. Boy, A. Bockisch, G. Antoch, *Eur. J. Radiol.* **2009**, *70*, 382–392.

[221] T. R. DeGrado, S. W. Baldwin, S. Y. Wang, M. D. Orr, R. P. Liao, H. S. Friedman, R. Reiman, D. T. Price, R. E. Coleman, *J. Nucl. Med.* **2001**, *42*, 1805–1814.

[222] A. Roivainen, S. Forsback, T. Grönroos, P. Lehikoinen, M. Kähkönen, E. Sutinen, H. Minn, *Eur. J. Nucl. Med.* **2000**, *27*, 25–32.

[223] M. M. Alauddin, J. G. Gelovani, *Curr. Med. Chem.* **2010**, *17*, 1010–1029.

[224] H. Barthel, M. C. Cleij, D. R. Collingridge, O. C. Hutchinson, S. Osman, Q. M. He, S. K. Luthra, F. Brady, P. M. Price, E. O. Aboagye, *Cancer Res.* **2003**, *63*, 3791–3798.

[225] R. Mansi, X. Wang, F. Forrer, B. Waser, R. Cescato, K. Graham, S. Borkowski, J. C. Reubi, H. R. Mäcke, *Eur. J. Nucl. Med. Mol. I.* **2011**, *38*, 97–107.

[226] T. Feizi, F. Fazio, W. C. Chai, C. H. Wong, *Curr. Opin. Struct. Biol.* **2003**, *13*, 637–645.

[227] T. Horlacher, P. H. Seeberger, *Chem. Soc. Rev.* **2008**, *37*, 1414–1422.

[228] C.-Y. Wu, P.-H. Liang, C.-H. Wong, *Org. Biomol. Chem.* **2009**, *7*, 2247–2254.

[229] J. C. Paulson, O. Blixt, B. E. Collins, *Nat. Chem. Biol.* **2006**, *2*, 238–248.

[230] Z.-L. Zhi, N. Laurent, A. K. Powel, R. Karamanska, M. Fais, J. Voglmeir, A. Wright, J. M. Blackburn, P. R. Crocker, D. A. Russell, S. Flitsch, R. A. Field, J. E. Turnbull, *ChemBioChem* **2008**, *9*, 1568–1575.

[231] F. Fazio, M. C. Bryan, O. Blixt, J. C. Paulson, C. H. Wong, *J. Am. Chem. Soc.* **2002**, *124*, 14397–14402.

[232] K. R. Love, P. H. Seeberger, *Angew. Chem. Int. Ed.* **2002**, *41*, 3583–3586.

[233] O. Blixt, S. Head, T. Mondala, C. Scanlan, M. E. Huflejt, R. Alvarez, M. C. Bryan, F. Fazio, D. Calarese, J. Stevens, N. Razi, D. J. Stevens, J. J. Skehel, I. van Die, D. R. Burton, I. A. Wilson, R. Cummings, N. Bovin, C. H. Wong, J. C. Paulson, *Proc. Natl. Acad. Sci. U. S. A.* **2004**, *101*, 17033–17038.

[234] C. D. Rillahan, E. Schwartz, R. McBride, V. V. Fokin, J. C. Paulson, *Angew. Chem. Int. Ed.* **2012**, *51*, 11014–11018.

[235] J. Seibel, H. Hellmuth, B. Hofer, A. M. Kicinska, B. Schmalbruch, *ChemBioChem* **2006**, *7*, 310–320.

[236] S. J. Park, I. J. Shin, *Angew. Chem. Int. Ed.* **2002**, *41*, 3180–3182.

[237] Z. Pei, H. Yu, M. Theurer, A. Waldén, P. Nilsson, M. Yan, O. Ramström, *ChemBioChem* **2007**, *8*, 166–168.

[238] S. Fukui, T. Feizi, C. Galustian, A. M. Lawson, W. G. Chai, *Nat. Biotechnol.* **2002**, *20*, 1011–1017.

[239] J. L. de Paz, C. Noti, F. Böhm, S. Werner, P. H. Seeberger, *Chem. Biol.* **2007**, *14*, 879–887.

[240] P.-H. Liang, S.-K. Wang, C.-H. Wong, *J. Am. Chem. Soc.* **2007**, *129*, 11177–11184.

[241] M. D. Disney, P. H. Seeberger, *Chem. Biol.* **2004**, *11*, 1701–1707.

[242] J. Stevens, O. Blixt, J. C. Paulson, I. A. Wilson, *Nat. Rev. Microbiol.* **2006**, *4*, 857–864.

[243] S. van de Linde, M. Heilemann, M. Sauer, *Annu. Rev. Phys. Chem.* **2012**, *63*, 519–540.

[244] E. Abbe, *Arch. Mikrosk. Anat.* **1873**, *9*, 413–420.

[245] S. W. Hell, *Science* **2007**, *316*, 1153–1158.

[246] S. W. Hell, J. Wichmann, *Opt. Lett.* **1994**, *19*, 780–782.

[247] M. J. Rust, M. Bates, X. Zhuang, *Nat. Methods* **2006**, *3*, 793–795.

[248] M. Heilemann, S. van de Linde, M. Schüttpelz, R. Kasper, B. Seefeldt, A. Mukherjee, P. Tinnefeld, M. Sauer, *Angew. Chem. Int. Ed.* **2008**, *47*, 6172–6176.

[249] M. Heilemann, S. van de Linde, A. Mukherjee, M. Sauer, *Angew. Chem. Int. Ed.* **2009**, *48*, 6903–6908.

[250] A. Varki, N. Sharon, *Essentials of Glycobiology*, 2^{nd} ed., pp. 1-23, Eds: A. Varki, R. D. Cummings, J. D. Esko, H. H. Freeze, P. Stanley, C. R. Bertozzi, G. W. Hart M. E. Etzler, Cold Spring Harbor Laboratory Press, New York, **2009**.

[251] E. Saxon, C. R. Bertozzi, *Annu. Rev. Cell Dev. Biol.* **2001**, *17*, 1–23.

[252] Z. Shriver, S. Raguram, R. Sasisekharan, *Nat. Rev. Drug Discov.* **2004**, *3*, 863–873.

[253] A. Varki, *Glycobiology* **1993**, *3*, 97–130.

[254] C. R. Bertozzi, L. L. Kiessling, *Science* **2001**, *291*, 2357–2364.

[255] J. A. Prescher, C. R. Bertozzi, *Cell* **2006**, *126*, 851–854.

[256] P. Sears, C.-H. Wong, *Angew. Chem. Int. Ed.* **1999**, *38*, 2301–2324.

[257] H. Kayser, R. Zeitler, C. Kannicht, D. Grunow, R. Nuck, W. Reutter, *J. Biol. Chem.* **1992**, *267*, 16934–16938.

[258] O. T. Keppler, S. Hinderlich, J. Langner, R. Schwartz-Albiez, W. Reutter, M. Pawlita, *Science* **1999**, *284*, 1372–1376.

[259] O. T. Keppler, P. Stehling, M. Herrmann, H. Kayser, D. Grunow, W. Reutter, M. Pawlita, *J. Biol. Chem.* **1995**, *270*, 1308–1314.

[260] L. K. Mahal, K. J. Yarema, C. R. Bertozzi, *Science* **1997**, *276*, 1125–1128.

[261] K. J. Yarema, L. K. Mahal, R. E. Bruehl, E. C. Rodriguez, C. R. Bertozzi, *J. Biol. Chem.* **1998**, *273*, 31168–31179.

[262] K. L. Kiick, E. Saxon, D. A. Tirrell, C. R. Bertozzi, *Proc. Natl. Acad. Sci. U. S. A.* **2002**, *99*, 19–24.

[263] E. Saxon, S. J. Luchansky, H. C. Hang, C. Yu, S. C. Lee, C. R. Bertozzi, *J. Am. Chem. Soc.* **2002**, *124*, 14893–14902.

[264] A. Homann, R.-u. Qamar, S. Serim, P. Dersch, J. Seibel, *Beilstein J. Org. Chem.* **2010**, *6*, doi:10.3762/bjoc.6.24.

[265] E. Memmel, A. Homann, T. A. Oelschlaeger, J. Seibel, *Chem. Commun.* **2013**, *49*, 7301–7303.

[266] X. Ning, J. Guo, M. A. Wolfert, G.-J. Boons, *Angew. Chem. Int. Ed.* **2008**, *47*, 2253–2255.

[267] A. Niederwieser, A.-K. Späte, N. Long Duc, C. Jüngst, W. Reutter, V. Wittmann, *Angew. Chem. Int. Ed.* **2013**, *52*, 4265–4268.

[268] H. Möller, V. Böhrsch, J. Bentrop, J. Bender, S. Hinderlich, C. P. R. Hackenberger, *Angew. Chem. Int. Ed.* **2012**, *51*, 5986–5990.

[269] R. Huisgen, G. Szeimies, L. Möbius, *Chem. Ber. Recl.* **1967**, *100*, 2494–2507.

[270] C. W. Tornøe, C. Christensen, M. Meldal, *J. Org. Chem.* **2002**, *67*, 3057–3064.

[271] V. V. Rostovtsev, L. G. Green, V. V. Fokin, K. B. Sharpless, *Angew. Chem. Int. Ed.* **2002**, *41*, 2596–2599.

[272] H. C. Kolb, M. G. Finn, K. B. Sharpless, *Angew. Chem. Int. Ed.* **2001**, *40*, 2004–2021.

[273] E. M. Sletten, C. R. Bertozzi, *Angew. Chem. Int. Ed.* **2009**, *48*, 6974–6998.

[274] N. J. Agard, J. A. Prescher, C. R. Bertozzi, *J. Am. Chem. Soc.* **2004**, *126*, 15046–15047.

[275] J. M. Baskin, J. A. Prescher, S. T. Laughlin, N. J. Agard, P. V. Chang, I. A. Miller, A. Lo, J. A. Codelli, C. R. Bertozzi, *Proc. Natl. Acad. Sci. U. S. A.* **2007**, *104*, 16793–16797.

[276] S. T. Laughlin, J. M. Baskin, S. L. Amacher, C. R. Bertozzi, *Science* **2008**, *320*, 664–667.

[277] K. E. Pace, H. P. Hahn, L. G. Baum, *Methods Enzymol.* **2003**, *363*, 499–518.

[278] J. Hirabayashi, H. Ayaki, G. Soma, K. Kasai, *Biochim. Biophys. Acta* **1989**, *1008*, 85–91.

[279] K. A. Stannard, P. M. Collins, K. Ito, E. M. Sullivan, S. A. Scott, E. Gabutero, I. D. Grice, P. Low, U. J. Nilsson, H. Leffler, H. Blanchard, S. J. Ralph, *Cancer Lett.* **2010**, *299*, 95–110.

[280] D. I. Liao, G. Kapadia, H. Ahmed, G. R. Vasta, O. Herzberg, *Proc. Natl. Acad. Sci. U. S. A.* **1994**, *91*, 1428–1432.

[281] Y. Bourne, B. Bolgiano, D. L. Liao, G. Strecker, P. Cantau, O. Herzberg, T. Feizi, C. Cambillau, *Nat. Struct. Biol.* **1994**, *1*, 863–870.

[282] J. T. Powell, P. L. Whitney, *Biochem. J.* **1984**, *223*, 769–774.

[283] D. Giguère, S. André, M.-A. Bonin, M.-A. Bellefleur, A. Provencal, P. Cloutier, B. Pucci, R. Roy, H.-J. Gabius, *Bioorg. Med. Chem.* **2011**, *19*, 3280–3287.

[284] P. Sörme, Y. N. Qian, P. G. Nyholm, H. Leffler, U. J. Nilsson, *ChemBioChem* **2002**, *3*, 183–189.

[285] A. Neumann, Bachelor thesis, Julius-Maximilians-Universität Würzburg, **2013**.

[286] J. L. de Paz, R. Ojeda, A. G. Barrientos, S. Penadés, M. Martin-Lomas, *Tetrahedron:Asymmetry* **2005**, *16*, 149–158.

[287] R. U. Lemieux, *Adv. Carbohydr. Chem.* **1954**, *9*, 1–57.

[288] R. U. Lemieux, C. Brice, G. Huber, *Can. J. Chem.* **1955**, *33*, 134–147.

[289] G. Zemplén, E. Pascu, *Ber. Deut. Chem. Ges.* **1929**, *62*, 1613–1614.

[290] J. M. Vega-Pérez, C. Palo-Nieto, I. Periñán, M. Vega-Holm, J. M. Calderón-Montano, M. López-Lázaro, F. Iglesias-Guerra, *Eur. J. Org. Chem.* **2012**, 1237–1252.

[291] P. Bindschädler, C. Noti, E. Castagnetti, P. H. Seeberger, *Helv. Chim. Acta* **2006**, *89*, 2591–2610.

[292] K. V. Rao, P. R. Patil, S. Atmakuri, K. P. R. Kartha, *Carbohydr. Res.* **2010**, *345*, 2709–2713.

[293] P. Deslongchamps, *Tetrahedron* **1975**, *31*, 2463–2490.

[294] S. Deng, U. Gangadharmath, C.-W. T. Chang, *J. Org. Chem.* **2006**, *71*, 5179–5185.

[295] J. Tamura, K. W. Neumann, T. Ogawa, *Bioorg. Med. Chem. Lett.* **1995**, *5*, 1351–1354.

[296] L. F. Leloir, C. E. Cardini, *J. Am. Chem. Soc.* **1957**, *79*, 6340–6341.

[297] L. F. Leloir, *Science* **1971**, *172*, 1299–1303.

[298] H. Paulsen, *Angew. Chem. Int. Edit. Engl.* **1982**, *21*, 155–173.

[299] S. J. Danishefsky, M. T. Bilodeau, *Angew. Chem. Int. Edit. Engl.* **1996**, *35*, 1380–1419.

[300] C.-H. Hsu, S.-C. Hung, C.-Y. Wu, C.-H. Wong, *Angew. Chem. Int. Ed.* **2011**, *50*, 11872–11923.

[301] W. Königs, E. Knorr, *Chem. Ber.* **1901**, *34*, 957–981.

[302] E. Fischer, K. Raske, *Chem. Ber.* **1909**, *42*, 1465–1476.

[303] G. Grundler, R. R. Schmidt, *Liebigs Ann. Chem.* **1984**, 1826–1847.

[304] R. R. Schmidt, *Angew. Chem. Int. Edit. Engl.* **1986**, *25*, 212–235.

[305] S. David, S. Hanessian, *Tetrahedron* **1985**, *41*, 643–663.

[306] H. Dong, Y. Zhou, X. Pan, F. Cui, W. Liu, J. Liu, O. Ramström, *J. Org. Chem.* **2012**, *77*, 1457–1467.

[307] T. B. Grindley, *Adv. Carbohydr. Chem. Biochem.* **1998**, *53*, 17–142.

[308] M. Hesse, H. Meier, B. Zeeh, *Spektroskopische Methoden in der organischen Chemie*, 6^{th} ed., Thieme, Stuttgart, **2002**.

[309] C. Janiak, *J. Chem. Soc. Dalton Trans.* **2000**, 3885–3896.

[310] K. Sander, T. Kottke, Y. Tanrikulu, E. Proschak, L. Weizel, E. H. Schneider, R. Seifert, G. Schneider, H. Stark, *Bioorg. Med. Chem.* **2009**, *17*, 7186–7196.

[311] R. Huisgen, *Angew. Chem. Int. Ed.* **1963**, *75*, 604–637.

[312] R. Huisgen, *Angew. Chem. Int. Ed.* **1963**, *75*, 742–754.

[313] B. T. Worrell, J. A. Malik, V. V. Fokin, *Science* **2013**, *340*, 457–460.

[314] F. Himo, T. Lovell, R. Hilgraf, V. V. Rostovtsev, L. Noodleman, K. B. Sharpless, V. V. Fokin, *J. Am. Chem. Soc.* **2005**, *127*, 210–216.

[315] J. E. Hein, V. V. Fokin, *Chem. Soc. Rev.* **2010**, *39*, 1302–1315.

[316] M. Meldal, C. W. Tornøe, *Chem. Rev.* **2008**, *108*, 2952–3015.

[317] Q. Wang, T. R. Chan, R. Hilgraf, V. V. Fokin, K. B. Sharpless, M. G. Finn, *J. Am. Chem. Soc.* **2003**, *125*, 3192–3193.

[318] N. P. Grimster, B. Stump, J. R. Fotsing, T. Weide, T. T. Talley, J. G. Yamauchi, A. Nemecz, C. Kim, K. Y. Ho, K. B. Sharpless, P. Taylor, V. V. Fokin, *J. Am. Chem. Soc.* **2012**, *134*, 6732–6740.

[319] J. Andersen, S. Bolvig, X. F. Liang, *Synlett* **2005**, 2941–2947.

[320] J. E. Ladbury, G. Klebe, E. Freire, *Nat. Rev. Drug Discov.* **2010**, *9*, 23–27.

[321] F. P. Schwarz, K. D. Puri, R. G. Bhat, A. Surolia, *J. Biol. Chem.* **1993**, *268*, 7668–7677.

[322] A. Biela, N. N. Nasief, M. Betz, A. Heine, D. Hangauer, G. Klebe, *Angew. Chem. Int. Ed.* **2013**, *52*, 1822–1828.

[323] E. Memmel, unpublished results, Julius-Maximilians-Universität Würzburg.

[324] A. D. Göhler, Dissertation, Julius-Maximilians-Universität Würzburg, **2012**.

[325] A. Bernardi, J. Jiménez-Barbero, A. Casnati, C. De Castro, T. Darbre, F. Fieschi, J. Finne, H. Funken, K.-E. Jaeger, M. Lahmann, T. K. Lindhorst, M. Marradi, P. Messner, A. Molinaro, P. V. Murphy, C. Nativi, S. Oscarson, S. Penadés, F. Peri, R. J. Pieters, O. Renaudet, J.-L. Reymond, B. Richichi, J. Rojo, F. Sansone, C. Schäffer, W. B. Turnbull, T. Velasco-Torrijos, S. Vidal, S. Vincent, T. Wennekes, H. Zuilhof, A. Imberty, *Chem. Soc. Rev.* **2013**, *42*, 4709–4727.

[326] E. M. Munoz, J. Correa, E. Fernandez-Megia, R. Riguera, *J. Am. Chem. Soc.* **2009**, *131*, 17765–17767.

[327] L. Song, J.-W. Tang, L. Owusu, M.-Z. Sun, J. Wu, J. Zhang, *Clin. Chim. Acta* **2014**, *431*, 185–191.

[328] V. Balan, Y. Wang, P. Nangia-Makker, D. Kho, M. Bajaj, D. Smith, L. Heilbrun, A. Raz, H. E., *Oncotarget* **2013**, *4*, 542–549.

[329] V. B. K. Pinnelli, M. Sirksiker, W. D. Silvia, *Intl. J. Chem. Pharm. Res.* **2013**, *2*, 081–094.

[330] M. Watanabe, I. Takemasa, N. Kaneko, Y. Yokoyama, E.-I. Matsuo, S. Iwasa, M. Mori, N. Matsuura, M. Monden, O. Nishimura, *Oncol. Rep.* **2011**, *25*, 1217–1226.

[331] F. van den Brûle, S. Califice, V. Castronovo, *Glycoconjugate J.* **2004**, *19*, 537–542.

[332] Y. Takenaka, T. Fukumori, A. Raz, *Glycoconjugate J.* **2004**, *19*, 543–549.

[333] P. Sörme, P. Arnoux, B. Kahl-Knutsson, H. Leffler, J. M. Rini, U. J. Nilsson, *J. Am. Chem. Soc.* **2005**, *127*, 1737–1743.

[334] S. Saussez, F. Lorfevre, T. Lequeux, G. Laurent, G. Chantrain, F. Vertongen, G. Toubeau, C. Decaestecker, R. Kiss, *Oral Oncol.* **2008**, *44*, 86–93.

[335] I. Iurisci, N. Tinari, C. Natoli, D. Angelucci, E. Cianchetti, S. Iacobelli, *Clin. Cancer Res.* **2000**, *6*, 1389–1393.

[336] S. Saussez, D. Glinoer, G. Chantrain, F. Pattou, B. Carnaille, S. André, H.-J. Gabius, G. Laurent, *Thyroid* **2008**, *18*, 705–712.

[337] R. Löser, R. Bergmann, M. Frizler, B. Mosch, L. Dombrowski, M. Kuchar, J. Steinbach, M. Gütschow, J. Pietzsch, *ChemMedChem* **2013**, *8*, 1330–1344.

[338] D. W. Kim, D.-S. Ahn, Y.-H. Oh, S. Lee, H. S. Kil, S. J. Oh, S. J. Lee, J. S. Kim, J. S. Ryu, D. H. Moon, D. Y. Chi, *J. Am. Chem. Soc.* **2006**, *128*, 16394–16397.

[339] J. Seibel, S. König, A. Göhler, S. Doose, E. Memmel, N. Bertleff, M. Sauer, *Expert Rev. Proteomics* **2013**, *10*, 25–31.

[340] M. S. Itano, C. Steinhauer, J. J. Schmied, C. Forthmann, P. Liu, A. K. Neumann, N. L. Thompson, P. Tinnefeld, K. Jacobson, *Biophys. J.* **2012**, *102*, 1534–1542.

[341] B. Belardi, G. P. O'Donoghue, A. W. Smith, J. T. Groves, C. R. Bertozzi, *J. Am. Chem. Soc.* **2012**, *134*, 9549–9552.

[342] S. Letschert, unpublished results, Julius-Maximilians-Universität Würzburg.

[343] S. Lee, H. Koo, J. H. Na, S. J. Han, H. S. Min, S. J. Lee, S. H. Kim, S. H. Yun, S. Y. Jeong, I. C. Kwon, K. Choi, K. Kim, *ACS Nano* **2014**, *8*, 2048–2063.

[344] L. F. Tietze, U. Bothe, *Chem.-Eur. J.* **1998**, *4*, 1179–1183.

[345] H. J. Allen, E. A. Z. Johnson, *Carbohydr. Res.* **1977**, *58*, 253–265.

[346] A. J. McCoy, R. W. Grosse-Kunstleve, P. D. Adams, M. D. Winn, L. C. Storoni, R. J. Read, *J. Appl. Crystallogr.* **2007**, *40*, 658–674.

[347] P. D. Adams, P. V. Afonine, G. Bunkóczi, V. B. Chen, I. W. Davis, N. Echols, J. J. Headd, L.-W. Hung, G. J. Kapral, R. W. Grosse-Kunstleve, A. J. McCoy, N. W. Moriarty, R. Oeffner, R. J. Read, D. C. Richardson, J. S. Richardson, T. C. Terwilliger, P. H. Zwart, *Acta Crystallogr. D* **2010**, *66*, 213–221.

[348] A. W. Schüttelkopf, D. M. F. van Aalten, *Acta Crystallogr. D* **2004**, *60*, 1355–1363.

Appendix A

List of Abbreviations

1D	one-dimensional
2D	two-dimensional
Å	Ångström
Ac	acetyl
$[\alpha]_D$	specific rotation
AEBSF	4-(2-aminoethyl)benzensulfonylfluorid
AP	aprotinin
APS	ammonium persulfate
Arg, R	arginine
ASF	asialofetuin
Asn, N	asparagine
Asp, D	aspartic acid
ATP	adenosine triphosphate
arom	aromatic
Bis-Tris	Bis(2-hydroxyethyl)amino-tris(hydroxymethyl)methane
bp	base pair(s)
BSA	bovine serum albumin
Bu	butyl
c	concentration
calcd.	calculated
cat.	catalytic
CD	cluster of differentiation
$CDCl_3$	*deutero*-chloroform
CDK	cyclin-dependent kinase
Con A	Concanavalin A
conc.	concentrated
COSY	^{1}H correlation spectroscopy (NMR)

CRD	carboydrate recognition domain
CSA	camphor-10-sulfonic acid
CT	computer tomography
Cy	cyclohexane
Cys, C	cysteine
d	day(s)
d	deutero
δ	chemical shift (NMR)
Da	Dalton
DBU	1,8-diazabicyclo[5.4.0]undec-7-ene
DDQ	2,3-dichloro-5,6-dicyano-*p*-benzoquinone
DEPT	distortionless enhancement by polarization transfer
DMF	*N*,*N*-dimethylformamide
dNTP	desoxynucleotide triphosphate
*d*STORM	direct stochastic reproduction microscopy
ECM	extracellular matrix
EDC	*N*-ethyl-3-(3-dimethylaminopropyl)-carbodiimide
EDTA	ethylenediaminetetraacetic acid
EE	ethyl acetate
eq.	equivalent(s)
ER	endoplasmatic reticulum
Escherichia coli	*E. coli*
ESI	electronspray ionization
Et	ethyl
FBLD	fragment-based lead discovery
FKBP	FK506 binding protein
FRET	Förster resonance energy transfer
g	gram(s)
Gln, Q	glutamine
Glu, E	glutamic acid
Gly, G	glycine
GTP	guanosine-triphosphate
h	hour(s)
HEPES	2-[4-(2-hydroxyethyl)piperazin-1-yl]ethanesulfonic acid
hGal	human galectin
HIF	hypoxia-inducible factor
His, H	histidine
HMBC	heteronuclear multiple bond correlation (NMR)
HRMS	high resolution mass spectrometry

HSQC	heteronuclear single quantum correlation (NMR)
HTS	high-throughput screening
Hz	Hertz (frequency)
IAA	iodoacetamide
IC_{50}	half maximal inhibitory concentration
IFN	interferon
IMAC	immobilized-metal affinity chromatography
IPTG	isopropyl-β-D-1-thiogalactoside
IR	infra-red
ITC	isothermal titration calorimetry
IUPAC	International Union of Pure and Applied Chemistry
J	coupling constant (NMR)
K_a	binding constant
K_d	dissociation constant
Kan	kanamycin
λ	wavelength
LacNAc	*N*-acetyllactosamine
LE	ligand efficiency
LG	leaving group
LIP	leupeptin
LPMSF	phenylmethylsulfonyl fluoride
Lys, K	lysine
m	meta
M	molar (c)
mAB	monoclonal antibody
MALDI	matrix-assisted laser desorption/ionization
Me	methyl
β-ME	β-mercaptoethanol
min	minute(s)
mol	mole(s)
MS	mass spectrometry
mw	micro wave
$\tilde{\nu}$	frequency (IR)
NHS	*N*-hydroxysuccinimide
Ni-NTA	Ni(II)-nitrilotriacetic acid
NMR	nuclear magnetic resonance
o	ortho
p	para
PBS	phosphate buffered saline

PCR	polymerase chain reaction
PE	petrol ether
PEG	polyethylene glycol
PEP	pepstatin
PET	positron emission tomography
Ph	phenyl
Phe, F	phenylalanine
PNA	peanut agglutinin
ppm	parts per million (NMR)
Pro, P	proline
quant.	quantitative
quart	quarternary
R	undefined substituent
R_f	retention factor (TLC)
rpm	revolutions per minute
rt	room temperature
RU	response unit(s)
s	secund(s)
sat.	saturated
SAP	serum amyloid P
SAR	structure activity relation
SDS-PAGE	sodium dodecyl sulfate polyacrylamide gel electrophoresis
Ser, S	serine
S_N2	bimolecular nucleophilic substitution
SPR	surface plasmon resonance
STD	saturation transfer difference
stddH_2O	sterile double destilled water
tert	tertiary
T	temperature
$t_{1/2}$	half-life time
TAE	tris-acetate EDTA
TBAHS	tetrabutylammonium hydrogensulfate
TBTA	tris[(1-benzyl-1*H*-1,2,3-triazol-4-yl)methyl]amine
TCEP	tris(2-carboxyethyl)phosphine
TDG	thiodigalactoside
TEMED	*N*,*N*,*N*',*N*'-tetramethylethylenediamine
TEV	tobacco etch virus
TFA	trifluoracetic acid

TFAA	trifluoracetic anhydride
Thr, T	threonine
TIL	tumor-infiltrating lymphocytes
tlc	thin layer chromatography
TMSOTf	trimethylsilyl trifluoromethanesulfonate
Tris	tris(hydroxymethyl)aminomethane
Trp, W	tryptophan
Ts	toluenesulfonyl
TS	thermal shift
Tyr, Y	tyrosine
UDP	uridine diphosphate
UV	ultra-violet
Val, V	valine
VEGF	vascular endothelial growth factor
WaterLOGSY	water-ligand observation with gradient spectroscopy

Appendix B

Experimental Data

B.1 Protein X-Ray Analysis

	LacNAc	**10**	**9a**
A. Data collection and processing			
Wavelength (Å)	0.97928	0.9793	0.97635
Space group	P21212	P21212	P21212
Unit cell parameters *a*, *b*, *c* (Å)	66.4, 85.5, 116.1	43.5, 58.1, 110.8	43.3, 58.4, 111.7
B. Diffraction data[a]			
Resolution range (Å)	50-1.40 (1.48-1.40)	50-1.20 (1.27-1.20)	50-1.42 (1.46-1.42)
Observed reflections (Å)	1839529 (289970)	526715 (59754)	226662 (16629)
Unique reflections	129742 (20603)	526715 (11795)	53620 (3915)
R(I)sym (%)	9.2 (95.0)	8.1 (95.2)	6.7 (99.2)
I/σ (I)	16.7 (1.5)	14.2 (1.5)	13.0 (1.8)
Completeness (%)	99.2 (98.4)	96.1 (83.5)	99.2 (99.4)
C. Refinement			
Resolution range (Å)	50-1.40	50-1.20	40.3-1.46
Reflections used in refinement	129632	84319	49184

	LacNAc	**10**	**9a**
Final *R*-values for all reflections[b] (work/free) (%)	16.2 (20.3)	15.1 (17.8)	15.0 (18.7)
No. of dimer molecules per AU	2	1	1
Protein residues	532	267	266
Ligand atoms	51	63	80
Water molecules	496	291	225
RMSD from ideality:			
Bond lengths (Å)	0.018	0.022	0.014
Bond angles (°)	2.02	2.04	1.62
Ramachandran plot:			
Residues in most favored regions (%)	98.0	96.2	96.8
Residues in allowed regions (%)	2.0	3.8	3.2
Residues in disallowed regions (%)	0.0	0.0	0.0
Mean B-factor (Å^2)	30.7	19.5	24.0
Protein	29.3	19.5	24.0
Ligand	24.2	25.7	33.8
Water molecules	44.6	35.2	36.5
PDB ID code	4Q26	4Q27	4Q1P

[a] Number in parenthesis indicate highest resolution shell.

[b] For calculation of R_{free} 5% of the reflections were excluded from the refinement process.

	9f	**9i**	**19**
A. Data collection and processing			
Wavelength (Å)	0.97036	0.9766	0.9766
Space group	P21212	P21212	P21212
Unit cell parameters *a*, *b*, *c* (Å)	43.1, 58.4, 111.2	43.3, 58.4, 111.1	43.2, 58.2, 111.2
B. Diffraction data[a]			
Resolution range (Å)	50-1.47 (1.51-1.47)	50-1.36 (1.44-1.36)	55-1.35 (1.43-1.35)
Observed reflections (Å)	189776 (14158)	481183 (61238)	426111 (58484)
Unique reflections	48330 (3554)	61064 (9391)	60692 (8975)
R(I)sym (%)	4.7 (91.5)	6.8 (124.1)	7.5 (177.1)
I/σ (I)	15.8 (1.8)	15.6 (1.5)	13.7 (1.26)
Completeness (%)	99.3 (99.6)	99.1 (95.5)	95.8 (88.9)
C. Refinement			
Resolution range (Å)	50-1.47	50-1.40	55-1.35
Reflections used in refinement	48323	56021	62132
Final *R*-values for all reflections[b] (work/free) (%)	15.6/19.7	18.2/19.5	15.6/17.9
No. of dimer molecules per AU	1	1	1
270266			
Ligand atoms	83	77	57
Water molecules	206	236	258
RMSD from ideality:			
Bond lengths (Å)	0.012	0.019	0.010
Bond angles (°)	1.67	2.08	1.43
Ramachandran plot:			

	9f	**9i**	**19**
Residues in most favored regions (%)	96.8	97.5	96.9
Residues in allowed regions (%)	3.2	2.5	2.8
Residues in disallowed regions (%)	0.0	0.0	0.0
Mean B-factor (Å^2)	28.1	24.8	22.1
Protein	27.0	22.8	20.4
Ligand	36.4	44.9	32.2
Water molecules	40.0	36.6	35.1
PDB ID code	4Q1R	4Q2F	-

[a] Numbers in parenthesis indicate highest resolution shell.

[b] For calculation of R_{free} 5% of the reflections were excluded from the refinement process.

The structure of ligand-free hGal-1 features the same space group (P212121) and similar unit cell parameters (43.3, 58.1 111.6 Å) to the structures of complexes between hGal-1 and synthetic ligands. Diffraction data of this structure as well as of the complex between hGal-1 and **23** were not fully refined and are not listed for that reason.

B.2 SPR Analysis

hGal-1

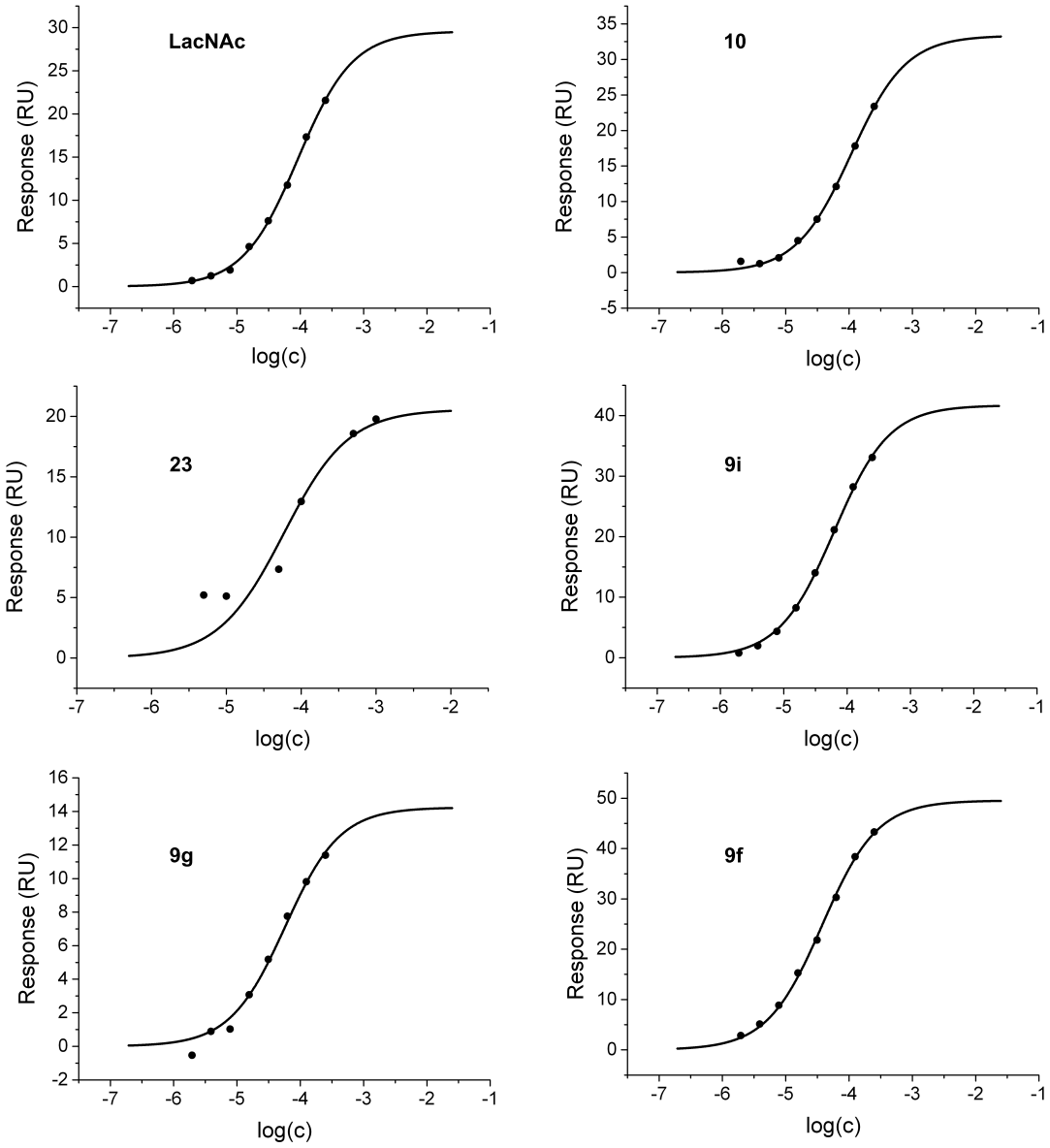

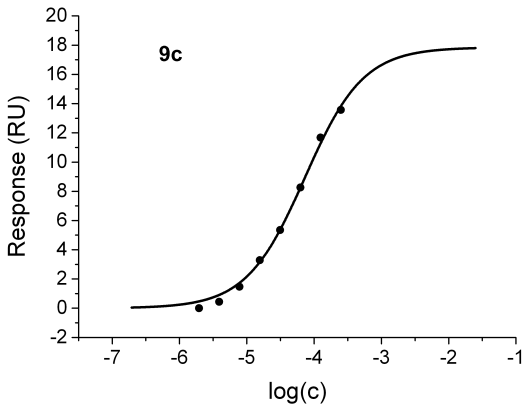
9c
Response (RU)
log(c)

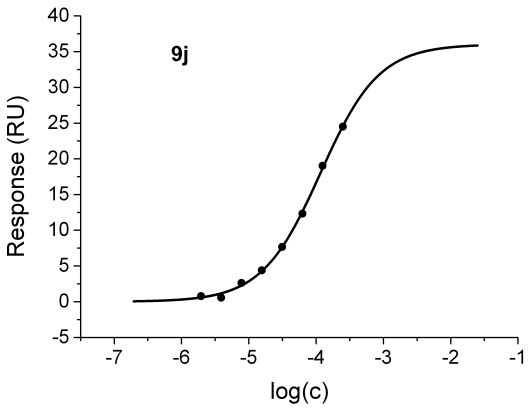
9j
Response (RU)
log(c)

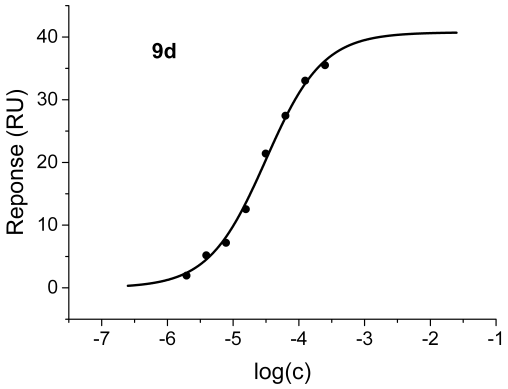
9d
Reponse (RU)
log(c)

hGal-3CRD

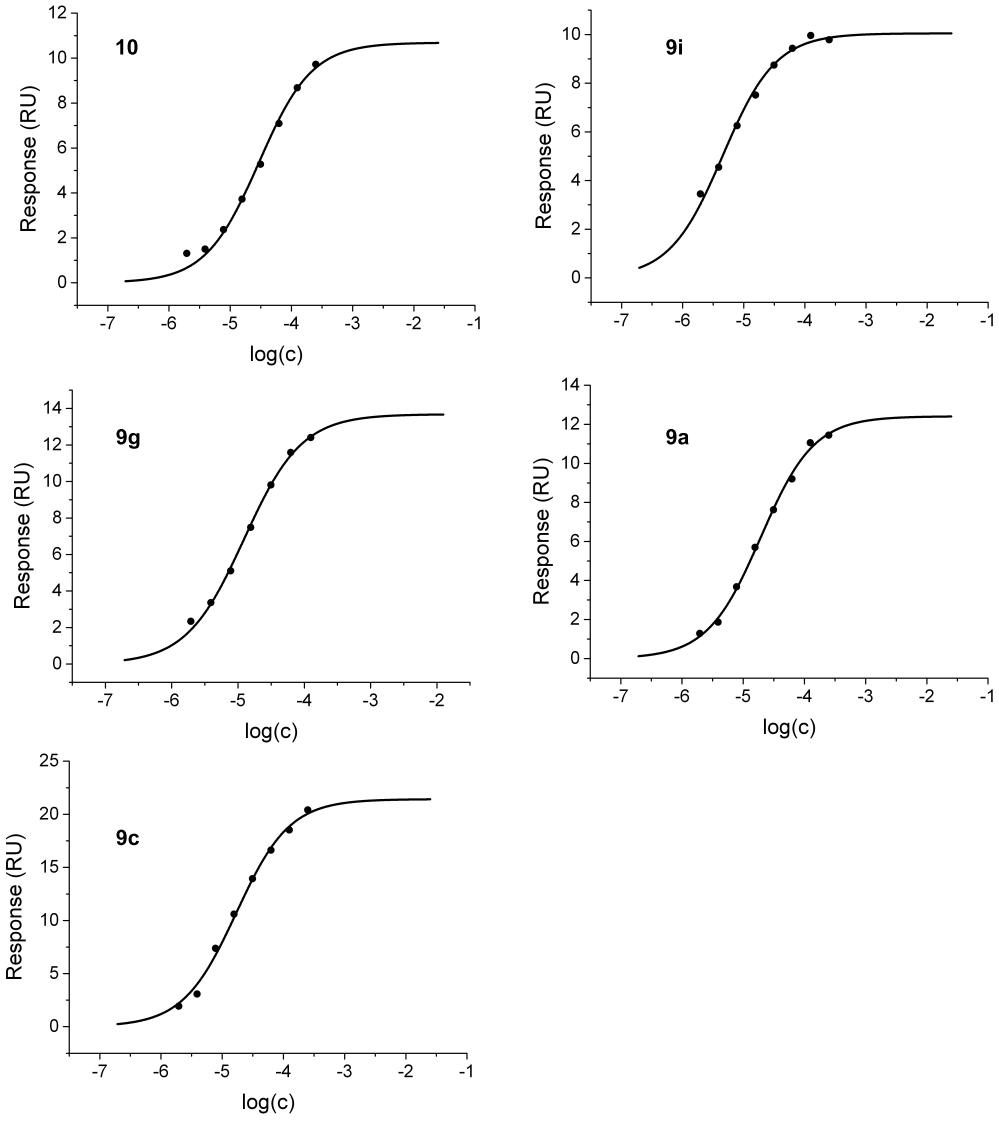
10
Response (RU)
log(c)
9i
Response (RU)
log(c)
9g
Response (RU)
log(c)
9a
Response (RU)
log(c)
9c
Response (RU)
log(c)

hGal-3FL

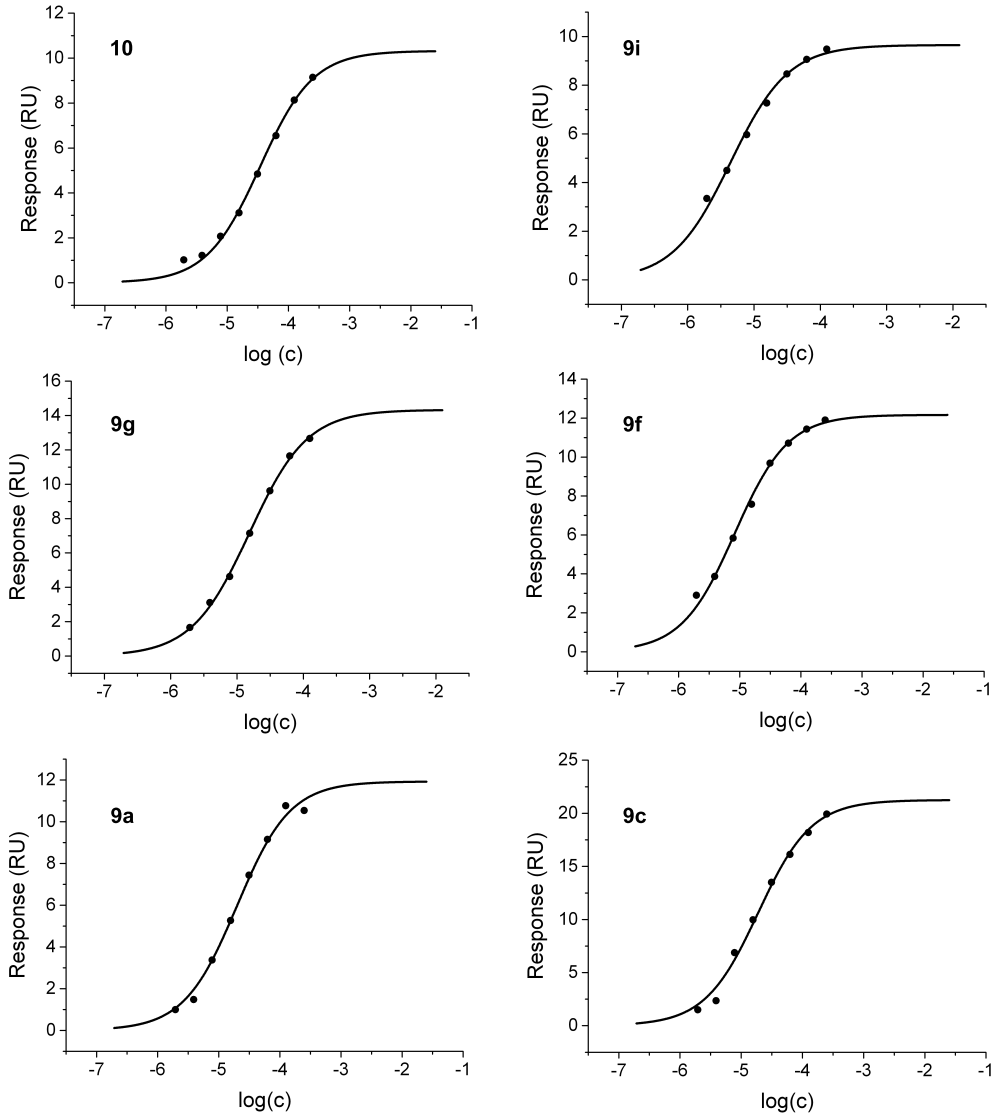
10
Response (RU)
log (c)
9i
Response (RU)
log(c)
9g
Response (RU)
log(c)
9f
Response (RU)
log(c)
9a
Response (RU)
log(c)
9c
Response (RU)
log(c)

B.3 ITC Analysis

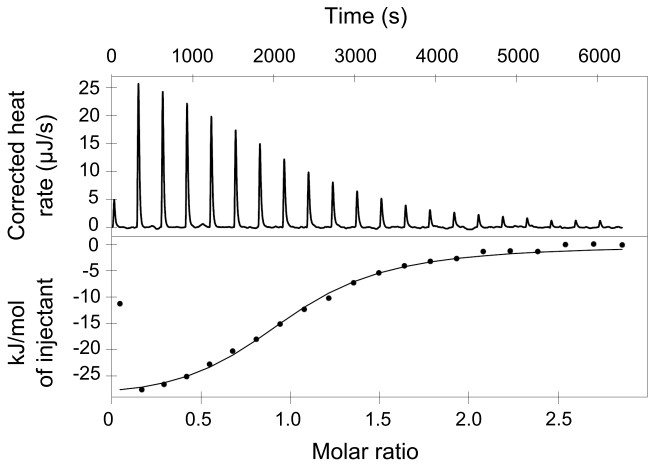

Fig. B.1 ITC titration diagram of **9f** (8.70 mM) to hGal-1 (1.00 mM) (upper part) and integrated heat change per titration with best fitted curve (lower part).

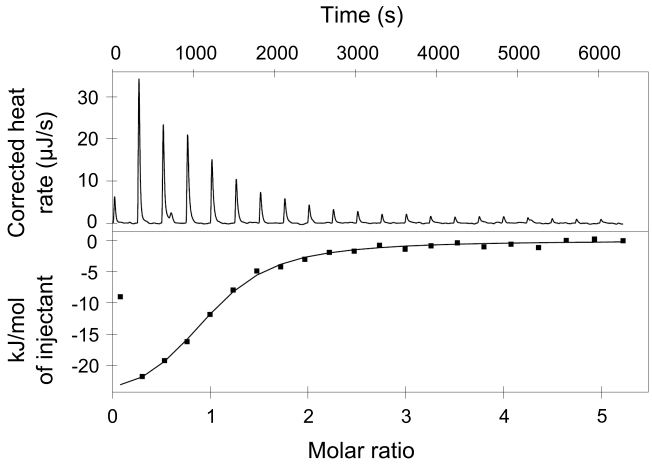

Fig. B.2 ITC titration diagram of **9j** (15.9 mM) to hGal-1 (1.00 mM) (upper part) and integrated heat change per titration with best fitted curve (lower part).

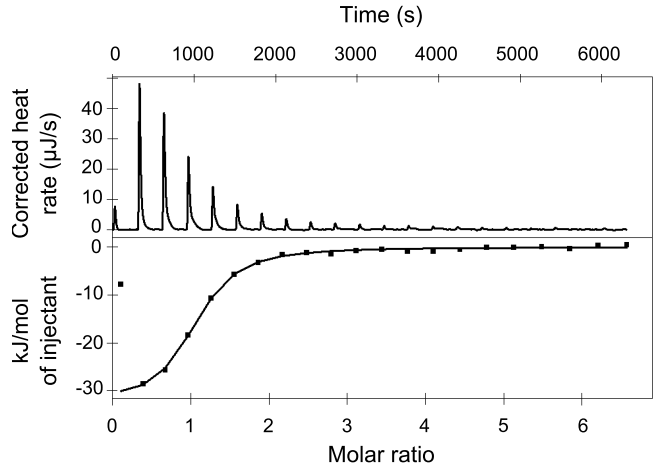

Fig. B.3 ITC titration diagram of LacNAc (20 mM) to hGal-1 (1.00 mM) (upper part) and integrated heat change per titration with best fitted curve (lower part).

B.4 NMR spectra of finals stage compounds

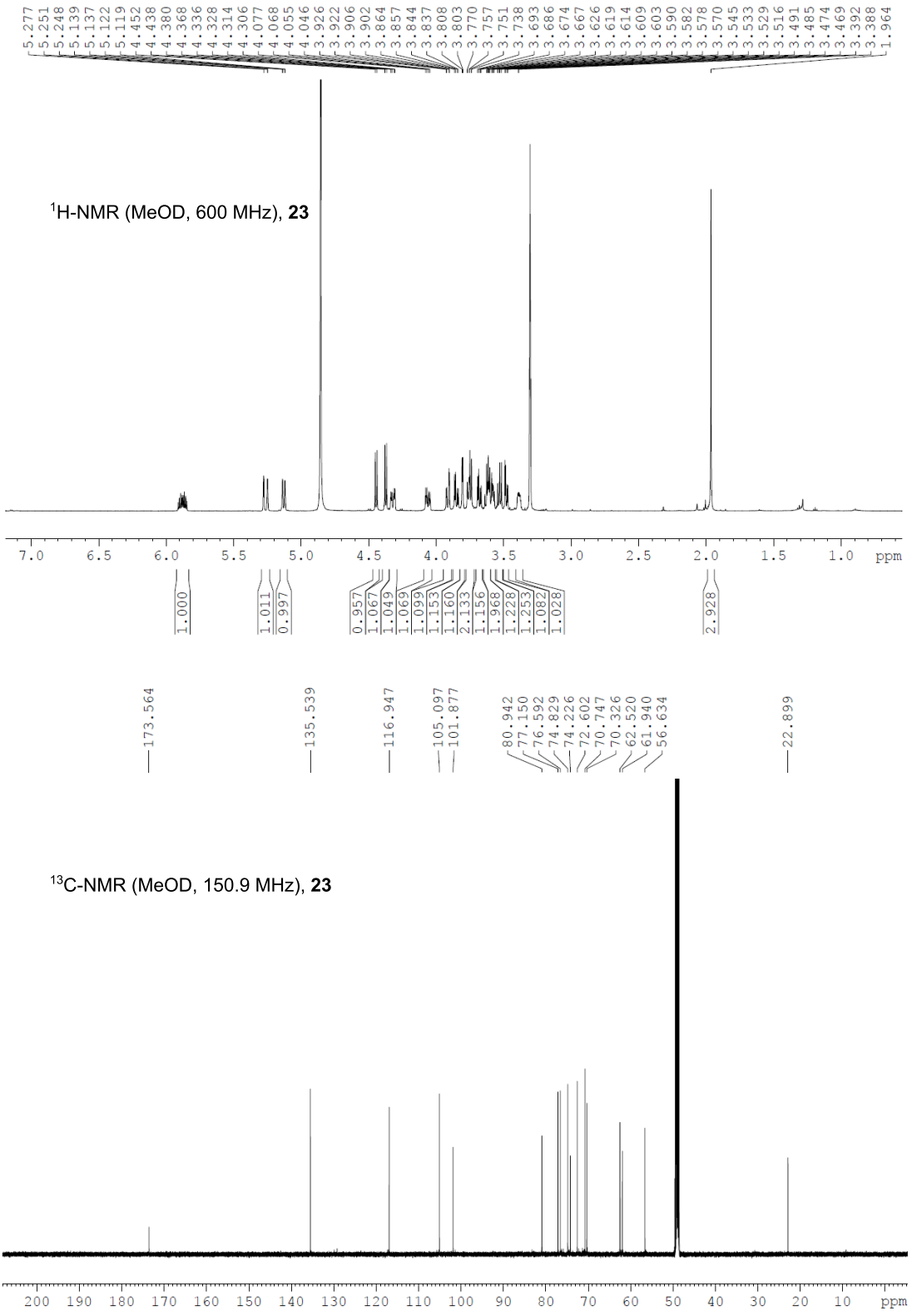

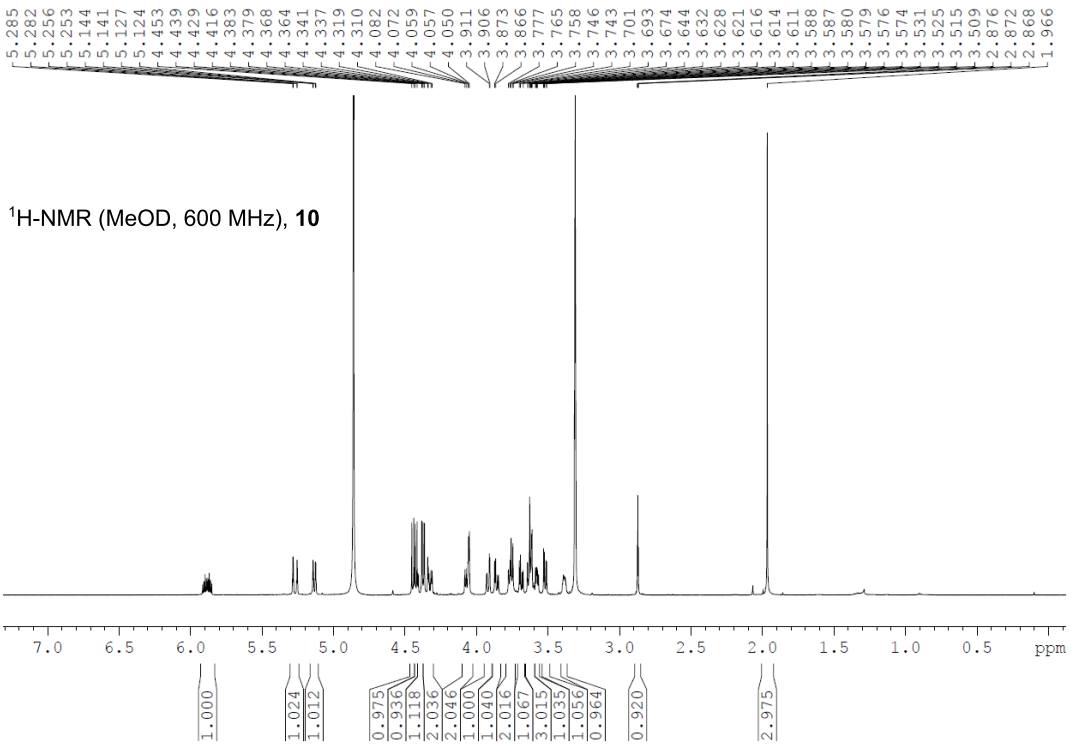

^{1}H-NMR (MeOD, 600 MHz), **10**

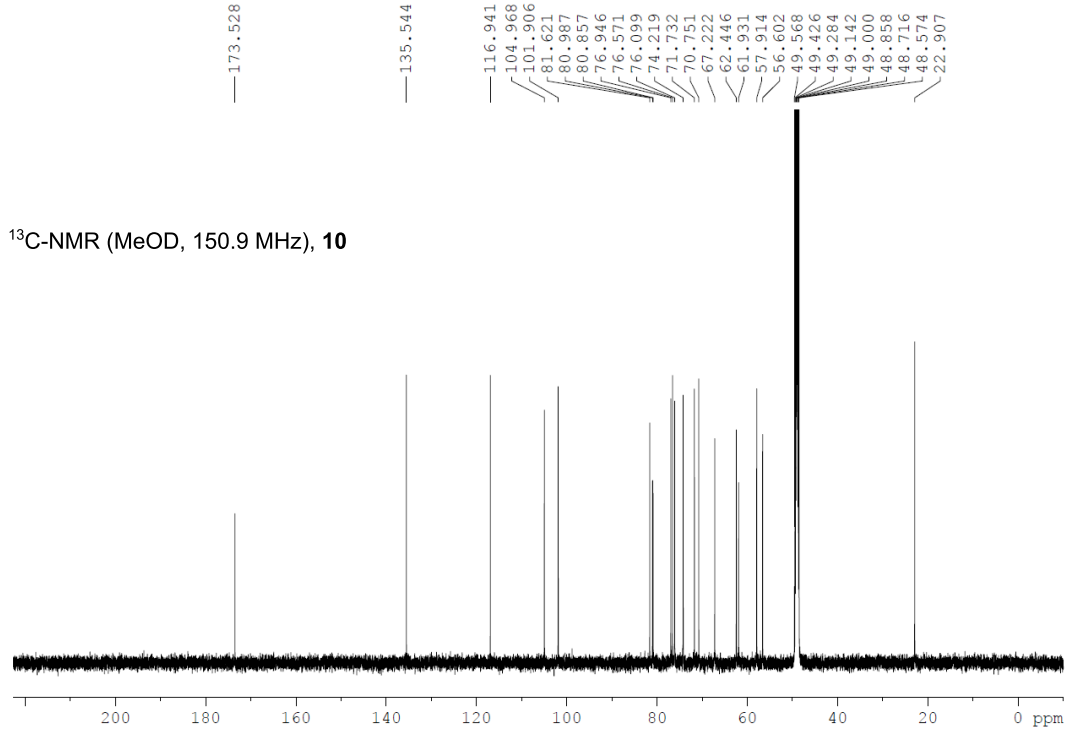

^{13}C-NMR (MeOD, 150.9 MHz), **10**

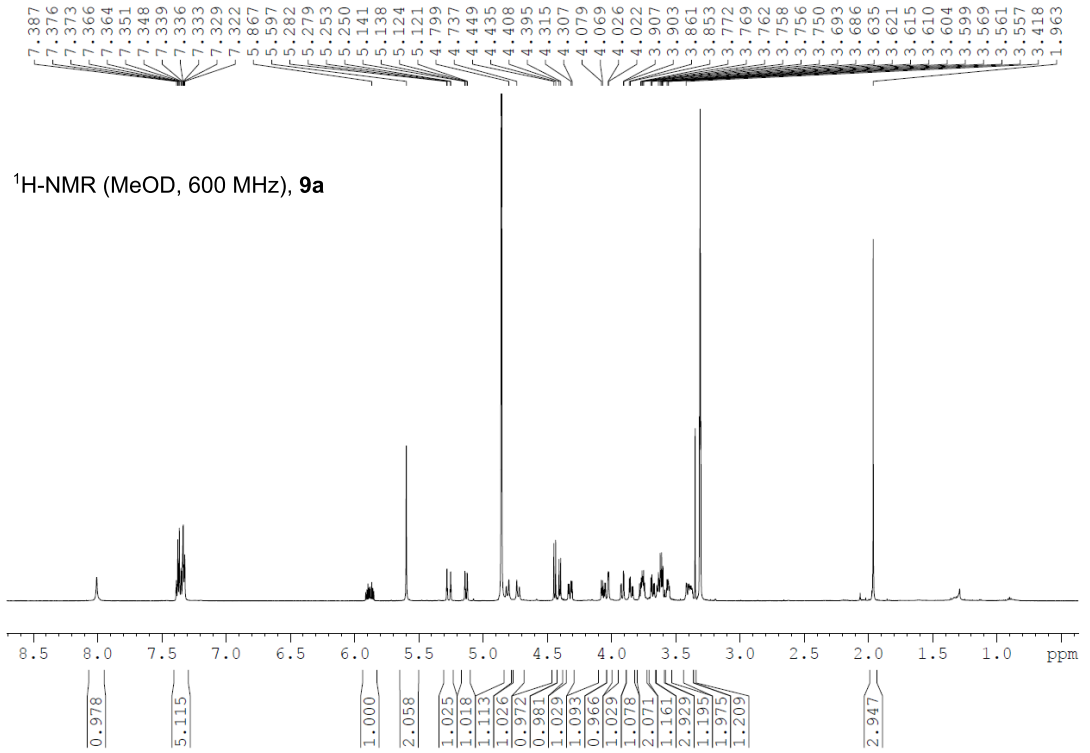

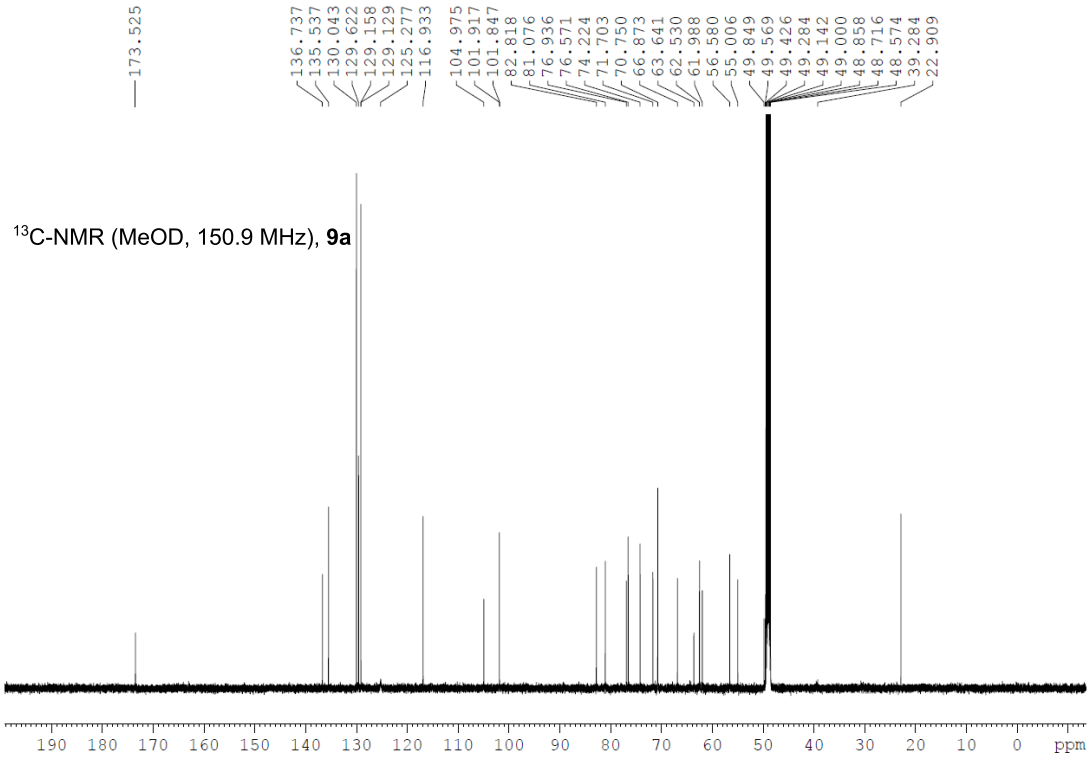

^{1}H-NMR (MeOD, 600 MHz), **9a**

^{13}C-NMR (MeOD, 150.9 MHz), **9a**

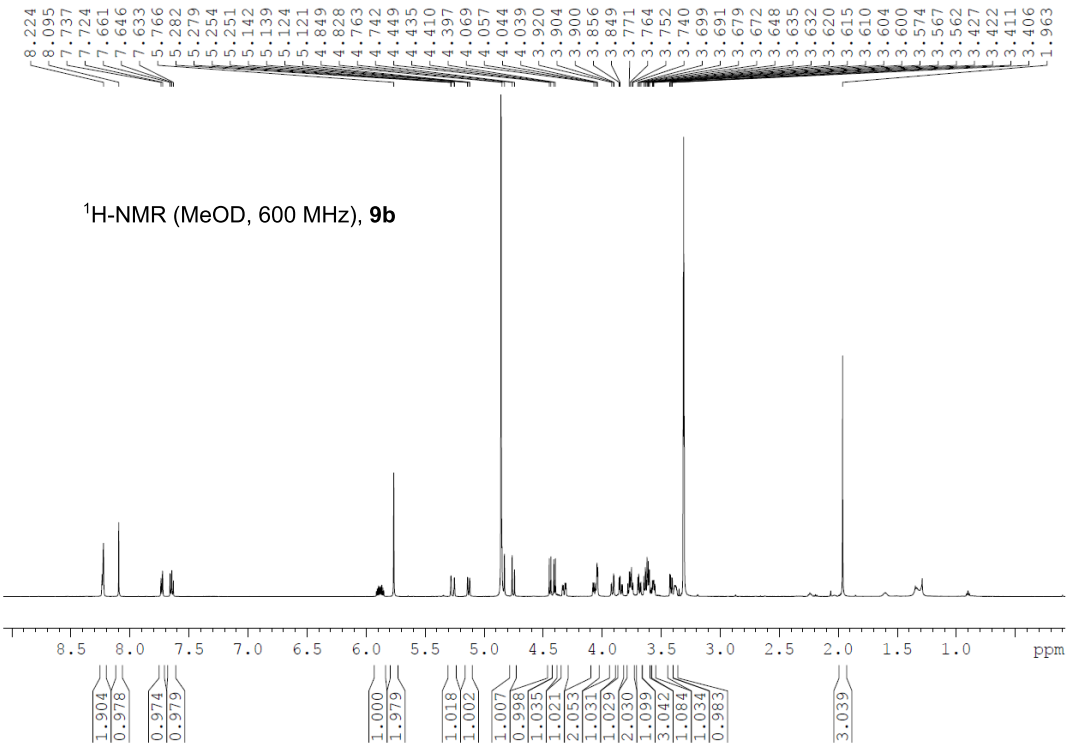

^{1}H-NMR (MeOD, 600 MHz), **9b**

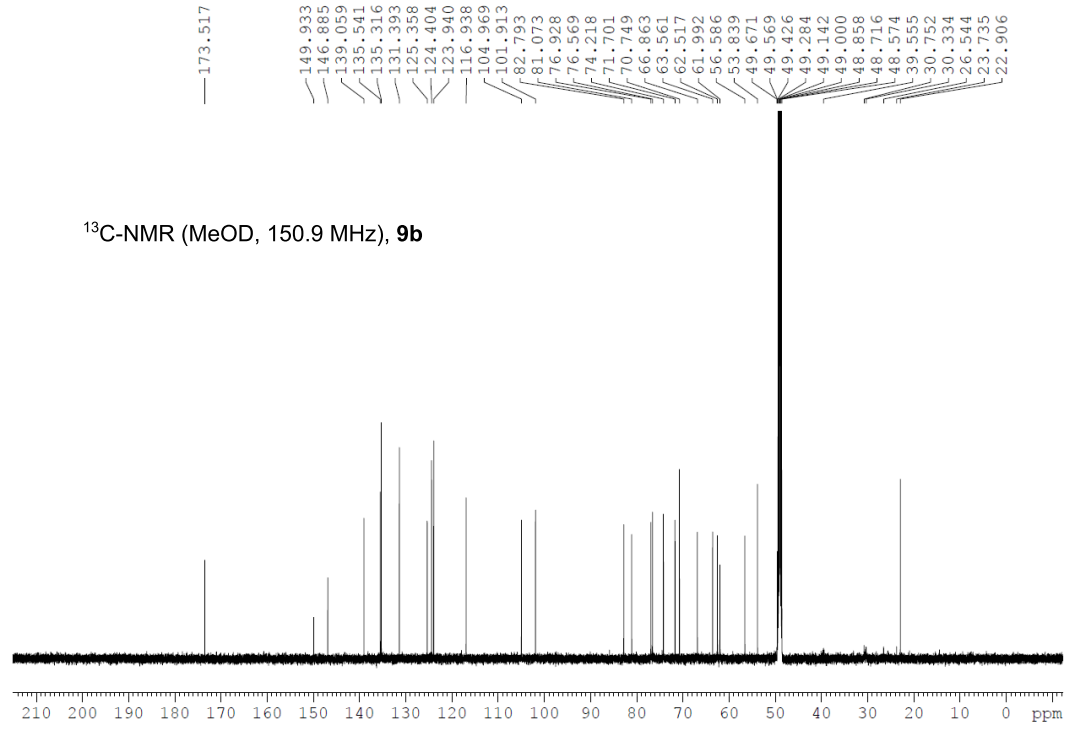

^{13}C-NMR (MeOD, 150.9 MHz), **9b**

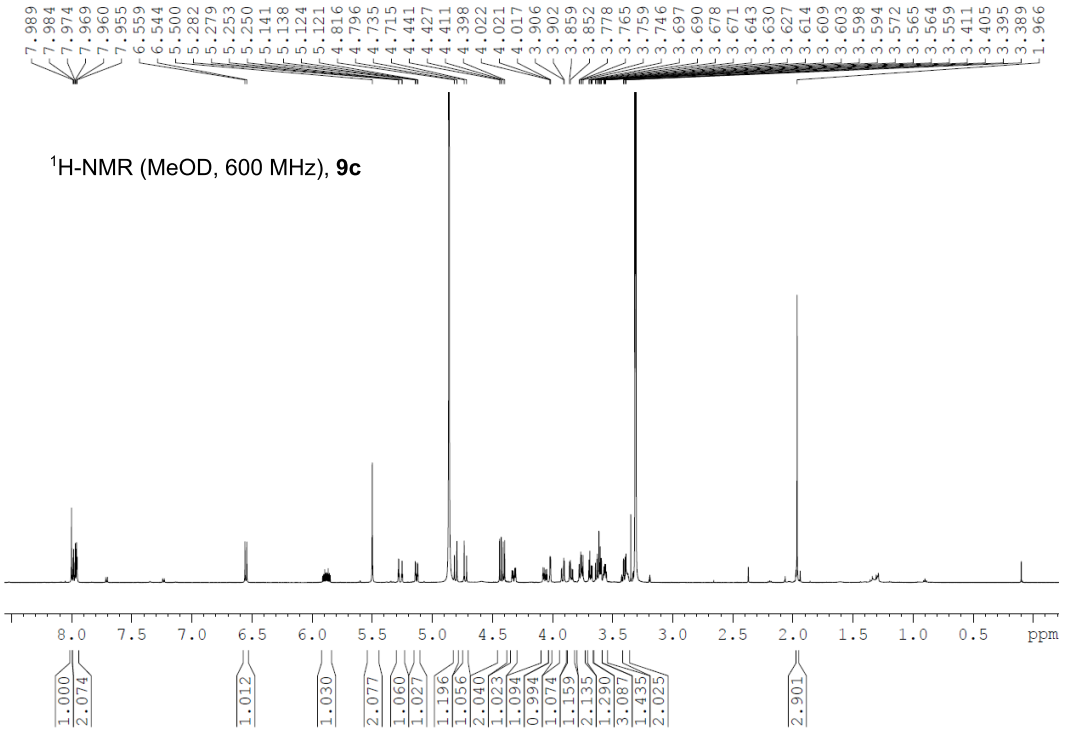

^{1}H-NMR (MeOD, 600 MHz), **9c**

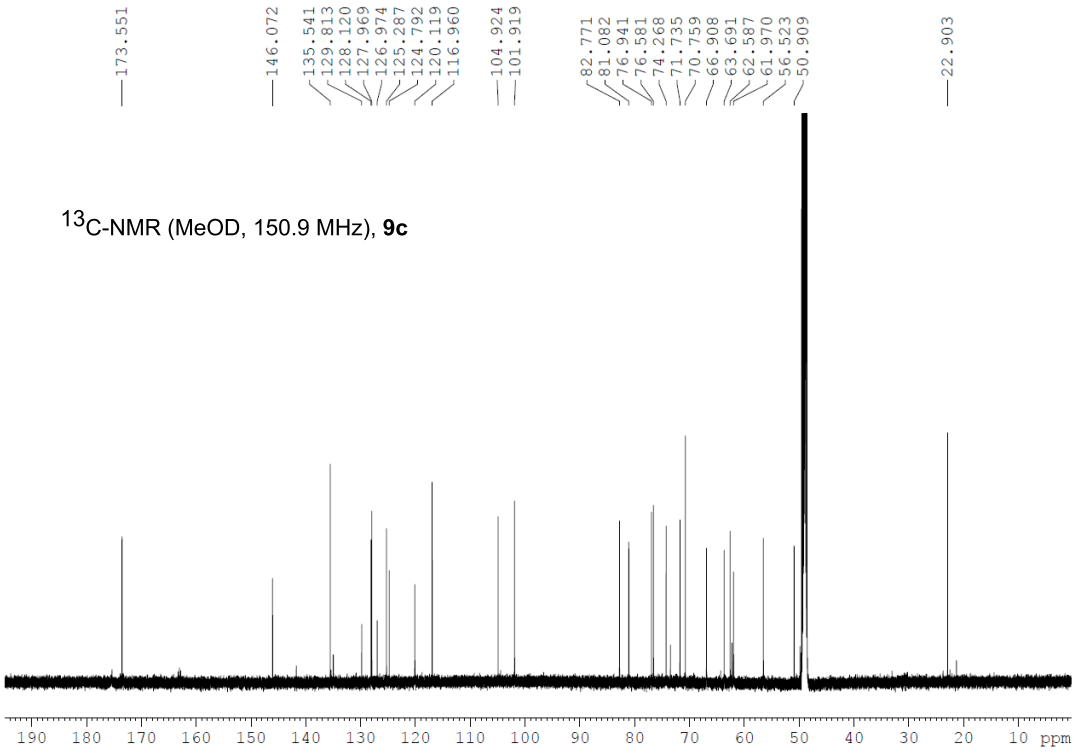

^{13}C-NMR (MeOD, 150.9 MHz), **9c**

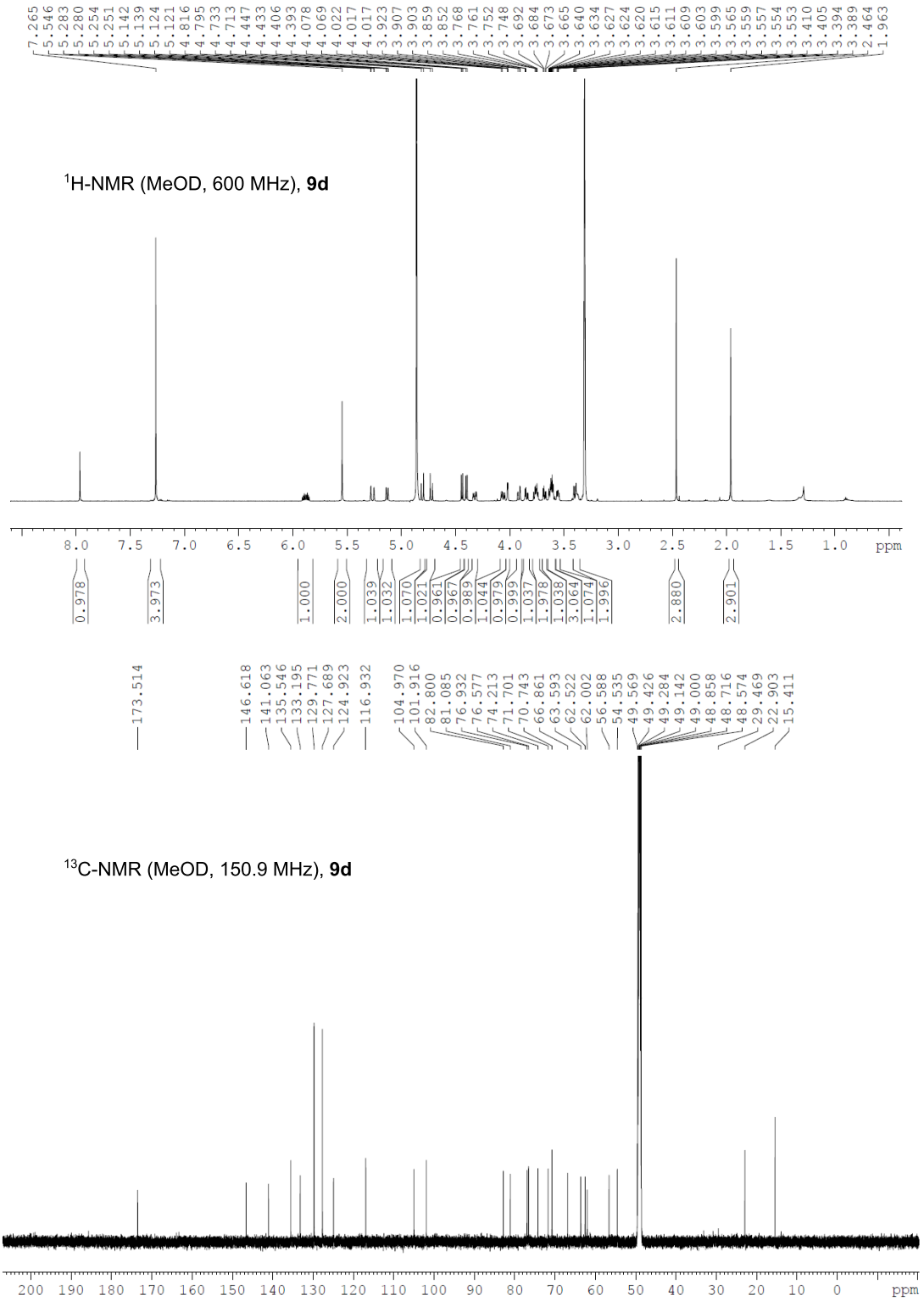
7.265
5.546
5.283
5.280
5.254
5.251
5.142
5.139
5.124
5.121
4.816
4.795
4.733
4.713
4.447
4.433
4.406
4.393
4.078
4.069
4.022
4.017
4.017
3.923
3.907
3.903
3.859
3.852
3.768
3.761
3.752
3.748
3.692
3.684
3.673
3.665
3.640
3.634
3.627
3.624
3.620
3.615
3.611
3.609
3.603
3.599
3.565
3.559
3.557
3.554
3.553
3.410
3.405
3.394
3.389
2.464
1.963
[1]H-NMR (MeOD, 600 MHz), 9d
8.0 7.5 7.0 6.5 6.0 5.5 5.0 4.5 4.0 3.5 3.0 2.5 2.0 1.5 1.0 ppm
0.978
3.973
1.000
2.000
1.039
1.032
1.070
1.021
0.961
0.967
0.989
1.044
0.979
0.999
1.037
1.978
1.038
3.064
1.074
1.996
2.880
2.901
173.514
146.618
141.063
135.546
133.195
129.771
127.689
124.923
116.932
104.970
101.916
82.800
81.085
76.932
76.577
74.213
71.701
70.743
66.861
63.593
62.522
62.002
56.588
54.535
49.569
49.426
49.284
49.142
49.000
48.858
48.716
48.574
29.469
22.903
15.411
[13]C-NMR (MeOD, 150.9 MHz), 9d
200 190 180 170 160 150 140 130 120 110 100 90 80 70 60 50 40 30 20 10 0 ppm

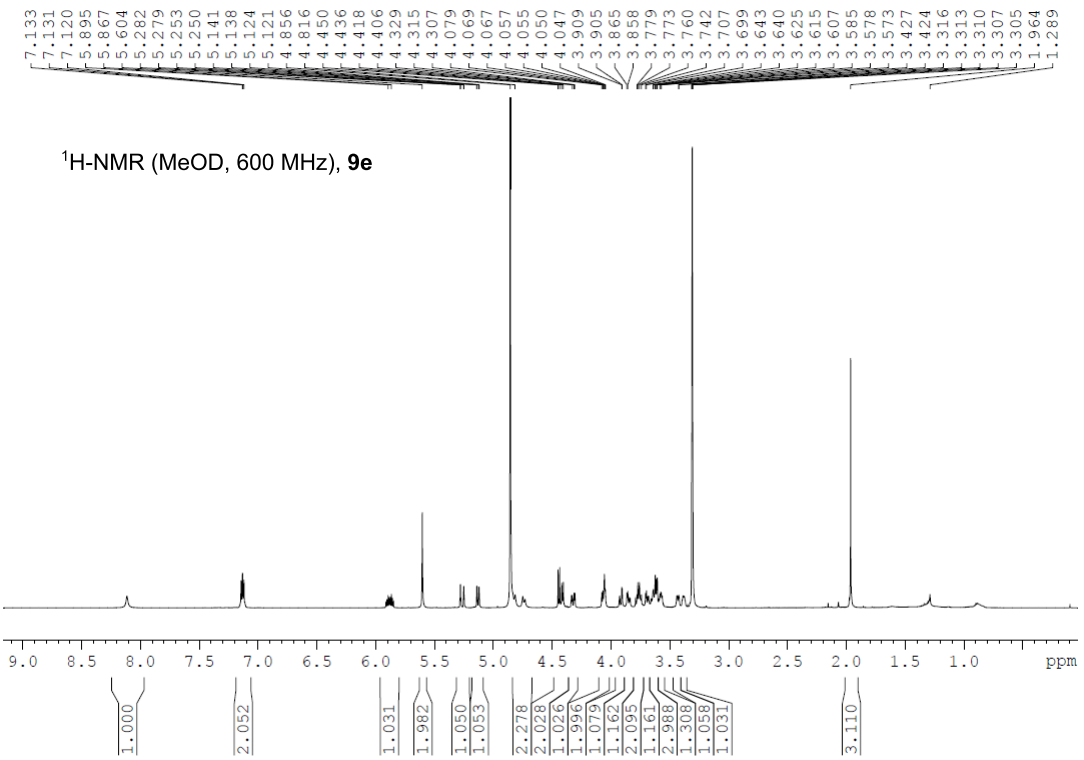

^{1}H-NMR (MeOD, 600 MHz), **9e**

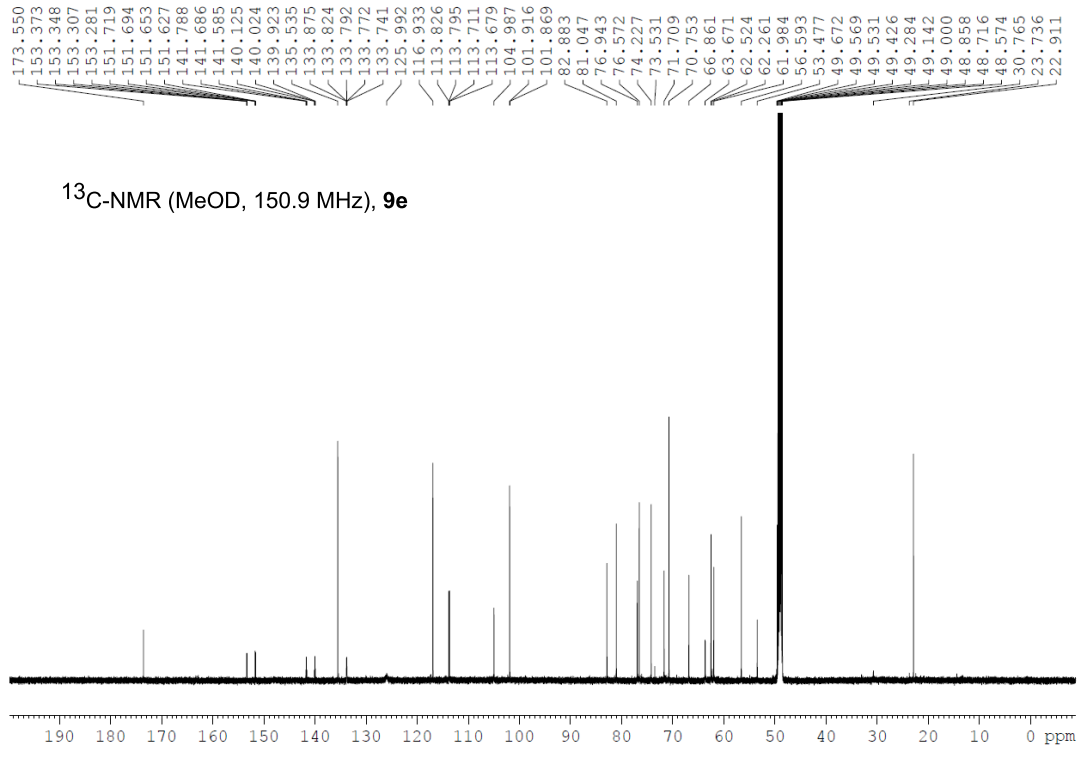

^{13}C-NMR (MeOD, 150.9 MHz), **9e**

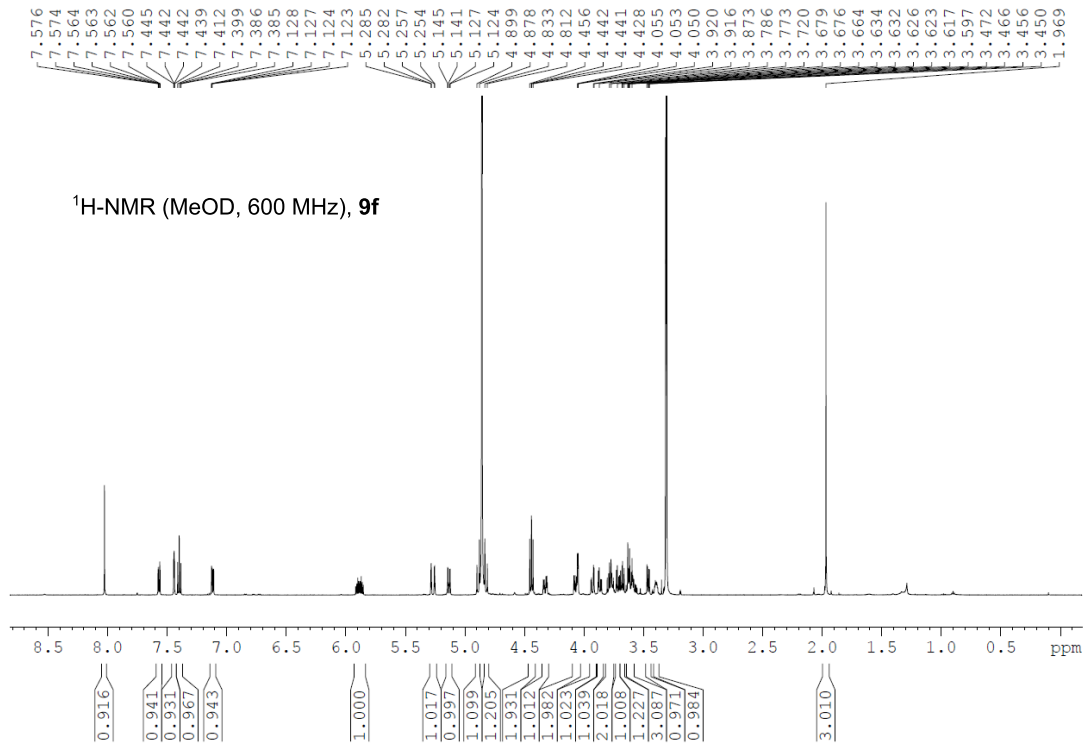

^{1}H-NMR (MeOD, 600 MHz), **9f**

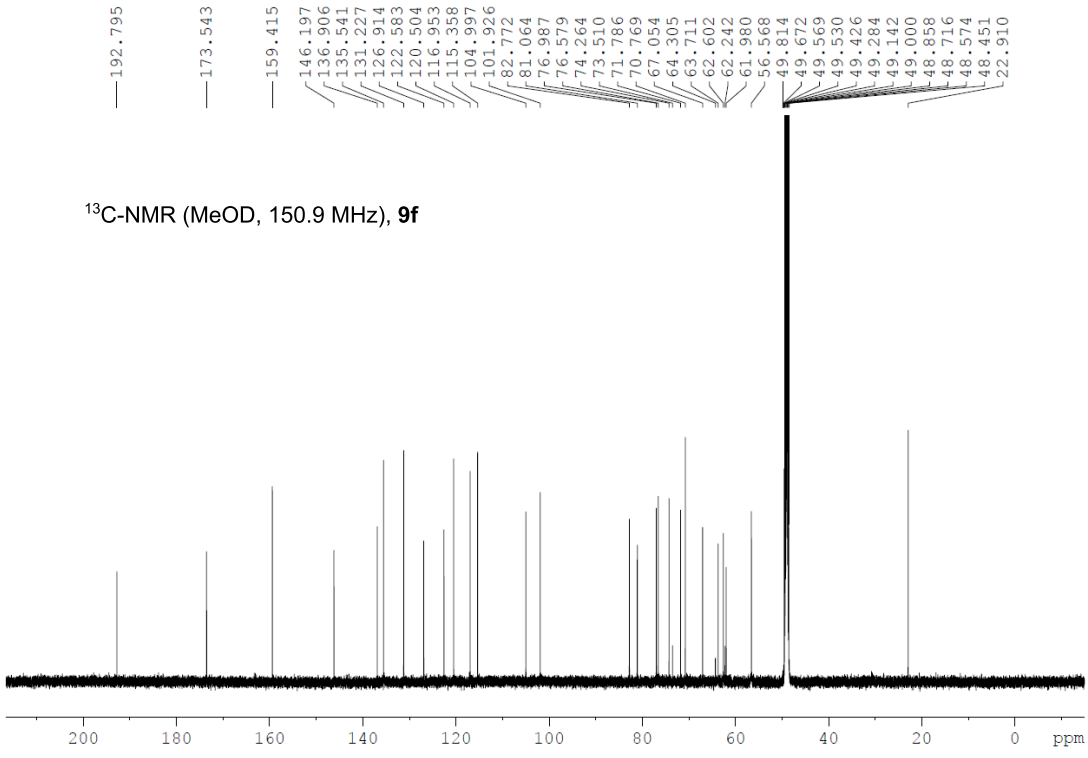

^{13}C-NMR (MeOD, 150.9 MHz), **9f**

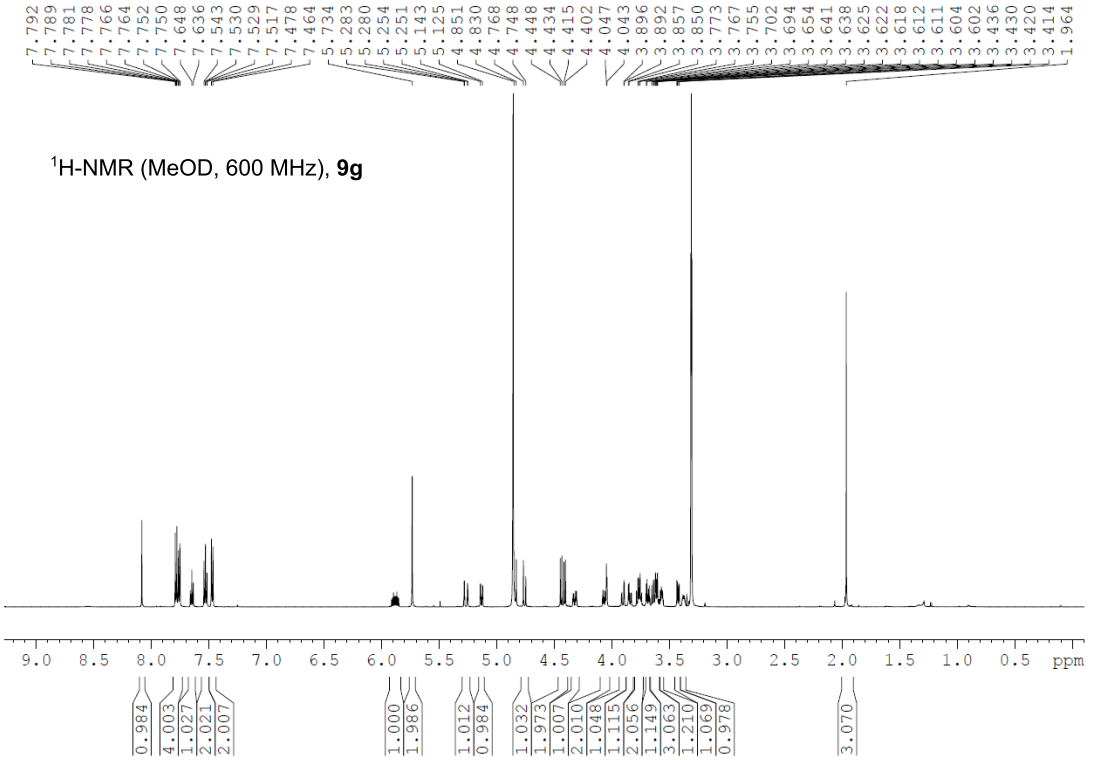
7.792
7.789
7.781
7.778
7.766
7.764
7.752
7.750
7.648
7.636
7.543
7.530
7.529
7.517
7.478
7.464
5.734
5.283
5.280
5.254
5.251
5.143
5.125
4.851
4.830
4.768
4.748
4.448
4.434
4.415
4.402
4.047
4.043
3.896
3.892
3.857
3.850
3.773
3.767
3.755
3.702
3.694
3.654
3.641
3.638
3.625
3.622
3.618
3.612
3.611
3.604
3.602
3.436
3.430
3.420
3.414
1.964
1H-NMR (MeOD, 600 MHz), 9g
9.0 8.5 8.0 7.5 7.0 6.5 6.0 5.5 5.0 4.5 4.0 3.5 3.0 2.5 2.0 1.5 1.0 0.5 ppm
0.984
4.003
1.027
2.021
2.007
1.000
1.986
1.012
0.984
1.032
1.973
1.007
2.010
1.048
1.115
2.056
1.149
3.063
1.210
1.069
0.978
3.070

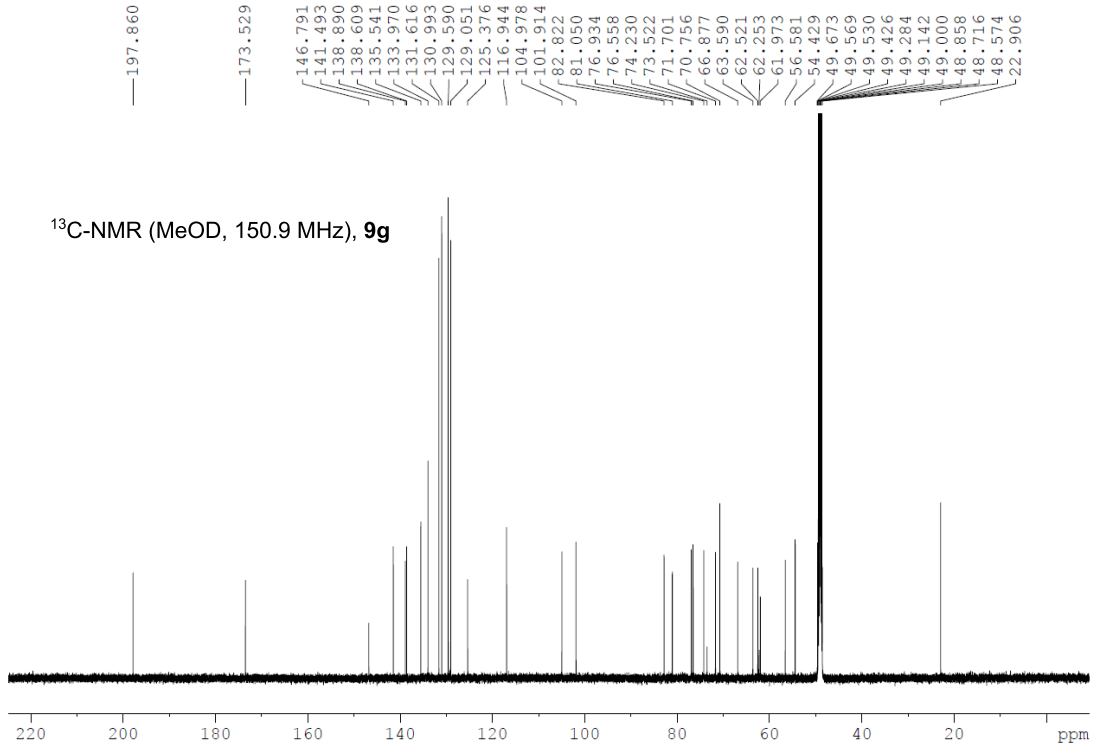
197.860
173.529
146.791
141.493
138.890
138.609
135.541
133.970
131.616
130.993
129.590
129.051
125.376
116.944
104.978
101.914
82.822
81.050
76.934
76.558
74.230
73.522
71.701
70.756
66.877
63.590
62.521
62.253
61.973
56.581
54.429
49.673
49.569
49.530
49.426
49.284
49.142
49.000
48.858
48.716
48.574
22.906
13C-NMR (MeOD, 150.9 MHz), 9g
220 200 180 160 140 120 100 80 60 40 20 ppm

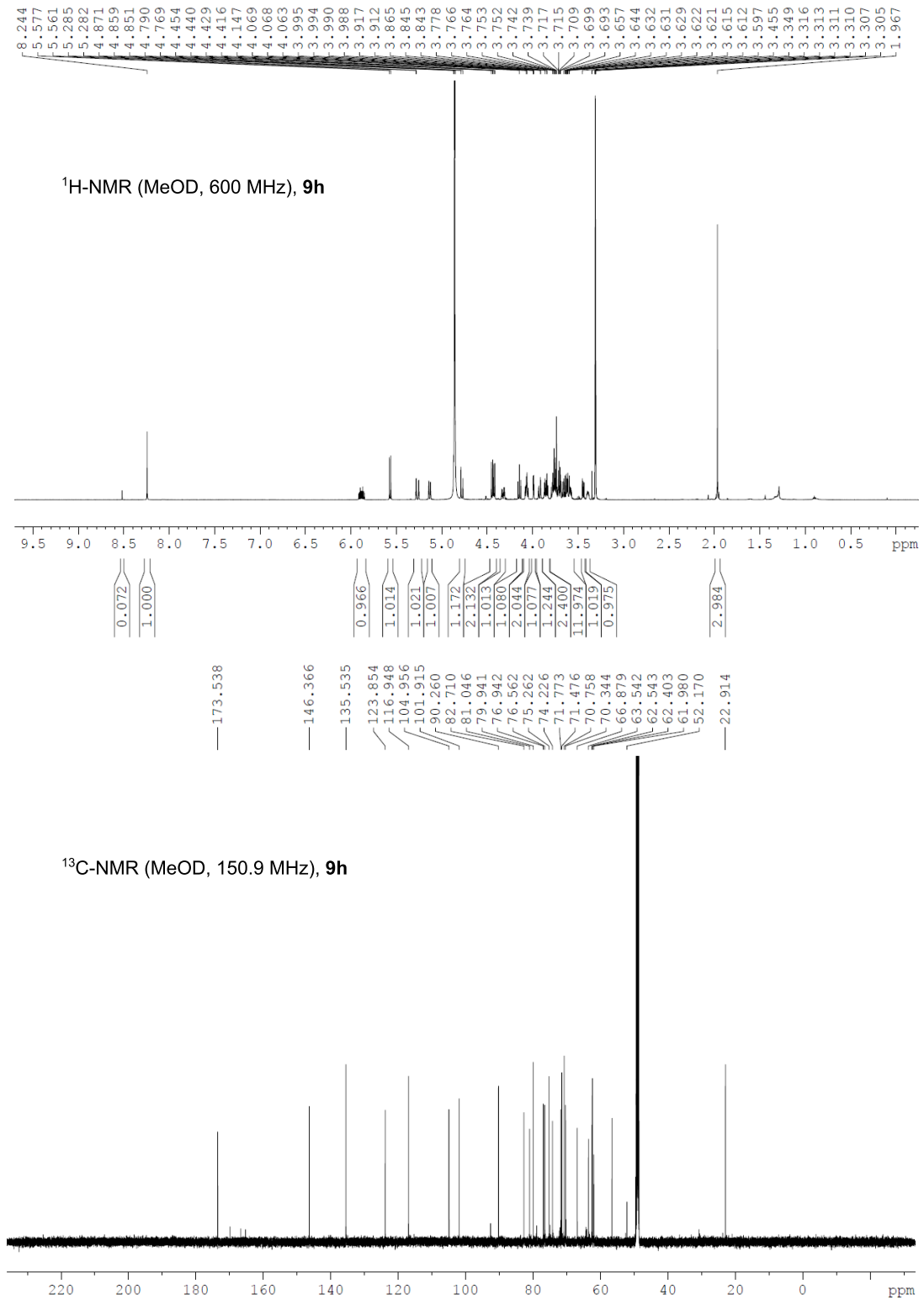
8.244
5.577
5.561
5.285
5.282
4.871
4.859
4.851
4.790
4.769
4.454
4.440
4.429
4.416
4.147
4.069
4.068
4.063
3.995
3.994
3.990
3.988
3.917
3.912
3.865
3.845
3.843
3.778
3.766
3.764
3.753
3.752
3.742
3.739
3.717
3.715
3.709
3.699
3.693
3.657
3.644
3.632
3.631
3.629
3.622
3.621
3.615
3.612
3.597
3.455
3.349
3.316
3.313
3.311
3.310
3.307
3.305
1.967
1H-NMR (MeOD, 600 MHz), 9h
9.5 9.0 8.5 8.0 7.5 7.0 6.5 6.0 5.5 5.0 4.5 4.0 3.5 3.0 2.5 2.0 1.5 1.0 0.5 ppm
0.072
1.000
0.966
1.014
1.021
1.007
1.172
2.132
1.013
1.080
2.044
1.077
1.244
2.400
11.974
1.019
0.975
2.984
173.538
146.366
135.535
123.854
116.948
104.956
101.915
90.260
82.710
81.046
79.941
76.942
76.562
75.262
74.226
71.773
71.476
70.758
70.344
66.879
63.542
62.543
62.403
61.980
52.170
22.914
13C-NMR (MeOD, 150.9 MHz), 9h
220 200 180 160 140 120 100 80 60 40 20 0 ppm

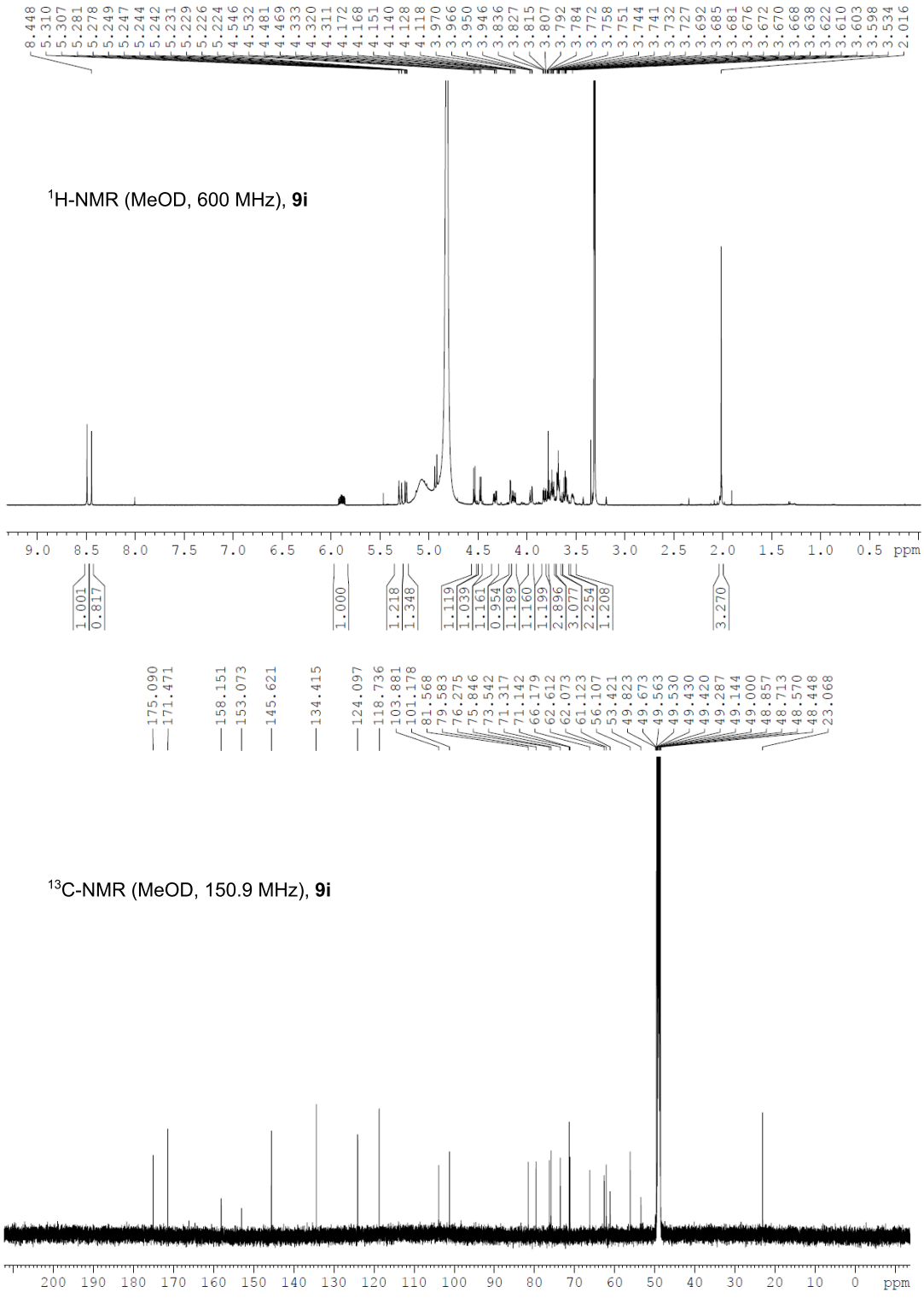
8.448
5.310
5.307
5.281
5.278
5.249
5.247
5.244
5.242
5.231
5.229
5.226
5.224
4.546
4.532
4.481
4.469
4.333
4.320
4.311
4.172
4.168
4.151
4.140
4.128
4.118
3.970
3.966
3.950
3.946
3.836
3.827
3.815
3.807
3.792
3.784
3.772
3.758
3.751
3.744
3.741
3.732
3.727
3.692
3.685
3.681
3.676
3.672
3.670
3.668
3.638
3.622
3.610
3.603
3.598
3.534
2.016
1H-NMR (MeOD, 600 MHz), 9i
9.0 8.5 8.0 7.5 7.0 6.5 6.0 5.5 5.0 4.5 4.0 3.5 3.0 2.5 2.0 1.5 1.0 0.5 ppm
1.001
0.817
1.000
1.218
1.348
1.119
1.039
1.161
0.954
1.189
1.160
1.199
2.896
3.077
2.254
1.208
3.270
175.090
171.471
158.151
153.073
145.621
134.415
124.097
118.736
103.881
101.178
81.568
79.583
76.275
75.846
73.542
71.317
71.142
66.179
62.612
62.073
61.123
56.107
53.421
49.823
49.673
49.563
49.530
49.430
49.420
49.287
49.144
49.000
48.857
48.713
48.570
48.448
23.068
13C-NMR (MeOD, 150.9 MHz), 9i
200 190 180 170 160 150 140 130 120 110 100 90 80 70 60 50 40 30 20 10 0 ppm

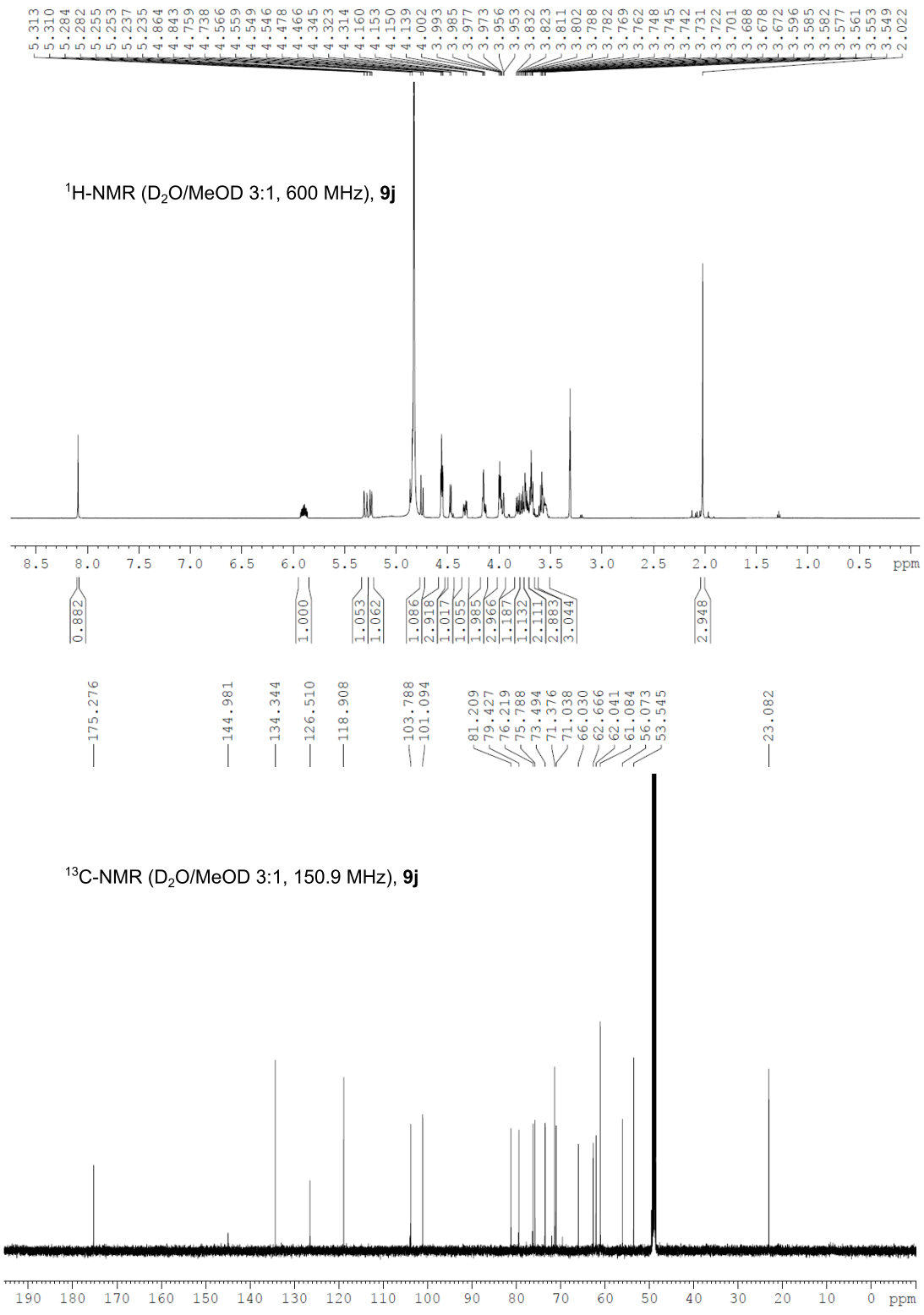
5.313
5.310
5.284
5.282
5.255
5.253
5.237
5.235
4.864
4.843
4.759
4.738
4.566
4.559
4.549
4.546
4.478
4.466
4.345
4.323
4.314
4.160
4.153
4.150
4.139
4.002
3.993
3.985
3.977
3.973
3.956
3.953
3.832
3.823
3.811
3.802
3.788
3.782
3.769
3.762
3.748
3.745
3.742
3.731
3.722
3.701
3.688
3.678
3.672
3.596
3.585
3.582
3.577
3.561
3.553
3.549
2.022
1H-NMR (D2O/MeOD 3:1, 600 MHz), 9j
8.5 8.0 7.5 7.0 6.5 6.0 5.5 5.0 4.5 4.0 3.5 3.0 2.5 2.0 1.5 1.0 0.5 ppm
0.882
1.000
1.053
1.062
1.086
2.918
1.017
1.055
1.985
2.966
1.187
1.132
2.111
2.883
3.044
2.948
175.276
144.981
134.344
126.510
118.908
103.788
101.094
81.209
79.427
76.219
75.788
73.494
71.376
71.038
66.030
62.666
62.041
61.084
56.073
53.545
23.082
13C-NMR (D2O/MeOD 3:1, 150.9 MHz), 9j
190 180 170 160 150 140 130 120 110 100 90 80 70 60 50 40 30 20 10 0 ppm

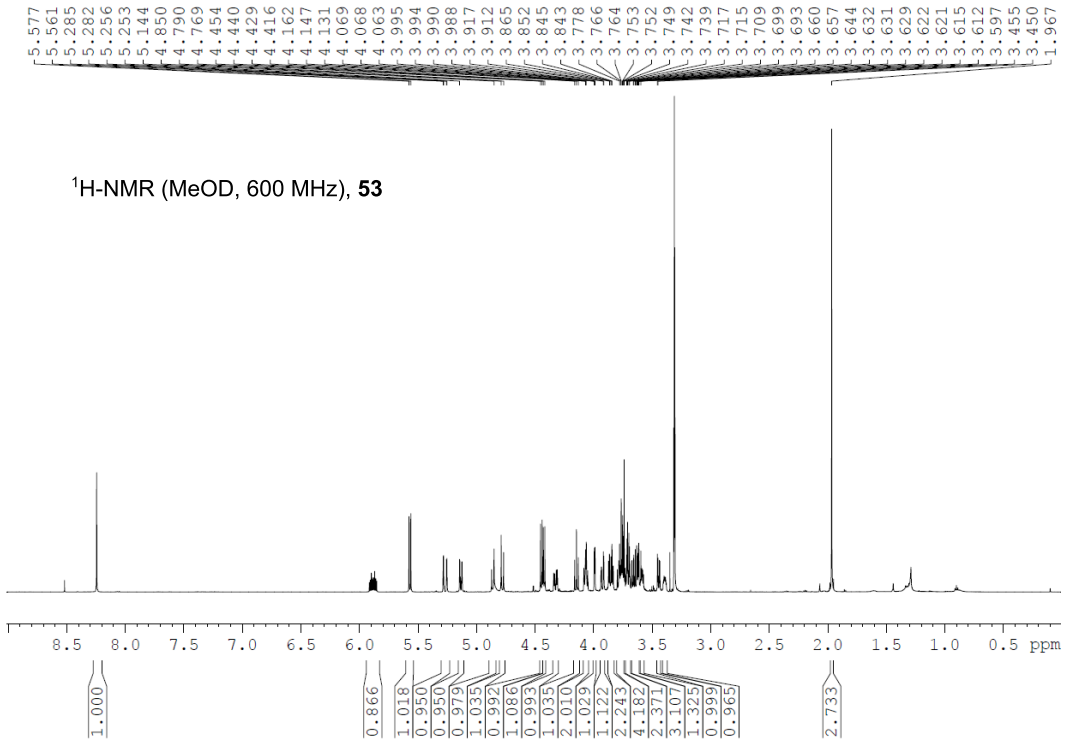

^{1}H-NMR (MeOD, 600 MHz), **53**

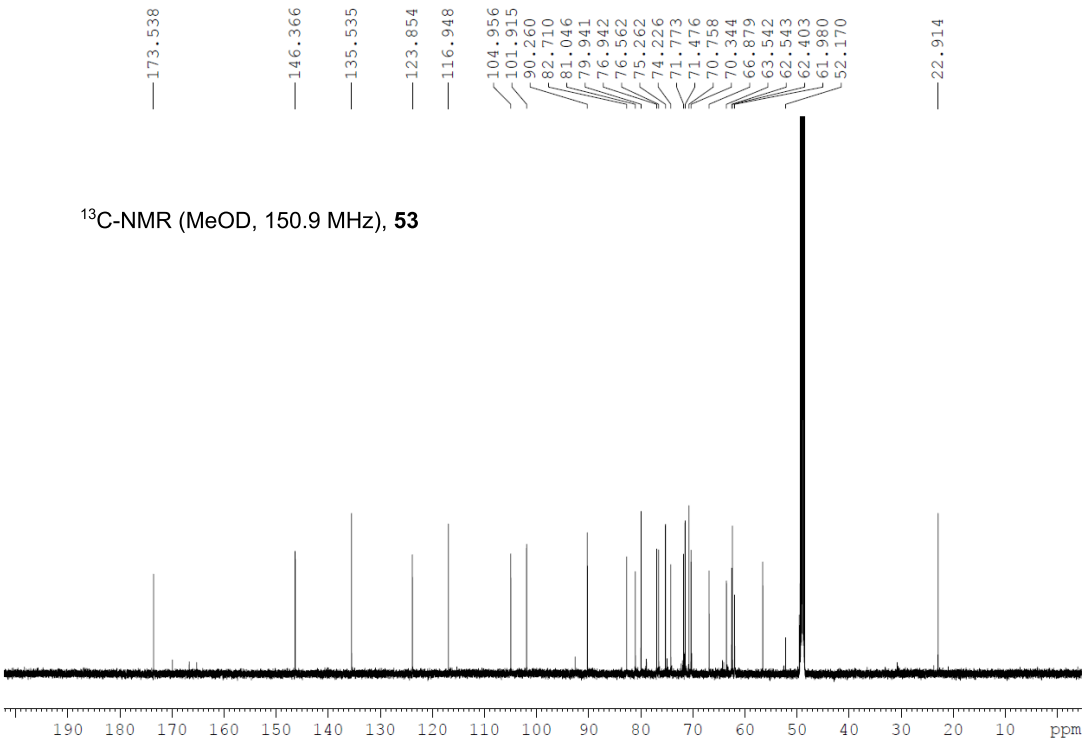

^{13}C-NMR (MeOD, 150.9 MHz), **53**

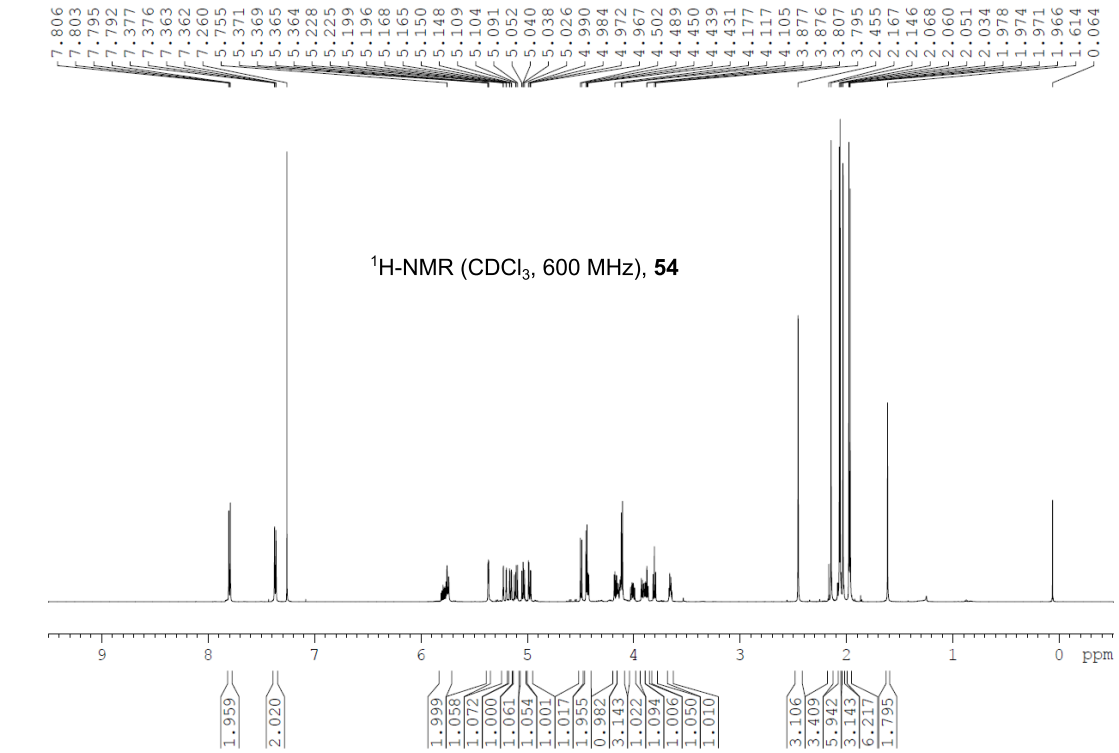

^{1}H-NMR ($CDCl_3$, 600 MHz), **54**

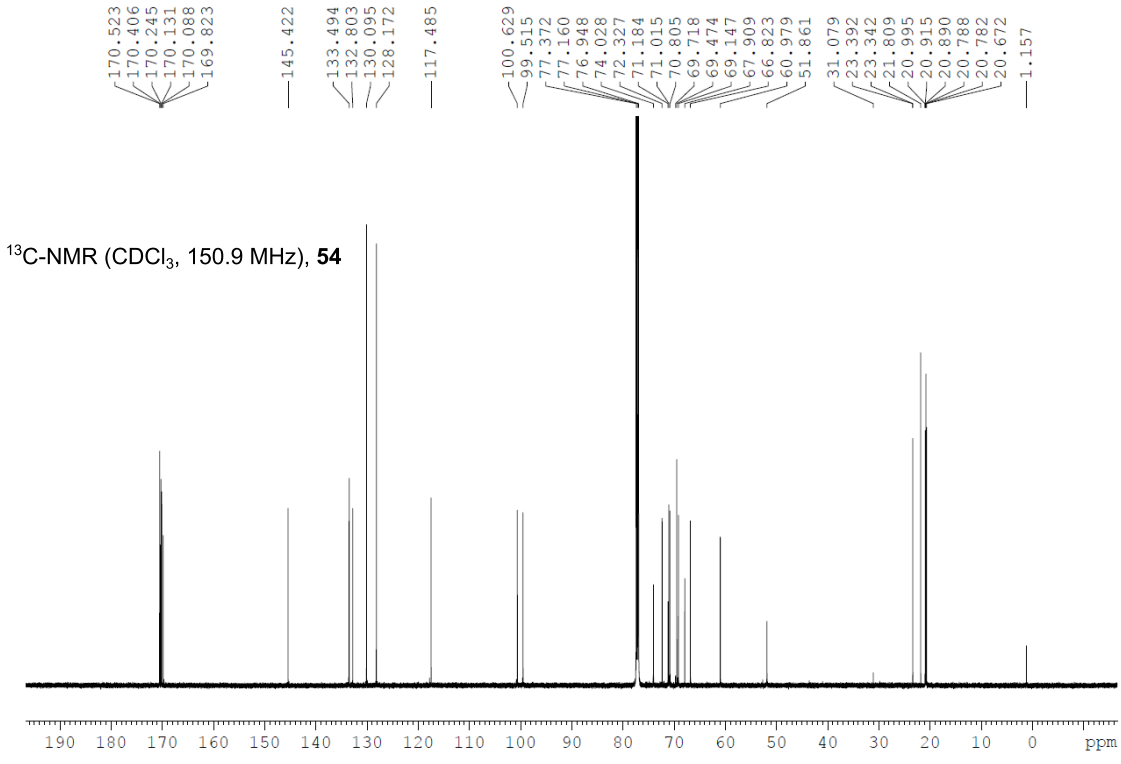

^{13}C-NMR ($CDCl_3$, 150.9 MHz), **54**

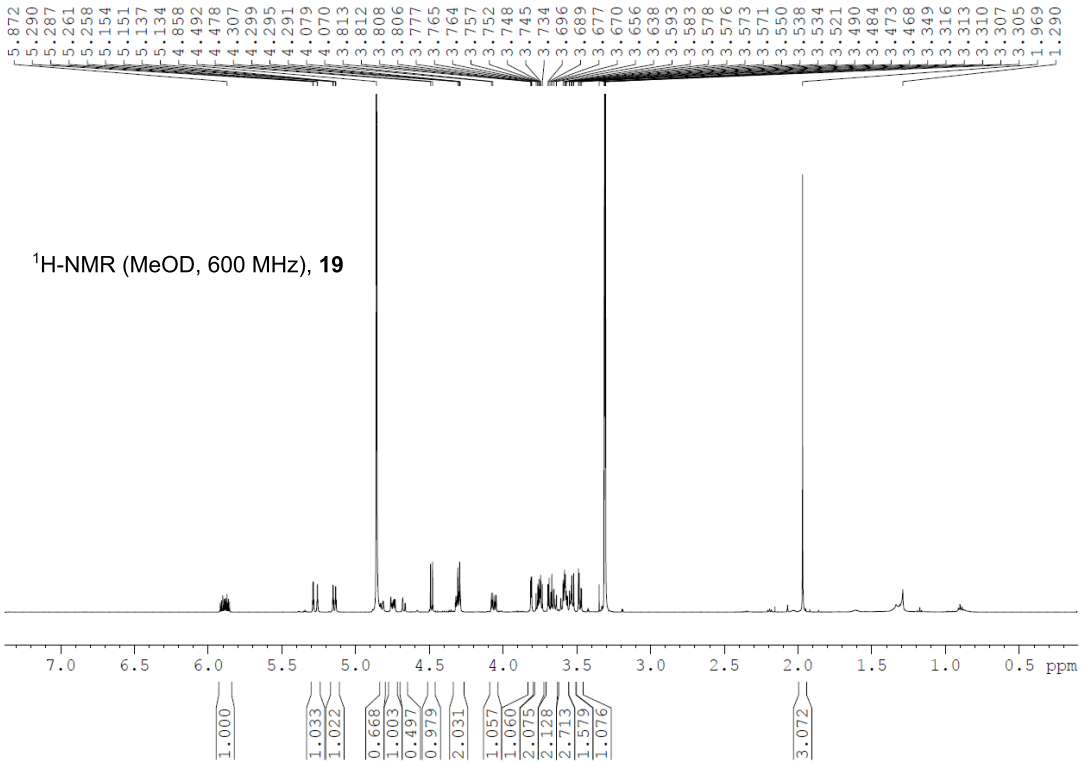

^{1}H-NMR (MeOD, 600 MHz), **19**

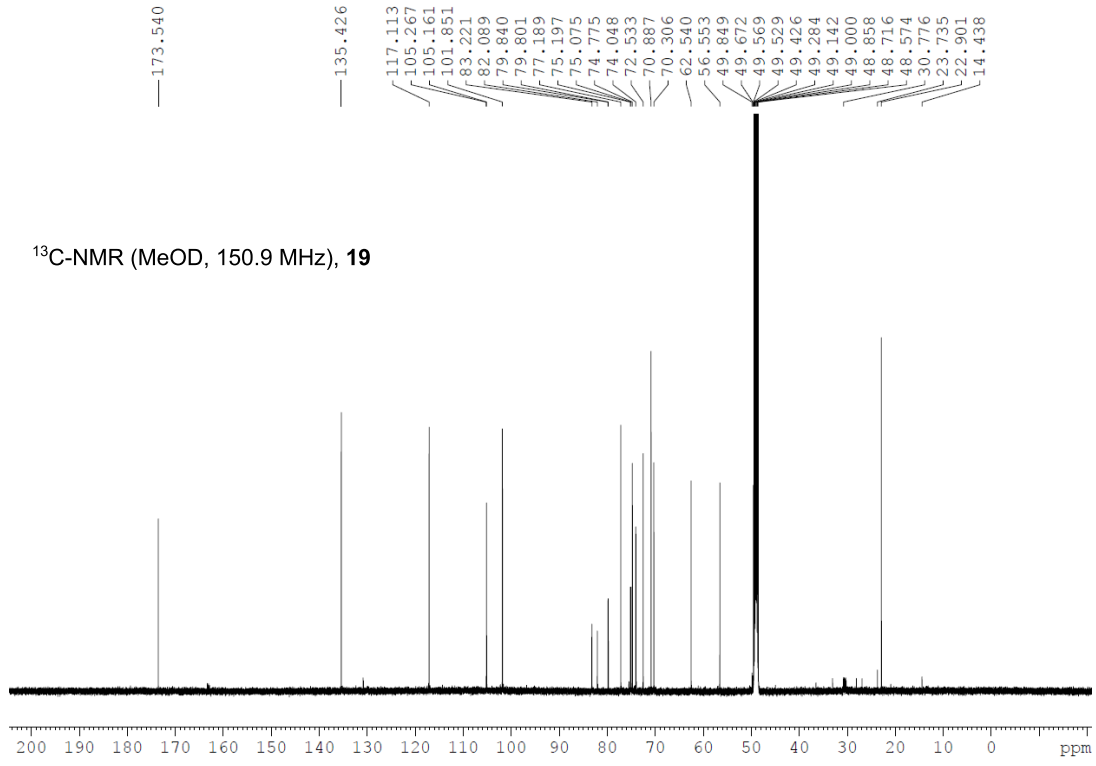

^{13}C-NMR (MeOD, 150.9 MHz), **19**

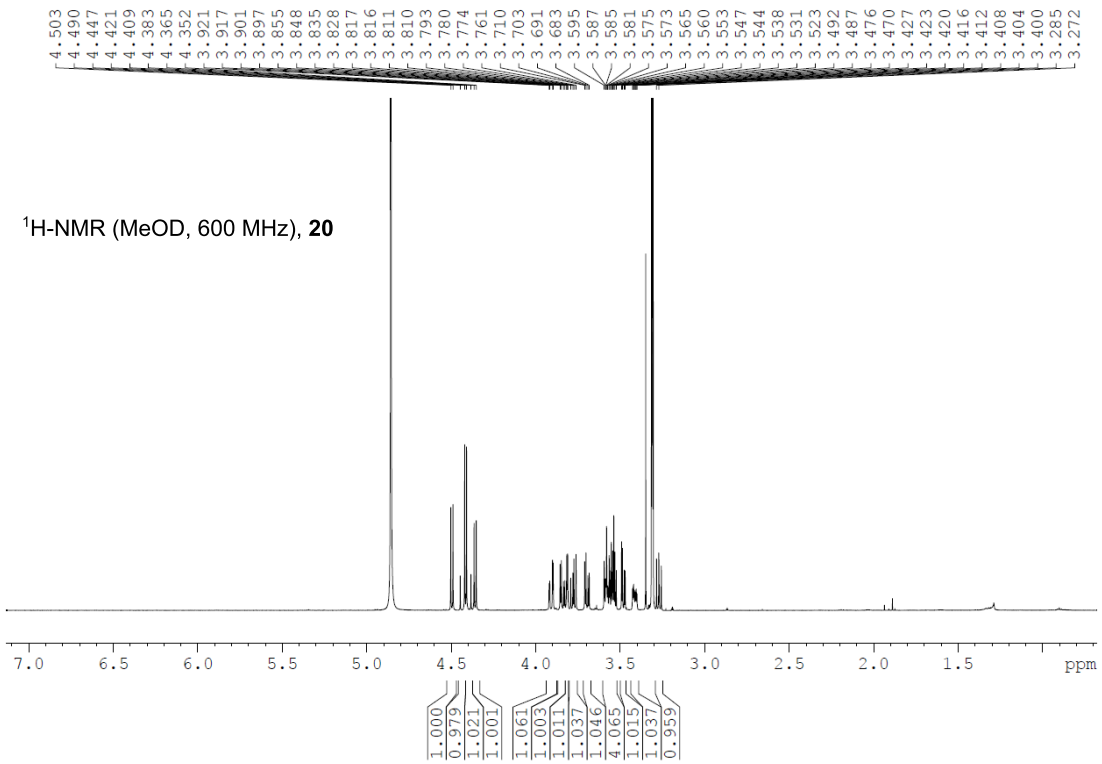

^{1}H-NMR (MeOD, 600 MHz), **20**

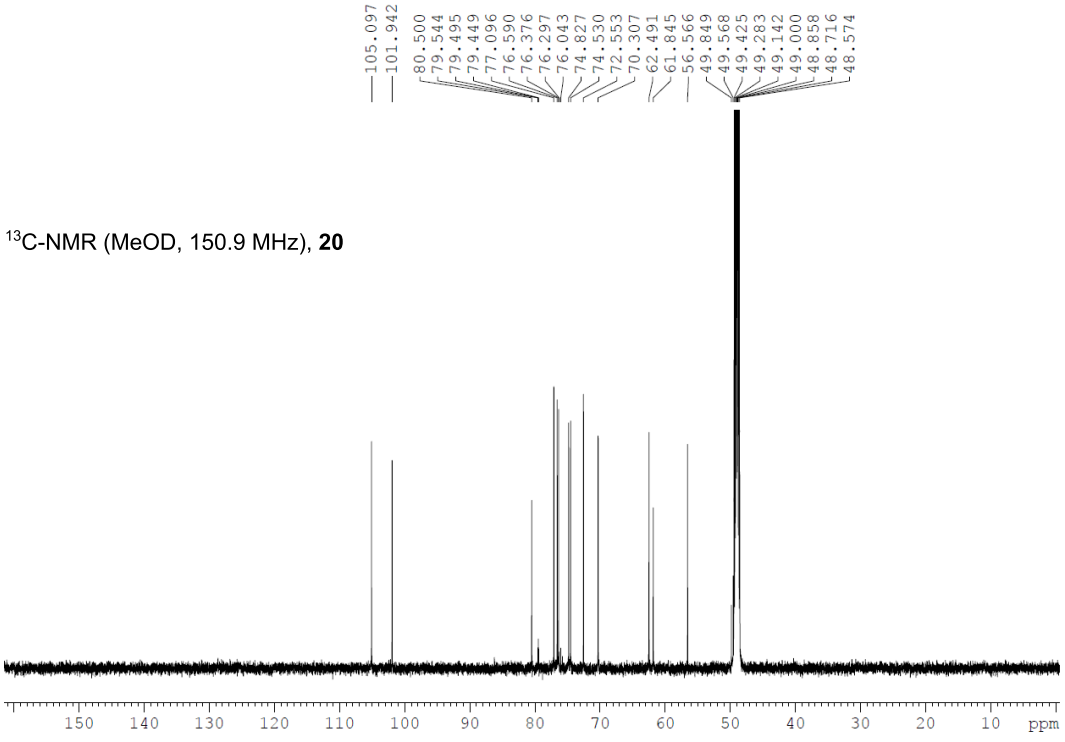

^{13}C-NMR (MeOD, 150.9 MHz), **20**

B.5 Structures of final stage compounds

Precursor molecules

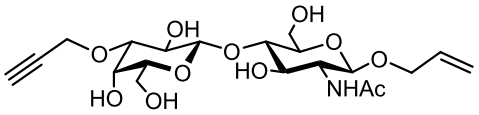

10

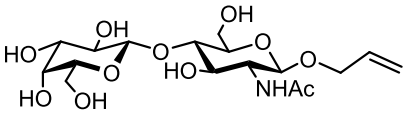

23

Click products

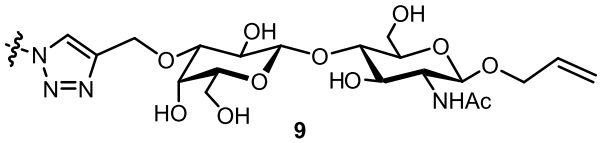

9

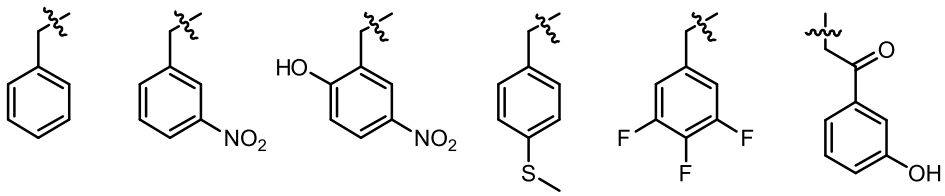

9a **9b** **9c** **9d** **9e** **9f**

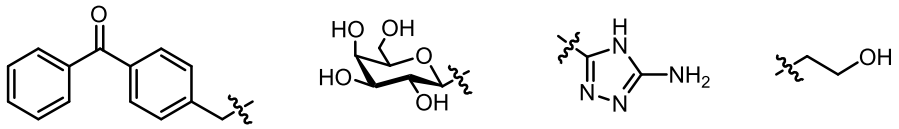

9g **9h** **9i** **9j**

Compounds for PET

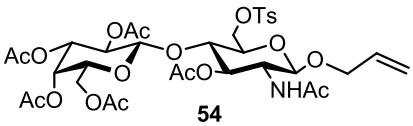

54

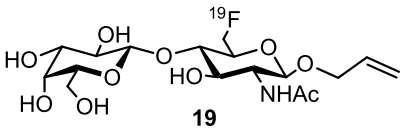

19

Lactose derivatives

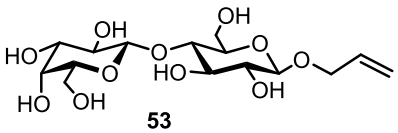

53

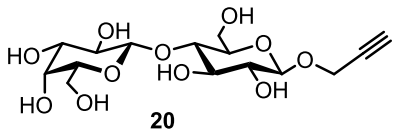

20

Appendix C

Acknowledgements

The presented work at the interface of chemistry, biophysics and medicine was performed in a highly inspiring atmosphere and with excellent support and contributions of many. Particularly, I would like to thank:

- **Prof. Dr. Jürgen Seibel** for the exciting and interdisciplinary galectin-1 project, his constant interest in my work and boundless enthusiasm for discussing chemical questions. I am indebted for his inexhaustible support in my academic education, the scientific freedom given to me and the possibility to participate in several cooperations, research projects and international conferences.

- **Dr. Teresa Tarragó** for being a great mentor for the last two years. I am deeply grateful for her outstanding commitment and unlimited efforts in promoting current und future steps of my scientific career. The **mentoring program** by the University of Würzburg has been an excellent complement to my Ph.D. thesis and, Tere, you turned it to such an exceptional experience. *¡Moltes gràcies!*

- The **Fonds der Chemischen Industrie** for financial support and the **Elite Network of Bavaria** for supporting my participation in the *Lindau Nobel Laureate Meeting 2013*.

- **Dr. Clemens Grimm** for introducing me into the research field of protein crystallography, his countless explanations and experienced advises. I am truly thankful for the possibility to perform all the crystallization experiments on my own in his lab and to be part of the single steps from crystal growing, synchrotron visits to structure determination.

- **Prof. Dr. Gisbert Schneider**, **Dr. Petra Schneider** and **Dr. Michael Reutlinger** for their warm welcome in Zürich and the opportunity to join SPR and ITC

experiments during my one-week stay. Your involvement enormously enriched our cooperation project and I greatly valued the scientific exchange and stimulating discussions.

- **Prof. Dr. Markus Sauer**, **Dr. Antonia Göhler**, **Dr. Sören Doose** and **Sebastian Letschert** for the exciting cooperation project on high resolution fluorescence microscopy of human cell surfaces. I highly appreciated the fruitful and enriching discussions and got fascinated by the intriguing power of your imaging techniques.

- My trainees **Nicolas Oppmann** and **Sophie Bender** for pushing forward the synthesis of LacNAc derivatives. Your independent and competent way of working had been of indispensable benefit for my projects and I really enjoyed working with you.

- **Anna Ulmer** and **Anne Neumann** for contributing to the galectin-1 project during your bachelor theses. Your research stays were a great pleasure and support to me!

- **Daniel Mann**, **Regina Wirth** and **Lisa Bischoff** for dedicating their practical trainings to carbohydrate synthesis and for enduring numerous column chromatographies.

- **Elisabeth Memmel** for creating such an enjoyable and motivating atmosphere in the lab, for always sharing her expertise and helpful advice, for expanding the galectin-1 project to the microarrays and for critical reading not only parts of this work. Your creative and amiable personality have greatly enriched my time in the Seibel group!

- **Dr. Matthias Grüne** and **Elfriede Ruckdeschel** for their competent and pleasant way of running the NMR facility.

- **Dr. Michael Büchner** and **Fritz Dadrich** for performing numerous mass spectrometry experiments.

- **Julian Görl** for his endless patience when guiding me through any computer-related "challenges".

- **Malte Timm**, **Jann-Patrick Pelz** and **Dr. Maria Ortiz Soto** for their support in planning and performing biochemical experiments.

- **Dr. Clemens Grimm**, **Dr. Maria Ortiz Soto**, **Elisabeth Memmel**, **Bernd Grünewald**, **Fabian Zieschang** and **Dr. Werner Bertleff** for careful proof-reading parts of my thesis.

- The Seibel group for the relaxing atmosphere and memorable excursions. In this context **Tim Walter**, **Alexander Mertsch** and **Michael Kraus** haven't been mentioned yet.
- **Dr. Christian Rewitz** and **Dr. Philipp Rudolf** for solving all of my LaTeX struggles.
- My dear friends **Jürgen**, **Sepp**, **Jo**, **Johannes**, **Eva** and **Markus** for all the great moments inside and outside of the lab and the unforgettable time in Würzburg.

Finally, I owe my thanks to my husband **Fabian**, my brother **Marco** and my parents **Gabriele** and **Werner** for their unconditional trust and support!